

Quantitative Transverse Relaxometry in Multiple Sclerosis

by

Md. Nasir Uddin

A thesis submitted in partial fulfillment of the requirements for the degree of

Doctor of Philosophy

Department of Biomedical Engineering
University of Alberta

© Md. Nasir Uddin, 2016

Abstract

Quantitative transverse relaxometry is an MRI method that has shown promise for study of iron accumulation and demyelination in healthy brain and in associated neurological disorders. Multiple sclerosis (MS) is one such neurodegenerative disorder in which iron accumulation in deep grey matter (DGM), demyelination in white matter and brain atrophy have been observed. This thesis concerns the development and application of transverse relaxation mapping to evaluate iron sensitivity and track the disease progression in relapsing-remitting MS (RRMS) using high field (4.7 T) as well as standard clinical (1.5 T) MRI.

A two-year longitudinal study was conducted to evaluate the changes in iron accumulation in MS DGM using spin echo based transverse relaxation rate (R_2) mapping methods and atrophy measurements. Relative to controls, measurable differences in DGM structures using R_2 mapping showed strong association with disease severity in patients with RRMS, particularly in the globus pallidus and the pulvinar. Atrophy of the globus pallidus over two years was related to R_2 increase.

At high fields such as 4.7 T, tissue heating is a major limitation of R_2 mapping using a typical multi-echo spin echo sequence. This sequence typically uses 16-32 echoes. To overcome the tissue heating limitation reduced echo train lengths were evaluated. Stimulated echo compensation was used to account for the use of non-ideal refocusing pulses. Consistent R_2 values were found with as few as 4 echoes compared to 20 echoes. Radiofrequency power savings through the use of reduced number of echoes enabled increased slice coverage without effects on R_2 from incidental magnetization transfer.

Quantitative transverse relaxometry methods can be used to evaluate iron accumulation in human brain. However, added iron specificity may be obtained by using subtractive measures. The benefits and limitations of within and between field difference transverse relaxometry methods ($R_2' = R_2^* - R_2$ and Field Dependent Relaxation Increase FDRI) for iron accumulation were compared in human brain and in an iron-doped agar phantom using 4.7 and 1.5 T. Using 4.7 T, R_2' was found to provide more specific iron measures due to its small intercept with estimated post-mortem iron concentration. However, in white matter, R_2' was highly sensitive to fiber orientation relative to B_0 which increases with field strength, while FDRI was much less sensitive to this orientation. Overall for brain iron correlation, the transverse relaxation difference methods added little value over a single R_2^* measurement at highest available field, which was 4.7 T.

Proton density (PD) and T_2 -weighted images have been part of clinical MRI protocols for MS for many years. From these images, quantitative T_2 maps were obtained using indirect and stimulated echo compensation. After demonstrating feasibility in healthy controls, seven-year changes in T_2 were examined retrospectively and correlated with disease severity and brain atrophy in MS brain. Changes in T_2 in brain structures particularly in globus pallidus, caudate and posterior internal capsule showed significant correlations with disease severity in MS over 7 years. Given the wide use of PD and T_2 -weighted images in MS clinical trials, this retrospective T_2 method may provide an additional measure of disease progression and state. Furthermore, the use of a dual echo PD and T_2 -weighted FSE would enable tracking of quantitative T_2 in clinical exams.

Preface

The research projects in this thesis received ethics approval from the University of Alberta Research Ethics Board. Chapter 2 of this thesis has been published as Uddin MN, Lebel RM, Seres P, Blevins G, Wilman AH, “*Spin echo transverse relaxation and atrophy in multiple sclerosis deep grey matter: A 2-year longitudinal study*”, *Multiple Sclerosis Journal* (2015); DOI: 10.1177/1352458515614091. Mr. Uddin was involved in study design, data analysis and drafted the original version of the manuscript. Dr. Lebel was involved in MRI method development and reviewing the manuscript. Mr. Seres was involved in recruiting volunteers and patients, data acquisition as well as reviewing the manuscript. Dr. Blevins performed clinical assessment of the MS patients and reviewed the manuscript. Dr. Wilman was the supervisory author and was involved with concept formulation, and manuscript composition. Chapter 3 has been published as Uddin MN, Lebel RM, Wilman AH, “*Transverse Relaxometry with Reduced Echo Train Lengths via Stimulated Echo Compensation*”, *Magnetic Resonance in Medicine* (2013) 70:1340–1346; doi: 10.1002/mrm.24568. Mr. Uddin performed all experimental work including data acquisition and analysis, and drafted the original version of the manuscript. Dr. Lebel reviewed the manuscript. Dr. Wilman was the supervisory author and was involved with concept formulation, study design and manuscript composition. Chapter 4 has been published as Uddin MN, Lebel RM, Wilman AH, “*Value of transverse relaxometry difference methods for iron in human brain*”, *Magnetic Resonance Imaging* (2015); doi: 10.1016/j.mri.2015.09.002. Mr. Uddin performed the experimental work, data collection, and analysis, and manuscript preparation. Dr. Wilman was the supervisory author and was involved with concept formulation and manuscript composition. All the authors were involved in editing and review of the manuscript. Chapter 5 has been submitted to *Journal of MRI* as “*Quantitative T_2 and atrophy in multiple sclerosis: A retrospective 7-year feasibility study using standard clinical brain images*”. Mr. Uddin was involved in data collection and analysis as well as drafting the original version of the manuscript. Ms. McPhee was involved in method development, data collection and revisions. Dr. Blevins performed clinical assessment of the MS patients and revisions. Dr. Wilman was the supervisory author and was involved with concept formulation and manuscript composition. All the authors read and approved the final version of the manuscript.

Dedicated

To

The memory of my father Md. Abdul Mazid (1940-2015)

Acknowledgements

I would like to express my deepest and sincere gratitude to my supervisor Dr. Alan Wilman for his constant guidance, tremendous support throughout my PhD. I feel very fortunate to have had such an excellent and conscientious supervisor. He has proven to be an exceptional role model.

I would also like to express my gratitude to my supervisory committee members (Dr. Richard Thompson and Dr. Keith Wachowicz) as well as to the remaining members of my examining committee (Dr. Atiyah Yahya, Dr. Christian Beaulieu and Dr. Jeff Dunn) for their in depth questions and comments, and inspiring discussions.

I would like to thank Kelly McPhee for her discussions on research, constructive suggestions and assistance in preparing for my defense. I appreciate the help from other students in Dr. Wilman's lab: Dr. Hongfu Sun, Dr. Andrew Walsh, Ahmed Elkady and Zhuozhi Dai. I am thankful to Peter Seres for helping me set up and perform my MRI experiments. I thank all the volunteers and patients with multiple sclerosis for their time participating in experiments.

Last but not least, I would like to thank my wife Sohely Pervin, and other family members for their kind support, love, sacrifice and guidance. A special thanks to our newborn son Saabiq Uddin who delighted me with his yells and smiles when I was preparing for defense.

Table of Contents

Chapter 1.	Introduction	1
1.1	Thesis Overview.....	1
1.2	Physics of MRI.....	1
1.2.1	Nuclear magnetization	2
1.2.2	Bloch equations and relaxation.....	3
1.2.3	Relaxation mechanism	6
1.2.4	Cross relaxation, chemical exchange and magnetization transfer	10
1.2.5	Free induction decay.....	12
1.2.6	Signal detection and reciprocity.....	13
1.3	Imaging.....	14
1.3.1	Contrast.....	14
1.3.2	Signal localization.....	15
1.3.3	Slice selection	16
1.3.4	Frequency Encoding	17
1.3.5	Phase Encoding.....	18
1.3.6	<i>K</i> -space and sampling requirement.....	18
1.3.7	Effect of field strength	21
1.4	Quantitative Relaxometry	23
1.4.1	Quantitative T_2 measurement.....	23

1.4.2	Quantitative T_2^* measurement	33
1.4.3	Previous work on transverse relaxometry	35
1.5	Human brain, Multiple Sclerosis and Iron	37
1.5.1	Brief description of human brain	37
1.5.2	Brain Iron	39
1.5.3	Multiple Sclerosis and MRI	42
1.5.4	Brain atrophy of MS	45
1.6	Thesis Objective	47
1.7	References	48
Chapter 2.	Spin echo transverse relaxation and atrophy in multiple sclerosis deep grey matter: A 2-year longitudinal study	61
2.1	Abstract	61
2.2	Introduction	62
2.3	Methods	64
2.3.1	Subjects	64
2.3.2	Magnetic resonance imaging	65
2.3.3	R_2 mapping.....	65
2.3.4	Image analysis.....	65
2.3.5	Statistical analysis.....	66
2.4	Results	69
2.5	Discussion	74

2.6	Acknowledgements	77
2.7	References	77
Chapter 3.	Transverse Relaxometry with Reduced Echo Train Lengths via Stimulated Echo Compensation	82
3.1	Abstract	82
3.2	Introduction	83
3.3	Methods	84
3.3.1	MRI Acquisition	84
3.3.2	T ₂ Fitting and Analysis	85
3.4	Results	85
3.5	Discussion	89
3.6	Acknowledgements	94
3.7	References	94
Chapter 4.	Value of transverse relaxometry difference methods for iron in human brain.....	100
4.1	Abstract	100
4.2	Introduction	101
4.3	Materials and Methods	103
4.3.1	MRI Acquisitions.....	103
4.3.2	In-vivo Experiments.....	104
4.3.3	Phantom Preparation.....	104

4.3.4	Data Analysis	105
4.3.5	Iron concentration using post-mortem data	105
4.3.6	Statistical Analysis.....	106
4.4	Results	106
4.5	Discussion	115
4.6	Acknowledgements	119
4.7	References	119
Chapter 5.	Quantitative T₂ and atrophy in multiple sclerosis: A retrospective 7-year feasibility study using standard clinical brain images.....	126
5.1	Abstract	126
5.2	Introduction	127
5.3	Methods.....	128
5.3.1	Subjects.....	128
5.3.2	MRI data acquisition.....	128
5.3.3	T ₂ mapping.....	130
5.3.4	Method Validation	130
5.3.5	Image analysis.....	132
5.3.6	Statistical analysis.....	133
5.4	Results	133
5.5	Discussion	138
5.6	Acknowledgements	142

5.7	References	142
Chapter 6.	Conclusion	148
6.1	Research Outcomes	148
6.1.1	Iron dynamics in MS DGM using 2-year longitudinal study	148
6.1.2	R ₂ mapping using reduced echoes	148
6.1.3	Value of transverse relaxometry difference methods	149
6.1.4	Long-term change in MS using only retrospective clinical MRI	149
6.2	Significant findings	150
6.3	Summary of the findings	150
6.4	Limitations	151
6.5	Future Work	152
6.6	In Closing	152
6.7	References	153
Bibliography.....	155

List of Tables

Table 1.1: Transverse relaxation times in healthy brain tissue from previous work	36
Table 2.1: Baseline demographic and clinical data	64
Table 2.2: Baseline Morphologic data	67
Table 2.3: Two year changes in R_2 and volume	72
Table 2.4: Correlation coefficients of relaxation rates (R_2) and normalized volumes in subcortical territories with MSSS, EDSS and Disease Duration (DD) over two years from patients	73
Table 2.5: Correlation coefficients of change in R_2 (ΔR_2) with change in volume (ΔV) in subcortical GM over two years	74
Table 3.1: Average T_2 values from 4 subjects for different number of slices and echoes using the stimulated echo fit.....	90
Table 4.1: Transverse relaxation rates (s^{-1}) and $FDRI/\Delta B_0$ (s^{-1}/T) in grey matter at 1.5 T and 4.7 T, with estimated iron deposits (mg/100g fresh wt.) from seventeen healthy subjects*	107
Table 4.2: Transverse relaxation rates (s^{-1}) and $FDRI/\Delta B_0$ (s^{-1}/T) in white matter at 1.5 T and 4.7 T, from seventeen healthy subjects*	108
Table 4.3: Slopes, y-intercepts and correlation at 1.5 T and 4.7 T obtained from caudate, putamen and globus pallidus*	113
Table 5.1: Patients demographic and clinical data.....	128
Table 5.2: Patients morphologic data.....	130
Table 5.3: Transverse relaxation times (T_2) in ms obtained from seven healthy controls using MESE via ISEC, two- point ISEC and two-point exponential fitting	131
Table 5.4: Transverse relaxation times (T_2) in ms obtained from fourteen patients with MS. Percent changes over time are reported with effect size.....	134

List of Figures

Figure 1.1: Relaxation principle: a) Spectral density functions $J(\omega_0)$ for three substances: bound water (long τ_c), structured water (medium τ_c) and free water (short τ_c). The number of protons undergoing oscillations at ω_0 is largest for structured water. b) Variation of relaxation times T_1 and T_2 with the rate of molecular tumbling. Molecular tumbling rate increases from bound water (large molecule), structured water (soft tissue) to free water (small molecule) (based on [7])...... 9

Figure 1.2: Magnetization transfer takes place via cross-relaxation or chemical exchange mechanisms..... 11

Figure 1.3: Magnetization transfer: Off-resonant RF pulse saturates the magnetization associated macromolecular protons of bound pool but not magnetization in free pool. The exchange of magnetization between the pools results in the reduction of magnetization of free water pool and hence its signal intensity. 12

Figure 1.4: MRI image of a brain (left) and corresponding k-space image (right) 20

Figure 1.5: Spin echo (a) and gradient echo (b) sequences with k-space trajectories 21

Figure 1.6: Multiecho spin echo (MESE) pulse sequence. Both excitation and refocusing pulses are slice selective. 25

Figure 1.7: Extended phase graph as a function of time for an arbitrary angle based on two refocusing pulses. Vertical axis is phase and horizontal axis is time. Solid lines along any diagonal pathways have phase changes while lines along the horizontal pathways have no phase changes during free precession period. Five echoes are formed with amplitude factors $M_{1,-1}$, $M_{1,-1,-1}$, $M_{1,0^*,1}$, $M_{0,1,-1}$ and $M_{1,1,-1}$ 30

Figure 1.8: Different coherent pathways for echo formation at constant echo spacing showing spin echoes (circle) and stimulated echo (asterisk)..... 32

Figure 1.9: (left) Effect of stimulated echoes for arbitrary flip angles (simulated with $T_1 = \infty$, $T_2 = 100\text{ms}$). 180° refocusing pulse follows perfect exponential decay while other lower flip angles experience stimulated echo. Increased amplitude of the second echo is due to

stimulated echo contribution. (Right) Ratio of first and second echo amplitudes for 90° pulse versus flip angle.	33
Figure 1.10: Pulse sequence diagram for a multiecho gradient echo sequence. Four echoes are shown. A monopolar acquisition is used to minimize artifacts between echoes.	34
Figure 1.11: Sketch of a typical nerve cell in the brain	37
Figure 1.12: Axial T1-MPRAGE (top row) and T2-FSE (bottom row) images showing several sub-cortical grey matter territories.....	40
Figure 2.1: R ₂ maps (a-c) and T ₁ -weighted image (d) from a 47 year MS patient. DGM ROIs are illustrated in color on the enlarged view (c) with manual regions of interest and on (d) obtained using FSL-FIRST segmentation. Head of caudate nucleus (cyan), putamen (magenta), globus pallidus (blue), thalamus (green), pulvinar (orange), substantia nigra (yellow) and red nucleus (red). Note thalamus includes pulvinar in (d).	67
Figure 2.2: Baseline and two year measurements of spin echo R ₂ and normalized volumes for some DGM regions and frontal WM from subjects with MS (red) and matched controls (green). GP, Globus pallidus; CD, head of caudate nucleus; PUT, putamen; TH, thalamus; RN, red nucleus; SN, substantia nigra; and FWM, frontal white matter. For volume measurements, thalamus included pulvinar, while for R ₂ mapping the pulvinar thalamus was considered separately.	68
Figure 2.3: Measured MSSS versus predicted MSSS obtained from multiple regression of the 2-year R ₂ difference measurements. Globus pallidus, pulvinar, thalamus and substantia nigra are included in the regression model. The regression line equation is $MSSS = 0.49*\Delta R_{2GP}+0.57*\Delta R_{2PUL}+0.56*\Delta R_{2SN}-1.84*\Delta R_{2TH}+3.31$, where ΔR_{2GP} , ΔR_{2PUL} , ΔR_{2SN} and ΔR_{2TH} are the differences in R ₂ over 2 years for globus pallidus, pulvinar, substantia nigra and thalamus excluding pulvinar.	69
Figure 2.4: Significant correlations between two year difference R ₂ measurements (ΔR_2) and MS severity score (MSSS) obtained by regression analysis for single structures: a) Globus pallidus, b) Pulvinar thalamus, c) Substantia nigra, and d) Thalamus.	71

Figure 2.5: Relationship between two year changes in relaxation rate (ΔR_2) and volume (ΔV) in globus pallidus for a) controls and b) patients with MS. 74

Figure 3.1: a) Signal decay from one subject for three territories, b-h) effect of number of echoes on the measured T_2 relaxation time using exponential fit or stimulated echo compensation averaged over 10 subjects in different brain regions. Error bars indicate inter-subject standard deviations. Due to heterogeneous B_1 and slice-selective refocusing, the exponential fit provides erroneous results in all cases. In contrast, stimulated echo compensation provides good results for four or more echoes, except in the case of CSF, where additional echoes are needed. 87

Figure 3.2: Effect of number of echoes on normalized flip angle maps (retrospective): a) 2 echoes, b) 3 echoes, c) 4 echoes and d) 20 echoes. Flip angle maps achieve stability with 3 or more echoes. 88

Figure 3.3: In-vivo R_2 maps: top row, stimulated echo fit; bottom row, exponential fit. In (a,d), 20 echoes are used, while (b,e) only 4 echoes. Difference maps are shown in (c,f) with stimulated echo (c) showing minimal change, but drastic differences for the exponential fit (f). Intensity scale is from 2.5 to 30 s^{-1} in images (a,b,d,e) and 0.68 to 7.5 s^{-1} for difference images (c,f). 89

Figure 3.4: In-vivo R_2 maps using stimulated echo compensation: a) 1 slice and 20 echoes, b) 2 slices and 20 echoes, c) 4 slices and 10 echoes and d) 8 slices and 5 echoes. Corresponding normalized flip angle maps for a) and d) are shown in (e, f) respectively, demonstrating consistent flip angle estimation with short echo trains. 91

Figure 3.5: Incidental magnetization transfer (MT) effects illustrated through the relationship between relative SNR and the number of slices acquired in four brain territories averaged over 4 subjects. As slice number was increased past 2, the number of echoes was correspondingly decreased to maintain the same total number of refocusing pulses (slices-echoes: 1-20, 2-20, 4-10, 8-5). Error bars represent inter-subject standard deviations. 93

Figure 4.1: In-vivo transverse relaxation maps from 4.7 T and 1.5 T: (a, b) R_2 , (c, d) R_2^* , (e, f) R_2' , where (a, c, e) were acquired at 4.7 T and (b, d, f) at 1.5 T. FDRI, which is the R_2 difference between fields, is shown in (g). Intensity scales are shown at right for the top and bottom rows. 109

Figure 4.2: In-vivo R_2^* maps at 4.7 T showing the effect of linear background field correction. (a, d) R_2^* map without background field correction, (b, e) R_2^* after background field correction and (c,f) difference maps of (a, b) and (d, e). Intensity scale from 0 to 100 s^{-1} for (a, b, d, e), while 0 to 50 s^{-1} for (c, f). Note the strong air-tissue susceptibility gradient arising from tissue near the frontal sinuses..... 110

Figure 4.3: Scatter plots: Relaxation rates (R_2 , R_2^* and R_2') versus estimated post-mortem iron concentration [Fe]: (a,c,e) at 4.7 T; (b,d,f) at 1.5 T; and (g) FDRI versus [Fe]. Best fit solid lines and linear regression parameters obtained using all data are shown, while dashed lines fit only caudate, putamen and globus pallidus (with regression parameters in Table 4.3). Note three different y-axis scales are used for R_2 (a,b), R_2^* (c,d) and difference methods (e-g). 111

Figure 4.4: Relationship between magnetite concentrations, relaxation rate R_2 and FDRI for eight different concentrations of iron in 1% agar gel. Linear regression parameters and best fit lines are shown. An example R_2 map from 1.5 T is shown in the inset. 112

Figure 4.5: (a-g) Box plots of transverse relaxation rates (R_2 , R_2^* , R_2') and FDRI (s^{-1}) in WM from seventeen healthy subjects with fiber orientations predominantly perpendicular (posterior corpus callosum, PCC and Optic radiation, OR) or parallel (posterior internal capsule, PIC and centrum semiovale, CS) to the main magnetic field. Red plus signs in the plots are outliers. Fractional anisotropy color maps obtained at 4.7 T (h-j) from one subject showing WM ROIs and fiber directions: (h) OR (green, anterior-posterior), (i) PIC (blue, inferior-superior), PCC (red, left-right), and (j) CS (blue, inferior-superior). Note two different y-axis scales are used for R_2 , R_2^* (a-d) and difference methods (e-g). 114

Figure 5.1: (a) Normalized flip angle map from a healthy brain obtained using double angle method at 1.5 T; (b) The normalized flip angle profiles from seven healthy subjects and the mean flip angle profile (thick line) obtained along the horizontal box in (a). 135

Figure 5.2: R_2 ($1/T_2$) maps obtained from a 29 year old healthy volunteer using: (a) full MESE via ISEC with actual flip angle map; (b, c) two-point exponential fit with PD and T_2 -weighted images (d, e) two-point ISEC fits using mean flip angle map averaged over seven healthy subjects; (b, d) FSE180° and (c, e) FSE150°. Note the exponential results differ greatly with flip angle (b vs. c), while the two point ISEC fits do not (d vs. e). 136

Figure 5.3: Baseline (a-c) and 7 year images (d-f) from a 31 year old MS patient. (a, d) Proton density (PD), (b, e) T₂-weighted spin echo images and (c, f) R₂ (1/T₂) maps with intensity scale.. R₂ values are increased in deep grey matter (head of caudate and globus pallidus) and ventricular enlargement occurs over 7 years..... 137

Figure 5.4: Baseline and 7-year T₂ measurements using two-point ISEC method for some DGM and WM structures from patients with MS. Thick black line is the averaged value over the MS cohort. Note different y-axis limits are used in most cases. b: baseline and f: final time point. 138

Figure 5.5: Predictors of disease severity and disability in MS using multiple regressions of the 7 year R₂ difference measurements with MS severity scores (MSSS) and with EDSS scores. Globus pallidus and caudate nucleus are included in the regression models. The regression line equations: MSSS (after 7 years) = $-0.71 \cdot \Delta T_{2GP} - 0.48 \cdot \Delta T_{2CD} + 1.83$; EDSS (after 7 years) = $-0.29 \cdot \Delta T_{2GP} - 0.13 \cdot \Delta T_{2CD} + 2.05$; where ΔT_{2GP} and ΔT_{2CD} are the differences in T₂ over 7 years for globus pallidus and head of caudate nucleus respectively..... 139

List of Symbols and Acronyms

\vec{B}	Magnetic field vector
B_0	Static magnetic field
B_1	Applied radiofrequency field
B_1^-	Receiver sensitivity of the coil
B_1^+	Transmit field
\vec{B}_L	Local dipolar magnetic field
BBB	Blood-brain barrier
BET	Brain extraction tool
BFG	Background field gradient
BW	Bandwidth
CD	Caudate nucleus
CGM	Cortical grey matter
CIS	Clinically isolated syndrome
CNS	Central nervous system
CPMG	Carr-Purcell-Meiboom-Gill pulse sequence
CS	Centrum semiovale
CSF	Cerebrospinal fluid
CT	Computed tomography
D	Diffusion coefficient
DD	Disease duration
DESPOT2	Driven equilibrium single pulse observation of T2
DGM	Deep grey matter
E	Energy
EDSS	Expanded Disability Status Scale
EPG	Extended phase graph
ES	Effect size
ESP	Echo spacing
ETL	Echo train length

FDR	False discovery rate
FDR1	Field Dependent R ₂ Increase
FIRST	FMRIB's integrated registration and segmentation tool
FLAIR	Fluid attenuated inversion recovery
FLASH	Fast low angle shot
FMRIB	Functional MRI of the brain
FOV	Field of view
FSE	Fast spin echo
FWM	Frontal white matter
G	Autocorrelation function
\vec{G}	Magnetic field gradient vector
G_{sl}	Slice select gradient
GCC	Genu of corpus callosum
GE	Gradient echo
GM	Grey matter
GP	Globus pallidus
GRASE	Gradient and spin echo
iMT	Incidental magnetization transfer
ISEC	Indirect and stimulated echo compensation
J	Spectral density function
K	Unit of k-space (inverse of distance)
k_B	Boltzmann constant
\vec{M}	Magnetization vector
M_0	Equilibrium magnetization
$M_{x,y,z}$	Magnetization components
\vec{M}_z	Longitudinal magnetization vector
\vec{M}_{xy}	Transverse magnetization vector
M_T^-	Dephasing transverse magnetization
$(M_T^*)^-$	Rephasing transverse magnetization
mcDESPOT	Multicomponent driven equilibrium single-pulse observation of T ₁ and T ₂

MESE	Multi-echo spin echo
MRI	Magnetic resonance imaging
MS	Multiple Sclerosis
MPRAGE	Magnetization Prepared Rapid Gradient Echo
MSSS	Multiple Sclerosis Severity Score
MT	Magnetization transfer
MWF	Myelin water fraction
n	Echo number
N_p	Number of spins aligned parallel to applied field
N_a	Number of spins aligned antiparallel to applied field
N_s	Number of spins available in the sample
NA	Not applicable
nB_1	Normalized flip angle
nB_{1av}	Normalized flip angle averaged over healthy subjects
N_{av}	Number of averaging
NAWM	Normal appearing white matter
NMR	Nuclear magnetic resonance
OR	Optic radiation
PBVC	Percentage brain volume change
PC	Percent change
PCC	Posterior part or splenium of corpus callosum
PD	Proton density
PDw	Proton density-weighted
PET	Positron emission tomography
PIC	Posterior internal capsule
PPMS	Primary progressive Multiple Sclerosis
PRMS	Progressive Relapsing Multiple Sclerosis
PUL	Pulvinar nucleus
PUT	Putamen
QSM	Quantitative susceptibility mapping
r	Correlation coefficients

R_1	Longitudinal relaxation rate
R_2	Irreversible transverse relaxation rate
R_2^*	Net transverse relaxation rate
R_2'	Reversible transverse relaxation rate
R_x	Rotational matrix
RF	Radiofrequency
RN	Red nucleus
ROI	Region of interest
RRMS	Relapsing Remitting Multiple Sclerosis
S_0	Signal intensity at equilibrium
SAR	Specific absorption rate
SD	Standard deviation
SE	Spin echo
SEC	Stimulated echo compensation
SIENAX	Structural Image Evaluation using Normalization of Atrophy Cross-sectional
SIENA	Structural Image Evaluation using Normalization of Atrophy
SN	Substantia nigra
SNR	Signal to noise ratio
SPECT	Single-photon emission tomography
SPMS	Secondary Progressive Multiple Sclerosis
SSFP	Steady state free precession
STIR	short τ inversion recovery
\vec{s}	Spin angular momentum
S_0	Signal intensity at equilibrium
$S(t)$	Signal induced across an RF coil
SWI	Susceptibility weighted imaging
T	Temperature
T	Tesla
T_1	Longitudinal relaxation time
T_2	Irreversible transverse relaxation time

T_2^*	Net transverse relaxation time
T_2'	Reversible transverse relaxation time
T_2w	T ₂ -weighted
TE	Echo time
TH	Thalamus
TI	Inversion time
TR	Repetition time
WB	Whole brain
WM	White matter
α	Flip angle
α_R	Refocusing flip angle
$\Delta x, y, z$	Voxel size
ΔG	Phase encoding step size
Δk_x	k-space step size along x direction
Δk_y	k-space step size along y direction
ΔT_2	Change in relaxation time over time
ΔV	Change in volume over time
γ	Gyromagnetic ratio
\hbar	Planck's constant
$\mathcal{H}_{dipolar}$	Dipolar Hamiltonian
ϑ_0	Larmor frequency
$\vec{\mu}$	Magnetic moment
μ_0	Permeability in the free space
ρ	Spin density
τ	RF pulse duration
τ_c	Correlation time
τ_D	Diffusion correlation time
ω	Angular frequency
ω_0	Larmor angular frequency

Chapter 1. Introduction

1.1 Thesis Overview

Magnetic Resonance Imaging (MRI) is a very successful imaging modality commonly used in clinical practice and for medical research purposes to provide visualization of internal structures of biological tissues. Compared to other imaging modalities such as x-ray, computed tomography (CT), positron emission tomography (PET) and single-photon emission tomography (SPECT), MRI uses non-ionizing radiofrequency (RF) radiation and provides excellent soft-tissue contrast that can be customized for anatomical identification and to understand the effect of diseases. For example, multiple sclerosis (MS) is a neurodegenerative disease which affects the central nervous system with inflammation, demyelination, and axonal loss. MRI is an essential tool to investigate MS disease processes and evolution using various contrast mechanisms at different time points.

This thesis is a combination of published research articles bound by introduction and conclusion chapters. In the first introductory chapter, the fundamental principles of MRI are described. This is followed by a short description of the brain, MS and the objectives of the thesis. Chapter 2 describes a two-year longitudinal study of quantitative T_2 and brain atrophy measurements in MS at 4.7 T. Quantitative T_2 in human brain using stimulated echo compensation via reduced echoes is presented in Chapter 3. Chapter 4 presents evaluation of brain iron using within and between field transverse relaxometry methods. Chapter 5 comprises a retrospective MRI study on MS using a two-echo T_2 fitting approach on a standard clinical scanner (1.5 T). It is followed by brief concluding remarks and recommended future directions in Chapter 6.

1.2 Physics of MRI

Basic MRI descriptions can be found in a series of textbooks [1-5]. In this work we refer mainly to the following text book [4].

1.2.1 Nuclear magnetization

Nuclear magnetic resonance arises from the interaction between the spin angular momentum and the external magnetic field producing resonant behavior of nuclei. Spin angular momentum, most commonly known just as spin, is the intrinsic property of nuclei of atoms as well as of electrons. The spin angular momentum is a vector and its magnitude can be expressed as

$$s = \hbar\sqrt{I(I + 1)} \quad (1.1)$$

where \hbar is the Planck's constant divided by 2π and I is the spin quantum number. Only nuclei with an odd number of protons and/or neutrons give rise to non-zero net spin and hence to the nuclear magnetic resonance phenomenon. The proton has a spin $\frac{1}{2}$ and possesses a nuclear magnetic moment associated with \vec{S} which is expressed as

$$\vec{\mu} = \gamma\vec{S} \quad (1.2)$$

where γ is the gyromagnetic ratio and $\gamma/2\pi = 42.576$ MHz/T for proton.

The orientation of spins in a sample is random and the total magnetic moment is close to zero in the absence of an external magnetic field. When placed in a magnetic field, spins align parallel and antiparallel to the applied magnetic field $\vec{B}_0 = B_0\hat{z}$. However, a whole sample contains many spins and the resultant magnetic moments are more likely to be aligned with the field, though the likelihood is relatively small. There are two quantized energy levels possessed by the magnetic moment of proton along the \hat{z} -axis. The energy difference between the two levels is given by

$$\Delta E = \gamma\hbar B_0 \quad (1.3)$$

The difference in energy levels leads to an imbalance in spin population, using the Boltzmann distribution formula

$$\frac{N_p}{N_a} = \exp\left(\frac{\Delta E}{k_B T}\right) \quad (1.4)$$

where N_p and N_a are the number of spins aligned parallel and antiparallel to the applied field, T is the temperature of the spin system and k_B is the Boltzmann constant. Since the energy difference between the levels is so small compared to the thermal energy, Eq. (1.4) can be written as

$$\frac{N_p}{N_a} \approx 1 + \left(\frac{\Delta E}{k_B T} \right). \quad (1.5)$$

The population difference is therefore

$$N_p - N_a \approx N_s \frac{\gamma \hbar B_0}{2k_B T} \quad (1.6)$$

where N_s is the total number of spins available in the sample. The total net magnetic moment or bulk magnetization, M , is the sum of all the individual magnetic moments μ , and can be written as [6]

$$M_0 = |\vec{M}_z| = \frac{\gamma \hbar}{2} (N_p - N_a) \approx N_s \frac{\gamma^2 \hbar^2 B_0}{4k_B T} \quad (1.7)$$

for proton.

Moreover, the energy difference between the levels is equivalent to the energy of electromagnetic wave, because the magnetic resonance phenomenon is achieved by applying an oscillatory magnetic field perpendicular to μ_z with frequency ϑ_0 , is given by

$$\Delta E = h\vartheta_0. \quad (1.8)$$

Combining Equations (1.3) and (1.8) yields Larmor equation

$$\omega_0 = \gamma B_0 \quad (1.9)$$

where $\omega_0 = \vartheta_0/2\pi$, angular frequency.

1.2.2 Bloch equations and relaxation

From the basic concepts of physics, if we place a spin system in the magnetic field \vec{B} , the magnetic moment μ of the system experiences a torque which is proportional to the temporal derivative of the angular momentum. Thus the equation of motion for a single magnetic moment can be generalized for the total magnetization \vec{M} as

$$\frac{d\vec{M}(t)}{dt} = \gamma \vec{M}(t) \times \vec{B}(t) \quad (1.10)$$

where $\vec{B}(t)$ may contain the time-dependent components as well as the static magnetic field \vec{B}_0 and torque $\vec{T} = \frac{d\vec{s}}{dt} = \vec{M} \times \vec{B}$.

The simple solutions of Eq. (1.10) describing a magnetization vector in a static magnetic field ($B = B_0 \hat{z}$) are

$$M_z(t) = M_z(0) \quad (1.11)$$

$$M_{xy}(t) = M_{xy}(0)e^{-i\omega_0 t} \quad (1.12)$$

where M_z and M_{xy} are the longitudinal (along the applied field) and transverse magnetization (perpendicular to the field) respectively. As well, transverse magnetization is complex and defined by $M_{xy} = M_x + iM_y$, ω_0 is the precessional frequency of the transverse magnetization as defined earlier in Eq. (1.9). Thus any transverse magnetization precesses with frequency ω_0 in xy -plane while longitudinal magnetizations remain stationary.

As there is no net transverse magnetization of a spin system in thermal equilibrium, a perturbation is required to initiate transverse magnetization and induce precession can be achieved by applying time dependent oscillating magnetic field, rotating about \vec{B}_0 at the Larmor frequency. Bulk magnetization of the sample now precesses about the combined field

$$B = \vec{B}_0 + \vec{B}_1 \quad (1.13)$$

It is easier to visualize the process if we use a new frame of reference, rotating about \vec{B}_0 at Larmor frequency, where precession about \vec{B}_0 appears stationary.

In the transverse plane,

$$\vec{B}_1 = 2B_1^{max}(t)\cos\omega t\hat{x} \quad (1.14)$$

where B_1^{max} is the maximum amplitude of the applied field, ω is the angular frequency of the RF field and \hat{x} is a unit vector along x -axis. This field oscillates only in one direction and can be decomposed into two circularly polarized fields rotating in opposite direction about the z axis

$$\vec{B}_1(t) = \vec{B}_1^+(t) + \vec{B}_1^-(t) \quad (1.15)$$

Where $\vec{B}_1^+(t) = B_1^{max}(t)(\cos\omega t\hat{x} + \sin\omega t\hat{y}) = B_1^{max}(t) e^{i\omega t}$ (1.16)

And $\vec{B}_1^-(t) = B_1^{max}(t)(\cos\omega t\hat{x} - \sin\omega t\hat{y}) = B_1^{max}(t) e^{-i\omega t}$ (1.17)

However, the B_1^+ component remains stationary in the rotating frame of reference while the B_1^- component rotates in the negative sense at a rate of 2ω and influences the spins to the

order of $\left(\frac{B_1}{2B_0}\right)^2$ which is very small number. Thus the effective magnetic field approached by the spin system in the rotating frame of reference is

$$\overrightarrow{B_{eff}} = B_1^{max} \hat{x}. \quad (1.18)$$

The solution of the Bloch Eq. with $\overrightarrow{B} = \overrightarrow{B_{eff}}$ is similar to Eqs. (1.11, 1.12) but with magnetization precessing about \hat{x} of rotating frame of reference by an angle α is then

$$\alpha = \int_0^\tau \gamma B_1(t) dt \quad (1.19)$$

where τ is the RF pulse duration. For a rectangular pulse envelope this flip angle is reduced to

$$\alpha = \gamma B_1 \tau. \quad (1.20)$$

The flip angle for the desired magnetization vector depends on the duration of the pulse and the amplitude of the applied B_1 field.

As stated earlier, a torque is induced on the magnetization due to B_1 field and consequently the magnetization M rotates away from its equilibrium position while continuing around the z -axis. However, M eventually returns to its equilibrium state as the result of the regrowth of the longitudinal component of the magnetization, M_z . The time constant governing the return to equilibrium is T_1 for regrowth of the longitudinal magnetization

$$\frac{dM_z}{dt} = -\frac{(M_z - M_0)}{T_1} \quad (1.21)$$

where M_0 is the longitudinal magnetization at equilibrium.

Another occurring phenomenon is the decaying of the transverse component, M_{xy} along with the regrowth of M_z . The time constant governing the return to equilibrium for the decay of transverse component of magnetization is T_2 .

$$\frac{dM_{xy}}{dt} = -\frac{M_{xy}}{T_2} \quad (1.22)$$

Practically, the signal decays faster than predicted T_2 , due to the magnetic field inhomogeneity causing little shifts in the resonant frequency. The time constant for this faster decay is related as

$$\frac{1}{T_2^*} = \frac{1}{T_2} + \frac{1}{T_2'} \quad (1.23)$$

where T_2' accounts for imperfections in the main magnetic field.

So the time dependent phenomenon of magnetization in the presence of applied $\vec{B}_1(t)$ field is described by the Bloch Eq.

$$\frac{d\vec{M}(t)}{dt} = \gamma \vec{M}(t) \times \vec{B}(t) - \frac{M_x \hat{x} + M_y \hat{y}}{T_2} - \frac{(M_z - M_0) \hat{z}}{T_1} \quad (1.24)$$

The solutions of the equations are then

$$M_z(t) = M_0(1 - e^{-t/T_1}) + M_z(0)e^{-t/T_1} \quad (1.25)$$

$$M_{xy}(t) = M_{xy}(0)e^{-i\omega_0 t} e^{-t/T_2} \quad (1.26)$$

1.2.3 Relaxation mechanism

Following a perturbation, the spin system approaches thermal equilibrium with the surrounding environment (i.e., lattice) via two simultaneous processes: polarization of longitudinal magnetization and decoherence of transverse spins. The longitudinal relaxation reflects a net change of spin states and there must be an exchange of energy between the spin states and the lattice. This exchange of spin states are stimulated by a perturbation of the magnetic field at the Larmor frequency. On the other hand, transverse relaxation can occur either through the exchange of energy or without energy exchanges into the lattice. Transverse relaxation takes place due to the magnetic field fluctuations at the nucleus and results in the loss of transverse magnetization. Fluctuating magnetic fields, mostly stemming from the dipole–dipole interactions between spins, will exchange energy with the spins until thermal equilibrium has been established. Inherently, any type of interaction that causes fluctuating magnetic fields is a possible source of spin relaxation. For spin $\frac{1}{2}$ particles in solution or in most aqueous tissues, dipole-dipole interaction is the dominant relaxation mechanism. The theory behind the dipole-dipole interaction for relaxation is described below.

Because of the Brownian motion and molecular tumbling magnetic moment of one spin influences the local magnetic field at other spin position arbitrarily. According to classical physics, a local dipolar magnetic field \vec{B}_L produced by a magnetic moment $\vec{\mu}$ is given by

$$\vec{B}_L = \frac{\mu_0}{4\pi} \left[\frac{3(\vec{\mu} \cdot \vec{r}) \cdot \vec{r}}{r^5} - \frac{\vec{\mu}}{r^3} \right] \quad (1.27)$$

where μ_0 is the permeability in the free space and $\vec{r} = r\hat{n}$, r is the separation between two spins and \hat{n} is the unit vector in the direction joining them. From the interaction energy ($E = -\vec{\mu} \cdot \vec{B}_L$) between two identical spins with angular momentum vectors \vec{S}_1 and \vec{S}_2 is then

$$E = \frac{\mu_0 \gamma_1 \gamma_2 \hbar^2}{4\pi r^3} [\vec{S}_1 \cdot \vec{S}_2 - 3(\vec{S}_1 \cdot \hat{n})(\vec{S}_2 \cdot \hat{n})] \quad (1.28)$$

Now if we transform \hat{n} into spherical coordinates, then the dipolar Hamiltonian can be written as

$$\mathcal{H}_{dipolar} = \frac{\mu_0 \gamma_1 \gamma_2 \hbar^2}{4\pi r^3} [A + B + C + D + E + F] \quad (1.29)$$

Where

$$A = S_{z1} S_{z2} (1 - 3\cos^2\theta) \quad (1.30a)$$

$$B = -\frac{1}{4} (S_1^+ S_1^- + S_1^- S_1^+) (1 - 3\cos^2\theta) \quad (1.30b)$$

$$C = -\frac{3}{2} (S_1^+ S_{z2} + S_{z1} S_2^+) \sin\theta \cos\theta e^{-i\varphi} \quad (1.30c)$$

$$D = -\frac{3}{2} (S_1^- S_{z2} + S_{z1} S_2^-) \sin\theta \cos\theta e^{i\varphi} \quad (1.30d)$$

$$E = -\frac{3}{4} (S_1^+ S_2^+) \sin^2\theta e^{-2i\varphi} \quad (1.30e)$$

$$F = -\frac{3}{4} (S_1^- S_2^-) \sin^2\theta e^{2i\varphi} \quad (1.30f)$$

In fact, the dipole-dipole interaction depends on the orientation of the two spins and their relative positions. In the above Eq. (1.29), A and B terms are known as secular term of $\mathcal{H}_{dipolar}$. The term ‘ A ’ represents static interactions as the spin operators ‘ S_{z1} ’ and ‘ S_{z2} ’ join like states. While ‘ B ’ term allows the spins to exchange their orientations via flip-flop interactions. However, both ‘ A ’ and ‘ B ’ terms allow the transitions between equal Zeeman energy states i.e., no transitions that lead to net exchange of spin orientation; eventually these terms do not contribute to longitudinal relaxation. The ‘ C ’ and ‘ D ’ terms allow transitions that lead to one of the spins to flip with transition energy of $\hbar\omega_0$, whereas ‘ E ’ and ‘ F ’ terms allow both the spins to flip with transition energy of $2\hbar\omega_0$ with the lattice. The ‘ C ’, ‘ D ’, ‘ E ’ and ‘ F ’ terms contribute to both transverse and longitudinal relaxation.

In order to get more insight into the relaxation, we can utilize perturbation formalism of quantum mechanics using dipolar Hamiltonian as the perturbation. As well, we need to introduce the autocorrelation function which is a decaying function and is expressed by [6]

$$G(t) = \overline{B_L^2} e^{-t/\tau_c} \quad (1.31)$$

where τ_c is the correlation time which corresponds to the average time taken for a molecule to rotate through one radian. As we know, relaxation is usually induced if the frequency components of the fluctuating magnetic field are pretty close to the Larmor frequency. These frequency components can be analyzed by Fourier transform of the autocorrelation function (form a Fourier transform pair $J(\omega) = \int_{-\infty}^{+\infty} G(\tau) e^{-i\omega\tau} d\tau$) known as spectral density function and is expressed by

$$J(\omega) = 2\overline{B_L^2} \frac{\tau_c}{1+\omega^2\tau^2} \quad (1.32)$$

and $J(\omega)$ implies the power available to induce relaxation as a function of the angular frequency. Figure 1.1(a) shows the spectral density function for various rotational motions: very fast motion $\omega^2\tau^2 \ll 1$, intermediate $\omega^2\tau^2 \approx 1$ and slow motion $\omega^2\tau^2 \gg 1$.

In terms of spectral density function relaxation can be expressed as

$$\frac{1}{T_1} = \frac{3\gamma^4\hbar^2}{2} I(I+1) [J_1(\omega_0) + J_2(2\omega_0)] \quad (1.33)$$

$$\frac{1}{T_2} = \frac{3\gamma^4\hbar^2}{4} I(I+1) \left[\frac{1}{2}J_0(0) + 5J_1(\omega_0) + \frac{1}{2}J_2(2\omega_0) \right] \quad (1.34)$$

where $J_0(0)$, $J_1(\omega_0)$ and $J_2(2\omega_0)$ are the Fourier transforms of the autocorrelation functions of three spatial terms $(1 - 3\cos^2\theta)/r^3$, $(\sin\theta\cos\theta e^{-i\varphi})/r^3$ and $(\sin^2\theta e^{-2i\varphi})/r^3$ in Eqs. (1.30).

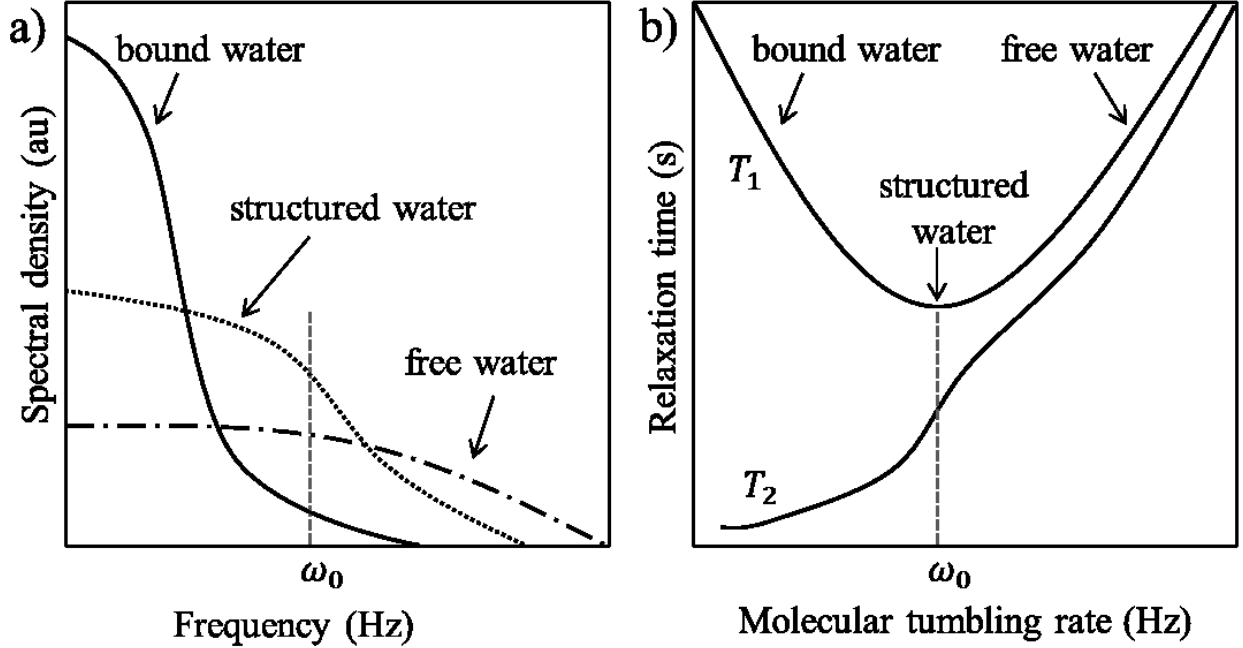


Figure 1.1: Relaxation principle: a) Spectral density functions $J(\omega_0)$ for three substances: bound water (long τ_c), structured water (medium τ_c) and free water (short τ_c). The number of protons undergoing oscillations at ω_0 is largest for structured water. b) Variation of relaxation times T_1 and T_2 with the rate of molecular tumbling. Molecular tumbling rate increases from bound water (large molecule), structured water (soft tissue) to free water (small molecule) (based on [7]).

$J_0(0)$ represents the static energy density and corresponds to the transition where there is no energy exchange between spin and lattice. This low frequency component contributes only to the transverse relaxation. However, $J_1(\omega_0)$ and $J_0(2\omega_0)$ are the energy densities of the fluctuating magnetic field at frequencies ω_0 and $2\omega_0$. As mentioned earlier, exchange energy for C, D terms is $\hbar\omega_0$ and for E, F terms is $2\hbar\omega_0$ in Eqs. (1.30) [8]. Thus for the spin relaxation, fluctuation of the magnetic field at certain resonance frequencies must be provided by the molecular motion. For spins at a constant separation r , the relaxation rates can be written as [7, 9],

$$\frac{1}{T_1} = \frac{2\gamma^4\hbar^2}{5r^6} I(I+1) \left[\frac{\tau_c}{1 + \omega_0^2\tau_c^2} + \frac{\tau_c}{1 + 4\omega_0^2\tau_c^2} \right] \quad (1.35)$$

$$\frac{1}{T_2} = \frac{\gamma^4 \hbar^2}{5r^6} I(I+1) \left[3\tau_c + \frac{5\tau_c}{1 + \omega_0^2 \tau_c^2} + \frac{2\tau_c}{1 + 4\omega_0^2 \tau_c^2} \right] \quad (1.36)$$

For non-viscous liquids such as water, the rotational motions are very fast ($\omega_0^2 \tau_c^2 \ll 1$). Combining the equations (1.35,1.36) gives

$$\frac{1}{T_2} = \frac{1}{T_1} = \frac{2\gamma^4 \hbar^2}{5r^6} I(I+1)\tau_c \quad (1.37)$$

Hence for water, the relaxation times are independent of frequency term (Eq.1.37), and T_1 and T_2 are similar under common magnetic field strengths. As well, relaxation rates are not affected by the field strength for very fast motion molecules. On the other hand, for solid the rotational motions are very slow ($\omega_0^2 \tau_c^2 \gg 1$), T_1 and T_2 are very different. For intermediate rotational motion ($\omega_0^2 \tau_c^2 \approx 1$) in viscous liquids, T_1 is frequency dependent while T_2 is less frequency dependent and always shorter than T_1 as frequency independent secular term dominates on T_2 [10, 11]. The relationship between relaxation times (T_1, T_2) and molecular tumbling rate (inverse of correlation time τ_c) is represented in Fig. 1.1 (b). It is showed that T_1 is always larger than or equal to T_2 . Note T_1 is strongly dependent on temperature. With the increase of temperature the molecular energies increase resulting the rapid fluctuation of local dipolar field, making them less effective at inducing relaxation. Substances with paramagnetic content also influence the relaxation processes.

Biological tissue contains diverse, free tumbling ions and molecules, proteins, lipids, and relatively immobilized or rigid macromolecules that may exchange with the protons in the water molecules. Moreover, biological tissues are heterogeneous and contain various types of cells or other structures, and may have multi-component relaxation times.

1.2.4 Cross relaxation, chemical exchange and magnetization transfer

The relationship between transverse relaxation and molecular motion can be explained by magnetization transfer (MT). MT can take place via several mechanisms like chemical exchange or cross relaxation, and relies on the difference in T_2 values between free, unbound water proton, and bound water proton to macromolecules. So, two pools of protons are considered: one is mobile pool for free water; and another is bound pool which is motionally restricted and linked with macromolecules in brain tissue. The mobile pool includes both the mobile bulk water molecules and water molecules bound to the macromolecular surface which is termed as

hydration water. These two water fraction exist in a chemical equilibrium state that can be considered as a single mobile pool. The hydration water molecules communicate with the bulk water molecules through diffusion. The transfer of magnetization from hydration water with the macromolecule protons occurs through a special form of dipole-dipole interactions and is termed as cross-relaxation. In cross-relaxation protons of bulk water and hydration water molecules exchange the chemically nonequivalent spins. Figure 1.2 depicts the mechanisms of cross-relaxation and chemical exchange. Previous work suggested that chemical exchange is not a significant factor in the MT processes [12, 13].

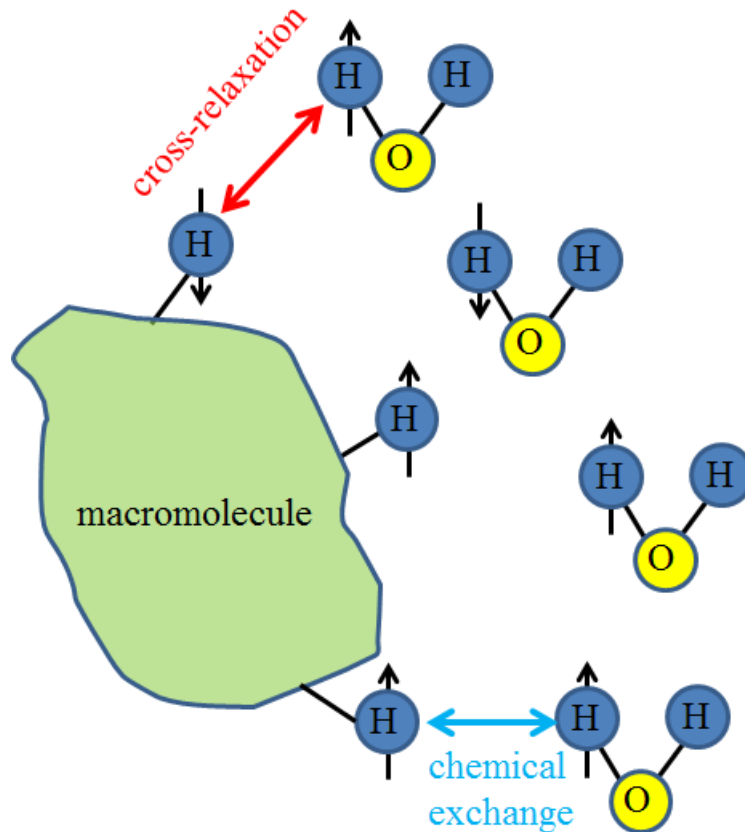


Figure 1.2: Magnetization transfer takes place via cross-relaxation or chemical exchange mechanisms.

We know free water protons have long T_2 values ($> 10 - 100 \text{ ms}$) because of fast molecular motion ($\tau_c \approx 3 \times 10^{-12} \text{ s}$) and free water has a very narrow resonance bandwidth ($10 - 100 \text{ Hz}$) around the Larmor frequency. Whereas, bound water protons have short T_2 ($<$

0.2 ms) due to restricted motion ($\tau_c \approx 10^{-8}s$) and bound water has broad frequency bandwidth (10 – 50 kHz). In addition, both pools have almost same Larmor frequency. However, the bound pool is not visible with conventional MRI as T_2 is too short. The magnetization or energy is continuously exchanged between the pools under normal condition. It is possible to perturb the bound pool and monitor the magnetization transfer effect on the mobile pool. If the bound pool is selectively saturated, there will be no net magnetization in the bound pool and eventually a variation between magnetization between the pools will be obtained. Magnetization will be transferred from the free pool to bound pool due to exchange or cross relaxation. The frequency bandwidths of two pools and the magnetization transfer mechanism are shown in Fig. 1.3. Saturation is achieved in several ways such as continuous wave (CW) irradiation, on-resonance binomial pulses and off-resonant RF pulse. Moreover, incidental magnetization transfer effect is observed specially in multi-slice imaging with multiecho spin echo sequence where slice selective excitation and refocusing pulses RF pulse act as off-resonance pulse for neighboring slices. More details on incidental magnetization transfer is given in section 1.4.1.4.3.

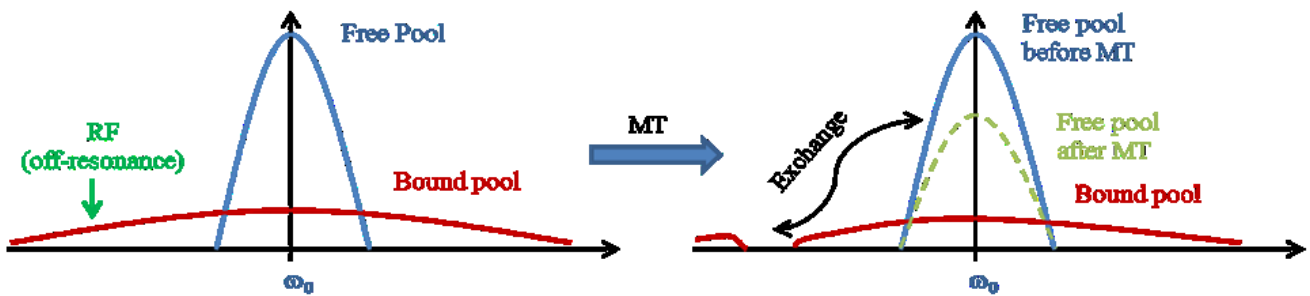


Figure 1.3: Magnetization transfer: Off-resonant RF pulse saturates the magnetization associated macromolecular protons of bound pool but not magnetization in free pool. The exchange of magnetization between the pools results in the reduction of magnetization of free water pool and hence its signal intensity.

1.2.5 Free induction decay

Free induction decay (FID) of nuclear magnetization is defined as the signal generated after the application of an excitation pulse. Usually a subject being imaged is placed in the uniform

magnetic field B_0 and the sample magnetization initially aligns to B_0 . An RF pulse is then applied to the RF coil, surrounding the subject, which can generate a time dependent magnetic field B_1 . The RF pulse, oscillating at the Larmor frequency, causes the spins to tip into the transverse plane. The time dependent *emf* or signal is induced into the coil by the net magnetization of the subject after switching off the RF pulse. The duration of the signal is ultimately limited by transverse relaxation and but the signal decays more rapidly due to the mutual interference between different NMR frequencies depending upon static magnetic field homogeneity. The overall FID signal is exponential in nature. In fact, FID duration is of the order of seconds for proton NMR but it might be in the range of microseconds in the case of solid state NMR where the NMR line shapes are not relaxation limited.

1.2.6 *Signal detection and reciprocity*

In MRI we measure the voltage (i.e., signal) from the coil and the magnetic field producing such voltage. According to reciprocity, the coil's ability to receive signal from a certain location is proportional to its ability to produce fields at that locations [14]. Therefore, complex RF signal from the imaging volume V has an expression of the type

$$S(t) = \int_V B_1^-(r).M(r).e^{-i(k.r+\omega_0 t)} dr \quad (1.38)$$

which implies that a signal $S(t)$ is induced across an RF coil by a time varying magnetization. In the above Eq. (1.38), $B_1^-(r)$ is the receive sensitivity of the coil and is expressed as $B_1^- = \frac{(B_{1x}-iB_{1y})^*}{2}$, a circularly polarized component rotating in sense opposite to that of the spins; $M(r)$ is the transverse magnetization, $k(t)$ is the position in k -space at time t which describes the phase accumulation due to the gradients and ω_0 is the Larmor frequency.

The stationary frame of reference is the basis of reciprocity principle. As discussed earlier, nuclear spins are only influenced by a B field rotating in the same sense as their precession and the B_1^+ , the transmit field, causes nutation of the spin. If quadrature PSD is used, the received signal is detected in the rotating frame of reference which depends on the counter rotating B_1^- . At low frequency, $B_1^+ \approx B_1^-$ while at high frequency B_1^+ and B_1^- differs significantly. Eventually the receive sensitivity depends on the B_1^- , the negatively rotating field component [15].

1.3 Imaging

In order to get MR images of the subject, spatial localization of the nuclear spins is required. Going back to the history, localization of NMR signal using a field gradient was proposed in 1973 by Lauterbur [16]. The key idea is to get a projection through an object using the NMR frequency encoding. By varying the direction of the field gradient applied during data acquisition, projections from different angles were then combined to form an image using the filtered back projection, a protocol borrowed from CT.

Due to the natural abundance and high gyro-magnetic ratio, hydrogen proton imaging is the natural choice and is vastly used in clinical MRI studies as well. Generally, MR imaging starts with signal excitation followed by spatial encoding and then need to isolate the proton density distribution using the Fourier transformation.

1.3.1 Contrast

Image contrast is important for tissue characterization in MRI. The MRI signal depends on the pulse sequence used for the scan and the tissue characterization parameters, which create the image contrast. There are three main sources of contrast in MRI which determine the signal intensity: T_1 relaxation, T_2 relaxation and spin density. T_1 relaxation times provide a large variation between soft tissues, making T_1 -weighted pulse sequences helpful for anatomical scans. T_2 relaxation times are highly sensitive to inflammation and can be useful for T_2 weighted imaging by which many diseases can be characterized by observing the T_2 values in tissue. In addition, spin density corresponds to the water content levels in proton MRI and provides relatively similar in most soft tissue [4].

In any pulse sequence used in MRI all three contrast mechanisms may present, however typically one of the contrast mechanism is emphasized. For example, the spin echo signal at point r can be expressed as

$$S \approx K\rho(r)(1 - e^{-TR/T_1(r)})e^{-TE/T_2(r)} \quad (1.39)$$

where K is a gain constant, $\rho(r)$ is the spin density at position r , TE and TR are the echo time and repetition time respectively. Manipulating TE and TR , the signal difference between different tissue types can be modified. For long TR and short TE , the MRI signal intensities depend on spin density $\rho(r)$. T_1 -weighted image can be obtained with short TE , and T_2 -weighted

image can be obtained with long TR . Moreover, image contrast can be modified by using an inversion pulse prior to the initial excitation pulse. For example, with the use of appropriate inversion recovery (IR) time cerebrospinal fluid (CSF) or fat can be suppressed from the image with fluid attenuated inversion recovery (FLAIR) or short τ inversion recovery (STIR) sequences respectively.

1.3.2 Signal localization

Signal localization is required in order to create an image of a subject and done by superimposing the spatially varying magnetic field onto B_0 , making ω_0 as function of position. Let us define the magnetic field as B_g which varies linearly along the x direction and is aligned along z -axis as

$$B_g = xG_x\hat{z} \quad (1.40)$$

where G_x is the x gradient. Larmor frequency then written as $\omega = \gamma(B_0 + xG_x)$. The gradients for all three axes can be written in matrix form

$$G = \begin{bmatrix} \frac{\partial B_x}{\partial x} \hat{x}\hat{x} & \frac{\partial B_x}{\partial y} \hat{x}\hat{y} & \frac{\partial B_x}{\partial z} \hat{x}\hat{z} \\ \frac{\partial B_y}{\partial x} \hat{y}\hat{x} & \frac{\partial B_y}{\partial y} \hat{y}\hat{y} & \frac{\partial B_y}{\partial z} \hat{y}\hat{z} \\ \frac{\partial B_z}{\partial x} \hat{z}\hat{x} & \frac{\partial B_z}{\partial y} \hat{z}\hat{y} & \frac{\partial B_z}{\partial z} \hat{z}\hat{z} \end{bmatrix} \quad (1.41)$$

However, the contribution x and y component of B_g on the Larmor frequency is very small and can be neglected because the main field B_0 is aligned in the z -direction. Therefore the expression for the gradient is reduced to

$$G = \frac{\partial B_z}{\partial x} \hat{x} + \frac{\partial B_z}{\partial y} \hat{y} + \frac{\partial B_z}{\partial z} \hat{z} \quad (1.42)$$

Usually an MRI machine has three gradient coils that produce G_x , G_y and G_z for three axes. As well, all the gradients are independent and orthogonal to each other. The total gradient field is then given by

$$G = G_x\hat{x} + G_y\hat{y} + G_z\hat{z} \quad (1.43)$$

The magnetic field at position \mathbf{r} is therefore

$$\vec{B}(\vec{r}) = (\vec{B}_0 + \vec{G} \cdot \vec{r})\hat{z} \quad (1.44)$$

Using the gradient field, signal localization can be achieved by using the following methods: slice selection, frequency encoding and phase encoding.

1.3.3 Slice selection

Slice selection is used for selective excitation of the spins in a sample. Here we need to apply a linear gradient usually along the z-axis which makes the Larmor frequency as a function of distance along the gradient axis. If we apply slice select gradient along z-axis, the Larmor frequency is then

$$\omega(z) = \gamma(B_0 + zG_{sl}) \quad (1.45)$$

With the application of an RF pulse into the sample, the spins will be affected by the RF pulse which have the resonance frequency same or close to that of the RF pulse and consequently a particular slice of the sample will be excited [17]. The slice thickness can be calculated by knowing the gradient amplitude and the position of the excited slice can be changed by changing the RF pulse bandwidth.

Now neglecting the relaxation effects, the sample magnetization evolution in presence of the slice select gradient G_{sl} can be described by the Bloch equations

$$\frac{dM_x}{dt} = \gamma M_y G_{sl} z \quad (1.46)$$

$$\frac{dM_y}{dt} = \gamma (M_z B_1(t) - M_x G_{sl} z) \quad (1.47)$$

$$\frac{dM_z}{dt} = \gamma M_y B_1(t) \quad (1.48)$$

If we use a new frame of reference (x', y', z') which rotates at the frequency $\gamma G_{sl} z$ around the z-axis, making the rotational frequency as a function of distance along the slice axis, the above equations (1.46-1.48) become (for the pulse extends from $(-T$ to $T)$)

$$\frac{dM_{x'}}{dt} = \gamma M_{z'} B_1(t) \sin(\gamma G_{sl} z'(t + T)) \quad (1.49)$$

$$\frac{dM_{y'}}{dt} = \gamma M_{z'} B_1(t) \cos(\gamma G_{sl} z'(t + T)) \quad (1.50)$$

$$\frac{dM_{z'}}{dt} = \gamma(M_{x'}B_{y'} - M_{y'}B_{x'}) \quad (1.51)$$

For simplicity, we assume that the variations in z-component of the magnetization are small (i.e., $\frac{dM_{z'}}{dt} \approx 0$), $M_{z'} \approx M_0$ and the spin response is linear. These assumptions work well for small angles situation. Using the complex notation $M_{+'} = M_{x'} + iM_{y'}$ we can write the above equations as

$$\frac{dM_{+'}}{dt} = i\gamma M_{z'} B_1(t) e^{i\gamma G_{sl}z'(t+T)} \quad (1.52)$$

Integrating Eq. (1.52) and then transforming into the original rotating frame of reference under the above assumptions we can get

$$M_{+}(z) = i\gamma M_0 e^{-i\gamma G_{sl}zT} \int_{-T}^T B_1(t) e^{i\gamma G_{sl}zt} dt \quad (1.53)$$

By replacing $\gamma G_{sl}z = \omega$, the above Eq. can be treated as the Fourier transform of $B_1(t)$. This implies that the excited slice profile is the result of Fourier transformation of the RF pulse envelope. So theoretically, if an infinitely long RF pulse is applied to an imaging object, an infinitely thin slice should be excited. However, the RF pulse has finite duration in practice so can give finite BW.

1.3.4 Frequency Encoding

If we perform slice selection only, no spatial information along the other two axes can be obtained from the resultant FID signal. So we need to apply gradients to encode the signal along these axes. For frequency encoding, a linear field gradient, G_x is applied during the readout so that precessional frequency of the spins changes to make up the signal as a function of position along the gradient axis.

$$\omega(x) = \omega_0 + \gamma G_x x \quad (1.54)$$

If we consider $\rho(x)$ as the projection of the spin density function along the x-axis, the signal would be then due to frequency encoding

$$S(t) = \int \rho(x) e^{-i(\omega_0 + \gamma G_x x)t} dx \quad (1.55)$$

In the rotating frame of reference with precession at Larmor frequency ω_0 , the ω_0 is removed leaving

$$S(t) = \int \rho(x)e^{-i(\gamma G_x t)x} dx \quad (1.56)$$

The above Eq. 1.56 has the form of Fourier transform pair. The Fourier transform of the signal $S(t)$ produces a projection $\rho(x)$ of the magnetization of the object imaged along the gradient axis. Usually the frequency encoding gradient and slice select gradient are applied orthogonal to each other and combination of both gradients can localize the signal to a column through the object.

1.3.5 Phase Encoding

Using slice selection and frequency encoding the MRI signal has been localized to a specific slice and encoded along one direction. In this case, spins in the same column precesses at the same frequency and thus all the spins are in the same phase. However, to get different relative phases of spins in the same column, a linear field gradient should be applied on the magnetization prior to the frequency encoding that produces a linear variation of phase of the spins. In phase encoding, applied usually along the y -axis, we need to excite the object with a constant gradient for different duration T_p before sampling each data point. Thus the acquired signal can be obtained by repeating the process for different T_p .

$$S(T_p) = \int \rho(y)e^{-i(\gamma G_y T_p)y} dy \quad (1.57)$$

The phase encoding is similar to frequency encoding and the signal is the Fourier transform of $\rho(y)$.

Therefore, combining slice selection, frequency encoding and phase encoding, basis of most common imaging sequence can be established.

1.3.6 K -space and sampling requirement

K -space is introduced as the reciprocal image space in MRI and considered as the Fourier space in which images are acquired before being Fourier transformed into image space. Mathematically, k -space is defined as

$$k(t) = \gamma \int_0^t G(\tau) d\tau \quad (1.58)$$

where $G = G_x\hat{x} + G_y\hat{y} + G_z\hat{z}$ is the gradient field vector, t is the duration of gradient pulse and, k has the unit of rad/m indicating the phase accumulation per distance. Thus the signal can be written as

$$S(k) = \int \rho(\vec{r})e^{-i\vec{k}\cdot\vec{r}} d\vec{r} \quad (1.59)$$

which shows the relationship between the image space signal, $\rho(\vec{r})$, and the k -space signal $S(k)$. The weighted sum of all points in the k -space contribute to each point in an MRI image. The central part of k -space indicates low spatial frequency regions (large image structure) while distant parts of the k -space indicate high spatial frequency (edges and fine details). Fig. 1.4 shows a T_2 -weighted spin echo image and it's corresponding k -space image. In addition, spin echo and gradient echo pulse sequence diagrams and their k -space trajectories are shown in Fig. 1.5.

However, it's not possible to sample a continuous function so discrete sampling is required. For 2D imaging if we assume the object being imaged has field of view (FOV) along frequency encoding and phase encoding directions as FOV_x and FOV_y , then satisfying Nyquist criteria we can write

$$\Delta k_x \leq \frac{1}{FOV_x}, \Delta k_y \leq \frac{1}{FOV_y} \quad (1.60)$$

And $\Delta k_x = \gamma G \Delta t, \Delta k_y = \gamma \Delta G \tau \quad (1.61)$

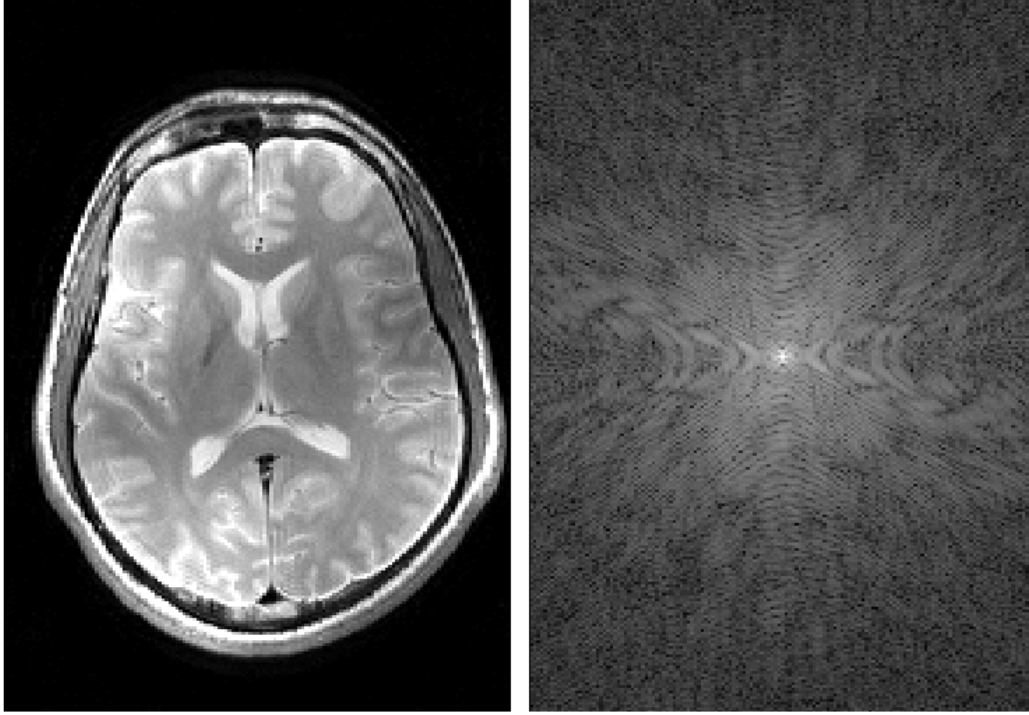


Figure 1.4: MRI image of a brain (left) and corresponding k-space image (right)

Where $\Delta k_x, \Delta k_y$ are k-space step size along x and y direction, G is frequency encoding gradient, ΔG is phase encoding step size and τ is phase encoding interval. Finally we can write the following requirements for MRI acquisition parameters:

$$\Delta t \leq \frac{1}{\gamma G FOV_x}, \Delta G_y \leq \frac{1}{\gamma \tau FOV_y} \quad (1.62)$$

Moreover, the spatial resolutions Δx and Δy are related to k-space extent ($2k_{max}$) by

$$\Delta x = \frac{1}{2k_{xmax}}, \Delta y = \frac{1}{2k_{ymax}} \quad (1.63)$$

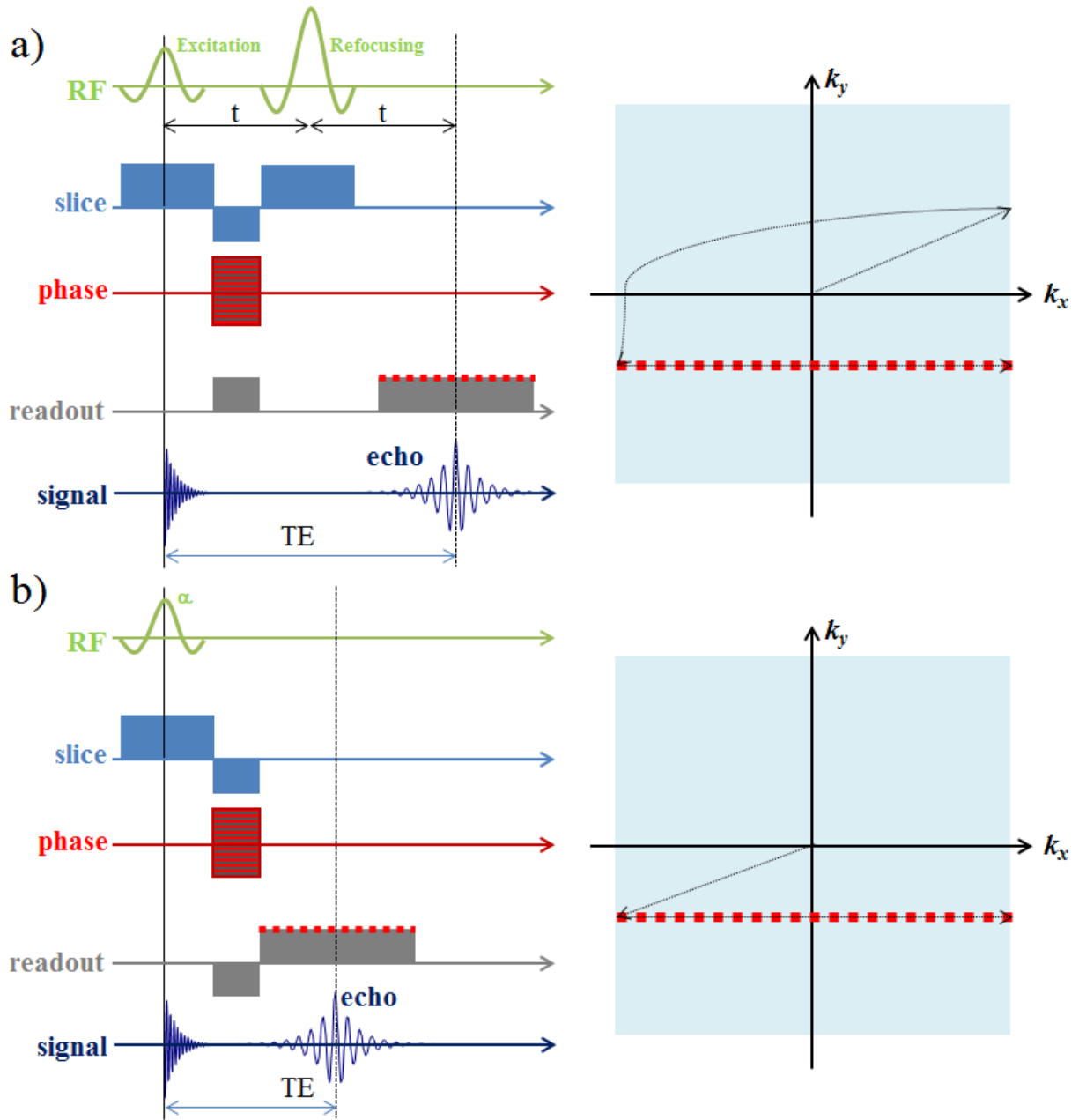


Figure 1.5: Spin echo (a) and gradient echo (b) sequences with k-space trajectories

1.3.7 Effect of field strength

The relaxation processes are affected by the main magnetic field. Previous studies indicate that T_1 values increase while T_2 and T_2^* values decrease with increasing field strength [18-22]. T_1 increases with the increase of field strength starting from very low field and field dependency decreases at high field [22] while T_2 remains almost constant up to 1.5 T [23]. Reasons behind the increasing T_1 with field strength are evident from the spectral density functions shown in Fig

1.1. As the energy difference between parallel and anti-parallel states increase, spins have less resonant energy states available in the lattice and thus energy is poorly transferred to the surroundings. For transverse relaxation times T_2 and T_2^* , reasons behind the decreasing tendency with field strength are due to the increased dephasing caused by the diffusion in local field gradients as well as due to the chemical exchange of protons between the different pools. Moreover, the dephasing rate and the chemical shift difference between the pools are field dependent which also causes decreased relaxation times at high field. The dephasing rate increases with field strength as the static field inhomogeneities are not recovered in T_2^* decay. Therefore T_2^* has more field dependency compared to T_2 .

High field imaging systems provide some advantages over lower field systems such as higher SNR, higher spatial resolution, better tissue contrast and increased T_1 for better background suppression in MR angiography; and increased chemical shift for MR spectroscopy. High field systems have strong sensitivity to magnetic susceptibility differences; exploiting this property improved contrast to noise and acquisition efficiency using susceptibility weighted imaging (SWI). Moreover, high field is highly sensitive to non-heme iron in the human brain. Previous studies showed high correlation between relaxation rates and estimated non-heme iron, and near linear increase in non-heme iron sensitivity was observed at multiple field strengths [24-27].

Though high magnetic field systems can be advantageous, they encounter some challenges related to image acquisition such as modified relaxation times, RF inhomogeneity, susceptibility gradients and the larger spectral separation. Therefore modification of pulse sequences is required. For the change of relaxation rates, modification is performed by altering imaging parameters such as TR, TE and flip angle in order to maintain the desired image contrast. The high RF power deposition is another vital problem of high fields and impedes imaging. RF power deposition varies quadratically with field strength [28] which limits the use of high-energy pulses. At higher field, another important problem is the central brightening due to the wavelength interference effects [15] and lower RF field at the periphery of the head due to the destructive interference. For example, multi-echo spin echo (MESE) or fast spin echo (FSE) employs multiple RF pulses prior to the read out and could encounter considerable variations in signal intensity and contrast.

1.4 Quantitative Relaxometry

1.4.1 Quantitative T_2 measurement

Transverse relaxation is characterized by the exponential decay of the MR signal in the transverse plane with a time constant T_2 . Usually, T_2 weighted imaging is used in clinical MRI diagnosis that provides a qualitative interpretation of disease. In certain cases, T_2 quantification, which provides an absolute measure of transverse relaxation independent of other factors, provides a metric that is preferable to relaxation weighting. In neurodegenerative conditions such as multiple sclerosis and Parkinson's disease, shorter T_2 times in deep grey matter (DGM) are indicative of iron accumulation and appear to correlate with disease severity [20, 29]. Past studies have also demonstrated that T_2 quantification plays an important role for detection of diseases [20, 30], tissue characterization of human body [31-37] and brain [38, 39]. Quantitative T_2 measurements are typically performed with a multi-echo spin echo sequence and T_2 values are calculated via mono- and multi-exponential fitting [40]. Besides these, some other techniques have been used for T_2 quantification such as T_2 -weighted Snapshot FLASH [41] inversion recovery TrueSSFP [42], partially spoiled SSFP [43] and driven equilibrium single pulse observation of T2 (DESPOT2) [44]. In this thesis, spin echo based T_2 quantification has been used. The spin echo sequence is discussed below.

1.4.1.1 Spin Echo sequence and CPMG

The spin echo was first devised by EL Hahn in 1950 for the quantification of relaxation and diffusion times in NMR experiments [45]. The spin echo sequence uses 90° RF pulse to excite the longitudinal magnetization, which undergoes free precession and then relaxation. It also dephases under the application of gradients and magnetic field inhomogeneities. A single or multiple 180° pulses refocuses the spins for the generation of signal echoes. The refocusing pulses are placed in the midway between the excitation pulse and the echo formation. The results are the nullification of the phase accumulation, and rewinding of the phase accumulation for later evolution into a coherent echo. Spin echo sequence refocuses the gradient and magnetic field inhomogeneities. Fig. 1.5 shows a two-pulse spin echo sequence. Typically, the refocusing pulse may not be exactly 180° , so crusher gradients are required which spatially dephase any transverse magnetization excited by the refocusing pulse.

Carr and Purcell [46] adjusted the Hahn spin echo sequence for the reduction of diffusion sensitivity by the addition of multiple refocusing pulses. These refocusing pulses are applied along the same direction as the 90° excitation pulse. Multiple refocusing pulses limit the phase dispersion in the inter-echo spacing due to the molecular diffusion. The time between the excitation pulse and the first refocusing pulse is τ and thus the first echo is formed at 2τ . And, n number of images can be acquired for n number of refocusing pulses with $TE = n * 2\tau$. Such a pulse sequence is also known as CP spin echo sequence. The rate at which the echoes are formed depends on how effectively the refocusing pulses are placed close together and the efficiency of the hardware used [2]. The diffusion effect can be reduced by using shorter τ . However, the drawback of the CP sequence is that any errors in the flip angles of the refocusing pulses will be cumulative and the following pulses will rotate the magnetization vectors progressively out of the transverse plane. Consequently there will be a significant loss of transverse magnetization and will not correspond to the true T_2 value. Later this CP spin echo sequence was refined by Meiboom and Gill [47] in order to minimize the flip angle error in refocusing pulses and the susceptibility effects in presence of inhomogeneous magnetic field B_1 . In their modification they applied refocusing pulses along the $-y'$ direction and the method is known as CPMG sequence. The basic idea is that for CP if the initial magnetization is in the direction of $+y'$ axis, the magnetization will be in the direction of $-y'$ axis after the first refocusing pulse and then will return to the direction of $+y'$ axis after the second refocusing pulse. Whereas for the CPMG, the magnetization will be remain in the direction of $+y'$ axis after each refocusing pulse as excitation pulse (90°) is applied in quadrature with the refocusing (180°) pulse.

1.4.1.2 Apparent T_2

As mentioned earlier, CPMG sequence reduces dephasing effects due to diffusion in an inhomogeneous magnetic field while Hahn spin echoes are more dependent on the diffusion effects. For constant TE, spins do not allow the phase accumulations due to susceptibility and gradient effects. On the other hand, Hahn spin echo uses a single refocusing pulse, the dephasing effect is larger for longer TE and due to lack of multiple refocusing pulses. Thus the Hahn spin echo is relatively more sensitive to the effect of the susceptibility gradients due to iron. With the diffusion term, spin echo signal magnitude is described by the following equation [46]:

$$S(t) = e^{-\left(\frac{\tau}{T_2} + \gamma^2 G(t)^2 D \tau^3 / 12 n^2\right)} \quad (1.64)$$

where τ is the echo spacing, D is the diffusion coefficient of the sample, $G(t)$ represents the magnetic field gradient, γ is the gyro-magnetic ratio and n the echo number which is equal to 1 for Hahn or single spin echo.

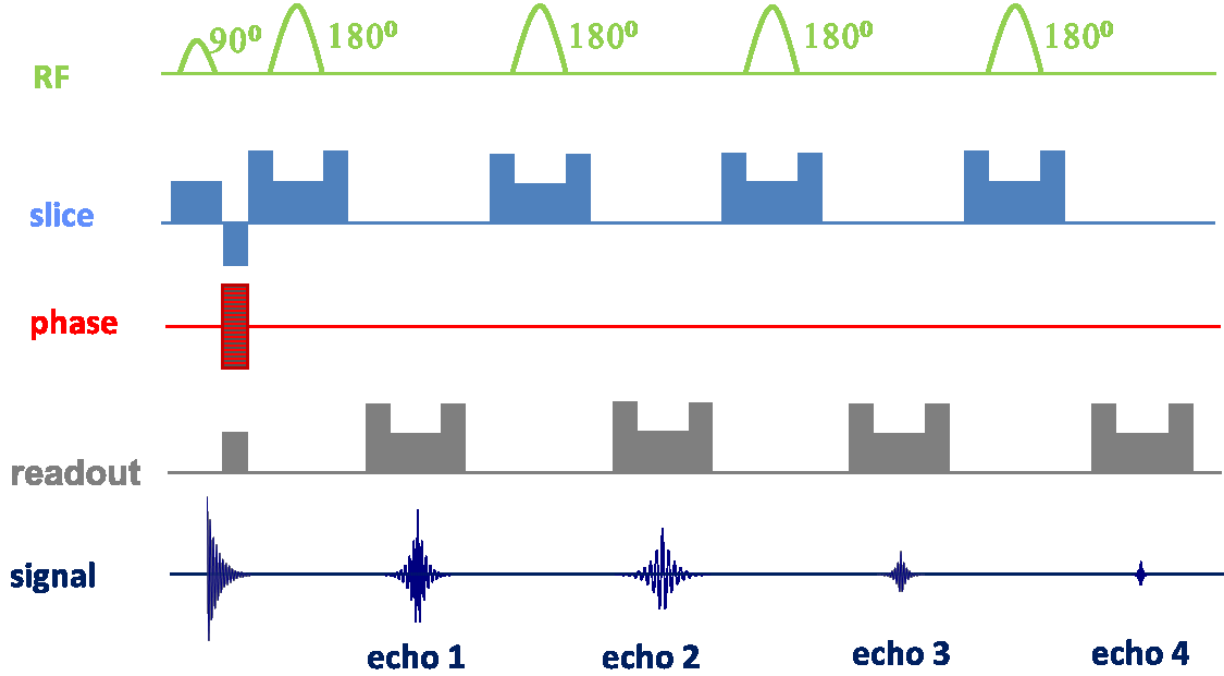


Figure 1.6: Multiecho spin echo (MESE) pulse sequence. Both excitation and refocusing pulses are slice selective.

Previous observations [48] indicate that the Hahn SE and CPMG SE do not provide same T_2 values. CPMG sequence depends on the selection of echo spacing, τ [49, 50] and the diffusion term $\gamma^2 G(t)^2 D$ in the above equation can be made small by choosing a small τ and hence more accurate T_2 can be obtained. However, the diffusion term and susceptibility term cannot be separated, and can be correlated with the iron content and true T_2 value for the tissue. If we consider a water molecule tumbles with the diffusion correlation time τ_D in presence of magnetic field inhomogeneity and the variation of the field perturbation $\Delta\omega$ in the same unit of Larmor frequency. The diffusion/susceptibility term can be explained in the motionally narrowed ($\Delta\omega\tau_D \ll 1$) and static ($\Delta\omega\tau_D \gg 1$) regimes [51-53]. Thus proton spins experiencing

inhomogeneous magnetic field and diffusion effects can be described by the apparent relaxation rate

$$R_2' = R_2 + \gamma^2 G^2 D \tau^2 / 12 \quad (1.65)$$

1.4.1.3 Spin echo based T_2 quantification

T_2 quantification is achieved by extending the principle of T_2 -weighting and images are generated with different TE values. In the multi-echo spin echo sequence (Fig. 1.5), each echo in the echo train is encoded with the same phase encoding gradient. Usually 16 to 32 echoes with 3-4 sec TR are used for T_2 measurement depending on the RF power deposition due to pulses at high field and scan time duration. A series of images are generated using the following equation

$$S_i(t) = S_0 e^{-TE_i/T_2} \quad (1.66)$$

where S_0 is signal intensity at equilibrium and proportional to mobile proton density, subscript i denotes the i th images with echo time TE_i . Using least square minimization, a pixel-by-pixel mono-exponential fitting is performed in order to get T_2 values at each pixel over the region of interest. However, non-ideal slice profiles and stimulated echoes are the major problems for this multi-echo spin echo sequence. More details will be discussed in the following sections.

1.4.1.4 Artefacts influencing T_2 measurement

Although the T_2 quantification using multi-echo spin echo is relatively simple and is considered as gold standard, there are some drawbacks that arise during the T_2 decay acquisition.

1.4.1.4.1 RF inhomogeneity

Ideally, all spins in the imaging object should be uniformly affected by the RF pulses used in the T_2 measurement. However, there are some sources that create a variable RF distribution. Such as, imperfections in transmit/receive field due to design limitations in the RF coil creates RF inhomogeneity causing certain regions of the imaging volume to receive more RF power than other regions. For this reason there will be some variation in flip angles across the imaging volume, which will introduce stimulated echoes and phase artifacts resulting in an erroneous T_2 measurement [2]. Tissue with large dielectric constant is another source of RF inhomogeneity and the effect is the reduction of RF wavelength even though the external RF field is uniform. At high field penetration distance of RF into the object is small due to the electrical conductivity

causing RF non-uniformity. Possible solutions are to use pulse sequences with adiabatic pulses [24] or stimulated echo compensation [54].

1.4.1.4.2 Specific absorption rate

Human tissues are conductive and current can pass through the human body. When the RF pulses are applied, the time varying RF field can induce small current according to Faraday's law that results energy being absorbed in the tissues. The RF energy absorbed by the body is known as specific absorption rate (SAR) and is measured in W/kg. The SAR of RF energy is proportional to $B_0^2 B_1^2$ [55]. SAR must be kept at the safe limits to prevent injury. The primary contribution of SAR stems from 180° refocusing pulses in the multi-echo spin echo sequence. In our case, the SAR limit was ~ 2 W/kg for brain at 4.7 T while the standard limits are 3.2 W/kg for head with exposure averaged of 10 minutes and 4 W/kg for whole body (15 minutes) [56].

1.4.1.4.3 Incidental magnetization transfer effect

A large number of slices for sufficient volume coverage is often desirable. However, each slice selective RF pulse acts as an off-resonant excitation pulse for neighboring slices in 2D multislice imaging. The result is the partial saturation of bound spins and gives rise to an incidental magnetization transfer (MT) effect. And, the effect of MT is increased for a pulse sequence in which a large number of RF pulses are employed and the MT effect is more obvious at high magnetic fields. Previous studies showed that MT effect is stronger in tissues with high macromolecular content such as, in WM. The resulting effect is signal loss in the tissue with higher content of macromolecules [57, 58]. The incidental MT effect on WM can be minimized by using an appropriate delay between the off-resonant excitation and on-resonance acquisition where the exchange between multicomponent pools are maximized. Moreover, T_2 measurements using multiecho spin echo sequence in single slice mode and 3D acquisitions are not affected by incidental MT effect.

1.4.1.4.4 Stimulated echoes

Stimulated echoes create major artifact in the T_2 decay curve [40]. Stimulated echoes are generated by the imperfect refocusing pulses in multi-echo spin echo sequences. These echoes can refocus later and mix with pure spin echoes, depending on the coherence pathway of the

magnetization. Stimulated echoes are T_1 weighted and lead to confound in spin echo T_2 measurement. Note the imperfection in refocusing pulses are due to the finite refocusing thickness, nonrectangular slice profile, RF interference effects and transmit calibration errors. The stimulated echoes can be eliminated by using variable spoiler gradients on either sides of the refocusing pulses [40]. The formation of stimulated echoes with their amplitudes and locations can be described by the extended phase graph which will be discussed in the section **1.4.1.5**.

1.4.1.4.5 Partial volume

Slice thickness can play an important role for accurate T_2 quantification. Selection of thin slice thickness can somewhat avoid partial volume effects that may introduce multi-exponential decay in the T_2 curve [59]. This is a problem in brain MRI where regions of white matter (WM), grey matter (GM) and cerebrospinal fluid (CSF) can overlap in the same voxel each having very different T_2 values.

1.4.1.4.6 Inter-echo spacing

Constant echo spacing (usually 10 ms) is typically used for T_2 quantification using multi-echo spin echo sequence [54, 60]. The multiecho spin echo T_2 measurement depends on inter echo spacing due to iron in subcortical GM structures of human brain [50, 61, 62]. Jensen *et al.* [61] proposed a quantitative model on relaxation rates ($R_2 = R_{2a} + \Delta R_2$) for investigating interecho spacing dependency where R_{2a} is the relaxation rate in absence of microscopic field inhomogeneities and is independent of interecho time, and ΔR_2 is the shift of inhomogeneities as a function of diffusion term. Moreover it was assumed the iron-rich oligodendrocytes act as randomly distributed magnetic spheres [61]. Previous simulation studies showed how T_2 values are varied with optimal interecho time and the number of echoes used [63, 64]. Therefore, short and constant echo spacing should be used in multiecho spin echo acquisition in order to control diffusion effects between refocusing pulses [50, 62].

1.4.1.5 Extended phase graph

The evolution of primary, secondary and stimulated echoes obtained from a series of refocusing pulses can be explained by extended phase graph (EPG) [65, 66]. It also provides more information about magnetization behavior that cannot be attained using a vector representation. If the relaxation effects are neglected during RF pulses, from Bloch equations, the magnetization

response to an on-resonance θ -pulse applied along x -direction in the rotating frame is described by the magnetizations immediately after the pulse that are given by

$$\overrightarrow{M_{x,y,z}^+} = R_x(\theta)\overrightarrow{M_{x,y,z}^-} \quad (1.67)$$

Where

$$R_x(\theta) = \begin{pmatrix} 1 & 0 & 0 \\ 0 & \cos\theta & \sin\theta \\ 0 & -\sin\theta & \cos\theta \end{pmatrix} \quad (1.68)$$

is a rotational matrix.

However, in absence of RF pulses, evolution of magnetization has two independent components while vectors have three components. Therefore replacing $(M_x \ M_y \ M_z)$ with $(M_T = M_x + iM_y \ M_z)$ we can write

$$M_T^+ = M_T^- \cos^2\left(\frac{\theta}{2}\right) + (M_T^*)^- \sin^2\left(\frac{\theta}{2}\right) + iM_z^- \sin\theta \quad (1.69)$$

$$M_z^+ = M_z^- \cos^2\left(\frac{\theta}{2}\right) - M_z^- \sin^2\left(\frac{\theta}{2}\right) - \frac{i}{2}((M_T^*)^- - M_T^-) \sin\theta \quad (1.70)$$

where M_T^- , $(M_T^*)^-$ and M_z^- are the dephasing transverse magnetization, rephasing transverse magnetization and longitudinal magnetization respectively. From the above equations it is observed that a certain fraction of M_T^- and M_z^- are specified to translate into M_T^+ and M_z^+ and there are six transfer terms that can be summarised as

Magnetization	Fractions	Model by
$M_T \rightarrow M_T, M_z \rightarrow M_z$	$\cos^2\left(\frac{\theta}{2}\right)$	0° pulse
$M_T \rightarrow M_T^*, M_z \rightarrow -M_z$	$\sin^2\left(\frac{\theta}{2}\right)$	180° pulse
$M_z \rightarrow M_y, M_y \rightarrow -M_z$	$\sin\theta$	90° pulse

Therefore any arbitrary RF pulse can be modelled as a weighted combination of 0° , 180° and 90° pulse with weighting of $\cos^2\left(\frac{\theta}{2}\right)$, $\sin^2\left(\frac{\theta}{2}\right)$ and $\sin\theta$ respectively. In summary, the 0° pulse has no effect on the magnetization but in the transverse plane there will be some phase development of the isochromats that will continue to evolve later, and the longitudinal

magnetization will stay in that direction regrowing towards equilibrium magnetisation. In contrast, the 180° pulse inverts the phase accumulation of transverse magnetization prior to the pulse such that all static field inhomogeneities are refocused and spin echoes are formed. The 90° pulse converts half of the transverse magnetization during the following free precession period into longitudinal magnetization while other half has its phase inverted prior to the phase stored as indicated in the Eq. (1.70).

Eqs. (1.69, 1.70) reveal that magnetization will break into different paths such as M_T , M_T^* and M_z at each pulse and have to track them separately. Extended phase graph allows for keeping track of all the pathways and to predict the location and the amplitude of the echo formations. Figure (1.7) shows the extended phase graph with three RF pulses creating five echoes: i) Hahn Spin echo is formed as a result of the action of first and second pulses; ii) virtual echo is formed due to the action of third pulse on first echo; iii) forms stimulated echo due to the combined effect of all three pulses; iv) and v) are spin echo formed due to the action of third pulse on FID signal from first and second pulses.

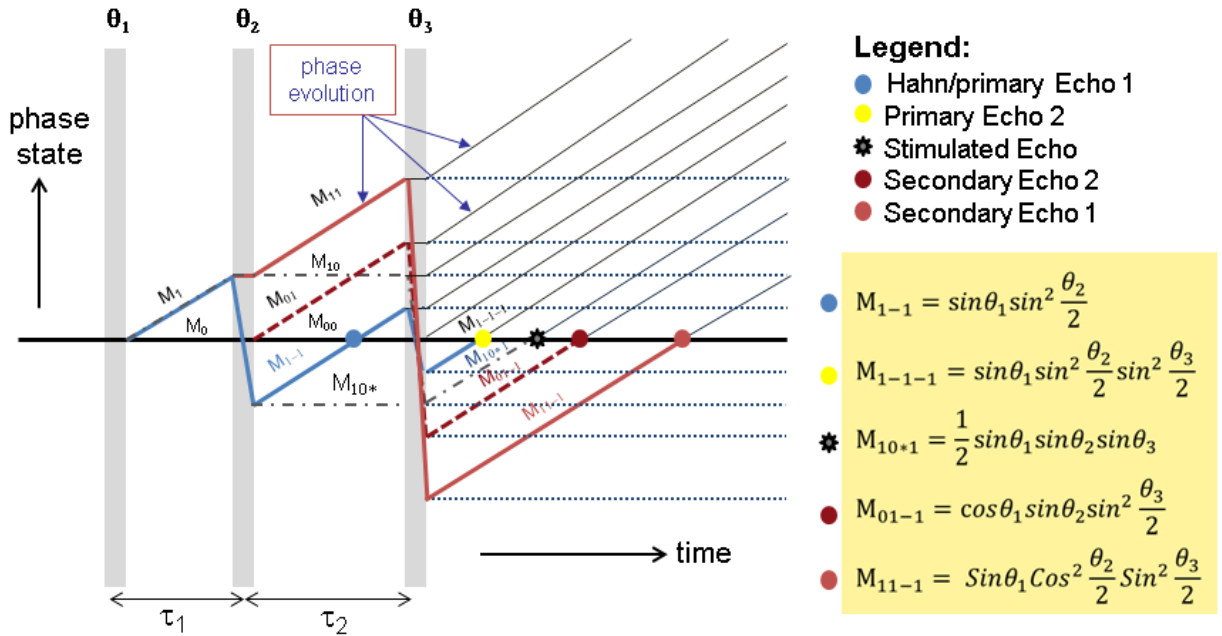


Figure 1.7: Extended phase graph as a function of time for an arbitrary angle based on two refocusing pulses. Vertical axis is phase and horizontal axis is time. Solid lines along any diagonal pathways have phase changes while lines along the horizontal pathways have no phase

changes during free precession period. Five echoes are formed with amplitude factors $M_{1,-1}$, $M_{1,-1,-1}$, $M_{1,0^*,1}$, $M_{0,1,-1}$ and $M_{1,1,-1}$.

When the relaxation effects are taken into account, the echoes are formed with amplitudes $\text{Sin}\theta_1 \text{Sin}^2 \frac{\theta_2}{2} e^{-\frac{2\tau_1}{T_2}}$ (primary spin echo 1, echo time $2\tau_1$), $\text{Sin}\theta_1 \text{Sin}^2 \frac{\theta_2}{2} \text{Sin}^2 \frac{\theta_3}{2} e^{-\frac{2\tau_2}{T_2}}$ (primary echo 2, echo time $2\tau_2$), $\frac{1}{2} \text{Sin}\theta_1 \text{Sin}\theta_2 \text{Sin}\theta_3 e^{-\frac{\tau_2}{T_1}} e^{-\frac{2\tau_1}{T_2}}$ (stimulated echo at echo time $2\tau_1 + \tau_2$), $\text{Cos}\theta_1 \text{Sin}\theta_2 \text{Sin}^2 \frac{\theta_3}{2} e^{-\frac{2(\tau_1 + 2\tau_2)}{T_2}}$ (secondary echo 2, echo time $\tau_1 + 2\tau_2$) and $\text{Sin}\theta_1 \text{Cos}^2 \frac{\theta_2}{2} \text{Sin}^2 \frac{\theta_3}{2} e^{-\frac{2(\tau_1 + \tau_2)}{T_2}}$ (secondary echo 1, echo time $2(\tau_1 + \tau_2)$).

However, the number of possible pathways can be reduced as well as the phase accumulations can be grouped into an integral number of phase intervals by using a constant interval between the refocusing pulses. Figure (1.8) shows an example where fixed spacing between refocusing pulses is used. It was suggested that constant spoiler gradients area must be used in order to get rid of all magnetization from stimulated and indirect echoes [67]. For more precise T_2 quantification from the decay curve is possible by taking into account all the coherent pathways involved [54].

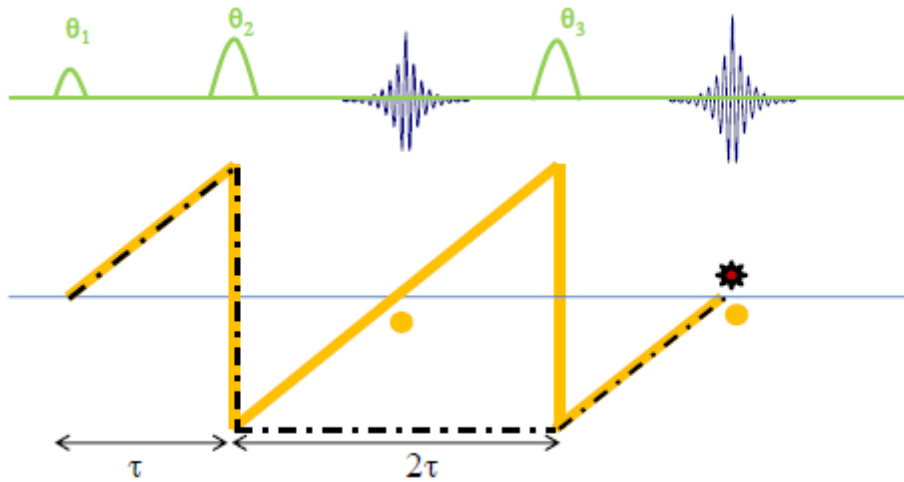


Figure 1.8: Different coherent pathways for echo formation at constant echo spacing showing spin echoes (circle) and stimulated echo (asterisk).

Now we know several echoes are created when imperfect refocusing pulses are applied in multiecho spin echo experiment. However, under the CPMG condition the secondary echoes can be eliminated by using crusher gradients. The effect of stimulated echo on flip angles is shown in Figure (1.9).

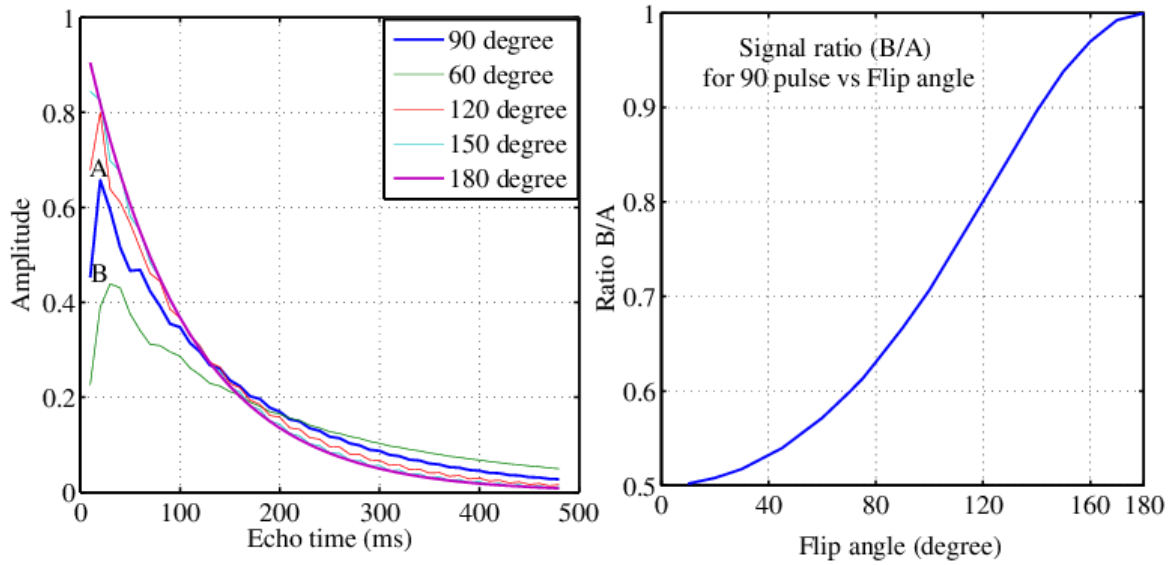


Figure 1.9: (left) Effect of stimulated echoes for arbitrary flip angles (simulated with $T_1 = \infty$, $T_2 = 100\text{ms}$). 180° refocusing pulse follows perfect exponential decay while other lower flip angles experience stimulated echo. Increased amplitude of the second echo is due to stimulated echo contribution. (Right) Ratio of first and second echo amplitudes (A and B) for 90° pulse versus flip angle.

1.4.2 Quantitative T_2^* measurement

In contrast to T_2 relaxation, T_2^* relaxation acquires a gradient echo signal generated through gradient reversal. The application of gradients induces dephasing of protons. When another gradient pulse with opposite polarity but same magnitude and duration is applied, the proton dephasing reversal occurs in the phase encoding direction producing an echo known as gradient echo. The echo is produced in the center of the readout with an application of refocusing lobe of equal area. For flow compensation, more lobes can be used to both slice selection and readout lobes. Longer TR is used for most of the longitudinal magnetization to recover in order to avoid T_1 -weighting and hence T_2^* contrast. The excitation angles are less than 90° and depend on TR choice. One big advantage of this sequence is its low tissue power deposition due to the use of reduced flip angles and no refocusing RF pulses.

Quantitative T_2^* can be obtained by collecting a series of gradient echo images with different echo times and fit the curve to estimate T_2^* in each voxel. A typical 3D multiecho gradient echo sequence is shown in Fig. (1.10).

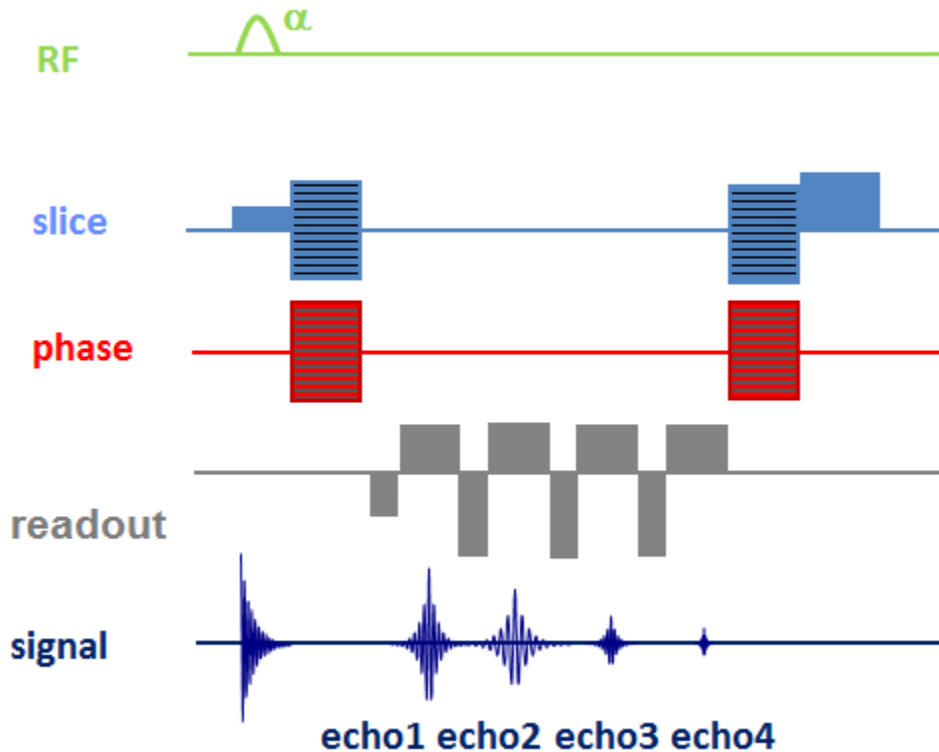


Figure 1.10: Pulse sequence diagram for a multiecho gradient echo sequence. Four echoes are shown. A monopolar acquisition is used to minimize artifacts between echoes.

One major issue of T_2^* mapping is unwanted signal loss due to the magnetic susceptibility difference near air-tissue boundaries or vessels, and the background field gradients are responsible for this signal loss. To date several methods have been proposed to minimize the effects from air-tissue boundaries such as gradient compensation, tailored RF pulses or post processing. In gradient compensation methods, signal loss is mitigated by combining a couple of gradient echo images whose refocusing slice select gradient lobes are varied successively [68, 69]. Whereas, tailored RF pulse method compensates the background gradient field effect by manipulating magnetization phase (quadratic or case specific) in the slice select direction to

reduce destructive interference at the echo time [70, 71]. Unfortunately, these methods may require long scan time, reduce SNR, or limit the slice coverage. On the other hand, post processing methods can compensate susceptibility induced signal loss more accurately with no additional cost due to scan time, SNR or resolution. In the post processing methods, signal loss due to dephasing effects is modelled as sinc modulated signal degradation arising from linear background field gradients through a rectangular voxel [72]. These signals can be spatially calculated from background field gradient map using the following Eq.

$$S = \text{sinc} \left(\frac{\gamma BFG_{x,y,z} \Delta x, y, z TE}{2} \right) \quad (1.71)$$

where signal S is a function of background field gradient ($BFG_{x,y,z}$), voxel size $\Delta x, y, z$ and echo time TE . However, this method may suffer from the contribution of artificially modulated signal arising due to susceptibility sources in the brain territories with very high iron concentration. Use of reduced voxel volume can compensate the dephasing effect but higher SNR and longer scan time are required. However, effects due to microscopic dephasing sources such as ferritin or hemosiderin cannot be eliminated or reduced by reducing the voxel volumes.

1.4.3 Previous work on transverse relaxometry

Transverse relaxation times (T_2 , T_2^* and T_2') can be obtained by using different methods. Table 1.1 shows the T_2 , T_2^* and T_2' values obtained using different methods at different field strengths that are extracted from previous work. For T_2 quantitation, several methods have been used including multi-echo spin echo (MESE), multiecho adiabatic spin echo (MASE), driven equilibrium single pulse observation of T_2 (DESPOT2), dual spin echo, and gradient echo sampling of free induction decay and echo (GESFIDE). Some of the methods are prone to SAR at higher field strengths. Extra care should be taken to quantify T_2 for more accuracy. T_2^* values can be obtained using multiecho gradient echo (MEGE), gradient echo spin echo (GESE), and spoiled 3D gradient echo (SPGR), while T_2' values can also be obtained by the GESFIDE sequence.

Table 1.1: Transverse relaxation times in healthy brain tissue from previous work

Tissue	T_2 (ms)	T_2^* (ms)	T_2' (ms)	Acq. method	B_0 (T)	Ref. No.
Globus pallidus	38±2			MESE SEC	4.7 T	[54]
	38±3			MASE	4.7 T	[24]
	39±2		85±14	GESFIDE	3.0 T	[26]
	50±3			Dual SE	1.5 T	[73]
	55±2			DESPOT2	1.5 T	[44]
	76±8	31±6	53±14	MESE, GESE	3.0 T	[74]
		27±5		SPGE	3.0 T	[75]
Putamen	55±3			MSE SEC	4.7 T	[54]
	50±3			MASE	4.7 T	[24]
	72±2			DESPOT2	1.5 T	[44]
	52±2		153±27	GESFIDE	3.0 T	[26]
	64±3			Dual SE	1.5 T	[76]
	88±6	47±7	99±29	MESE, GESE	3.0 T	[74]
		39±4		SPGE	3.0 T	[75]
Caudate	60±3			MESE SEC	4.7 T	[54]
	56±3			MASE	4.7 T	[24]
	79±2			DESPOT2	1.5 T	[44]
	59±4		151±32	GESFIDE	3.0 T	[26]
	66±3			Dual SE	1.5 T	[73]
	95±8	53±6	114±27	MESE, GESE	3.0 T	[74]
		27±4		SPGE	3.0 T	[75]
Substantia nigra	42±4		89±18	GESFIDE	3.0 T	[26]
	35±4	27±2	110±57	MESE, MEGE	3.0 T	[77]
		27±4		SPGE	3.0 T	[75]
Red nucleus	46±4		97±24	GESFIDE	3.0 T	[26]
		31±3		MESE, GESE	3.0 T	[74]
Thalamus	53±2			MESE SEC	4.7 T	[54]
	56±3			MASE	4.7 T	[24]
	72±2			DESPOT2	1.5 T	[44]
	87±3			CPMG	1.5 T	[78]
	94±6	50±6	105±22	MESE, GESE	3.0 T	[74]
		51±6		SPGE	3.0 T	[75]
Frontal WM	53±3			MESE SEC	4.7 T	[54]
	53±2			MASE	4.7 T	[24]
	56±4		285±112	GESFIDE	3.0 T	[26]
	69±2			DESPOT2	1.5 T	[44]
	65±3			Dual SE	1.5 T	[73]
	90±9	48±5	101±23	MESE, GESE	3.0 T	[74]

1.5 Human brain, Multiple Sclerosis and Iron

1.5.1 Brief description of human brain

The human brain is composed of three principle structures: the cerebrum, the brainstem, and the cerebellum. The largest component of the brain is the cerebrum. It is divided into large, paired cerebral hemispheres that are connected by the corpus callosum. Each of the hemispheres is further divided into four lobes such as the frontal lobe, the temporal lobe, the parietal lobe, and the occipital lobe. The cerebrum is also composed of cerebral cortex, basal ganglia and limbic system. The cerebrum is involved in several functions including sensations, intellect, memory, complex movements, higher mental functions such as conscious thoughts and action. Brainstem is located underneath the limbic system. The structure includes a variety of important processing centers that relay information from or towards the cerebrum or cerebellum. The brainstem is made of the medulla oblongata, pons, and midbrain. The brainstem is responsible for vital functions such as breathing, heartbeat, and blood pressure. The cerebellum is located at the bottom of the brain and contains the posterior fossa, dorsal to the pons and medulla oblongata. The cerebellum is associated with coordination of movement, posture and balance [79].

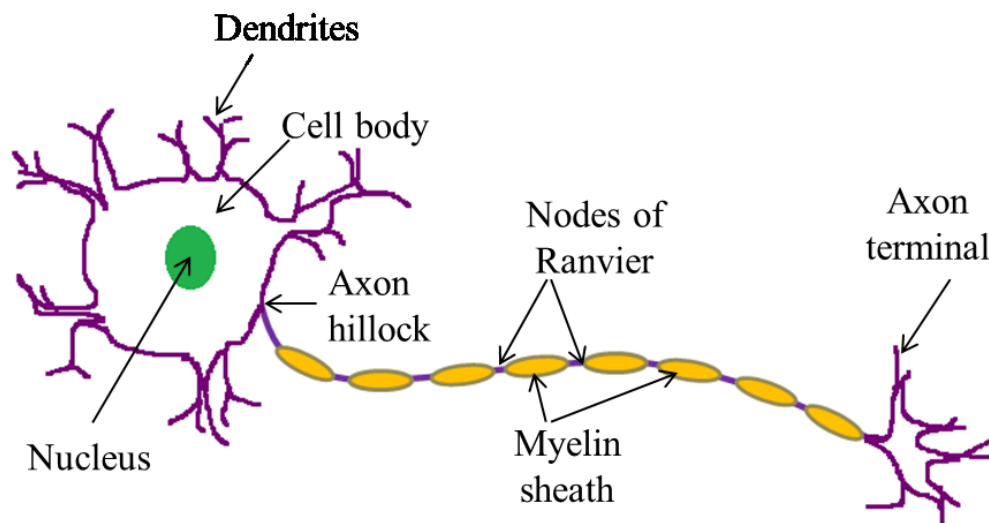


Figure 1.11: Sketch of a typical nerve cell in the brain

Microscopically, the brain is composed of neurons (or nerve cells) and neuroglia (or glial cells). Neurons form the basis of communication in the body such as receiving, processing,

integrating and transmitting information. On the other hand, glial cells function as the physical support for neurons. Figure (1.11) shows a sketch of a typical nerve cell. A neuron is electrically excitable that relays information via electrical and chemical signaling. There are $\sim 10^{11}$ neurons with 10^{13} - 10^{14} connections between them in a typical human brain. A neuron is made up of cell body, dendrites and the axon. The cell body (or soma) contains a large, round nucleus and acts as a metabolic center of the cell. Dendrites are highly branched thin structures which extend out from the cell body. Each branch of dendrites has dendritic spines which represents ~ 80 - 90% of total surface area of neuron. Dendrites play important roles in intercellular communication. An axon is a long process capable of transmitting electric impulses also known as action potentials over distances up to 1 m and range from $0.2 - 20\ \mu\text{m}$. The initial segment or base of the axon is attached to the cell body through axon hillock. Axons are insulated by myelin sheath for quick propagation of the signals. The regions that are unmyelinated and periodically interspersed between the segments of myelin sheaths are termed as the nodes of Ranvier. The end of the axon branches of one neuron is connected with cell body or dendrites of another neuron, is known as synapse. Every synapse involves two cells: pre-synaptic, which releases signals (neurotransmitter, chemical, electrical) and includes synaptic terminal; and the post-synaptic cell, which receives signal. The branches of a neuron can form synaptic connections with about 100 other neurons.

We already know the glial cells act as supporting structures to neurons. There are four types of glial cells are found in CNS: ependymal cells, astrocytes, oligodendrocytes and microglia. Ependymal cells line the ventricular system of the brain. These cells assist in producing, circulating and monitoring CSF. CSF is contained in the ventricles and is mostly produced by modified ependymal cells in choroid plexus. The CSF surrounds the exposed surfaces of CNS and has several functions including the cushioning the brain and spinal cord, transporting nutrients and chemical stability. Astrocytes are the most abundant cell in the brain. These cells have many functions, including maintenance of blood-brain barrier (BBB), guidance of neuron development, regulating iron, modulation of synaptic transmission and repairing of damaged neural tissue. Microglia nuclei are least abundant and the smallest glial cells in the CNS. These cells engulf cellular debris, waste products and pathogens by phagocytosis. Oligodendrocytes provide support and insulate the axons by creating the myelin sheath which is composed of $\sim 80\%$ lipid and $\sim 20\%$ protein. Such an axon is termed a myelinated axon. A single

oligodendrocyte myelinates segments of numerous axons. Myelinated axons have a whitish appearance due to the lipid in the myelin. For this reason, the territories dominated by myelinated axons are termed as white matter (WM). WM contains of 50% of the human brain by volume and 50% of WM weight is occupied by myelin. On the other hand, regions containing neural cell bodies, neuropil (dendrites and unmyelinated axons), glial cells and capillaries have a dusky grey color and make up the grey matter (GM). GM is distributed mostly at the exterior of the brain forming its cortex, in the cerebellum, in the brain stem (substantia nigra, red nucleus) as well as in the depth of the cerebrum (thalamus, hypothalamus, sub-thalamus, and basal ganglia). The basal ganglia contain globus pallidus, putamen, and caudate nucleus. T_1 and T_2 weighted MR images of DGM structures are shown in Figure (1.11). As a whole, basal ganglia are associated with movement control. Usually caudate and putamen receive information from the sensory, motor control regions of the cerebral cortex. Information is then processed in caudate, putamen and globus pallidus. Most of the output leaves the globus pallidus and synapse to the thalamus and then information is projected to suitable regions of the cerebral cortex. That is, through this feedback looping the basal ganglia structures alter the motor control information issued by the cerebral cortex.

1.5.2 Brain Iron

Iron is one of the essential metal ions for biological functions such as DNA synthesis, gene expression, myelination, neurotransmission, and mitochondrial electron transport in the human brain [80, 81]. Iron is paramagnetic in nature and occurs with adequate concentration (above ~ 0.1 mM) which can change the MRI signal. In contrary, some other important metal ions such as copper, manganese etc. are contained in the human brain but with inadequate concentrations to change the MRI relaxation rates except under some abnormal neurological conditions [20].

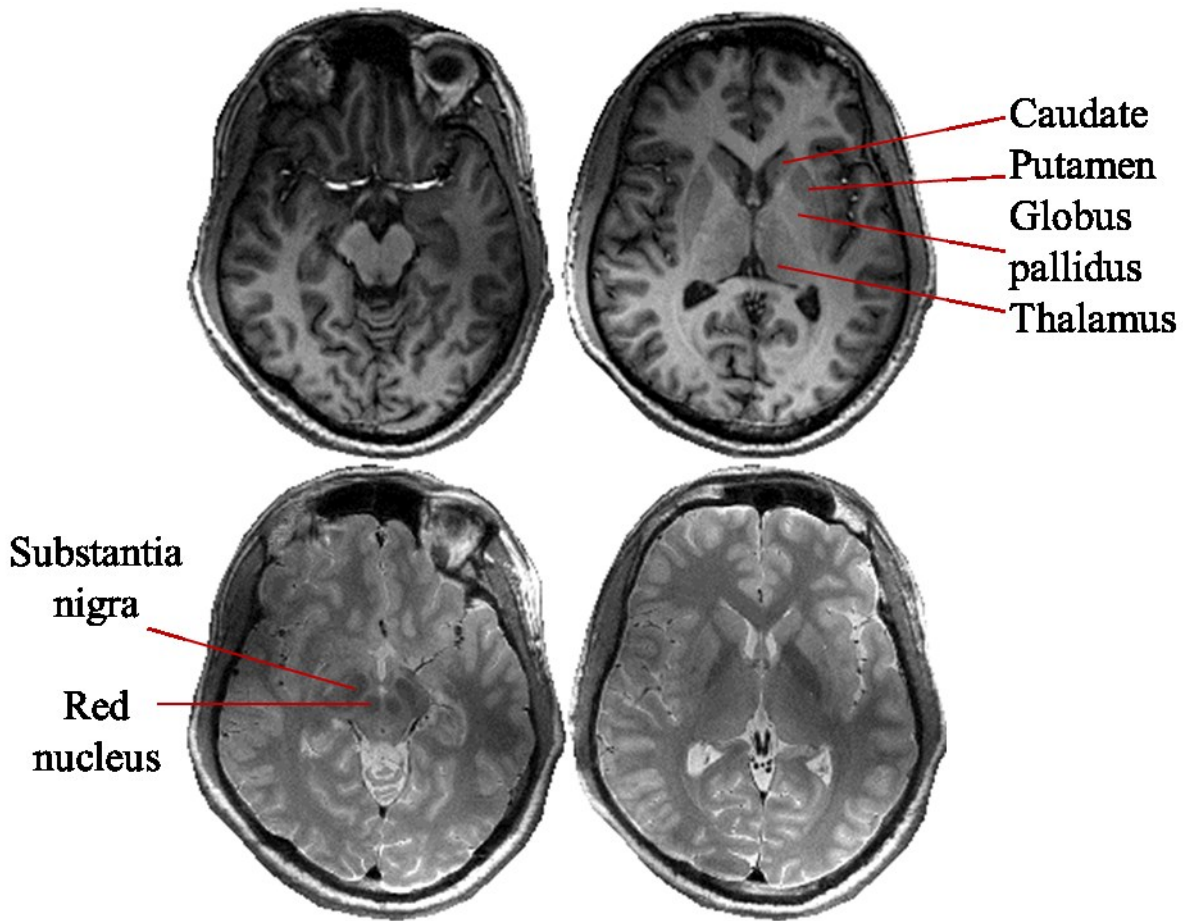


Figure 1.12: Axial T1-MPRAGE (top row) and T2-FSE (bottom row) images showing several sub-cortical grey matter territories

Based on the chemical composition, there are two groups of iron found in the brain: heme and non-heme. Heme iron in the form of hemoglobin is usually present in the red blood cells of the vascular blood pool. Hematomas are formed when blood goes into the brain under the hemorrhagic pathological condition. Due to hemolysis, hemoglobin is released and then taken up by the glial cells and within a couple of weeks heme iron is transformed into ferritin and hemosiderin.

The normal adult human brain contains approximately 60 mg of non-heme iron distributed in the neurons and glial cells [82]. The non-heme iron is stored mainly in ferritin and hemosiderin. It can be found mostly in oligodendrocytes and about one third of the non heme brain can be extracted in the form of ferritin [82]. Ferritin is a protein with the shape of a hollow

spherical shell that contains about 2000 to 4500 iron atoms [83]. Inside the shell, the iron is believed to be stored in the Fe(III) oxidation state [84] which is incorporated in the ferrihydrite crystal ($5\text{Fe}_2\text{O}_3 \cdot 9\text{H}_2\text{O}$) attached to the inner wall of the shell. The spherical protein shell consists of 24 polypeptide subunit chains, surrounding an aqueous cavity with diameters of about 8-12 nm. However, the real structure of the ferritin are not clearly defined yet, whether it's really ferrihydrite or a mixture of different iron oxide phases [85, 86]. In fact, it's very important to know the exact form of ferritin for the protein's ability to store and release the iron in controlled fashion. Moreover, hemosiderin may deposit in diseases associated with iron overload and can appear in the degraded form of ferritin where degradation is due to lysosomes [87].

The distribution of non-heme brain iron is not homogeneous [82, 88, 89]. Histological assessments suggest the highest concentration of iron in brain is contained by the extrapyramidal nuclei such as globus pallidus, putamen, caudate nucleus, red nucleus and substantia nigra. Previous report [82] indicates that the average concentrations of non heme iron per 100 mg wet tissue in an adult human brain are 21 mg in globus pallidus, 13 mg in putamen, 18.5 mg in substantia nigra, 4.8 mg in thalamus, and 4.2 mg in frontal WM.

Non-heme iron has a key role for myelination in the central nervous system. It is a vital redox metal that can accept or donate electrons to contribute to DNA synthesis and for the electro transport chain in the brain. However, excess unchelated iron ions are extremely toxic to the tissue and also can produce extremely reactive hydroxyl radicals via Fenton reactions [$\text{Fe(II)} + \text{H}_2\text{O}_2 \rightarrow \cdot\text{OH} + \text{Fe(III)}$] [90-92]. The hydroxyl radical ($\cdot\text{OH}$), can denature proteins, DNA and damage macromolecules such as lipids, amino acids and nucleic acids. The reactivity of the hydroxyl radical depends on the diffusion time in the scale of micro second. Therefore, anomalous high storage of iron and chelation are thought as the main causes for neurodegenerative diseases.

In multiple sclerosis, oligodendrocytes are mostly destroyed as these cells contain a highest fraction of non-heme iron. Also previous studies suggested that there are some increased iron accumulation in the brain especially in the mid brain of MS patients [29]. In Parkinson's disease, increased iron accumulation in the basal ganglia structures has been reported in the past work [93].

MRI is a useful technique to measure iron content with the consideration that relaxation rates and susceptibility phase are strongly altered in the presence of iron. Previous report [29] has presumed the probable territories of iron content by investigating the T₂ hypo-intensity and shortening of the relaxation times. Iron related relaxation is complex in nature.

1.5.2.1 FDRI

Field Dependent R₂ Increase (FDRI), a method developed by Bartzokis [94], is defined as the degree at which measured R₂ values are affected by the MRI field strengths.

$$FDRI = 1/T_{2 \text{ high field}} - 1/T_{2 \text{ low field}} \quad (1.72)$$

FDRI is a specific measure of non-heme iron that is in the form of ferritin molecules. The method is based on field dependent dephasing mechanisms. The protocol by Bartzokis includes a dual-echo CPMG with TR/TE=2500/20, 90 ms at 0.5 T and 1.5 T keeping the same slice location in both the field strength. Moreover, FSE at 1.5,3.0 T [95] and twice refocused adiabatic pulses at higher field [25] have been used to get more iron specificity. Previous studies [94] indicate that basal ganglia in DGM demonstrate large FDRI values as these regions have field dependent dephasing mechanisms implying the basal ganglia has highest iron concentration in the brain. While WM does not demonstrate large FDRI values due to the field independent dephasing dominates in these regions. Bartzokis *et.al.* have done FDRI measurement for several neurological disorders such as Alzheimer's disease, Huntington's disease, as well as aging based on the correlation with Hallgren's equations. [82, 94]. Using the FDRI technique it has been shown that globus pallidus, putamen, red nucleus, substantia nigra have increased FDRI [96, 97].

1.5.3 Multiple Sclerosis and MRI

Multiple sclerosis (MS) is an autoimmune disease of the CNS in humans affecting the brain (mostly cerebrum, cerebellum, brain stem, optic nerve) and the spine, and is characterized by demyelination, inflammation, and neurodegeneration. In most cases MS causes the breakdown of myelin sheaths surrounding the axons and then form WM sclerosis and consequently neural connections are reduced. It is also termed as disseminated sclerosis and has broad range of symptoms and signs [98]. The age of onset of MS usually occurs in early adulthood, between 15 to 40 years and women are affected twice by number than men. The prevalence rate is in the range between 2 and 350 per 100,000. [99-101]. MS is most common in North America,

Northern Europe and affecting over 50,000 peoples in Canada. The rate to be affected by MS is very low in Asia, Africa and South America. The genetic and environmental and infectious factors are thought to be the precursors of the disease.

Nerve cells in brain and spinal cord are affected by the MS and do not allow to communicate efficiently with each other. Usually signals are passed through axons which are covered with insulated myelin. In MS, myelins are damaged and axons cannot conduct the signals [102]. MS is mostly myelin loss related plaques. The causes of the disease remains unknown though most of the information about the mechanism processes concerned with the disease are hinted using epidemiological studies and there is no cure till now.

Major symptoms of the disease are coordination impairment, depression, visual impairment, loss of sensitivity, numbness, cognitive and sensory impairment, bladder and bowel difficulties. Patients disability progression and symptom are commonly assessed by Kurtzke Expanded Disability Status Scale (EDSS) [103]. The EDSS is expressed into a range of numerical numbers from 0 to 10 based on the disability of the eight functional systems such as cerebellar, cerebral, brainstem, pyramidal, bladder/ bowel, mental, visual and others. The score 0 represents a normal neurological exam while 10 indicates death due to MS. Other scores, such as 1.0 to 4.5 is for fully ambulatory MS patients and 5.0 to 9.5 is for the impairment to ambulation.

There are four disease categories identified in MS. They are: Relapsing Remitting MS (RRMS), Primary progressive MS (PPMS), Secondary Progressive MS (SPMS) and Progressive Relapsing MS (PRMS). RRMS is the most common form (about 65-80%) of the MS disease and the patients experience an attack or a series of attack followed by partial or a complete disappearance of the symptom or remission. Disability gradually increases and about 50% of RRMS may persist for about 10 years before the onset of SPMS where there is no real period of remission. PPMS, commonly found in men, is considered as gradual clinical decline and disability progresses continuously despite some partial relapses. About 10-20% of MS individuals begin with PPMS. PRMS is a rarer form of MS where disability progresses with acute attacks throughout and there is no relief from accumulated symptoms.

In patho-physiology, MS is mostly characterized by main damage to WM, referred to as *lesions* or *plaques*. However, lesions can also occur in cortical and sub-cortical GM, and normal appearing WM (NAWM). The formation of WM lesions is due to the demyelination which arises

from an autoimmune response affecting antigens. The source of these antigens is some myelin basis proteins. Lesions have been linked with the breakdown of the blood brain barrier (BBB) which allows monocytes and lymphocytes to reach and attack the myelin sheath, destroys oligodendrocytes and damages neurons [104-106]. At the initial stage of demyelination there might be some possibilities of partial remyelination which results in thinner myelin with shorter inter-node distances. Repeated cycles of demyelination and remyelination form permanent lesions. Previous literature [107, 108] suggested the presence of progressive astrogliosis, demyelination and remyelination in the normal appearing tissue in RRMS. Histochemical observation indicates neuronal loss and atrophy in cortical GM [108].

Magnetic resonance imaging provides a very powerful tool for disease diagnosis and it helps to enhance our understanding of the pathology. Usually MRI techniques such as SE, GE, SWI etc. are used to characterize MS. T_2 -weighted (T_2w) and Proton density-weighted (PDw) acquisitions provides hyper-intensity in the WM lesions territories, reflecting the increased water content at different stages of lesion evolution. PDw , useful for peri-ventricular lesions, can distinguish the WM lesions and CSF. While T_2w imaging is sensitive to lesions of the cerebrum and distinguished from CSF with a fluid attenuated inverse recovery (FLAIR) scan. T_2w provides more lesions information than T_1w . Previous relaxation studies on MS found that some acute lesions have abnormally high T_1 in T_1 -weighted images but with time T_1 of acute lesions decreased and become same as that of chronic lesions [109]. These hypo-intense territories (increased T_1) are recognized as the demyelination and loss of glial and neuronal cells. And, gradual T_1 recovery may be due to partial remyelination. T_1 relaxation can be enhanced by the use of contrast agent containing paramagnetic gadolinium which can reveal the BBB leakage and indicate the site of active lesions [110, 111]. These conventional techniques are used to diagnosis MS but sometimes does not provide accurate information about the disease symptoms [110, 111]. However, some other advanced MRI techniques have been developed to explore the potential specificity for MS studies using the specific measurement using the tissue properties [30]. For example, Magnetization transfer (MT) imaging is used to get information from bound and free macromolecules, and its quantitative measure indicates the myelin content [112, 113]. Moreover, multi-component T_2 analysis can give information about myelin water fraction (MWF) [114]. Reduced MWF is observed in WM lesions and in NAWM [115]. Susceptibility weighted imaging (SWI) is sensitive to magnetic susceptibility of the tissues and phase

enhancement is observed in the cortical grey matter structures and in lesions [116-118]. As well, some MRI studies [116, 119] and histology [119] suggest that irons are accumulated in the brains of MS patients. However, the disease progression due to the iron accumulation is not fully understood.

1.5.4 Brain atrophy of MS

Brain atrophy is very attractive and clinically relevant MRI-based measure in MS though it is not used in routine clinical exams. It is defined as the loss of brain tissue (both myelin and axons). It can affect the whole brain or specific structures of brain tissue and can lead irreversible neurological and cognitive impairment. Several studies reported the correlation between atrophy and cognitive impairment, EDSS, and MSSS scores. The exact mechanism of brain atrophy in MS is still elusive. The brain atrophy is observed in all stages of MS. Previous studies suggested that the brain volume decreases by 0.6-1% per year in patients with MS while in controls this change is 0.1-0.3% per year [120-122]. Similar annual rates of atrophy are reported in different disease subtypes. It seems that atrophy progression rate does not depend of disease subtypes [123]. However, greater annual rate of ventricular enlargement is found in SPMS compared to that of RRMS [124]. The unusual rates of atrophy progression might be due to other factors such as environmental and genetic loads [125].

Although MS is known as a WM disease, atrophy occurs in both WM and GM. However, GM atrophy has been considered as more sensitive biomarker of disease process in MS compared to whole brain (WB) atrophy or WM atrophy. It has also been suggested that rate of change of GM atrophy accelerates as the disease progresses [126, 127]. On the other hand, WM volume remains almost same during the course of disease. GM atrophy can be used as a better predictor of disability and cognitive impairment compared to WM atrophy [128]. Atrophy also occurs in different regions of the brain at different disease processes in MS. For instance, volume loss in the thalamus and hypothalamus was identified in patients with CIS [129, 130]. But some other studies found the involvement of DGM atrophy in CIS [130-132]. Atrophy of DGM structures, the cerebellum and the brainstem are found to be involved in RRMS and SPMS [133]. Moreover, iron accumulation and atrophy are related in MS DGM [134].

Several methods including automated, manual and semi-automated methods are used for atrophy measurements. Manual methods are simple and do not require software but there are

some limitations on using manual methods such as poor reproducibility, high measurement variability, and low precision [135]. To get better reliability and precision, an experienced operator is required who is good at interpreting neuroanatomy and pathology from the sequence used. Also manual segmentation is time consuming and is rarely used for multislice or 3D image sets. In order to get improved speed and reproducibility, semi-automated methods can be used instead of using manual methods. Previous studies have used semi-automated segmentation methods to assess brain atrophy and found similar results compared to automated methods [136]. On the other hand, automated methods are more robust and attractive due to the increased efficiency, objectivity, reliability and precision. To date, many automated methods exist to measure atrophy. Most of the automated methods are intensity-based in which segmentation is derived from the difference in signal intensity in the brain parenchyma and CSF alone. Depending on the operator's experience on neuroanatomy and tissue pathology in MS, as well as the robustness of the software, automated methods can be the most promising and time-saving methods. However, accuracy, reproducibility and precision of atrophy measurement methods may be dependent critically on the specific imaging parameters (i.e., TE, TR, flip angle, slice thickness etc.) of the pulse sequence employed [137].

Cross sectional and longitudinal studies are used to evaluate brain atrophy. Cross sectional or single time point measurements of the brain volume, ventricular width or area are performed on patients with MS. Brain atrophy of MS can be predicted by comparing the measurements with that of controls. However, brain atrophy using single time-point measurements can be difficult to interpret because of wide variability of measurements among the subjects. However, disease progression and rate of atrophy measurements can be predicted more precisely by longitudinal study. These can be obtained by subtracting a serial cross sectional measurements or by using automated registration methods such as FSL SIENAX, SIENA, FIRST etc.

SIENAX (Structural Image Evaluation using Normalization of Atrophy Cross-sectional), part of FSL, uses automated algorithm to estimate normalized volumes of WM, GM, cortical GM, ventricular CSF, as well as whole brain [138]. SIENAX uses the brain extraction tool (BET) to extract brain by stripping non-brain tissues and estimate the outer skull surface [139]. SIENAX estimates the scaling between subject's image and standard space by using the brain and skull images and then register the brain image to standard space (Montreal nNurological

Institute (MNI) standard template, MNI-152). The method is robust and accurate with brain volume measurement error of 0.5-1% for cross-sectional study and 0.15% for longitudinal study [138].

SIENA (Structural Image Evaluation using Normalization of Atrophy) is the longitudinal version of SIENAX. Similar to SIENAX, it segments brain from non-brain tissue and estimates the outer skull surface and then registers serial brain images to standard space after scaling. SIENA produces percentage brain volume change (PBVC) on the basis of the movement of the image edges with sub-voxel accuracy of 0.15% error [140].

In order to get individual volumes of subcortical structures in the human brain, FSL FIRST (FMRIB's integrated registration and segmentation tool) can be used. FIRST is a model-based segmentation method [141]. It uses manually labelled T1-weighted images provided by the Centre for Morphometric Analysis (CMA), Boston to construct automated segmentation of subcortical structures such as left and right of globus pallidus, caudate nucleus, putamen, thalamus, amygdala, hippocampus, accumbens, as well as the brainstem.

1.6 Thesis Objective

The goal of this thesis was to improve and apply transverse relaxometry methods for better understanding of human brain and MS. Quantitative relaxometry methods provide absolute measure of tissue specific changes. These methods can play a vital role to identify the disease processes and state in the patients with MS. The following specific aims were identified; and each of them is the basis of the following chapters:

- To determine a potential biomarker and to understand the iron dynamics in MS, T_2 relaxometry of healthy controls and patients were compared, and correlated with disability and brain atrophy of MS.
- To improve multi-echo spin echo T_2 mapping method by employing reduced echo train lengths through stimulated echo compensation.
- To evaluate the iron sensitivity in human brain by using relaxometry difference methods at 1.5 T and 4.7 T.

- To investigate the disease progression and state of MS by long term longitudinal study on retrospective data obtained from clinically available sequences using two-echo fitting approach for quantitative T_2 method and brain atrophy measurements.

1.7 References

1. Ray Hashman Hashemi WGB, Christopher J. Lisanti. *MRI: The Basics*. Third ed.: Lippincott Williams & Wilkins, 2010, p.400.
2. Tofts P. *Quantitative MRI of the Brain: Measuring Changes Caused by Disease*. Oxford: Blackwell Science Publ, 2003, p.1-657.
3. Matt A. Bernstein KFK, Xiaohong Joe Zhou *Handbook of MRI Pulse Sequences*. 1 edition ed.: Academic Press, 2004.
4. Zhi-Pei Liang PCL. *Principles of Magnetic Resonance Imaging: A Signal Processing Perspective*. 1 edition ed.: Wiley-IEEE Press, 1999, p.416.
5. E. Mark Haacke RWBMRT, Ramesh Venkatesan. *MRI Physical Principles and Sequence Design*. 1 edition ed.: Wiley-Liss, 1999.
6. de Graaf RA. *In vivo NMR spectroscopy: principles and techniques*. 2nd edition ed.: John Wiley @ Sons, Ltd., 2007.
7. Bloembergen N, Purcell EM and Pound RV. Relaxation effects in nuclear magnetic resonance absorption. *Physical Review*. 1948; 73: 679-712.
8. Abragam A. *The principles of nuclear magnetism* Oxford : Clarendon Press, 1961, p.599.
9. Stark DD. *Magnetic resonance imaging*. St. Louis : C.V. Mosby Co., 1992.
10. Allen D. Elster MD JHBM. *Questions and Answers in Magnetic Resonance Imaging*. 2nd ed.: Mosby, 2000.
11. McRobbie DW. *MRI from Picture to Proton*. 2nd ed.: Cambridge University Press, 2007.
12. Eng J, Ceckler TL and Balaban RS. Quantitative ^1H magnetization transfer imaging in vivo. *Magnetic Resonance in Medicine*. 1991; 17: 304-14.

13. De Boer R. Magnetization transfer contrast.
14. Hoult DI. The principle of reciprocity in signal strength calculations - A mathematical guide. *Concepts in magnetic Resonance*. 2000; 12: 173-87.
15. Collins CM, Liu W, Schreiber W, Yang QX and Smith MB. Central brightening due to constructive interference with, without, and despite dielectric resonance. *Journal of Magnetic Resonance Imaging*. 2005; 21: 192-6.
16. Lauterbur PC. Image Formation by Induced Local Interactions: Examples Employing Nuclear Magnetic Resonance. *Nature*. 1973: 190-1.
17. D Hoult CNC. *Biomedical Magnetic Resonance Technology* Taylor & Francis, 1989, p.250.
18. Michaeli S, Garwood M, Zhu XH, et al. Proton T2 relaxation study of water, N-acetylaspartate, and creatine in human brain using Hahn and Carr-Purcell spin echoes at 4T and 7T. *Magnetic Resonance in Medicine*. 2002; 47: 629-33.
19. Norris DG. High field human imaging. *Journal of Magnetic Resonance Imaging*. 2003; 18: 519-29.
20. Schenck JF and Zimmerman EA. High-field magnetic resonance imaging of brain iron: birth of a biomarker? *NMR in Biomedicine*. 2004; 17: 433-45.
21. de Graaf RA, Brown PB, McIntyre S, Nixon TW, Behar KL and Rothman DL. High magnetic field water and metabolite proton T1 and T2 relaxation in rat brain in vivo. *Magnetic Resonance in Medicine*. 2006; 56: 386-94.
22. Rooney WD, Johnson G, Li X, et al. Magnetic field and tissue dependencies of human brain longitudinal $^1\text{H}_2\text{O}$ relaxation in vivo. *Magnetic Resonance in Medicine*. 2007; 57: 308-18.
23. Johnson GA, Herfkens RJ and Brown MA. Tissue relaxation time - invivo field-dependence. *Radiology*. 1985; 156: 805-10.
24. Mitsumori F, Watanabe H and Takaya N. Estimation of Brain Iron Concentration In Vivo Using a Linear Relationship Between Regional Iron and Apparent Transverse Relaxation Rate of the Tissue Water at 4.7T. *Magnetic Resonance in Medicine*. 2009; 62: 1326-30.

25. Mitsumori F, Watanabe H, Takaya N, et al. Toward understanding transverse relaxation in human brain through its field dependence. *Magnetic Resonance in Medicine*. 2012; 68: 947-53.
26. Gelman N, Gorell JM, Barker PB, et al. MR imaging of human brain at 3.0 T: preliminary report on transverse relaxation rates and relation to estimated iron content. *Radiology*. 1999; 210: 759-67.
27. Gelman N, Ewing JR, Gorell JM, Spickler EM and Solomon EG. Interregional variation of longitudinal relaxation rates in human brain at 3.0 T: Relation to estimated iron and water contents. *Magnetic Resonance in Medicine*. 2001; 45: 71-9.
28. Hoult DI, Chen CN and Sank VJ. The field-dependence of NMR imaging .2. Arguments concerning an optimal field-strength. *Magnetic Resonance in Medicine*. 1986; 3: 730-46.
29. Lebel RM, Eissa A, Seres P, Blevins G and Wilman AH. Quantitative high-field imaging of sub-cortical gray matter in multiple sclerosis. *Multiple Sclerosis Journal*. 2012; 18: 433-41.
30. MacKay AL, Vavasour IM, Rauscher A, et al. MR Relaxation in Multiple Sclerosis. *Neuroimaging Clinics of North America*. 2009; 19: 1-26.
31. Dardzinski BJ, Mosher TJ, Li SZ, VanSlyke MA and Smith MB. Spatial variation of T2 in human articular cartilage. *Radiology*. 1997; 205: 546-50.
32. St Pierre TG, Clark PR, Chua-Anusorn W, et al. Non-invasive measurement and imaging of liver iron concentrations using proton magnetic resonance. *Blood*. 2005; 105: 855-61.
33. Perry J, Haughton V, Anderson PA, Wu Y, Fine J and Mistretta C. The value of T2 relaxation times to characterize lumbar intervertebral disks: Preliminary results. *American Journal of Neuroradiology*. 2006; 27: 337-42.
34. Hosch W, Bock M, Libicher M, et al. MR-Relaxometry of myocardial tissue - Significant elevation of T1 and T2 relaxation times in cardiac amyloidosis. *Investigative Radiology*. 2007; 42: 636-42.
35. White LM, Sussman MS, Hurtig M, Probyn L, Tomlinson G and Kandel R. Cartilage T2 assessment: Differentiation of normal hyaline cartilage and reparative tissue after arthroscopic cartilage repair in equine subjects. *Radiology*. 2006; 241: 407-14.

36. Martin AJ, Poon CS, Thomas GM, Kapusta LR, Shaw PA and Henkelman RM. MR evaluation of cervical cancer in hysterectomy specimens: correlation of quantitative T2 measurement and histology. *J Magn Reson Imaging*. 1994; 4: 779-86.
37. Liney GP, Knowles AJ, Manton DJ, Turnbull LW, Blackband SJ and Horsman A. Comparison of conventional single echo and multi-echo sequences with a fast spin echo sequence for quantitative T2 mapping: Application to the prostate. *Journal of Magnetic Resonance Imaging*. 1996; 6: 603-7.
38. Whittall KP, MacKay AL, Graeb DA, Nugent RA, Li DKB and Paty DW. In vivo measurement of T2 distributions and water contents in normal human brain. *Magnetic Resonance in Medicine*. 1997; 37: 34-43.
39. MacKay A, Laule C, Vavasour I, Bjarnason T, Kolind S and Madler B. Insights into brain microstructure from the T2 distribution. *Magnetic Resonance Imaging*. 2006; 24: 515-25.
40. Poon CS and Henkelman RM. Practical T2 quantitation for clinical applications. *Journal of Magnetic Resonance Imaging*. 1992; 2: 541-53.
41. Deichmann R, Adolf H, Noth U, Morrissey S, Schwarzbauer C and Haase A. Fast T2 mapping with snapshot flash imaging. *Magnetic Resonance Imaging*. 1995; 13: 633-9.
42. Schmitt P, Griswold MA, Jakob PM, et al. Inversion recovery TrueFISP: Quantification of T1, T2, and spin density. *Magnetic Resonance in Medicine*. 2004; 51: 661-7.
43. Bieri O, Scheffler K, Welsch GH, Trattning S, Mamisch TC and Ganter C. Quantitative Mapping of T2 Using Partial Spoiling. *Magnetic Resonance in Medicine*. 2011; 66: 410-8.
44. Deoni SCL, Rutt BK and Peters TM. Rapid combined T1 and T2 mapping using gradient recalled acquisition in the steady state. *Magnetic Resonance in Medicine*. 2003; 49: 515-26.
45. Hahn EL. Spin echoes. *Physical Review*. 1950; 80: 580-94.
46. Carr HY and Purcell EM. Effects of diffusion on free precession in nuclear magnetic resonance experiments. *Physical Review*. 1954; 94: 630-8.
47. Meiboom S and Gill D. Modified spin-echo method for measuring nuclear relaxation times. *Rev Sci Instrum*. 1958; 29: 688-91.

48. Whitaker CDS SP, Beversdorf DQ, Santi MS, Dashner RA, Chakeres DW, Schmalbrock P. T2 and T2* Relaxation in Normal and Alzheimer's Formalin Fixed Hippocampus at 8 T. *International Society of Magnetic Resonance in Medicine*. Honolulu, Hawaii.2002, p. 1274.
49. Ye FQ, Martin W and Allen PS. Estimation of brain iron in vivo by means of the interecho time dependence of image contrast. *Magnetic Resonance in Medicine*. 1996; 36: 153-8.
50. Bartha R, Michaeli S, Merkle H, et al. In vivo (H₂O) H1 T2(dagger) measurement in the human occipital lobe at 4T and 7T by Carr-Purcell MRI: Detection of microscopic susceptibility contrast. *Magnetic Resonance in Medicine*. 2002; 47: 742-50.
51. Hardy P and Henkelman RM. On the transverse relaxation rate enhancement induced by diffusion of spins through inhomogeneous fields. *Magnetic Resonance in Medicine*. 1991; 17: 348-56.
52. Weisskoff RM, Zuo CS, Boxerman JL and Rosen BR. Microscopic susceptibility variation and transverse relaxation - theory and experiment. *Magnetic Resonance in Medicine*. 1994; 31: 601-10.
53. Yablonskiy DA and Haacke EM. Theory of NMR signal behavior in magnetically inhomogeneous tissues - the static dephasing regime. *Magnetic Resonance in Medicine*. 1994; 32: 749-63.
54. Lebel RM and Wilman AH. Transverse relaxometry with stimulated echo compensation. *Magnetic Resonance in Medicine*. 2010; 64: 1005-14.
55. Haacke EM, Brown R, Thompson M and Venkatesan R. Magnetic resonance imaging: physical principles and sequence design. 1999. *New York: A John Wiley and Sons*.
56. FDA. Criteria for Significant Risk Investigations of Magnetic Resonance Diagnostic Devices. In: Staff GflaFaDA, (ed.). USA2014.
57. Weigel M, Helms G and Hennig J. Investigation and modeling of magnetization transfer effects in two-dimensional multislice turbo spin echo sequences with low constant or variable flip angles at 3 T. *Magnetic Resonance in Medicine*. 2010; 63: 230-4.

58. Chang Y, Bae SJ, Lee YJ, et al. Incidental magnetization transfer effects in multislice brain MRI at 3.0 T. *Journal of Magnetic Resonance Imaging*. 2007; 25: 862-5.
59. Miller DH, Johnson G, Tofts PS, Macmanus D and McDonald WI. Precise relaxation-time measurements of normal-appearing white matter in inflammatory central nervous-system disease. *Magnetic Resonance in Medicine*. 1989; 11: 331-6.
60. Prasloski T, Mädler B, Xiang QS, MacKay A and Jones C. Applications of stimulated echo correction to multicomponent T2 analysis. *Magnetic Resonance in Medicine*. 2012; 67: 1803-14.
61. Jensen JH, Chandra R and Yu H. Quantitative model for the interecho time dependence of the CPMG relaxation rate in iron-rich gray matter. *Magnetic Resonance in Medicine*. 2001; 46: 159-65.
62. Ye FQ, Martin WRW and Allen PS. Estimation of brain iron in vivo by means of the interecho time dependence of image contrast. *Magnetic Resonance in Medicine*. 1996; 36: 153-8.
63. Jones JA, Hodgkinson P, Barker AL and Hore PJ. Optimal sampling strategies for the measurement of spin-spin relaxation times. *Journal of Magnetic Resonance Series B*. 1996; 113: 25-34.
64. Dula AN, Gochberg DF and Does MD. Optimal echo spacing for multi-echo imaging measurements of Bi-exponential T2 relaxation. *Journal of Magnetic Resonance*. 2009; 196: 149-56.
65. Hennig J, Nauerth A and Friedburg H. RARE imaging - a fast imaging method for clinical MR. *Magnetic Resonance in Medicine*. 1986; 3: 823-33.
66. Jones C, Xiang Q, Whittall K and MacKay A. Calculating T2 and B1 from decay curves collected with non-180 refocusing pulses. Proceedings of 11th Annual Meeting, International Society for Magnetic Resonance in Medicine, 2003, p. 1018.
67. Hennig J. Multiecho Imaging Sequences With Low Refocusing Flip Angles. *Journal of Magnetic Resonance*. 1988; 78: 397-407.

68. Wild JM, Martin WRW and Allen PS. Multiple gradient echo sequence optimized for rapid, single-scan mapping of R-2(*) at high B-0. *Magnetic Resonance in Medicine*. 2002; 48: 867-76.
69. Yang QX, Williams GD, Demeure RJ, Mosher TJ and Smith MB. Removal of local field gradient artifacts in T-2*-weighted images at high fields by gradient-echo slice excitation profile imaging. *Magnetic Resonance in Medicine*. 1998; 39: 402-9.
70. Cho ZH and Ro YM. Reduction of susceptibility artifact in gradient-echo imaging. *Magnetic Resonance in Medicine*. 1992; 23: 193-200.
71. Chen NK and Wyrwicz AM. Removal of intravoxel dephasing artifact in gradient-echo images using a field-map based RF refocusing technique. *Magnetic Resonance in Medicine*. 1999; 42: 807-12.
72. Fernandez-Seara MA and Wehrli FW. Postprocessing technique to correct for background gradients in image-based R2* measurements. *Magnetic Resonance in Medicine*. 2000; 44: 358-66.
73. Bartzokis G, Beckson M, Hance DB, Marx P, Foster JA and Marder SR. MR evaluation of age-related increase of brain iron in young adult and older normal males. *Magnetic Resonance Imaging*. 1997; 15: 29-35.
74. Sedlacik J, Boelmans K, Lobel U, Holst B, Siemonsen S and Fiehler J. Reversible, irreversible and effective transverse relaxation rates in normal aging brain at 3T. *Neuroimage*. 2014; 84: 1032-41.
75. Ropele S, Kilsdonk ID, Wattjes MP, et al. Determinants of iron accumulation in deep grey matter of multiple sclerosis patients. *Multiple Sclerosis Journal*. 2014; 20: 1692-8.
76. Bartzokis G, Sultzer D, Mintz J, et al. In-vivo evaluation of brain iron in Alzheimers-disease and normal subjects using MRI. *Biological Psychiatry*. 1994; 35: 480-7.
77. Ordidge RJ, Gorell JM, Deniau JC, Knight RA and Helpert JA. Assessment of relative brain iron concentrations using T2-weighted and T2*-weighted MRI at 3 Tesla. *Magnetic Resonance in Medicine*. 1994; 32: 335-41.

78. Vymazal J, Righini A, Brooks RA, et al. T1 and T2 in the brain of healthy subjects, patients with Parkinson disease, and patients with multiple system atrophy: Relation to iron content. *Radiology*. 1999; 211: 489-95.
79. Frederic H. Martini JLN, Edwin F. Bartholomew. *Fundamentals of Anatomy & Physiology*. 9th edition ed.: Benjamin Cummings, 2011.
80. Youdim MBH, Benshachar D and Riederer P. Iron in brain-function and dysfunction with emphasis on Parkinsons-disease. *European Neurology*. 1991; 31: 34-40.
81. Benarroch EE. Brain iron homeostasis and neurodegenerative disease. *Neurology*. 2009; 72: 1436-40.
82. Hallgren B and Sourander P. The effect of age on the non-haemin iron in the human brain. *Journal of Neurochemistry*. 1958; 3: 41-51.
83. Brooks RA, Vymazal J, Goldfarb RB, Bulte JWM and Aisen P. Relaxometry and magnetometry of ferritin. *Magnetic Resonance in Medicine*. 1998; 40: 227-35.
84. Andrews SC, Arosio P, Bottke W, et al. Structure, function, and evolution of ferritins. *Journal of Inorganic Biochemistry*. 1992; 47: 161-74.
85. Makhlof SA, Parker FT and Berkowitz AE. Magnetic hysteresis anomalies in ferritin. *Physical Review B*. 1997; 55: 14717-20.
86. Cowley JM, Janney DE, Gerkin RC and Buseck PR. The structure of ferritin cores determined by electron nanodiffraction. *Journal of Structural Biology*. 2000; 131: 210-6.
87. S C Andrews AT, and P M Harrison. Siderosomal ferritin. The missing link between ferritin and haemosiderin? *Biochem J*. 1987: 439-46
88. Drayer B, Burger P, Darwin R, Riederer S, Herfkens R and Johnson G. MRI of brain iron. *American Journal of Roentgenology*. 1986; 147: 103-10.
89. Connor JR, Menzies SL, Stmartin SM and Mufson EJ. Cellular-distribution of transferrin, ferritin, and iron in normal and aged human brains. *Journal of Neuroscience Research*. 1990; 27: 595-611.

90. Koppenol WH. The Haber-Weiss cycle - 70 years later. *Redox Rep.* 2001; 6: 229-34.
91. Galaris D and Pantopoulos K. Oxidative stress and iron homeostasis: Mechanistic and health aspects. *Critical Reviews in Clinical Laboratory Sciences.* 2008; 45: 1-23.
92. Kell DB. Iron behaving badly: inappropriate iron chelation as a major contributor to the aetiology of vascular and other progressive inflammatory and degenerative diseases. *Bmc Medical Genomics.* 2009; 2.
93. Dexter DT, Carayon A, Javoyagid F, et al. Alterations in the levels of iron, ferritin and other trace-metals in parkinsons-disease and other neurodegenerative diseases affecting the basal ganglia. *Brain.* 1991; 114: 1953-75.
94. Bartzokis G, Aravagiri M, Oldendorf WH, Mintz J and Marder SR. Field dependent transverse relaxation rate increase may be a specific measure of tissue iron stores. *Magnetic Resonance in Medicine.* 1993; 29: 459-64.
95. Sullivan EV, Adalsteinsson E, Rohlfing T and Pfefferbaum A. Relevance of Iron Deposition in Deep Gray Matter Brain Structures to Cognitive and Motor Performance in Healthy Elderly Men and Women: Exploratory Findings. *Brain Imaging and Behavior.* 2009; 3: 167-75.
96. Parsey RV and Krishnan KRR. A new MRI ratio method for in-vivo estimation of signal hypointensity in aging and Alzheimer's disease. *Progress in Neuro-Psychopharmacology & Biological Psychiatry.* 1997; 21: 1257-67.
97. Schenck JF. Imaging of brain iron by magnetic resonance: T2 relaxation at different field strengths. *Journal of the Neurological Sciences.* 1995; 134: 10-8.
98. Compston A and Coles A. Multiple sclerosis. *Lancet.* 2008; 372: 1502-17.
99. Rosati G. The prevalence of multiple sclerosis in the world: an update. *Neurological Sciences.* 2001; 22: 117-39.
100. Kurtzke JF. Multiple sclerosis in time and space: Geographic clues to cause. *Journal of Neurovirology.* 2000; 6: S134-S40.
101. Beck CA, Metz LM, Svenson LW and Patten SB. Regional variation of multiple sclerosis prevalence in Canada. *Multiple sclerosis.* 2005; 11: 516-9.

102. Compston A and Coles A. Multiple sclerosis *Lancet*. 2002; 360: 648-.
103. Kurtzke JF. Rating Neurologic Impairment In Multiple-Sclerosis - An Expanded Disability Status Scale (EDSS). *Neurology*. 1983; 33: 1444-52.
104. Lassmann H, Brueck W and Lucchinetti CF. The immunopathology of multiple sclerosis: An overview. *Brain Pathology*. 2007; 17: 210-8.
105. Fransson ME, Liljenfeldt LSE, Fagius J, Totterman TH and Loskog ASI. The T-cell pool is anergized in patients with multiple sclerosis in remission. *Immunology*. 2009; 126: 92-101.
106. Benveniste EN. Role of macrophages/microglia in multiple sclerosis and experimental allergic encephalomyelitis. *Journal of Molecular Medicine-Imm*. 1997; 75: 165-73.
107. Kirov II, Patil V, Babb JS, Rusinek H, Herbert J and Gonen O. MR spectroscopy indicates diffuse multiple sclerosis activity during remission. *Journal of Neurology Neurosurgery and Psychiatry*. 2009; 80: 1330-6.
108. Vercellino M, Masera S, Lorenzatti M, et al. Demyelination, Inflammation, and Neurodegeneration in Multiple Sclerosis Deep Gray Matter. *Journal of Neuropathology and Experimental Neurology*. 2009; 68: 489-502.
109. Ormerod IEC, Bronstein A, Rudge P, et al. Magnetic-Resonance-Imaging In Clinically Isolated Lesions Of The Brain-Stem. *Journal of Neurology Neurosurgery and Psychiatry*. 1986; 49: 737-43.
110. Vanwalderveen MAA, Barkhof F, Hommes OR, et al. Correlating MRI and clinical-disease activity in Multiple-Sclerosis - relevance of hypointense lesions on short-TR short-TE (T1-weighted) spin-echo images. *Neurology*. 1995; 45: 1684-90.
111. Miki Y, Grossman RI, Udupa JK, et al. Relapsing-remitting multiple sclerosis: Longitudinal analysis of MR images - Lack of correlation between changes in T2 lesion volume and clinical findings. *Radiology*. 1999; 213: 395-9.
112. Henkelman RM, Stanisz GJ and Graham SJ. Magnetization transfer in MRI: a review. *NMR in Biomedicine*. 2001; 14: 57-64.

113. Schmierer K, Wheeler-Kingshott CAM, Tozer DJ, et al. Quantitative magnetic resonance of postmortem multiple sclerosis brain before and after fixation. *Magnetic Resonance in Medicine*. 2008; 59: 268-77.
114. Mackay A, Whittall K, Adler J, Li D, Paty D and Graeb D. In-Vivo Visualization Of Myelin Water In Brain By Magnetic-Resonance. *Magnetic Resonance in Medicine*. 1994; 31: 673-7.
115. Laule C, Vavasour IM, Moore GRW, et al. Water content and myelin water fraction in multiple sclerosis - A T2 relaxation study. *Journal of neurology*. 2004; 251: 284-93.
116. Hammond KE, Metcalf M, Carvajal L, et al. Quantitative In Vivo Magnetic Resonance Imaging of Multiple Sclerosis at 7 Tesla with Sensitivity to Iron. *Annals of Neurology*. 2008; 64: 707-13.
117. Haacke EM, Makki M, Ge Y, et al. Characterizing Iron Deposition in Multiple Sclerosis Lesions Using Susceptibility Weighted Imaging. *Journal of Magnetic Resonance Imaging*. 2009; 29: 537-44.
118. Eissa A, Lebel RM, Korzan JR, et al. Detecting Lesions in Multiple Sclerosis at 4.7 Tesla Using Phase Susceptibility-Weighting and T2-Weighting. *Journal of Magnetic Resonance Imaging*. 2009; 30: 737-42.
119. Craelius W, Migdal M, Luessenhop C, Sugar A and Mihalakis I. Iron deposits surrounding multiple sclerosis plaques. *Archives of pathology & laboratory medicine*. 1982; 106: 397.
120. Anderson VM, Fox NC and Miller DH. Magnetic resonance imaging measures of brain atrophy in multiple sclerosis. *Journal of Magnetic Resonance Imaging*. 2006; 23: 605-18.
121. Bermel RA and Bakshi R. The measurement and clinical relevance of brain atrophy in multiple sclerosis. *Lancet neurology*. 2006; 5: 158-70.
122. Coffey CE, Wilkinson WE, Parashos IA, et al. Quantitative cerebral anatomy of the aging human brain - a cross-sectional study using magnetic resonance imaging. *Neurology*. 1992; 42: 527-36.

123. Kalkers NF, Ameziane N, Bot JCJ, Minneboo A, Polman CH and Barkhof F. Longitudinal brain volume measurement in multiple sclerosis - Rate of brain atrophy is independent of the disease subtype. *Archives of Neurology*. 2002; 59: 1572-6.
124. Dalton CM, Miszkiele KA, O'Connor PW, Plant GT, Rice GPA and Miller DH. Ventricular enlargement in MS - One-year change at various stages of disease. *Neurology*. 2006; 66: 693-8.
125. De Stefano N, Cocco E, Lai M, et al. Imaging brain damage in first-degree relatives of sporadic and familial multiple sclerosis. *Annals of Neurology*. 2006; 59: 634-9.
126. Fisniku LK, Chard DT, Jackson JS, et al. Gray matter atrophy is related to long-term disability in multiple sclerosis. *Annals of Neurology*. 2008; 64: 247-54.
127. Fisher E, Lee JC, Nakamura K and Rudick RA. Gray matter atrophy in multiple sclerosis: A longitudinal study. *Annals of Neurology*. 2008; 64: 255-65.
128. Roosendaal SD, Bendfeldt K, Vrenken H, et al. Grey matter volume in a large cohort of MS patients: relation to MRI parameters and disability. *Multiple Sclerosis Journal*. 2011; 17: 1098-106.
129. Henry RG, Shieh M, Okuda DT, Evangelista A, Gorno-Tempini ML and Pelletier D. Regional grey matter atrophy in clinically isolated syndromes at presentation. *Journal of Neurology Neurosurgery and Psychiatry*. 2008; 79: 1236-44.
130. Zivadinov R, Havrdova E, Bergsland N, et al. Thalamic Atrophy Is Associated with Development of Clinically Definite Multiple Sclerosis. *Radiology*. 2013; 268: 831-41.
131. Audoin B, Zaaraoui W, Reuter F, et al. Atrophy mainly affects the limbic system and the deep grey matter at the first stage of multiple sclerosis. *Journal of Neurology Neurosurgery and Psychiatry*. 2010; 81: 690-5.
132. Bergsland N, Horakova D, Dwyer MG, et al. Subcortical and Cortical Gray Matter Atrophy in a Large Sample of Patients with Clinically Isolated Syndrome and Early Relapsing-Remitting Multiple Sclerosis. *American Journal of Neuroradiology*. 2012; 33: 1573-8.
133. Filippi M and Agosta F. Imaging Biomarkers in Multiple Sclerosis. *Journal of Magnetic Resonance Imaging*. 2010; 31: 770-88.

134. Khalil M, Langkammer C, Pichler A, et al. Dynamics of brain iron levels in multiple sclerosis A longitudinal 3T MRI study. *Neurology*. 2015; 2396-402.
135. Pelletier D, Garrison K and Henry R. Measurement of whole-brain atrophy in multiple sclerosis. *Journal of Neuroimaging*. 2004; 14: 11S-9S.
136. Bermel RA, Puli SR, Fabiano AJ, et al. Gray matter MRI T2 hypointensity predicts longitudinal brain atrophy in multiple sclerosis: Effect of intramuscular interferon beta-1a treatment. *Neurology*. 2003; 60: A422-A.
137. Horsfield MA, Rovaris M, Rocca MA, et al. Whole-brain atrophy in multiple sclerosis measured by two segmentation processes from various MRI sequences. *Journal of the Neurological Sciences*. 2003; 216: 169-77.
138. Smith SM, Zhang YY, Jenkinson M, et al. Accurate, robust, and automated longitudinal and cross-sectional brain change analysis. *Neuroimage*. 2002; 17: 479-89.
139. Smith SM. Fast robust automated brain extraction. *Hum Brain Mapp*. 2002; 17: 143-55.
140. Smith SM, De Stefano N, Jenkinson M and Matthews PM. Normalized accurate measurement of longitudinal brain change. *Journal of Computer Assisted Tomography*. 2001; 25: 466-75.
141. Patenaude B, Smith SM, Kennedy DN and Jenkinson M. A Bayesian model of shape and appearance for subcortical brain segmentation. *Neuroimage*. 2011; 56: 907-22.

Chapter 2. Spin echo transverse relaxation and atrophy in multiple sclerosis deep grey matter: A 2-year longitudinal study¹

2.1 Abstract

Background: Deep grey matter (DGM) is affected in relapsing-remitting multiple sclerosis (RRMS) and may be studied using short-term longitudinal MRI.

Objective: To investigate 2-year changes in spin echo transverse relaxation rate (R_2) and atrophy in DGM and its relationship with disease severity in RRMS patients.

Methods: Twenty six RRMS patients and 26 matched controls were imaged at 4.7 T. Multi-echo spin echo R_2 maps and atrophy measurements were obtained in DGM at baseline and 2-year follow-up. Differences between MRI measures and correlations to disease severity were examined.

Results: After 2 years, mean R_2 values in globus pallidus and pulvinar increased by ~4% ($p < 0.001$) in patients and <1.7% in controls. Two-year changes in R_2 showed significant correlation to disease severity in globus pallidus, pulvinar, substantia nigra and thalamus. Multiple regression of the 2-year R_2 difference using these four DGM structures as variables, yielded high correlation with disease severity ($r = 0.83$, $p < 0.001$). Two-year changes in volume and R_2 showed significant correlation only for globus pallidus in MS ($p < 0.05$).

Conclusions: Two-year difference R_2 measurements in DGM correlate to disease severity in MS. R_2 mapping and atrophy measurements over 2 years can be used to identify changes in DGM in MS.

¹ This section has been published. Uddin MN, Lebel RM, Seres P, Blevins G, and Wilman AH, Spin echo transverse relaxation and atrophy in multiple sclerosis deep grey matter: A 2-year longitudinal study; Multiple Sclerosis Journal (2015); DOI: 10.1177/1352458515614091

2.2 Introduction

Multiple sclerosis (MS) is an idiopathic neurodegenerative disease sustained by inflammation, with demyelinating processes and neuronal loss (1). Abnormal iron accumulation is also found in the brain in MS. Histologically, excess iron accumulation is observed in the basal ganglia and thalamus, in macrophages and microglial cells, as well as in and around MS lesions (1,2). On the other hand, iron levels tend to decrease with increasing disease duration in normal appearing white matter (WM) of patients with MS due to demyelination and loss of oligodendrocytes (3).

Iron serves as an important cofactor for several biochemical processes in the human brain including neurotransmitter metabolism, myelin synthesis, remyelination and mitochondrial energy generation (1). The iron level in deep grey matter (DGM) usually increases with normal aging, except in thalamus, and DGM nuclei have most iron content stored in ferritin (4). Although excess iron accumulation has been observed in MS, the pathologic process is not yet fully understood. However, presence of excessive levels of iron can exert oxidative stress due to increased production of free radicals, block remyelination processes, as well as enhance inflammation by activating microglia and macrophages, leading in cell death (1). Therefore, monitoring the iron accumulation in DGM and relating this to disease severity may provide more information about MS.

Many MRI methods are iron-sensitive and can be used to indirectly evaluate brain iron and related damage in patients with MS. However, MRI measures are not specific to iron and can be sensitive to many biological processes including inflammation, calcification, demyelination, cell loss, as well as iron accumulation. Nevertheless, in iron-rich DGM, image contrast for transverse relaxation and susceptibility images is typically dominated by stored ferric iron (5). Previous cross-sectional studies in DGM in MS suggest increased iron accumulation using transverse relaxation (T_2) weighted images or quantitative MRI measures (2,6-8). The MRI measures in DGM correlate with measures of cognitive dysfunction, disease severity and brain atrophy (6-9).

T_2 -weighted MRI, which uses spin-echo refocusing, is a standard method used in most clinical MS exams and has demonstrated reduced DGM signal in MS suggestive of iron and related to disease progression (6,10). However, a more sensitive and accurate assessment of iron levels can be obtained using quantitative MRI methods and by using a higher magnetic field. To

date numerous quantitative MRI methods have been used in cross-sectional study to evaluate iron accumulation in patients with MS, including the spin-echo, and gradient-echo transverse relaxation rates R_2 and R_2^* , and quantitative susceptibility mapping (QSM) with the latter two methods being used in many recent cross-sectional studies in MS (7,8,11). Since baseline iron levels can vary between healthy subjects; longitudinal study may be more effective to monitor excessive iron accumulation in MS. For longitudinal study, R_2^* mapping and brain atrophy measurements have been used (12-14). In contrast, spin-echo R_2 measurements have not yet been applied to longitudinal MS studies of DGM. Disadvantages of R_2 mapping are the need to monitor for incomplete refocusing, increased scan time which can limit slice coverage and reduced iron sensitivity in comparison to R_2^* mapping (7). Advantages of R_2 mapping include use of a clinically-relevant contrast mechanism, since T_2 ($=1/R_2$)-weighted images are standard in most clinical MRI exams, and the use of spin-echo refocusing which provides robust images that refocus static background fields such as those arising from air-tissue interfaces.

In MS brain, the atrophy of GM and WM has been studied extensively. Several previous works demonstrated that annual brain volume decreases are typically very small (0.6-1%) in MS patients. Compared to WM atrophy, GM atrophy shows stronger correlation with MS severity and cognitive impairment (15,16). However, the pattern of atrophy measurements might be different in different disease subtypes (17). For example, in relapsing-remitting MS (RRMS) subcortical damage is prominent (18). Previous works have shown an association between DGM atrophy and disability progression of MS (14-16,18).

Management of MS lacks biological markers that correlate with the disease state and stage that are measurable in short time periods. In development of new treatments, measurable outcomes require large clinical trials with large patient numbers and long periods of observation (14). One of the results is that exploring potential new treatments is significantly impaired by these issues of time and resources. In management of MS, similarly, changes in treatment and state of the disease are followed by long periods of observation to appreciate the effect of treatment. Changes in the stage of the disease from relapsing to progressive forms are defined by the clinical course in a retrospective, rather than prospective fashion. Development of biological markers to address these issues is important. Here, we examine the 2-year time course of spin-echo R_2 mapping and brain atrophy in DGM nuclei of RRMS subjects and matched healthy controls, and relate the findings to disease severity.

2.3 Methods

2.3.1 Subjects

Twenty six patients with a diagnosis of RRMS and fitting the revised McDonald criteria (19) and 26 age- and gender-matched controls were studied prospectively, after obtaining ethical approval and informed consent according to institutional regulations. The participants underwent a baseline and 2-year MRI, between 06/2009-12/2014. For inclusion into the study, control subjects had to be free of neurological disease. Table 2.1 presents an overview on the demographic and clinical data including the Expanded Disability Status Scale (EDSS) score and MS Severity Score (MSSS).

Table 2.1: Baseline demographic and clinical data

Variable	Controls	Patients	<i>p</i> -value
Number of participants	26	26	NA
Gender, M/F	7/18	6/19	NA
Overall Age (years)	37.82 ±9.05	38.14±8.86	0.31
Age-Female (years)	36.84±8.14	38.76±7.77	0.20
Age-Male (years)	38.65±11.47	38.67±11.38	0.93
Time to MRI follow-up (years)	2.05±0.20	2.01±0.10	0.75
Disease duration (years) [‡]	NA	5.28±3.44	NA
Baseline EDSS score [†]	NA	2.42±0.97	NA
Follow-up EDSS score	NA	2.53±0.89	NA
Baseline MSSS	NA	4.08±1.79	NA
Follow-up MSSS	NA	3.97±1.77	NA

Note: data are mean ± standard deviation for subjects at baseline. *p*-values were obtained using paired sample t-test. EDSS: Expanded Disability Status Scale; MSSS: Multiple Sclerosis Severity Score; NA: not applicable.

[‡] Disease duration range: 0 – 10 years. [†] EDSS range: 1 - 4.

2.3.2 Magnetic resonance imaging

All subjects were imaged at 4.7 T. For R_2 mapping, a two dimensional multiple-echo spin-echo sequence was employed in the axial plane covering 2.4 cm centered on the DGM of interest and using the following parameters: repetition time 4000 ms, echo spacing 10 ms, number of echoes 20, first echo time 10 ms, flip angle 90° - 180° - 180° ..., voxel size $1.0 \times 1.25 \times 4 \text{ mm}^3$, receiver bandwidth 50 kHz; number of slices 6, total scan time 13.5 min. For assessing brain volume, a whole-brain T_1 -weighted 3D Magnetization Prepared Rapid Gradient Echo (MPRAGE) sequence was used (echo time 4.5 ms; repetition time 8.5 ms; number of slices 84; inversion time 300 ms; sequential phase encoding, voxel volume 1.5 mm^3 ; scan time 5 min). For the 2-year scan, the baseline scan prescription was repeated with alignment based on multidirectional localizers and careful head placement within the magnet.

2.3.3 R_2 mapping

R_2 maps were computed on a pixel-by-pixel basis using stimulated echo compensation (20), which accounts for imperfect radiofrequency (RF) refocusing. This method extracts R_2 from the spin response calculated from the extended phase graph algorithm (21) beginning with the knowledge of sequence timing and the RF pulse shapes. The assumption of negligible longitudinal relaxation recovery relative to T_2 decay during the echo train was also used.

2.3.4 Image analysis

For R_2 maps, manual region-of-interest (ROI) analysis was performed for each subject using ImageJ (22). Bilateral ROIs, traced using the R_2 maps and the first spin-echo image, were chosen in iron-rich DGM structures (globus pallidus, putamen, head of caudate nucleus, substantia nigra, red nucleus, pulvinar nucleus, thalamus excluding pulvinar) as well as frontal WM and posterior internal capsule. R_2 values, obtained from ROIs, were averaged over left and right sides of the brain for each subject. In cases of misalignment between the baseline and 2-year scan, R_2 maps were manually registered using ImageJ after skull-stripping using brain extraction tool (BET), a part of functional MRI of the brain (FMRIB) software library (<http://www.fmrib.ox.ac.uk/fsl>) (23).

Using the 3D T₁-weighted MPRAGE images, baseline values of whole brain volume, whole GM, cortical GM and whole WM volumes were obtained using structural image evaluation using normalization of atrophy cross-sectional (SIENAX) (24), while 2-year percent changes were obtained using structural image evaluation using normalization of atrophy (SIENA) (24). Using FMRIB's integrated registration and segmentation tool (FIRST) (25) we also obtained separate volumes of the DGM structures (caudate, putamen, globus pallidus, and thalamus) at each time point. All the volumes were then normalized relative to whole head volume for each subject.

2.3.5 Statistical analysis

Statistical analyses were performed using SPSS (IBM, Armonk, NY). A p-value of less than 0.05 was considered as statistically significant. Kolmogorov-Smirnov test was used to assess the normal distribution of data. A paired sample t-test and Wilcoxon test were performed to test pairwise differences over time and within groups for both patients and controls over 2 years. Intra-subject reliability was also performed for four persons who underwent two scans in the same day. Each exam was analyzed separately by the same observer with ROIs manually drawn for each brain region. Intra-rater reliability was analyzed using intra-class correlations. Percent change between inter-control and inter-patient mean and standard deviation was calculated for each structure in the brain for changes in R₂ and volume over 2 years. Spearman and Pearson correlations were used to calculate the correlation coefficients between clinical and demographic data (Spearman: MSSS, EDSS, disease duration; Pearson: age, regional and whole brain volumes). False discovery rate (FDR) correction was used to correct the p values for multiple comparisons between groups where corrected values for q<0.05 were considered as significant. The effect size was also reported. Single and multiple linear regression models were used to determine the correlation between 2-year changes in R₂ and MSSS. Age was used as covariate in the regression models. Note that MSSS was calculated from EDSS and disease duration using MSSStest software (26), thus MSSS represents an adjusted EDSS score for disease duration.

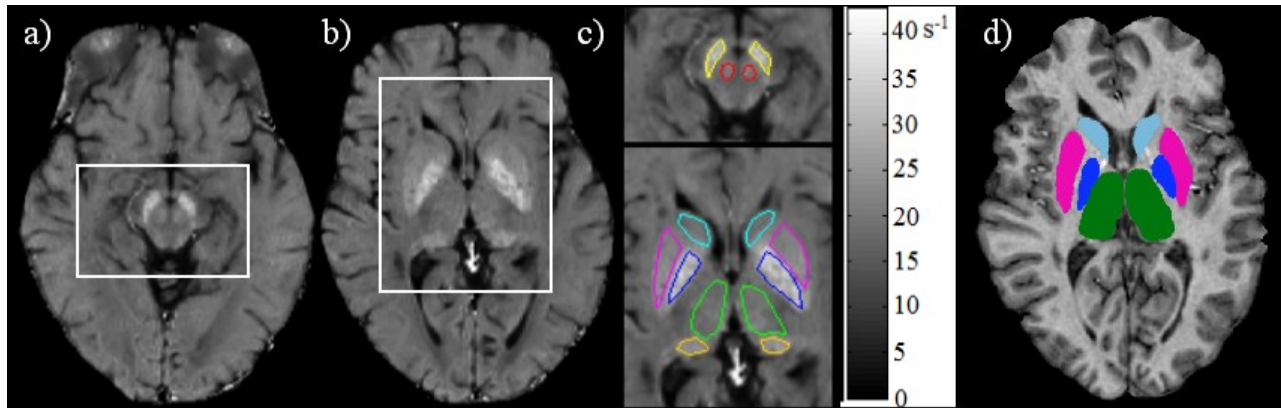


Figure 2.1: R_2 maps (a-c) and T_1 -weighted image (d) from a 47 year MS patient. DGM ROIs are illustrated in color on the enlarged view (c) with manual regions of interest and on (d) obtained using FSL-FIRST segmentation. Head of caudate nucleus (cyan), putamen (magenta), globus pallidus (blue), thalamus (green), pulvinar (orange), substantia nigra (yellow) and red nucleus (red). Note thalamus includes pulvinar in (d).

Table 2.2: Baseline Morphologic data

Regions	Controls (cm ³)	Patients (cm ³)	p-value
Whole Brain volume	1438.33±77.56	1414.04±71.59	0.146
Grey Matter volume	721.61±51.589	708.12±40.5	0.155
White Matter volume	714.72±33.02	705.92±40.44	0.319
Cortical Volume	563.59±37.29	547.84±28.55	0.067
Ventricular volume	36.25±16.88	42.02±16.27	0.199
Caudate nucleus	7.85±1.16	6.57±1.20	0.007
Putamen	10.86±1.53	9.16±2.19	0.007
Globus pallidus	3.33±0.49	2.89±0.72	0.013
Thalamus [†]	15.68±2.48	13.91±2.28	0.029

Note: data are mean \pm standard deviation for subjects at baseline. Volumes were normalized relative to whole head volume; p-values were obtained using paired sample t-test.

Italic bold-faced values are significant with $p < 0.05$.

[†] Thalamus includes pulvinar for volume measurements.

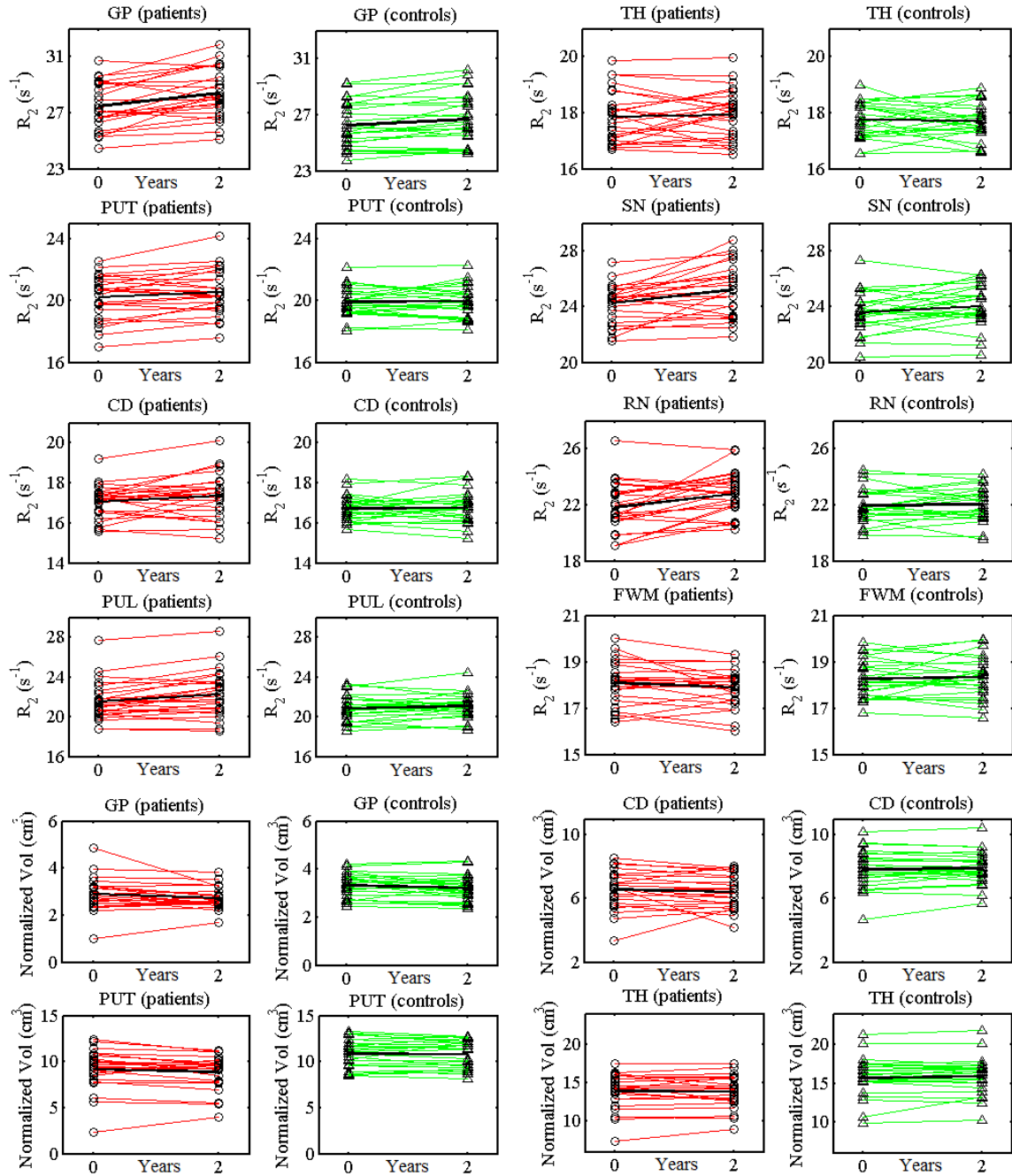


Figure 2.2: Baseline and two year measurements of spin echo R_2 and normalized volumes for some DGM regions and frontal WM from subjects with MS (red) and matched controls (green). GP, Globus pallidus; CD, head of caudate nucleus; PUT, putamen; TH, thalamus; RN, red nucleus; SN, substantia nigra; and FWM, frontal white matter. For volume measurements, thalamus included pulvinar, while for R2 mapping the pulvinar thalamus was considered separately.

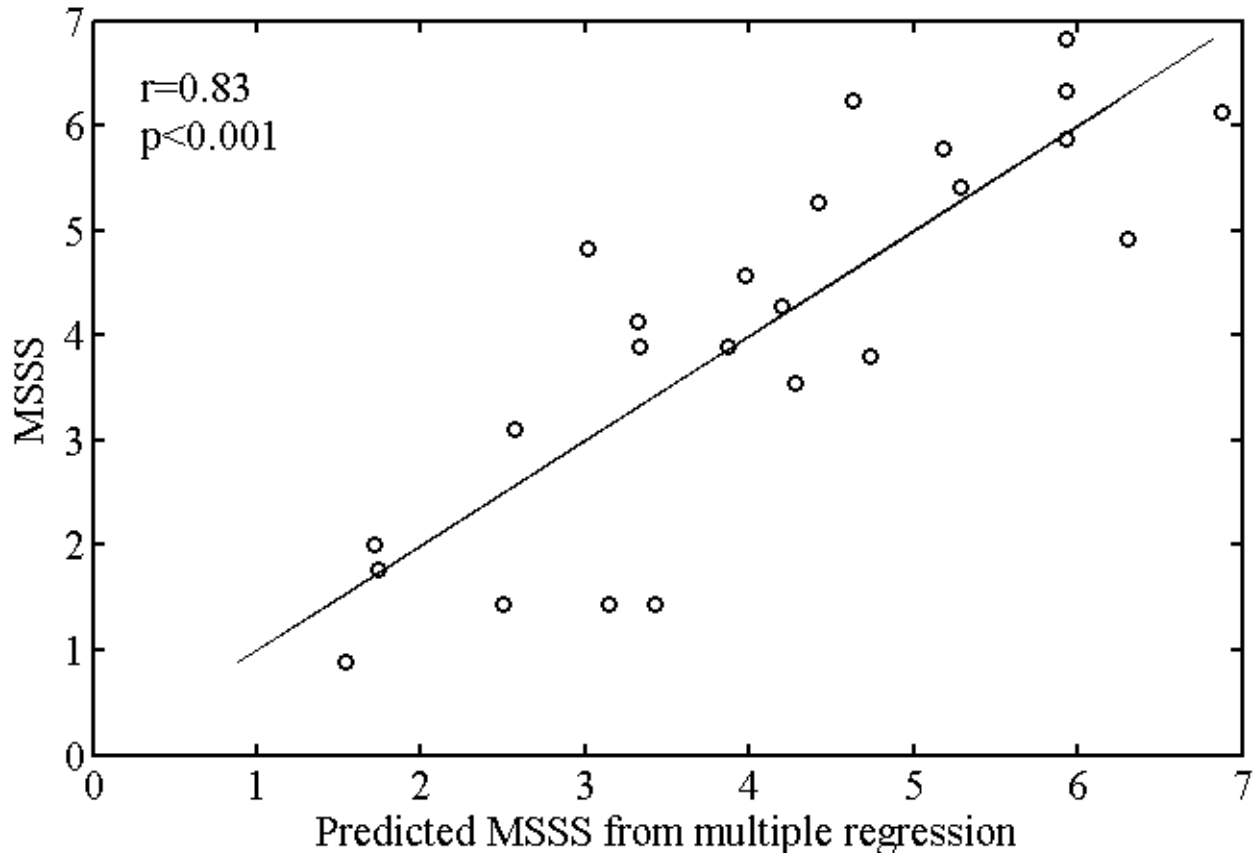


Figure 2.3: Measured MSSS versus predicted MSSS obtained from multiple regression of the 2-year R_2 difference measurements. Globus pallidus, pulvinar, thalamus and substantia nigra are included in the regression model. The regression line equation is $MSSS = 0.49 \cdot \Delta R_{2GP} + 0.57 \cdot \Delta R_{2PUL} + 0.56 \cdot \Delta R_{2SN} - 1.84 \cdot \Delta R_{2TH} + 3.31$, where ΔR_{2GP} , ΔR_{2PUL} , ΔR_{2SN} and ΔR_{2TH} are the differences in R_2 over 2 years for globus pallidus, pulvinar, substantia nigra and thalamus excluding pulvinar.

2.4 Results

Subject demographics, clinical and volumetric data are summarized in Tables 2.1 and 2.2 respectively. Figure 2.1 presents example R_2 maps from an MS patient showing hyperintense iron-rich DGM. Two-year follow-up R_2 values in DGM structures and frontal WM, and normalized volumes of DGM structures are shown in Fig. 2.2 for both controls and patients. For test-retest reliability, we found high intra-class correlations for each structure (mean 0.984 for R_2 and 0.988 for volume measurements). We obtained significant changes over 2 years in pulvinar

(R_2 increased by 4.4%), substantia nigra (R_2 increased by 4.8%) and globus pallidus (R_2 increased by 3.8%) with relatively large effect size (Table 2.3). R_2 values for posterior internal capsule and frontal WM did not show significant group difference, however R_2 values were reduced over 2-years (posterior internal capsule by 0.6% while frontal WM by 1%), which might be due to demyelination, increased water content or axonal loss. While for controls, none of the structures showed more than 1.7% change in R_2 over 2 years. Mean volume of globus pallidus, putamen and caudate as well as cortical GM volume decreased over 2 years for patients and controls, but was not statistically significant. However, atrophy rates of these structures were significantly different between patients and controls, and showed large effect size. Most of the DGM structures showed group differences in R_2 and volumes between MS patients and controls (Table 2.3), consistent with previous work using R_2^* mapping (12,27).

Multiple regression using four DGM structures as variables, yielded 2-year difference R_2 values with high correlation to MSSS ($r=0.83$, $p<0.001$). Figure 2.3 shows the plot of MSSS at baseline versus predicted MSSS, where predicted MSSS was obtained using the Equation: $MSSS = 0.49*\Delta R_{2GP} + 0.57*\Delta R_{2PUL} + 0.56*\Delta R_{2SN} - 1.84*\Delta R_{2TH} + 3.1$, where ΔR_{2GP} , ΔR_{2PUL} , ΔR_{2SN} and ΔR_{2TH} are the difference in R_2 over 2 years for globus pallidus, pulvinar, substantia nigra and thalamus excluding pulvinar, respectively. Baseline R_2 measurement correlated to MSSS only in the substantia nigra and can be used as a predictor ($r=0.47$, $p<0.05$) as follows: $MSSS = 0.26*R_{2SN} + 23.32$, where R_{2SN} is the baseline R_2 of substantia nigra. Independent regression analysis showed significant correlations with MSSS for some DGM structures in 2-year difference R_2 (Fig. 2.4), but no significant correlations were found for 2-year volume changes. Note that thalamus showed an inverse relationship compared to all the other R_2 measures. In addition, 2-year difference R_2 values for globus pallidus, substantia nigra and pulvinar correlated significantly with EDSS score. Correlations between 2-year changes in R_2 and volumes with MSSS, EDSS and disease duration are summarized in Table 2.4. Compared to a previous studies with R_2^* (12,13), we found a similar trend of 2-year changes over the follow-up time for most DGM structures. Volumes of cortical GM correlated negatively to baseline R_2 for globus pallidus (-0.42), putamen (-0.42), pulvinar (-0.33) and substantia nigra (-0.43) with $p<0.05$. In addition, volumes of whole GM showed negative correlations with baseline R_2 for globus pallidus (-0.57) and putamen (-0.56), while ventricular volume correlated positively with baseline R_2 in pulvinar (0.53) and substantia nigra (0.42) in MS patients with $p<0.05$. Table 2.5 reports the correlation

between 2-year changes in R_2 and subcortical volume of each DGM nuclei. Volume reduction in globus pallidus significantly correlated to increase in R_2 over 2 years for subjects with MS (Fig. 2.5).

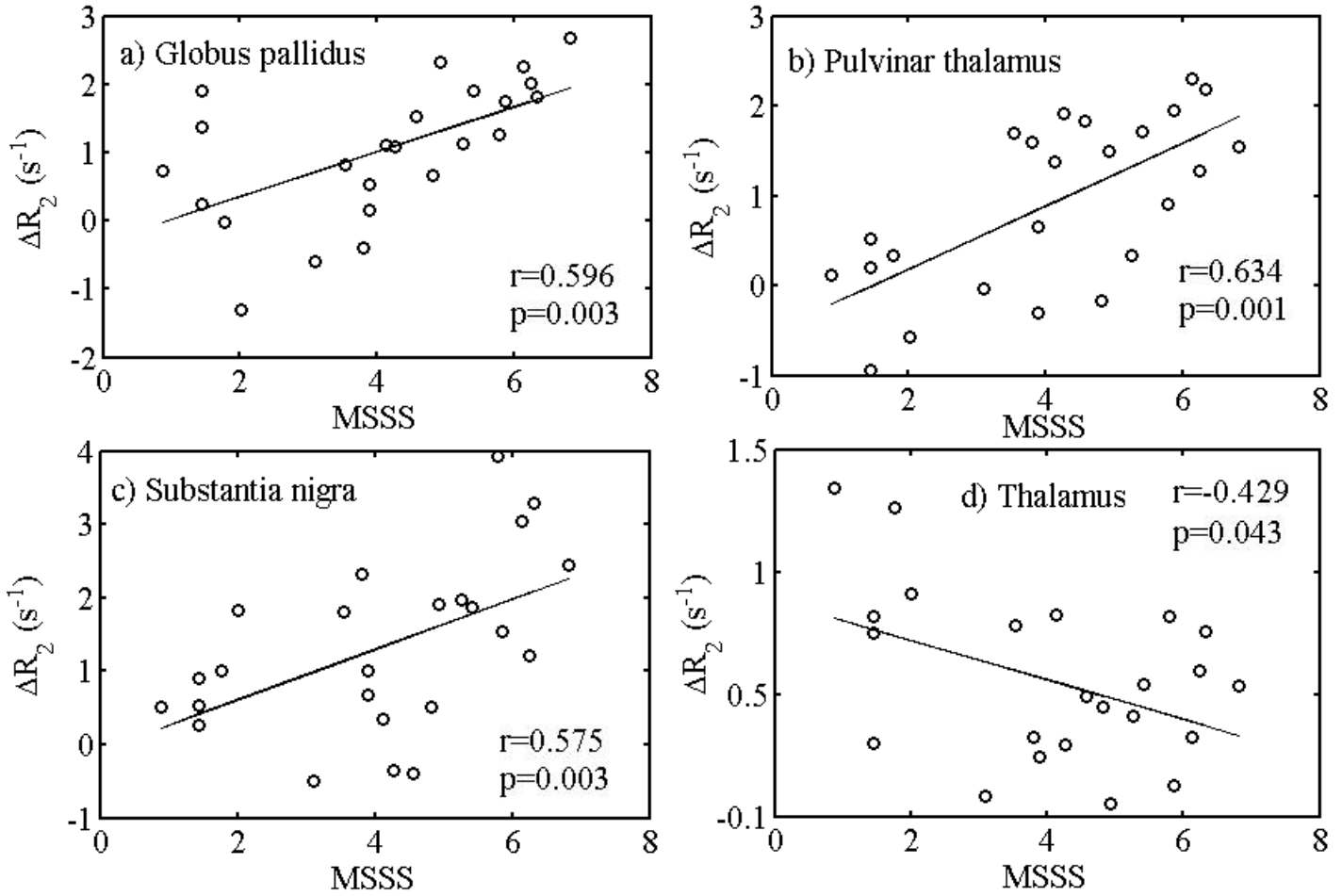


Figure 2.4: Significant correlations between two year difference R_2 measurements (ΔR_2) and MS severity score (MSSS) obtained by regression analysis for single structures: a) Globus pallidus, b) Pulvinar thalamus, c) Substantia nigra, and d) Thalamus.

Table 2.3: Two year changes in R₂ and volume

		R₂ MEASUREMENTS				VOLUME MEASUREMENTS		
Region and Group		Baseline R₂ mean (SD) in ms	R₂ % change in 2 years	Effect size over time	Effect size in group	Volume % change in 2 years	Effect size over time	Effect size in group
Globus pallidus	P	27.41 (2.11)	3.79	<u>0.60</u>	<u>0.96</u>	-3.80	-0.19	<u>-0.54</u>
	C	26.24 (1.62)	1.73	0.26		-2.01	-0.11	
Putamen	P	20.14 (1.42)	1.77	0.24	0.41	-2.77	0.16	<u>-0.98</u>
	C	19.94 (0.92)	0.15	0.03		-1.53	-0.10	
Caudate	P	17.06 (0.84)	2.14	0.37	0.71	-1.51	-0.11	<u>-1.11</u>
	C	16.72 (0.62)	0.21	0.05		0.25	0.02	
Thalamus	P	17.91 (0.91)	0.15	0.06	0.32	-0.46 [†]	0.03	<u>-0.67</u>
	C	17.76 (0.65)	0.21	-0.06		0.89	0.05	
Pulvinar	P	21.58 (1.98)	4.42	<u>0.41</u>	0.72	--	--	--
	C	20.85 (1.30)	1.08	0.18		--	--	
Substantia Nigra	P	24.39 (1.34)	4.75	0.63	<u>0.81</u>	--	--	--
	C	23.62 (1.47)	1.72	0.27		--	--	
Red nucleus	P	21.92 (1.95)	3.35	0.44	0.47	--	--	--
	C	21.96 (1.21)	0.48	0.09		--	--	
Frontal WM	P	18.12 (0.95)	-1.06	-0.21	-0.49	--	--	--
	C	18.27 (0.83)	0.42	0.09		--	--	
Posterior IC	P	13.79 (0.59)	-0.58	-0.14	-0.51	--	--	--
	C	13.89 (0.62)	0.23	0.24		--	--	
Cortical GM	P	--	--	--	--	-1.53	-0.11	-0.14
	C	--	--	--		-0.02	-0.01	

Note: p values are obtained using paired sample t-test and Wilcoxon test. Italic bold faced values are significant with $p < 0.05$ and underlined values at $p < 0.001$ after FDR correction with $q < 0.05$. Effect size is defined as the difference of two group means divided by the average of standard deviations.

† Thalamus included pulvinar for volume. P, Patients; C, Controls; SD, Standard deviation.

Table 2.4: Correlation coefficients of relaxation rates (R_2) and normalized volumes in subcortical territories with MSSS, EDSS and Disease Duration (DD) over two years from patients

Region		BASELINE		2 YEARS DIFFERENCE	
		R_2	Volume	ΔR_2	Δ Volume
Globus Pallidus	MSSS	0.389 (0.071)	0.336 (0.127)	<i>0.596 (0.003)</i>	-0.179 (0.412)
	EDSS	0.356 (0.085)	-0.139 (0.502)	<i>0.499 (0.013)</i>	-0.286 (0.176)
	DD	-0.065 (0.765)	0.253 (0.231)	-0.178 (0.406)	-0.197 (0.231)
Putamen	MSSS	0.177 (0.369)	0.357 (0.066)	0.020 (0.728)	-0.276 (0.251)
	EDSS	0.221 (0.229)	-0.171 (0.416)	0.039 (0.857)	-0.097 (0.653)
	DD	0.036 (0.768)	0.288 (0.173)	0.167 (0.436)	0.273 (0.181)
Caudate Nucleus	MSSS	0.165 (0.367)	-0.019 (0.711)	-0.140 (0.515)	-0.243 (0.291)
	EDSS	0.276 (0.125)	0.064 (0.780)	-0.079 (0.974)	-0.145 (0.833)
	DD	0.153 (0.443)	0.054 (0.802)	-0.175 (0.414)	0.189 (0.377)
Thalamus	MSSS	0.119 (0.551)	0.356 (0.127)	<i>-0.429 (0.043)</i>	-0.396 (0.053)
	EDSS	0.115 (0.654)	-0.014 (0.923)	-0.045 (0.236)	-0.233 (0.135)
	DD	-0.37 (0.855)	0.317 (0.132)	-0.173 (0.420)	-0.389 (0.171)
Pulvinar Thalamus	MSSS	0.411 (0.143)	--	<i>0.634 (0.001)</i>	--
	EDSS	0.288 (0.111)	--	<i>0.468 (0.021)</i>	--
	DD	-0.182 (0.318)	--	-0.222 (0.298)	--
Substantia Nigra	MSSS	<i>0.466 (0.022)</i>	--	<i>0.575 (0.003)</i>	--
	EDSS	0.304 (0.141)	--	<i>0.409 (0.047)</i>	--
	DD	-0.182 (0.412)	--	-0.172 (0.422)	--
Red Nucleus	MSSS	0.434 (0.053)	--	0.410 (0.056)	--
	EDSS	0.182 (0.121)	--	0.082 (0.702)	--
	DD	-0.232 (0.319)	--	-0.279 (0.186)	--

Note: Data are correlations and p values are in parentheses. Thalamus included pulvinar for volume measurements. ΔR_2 : change in R_2 over 2 years; Δ Volume: change in volume over 2 years. Italic bold-faced values were significant with $p < 0.05$.

Table 2.5: Correlation coefficients of change in R_2 (ΔR_2) with change in volume (ΔV) in subcortical GM over two years

	Globus Pallidus	Putamen	Caudate Nucleus	Thalamus[†]
Patients	-0.479 (0.037)	-0.291 (0.189)	-0.228 (0.308)	-0.193 (0.391)
Controls	-0.114 (0.646)	0.172 (0.421)	-0.185 (0.388)	0.119 (0.570)

Note: Data are correlation coefficients and p values are in parentheses.

Italic bold-faced values were significant with $p < 0.05$.

[†] Thalamus including pulvinar.

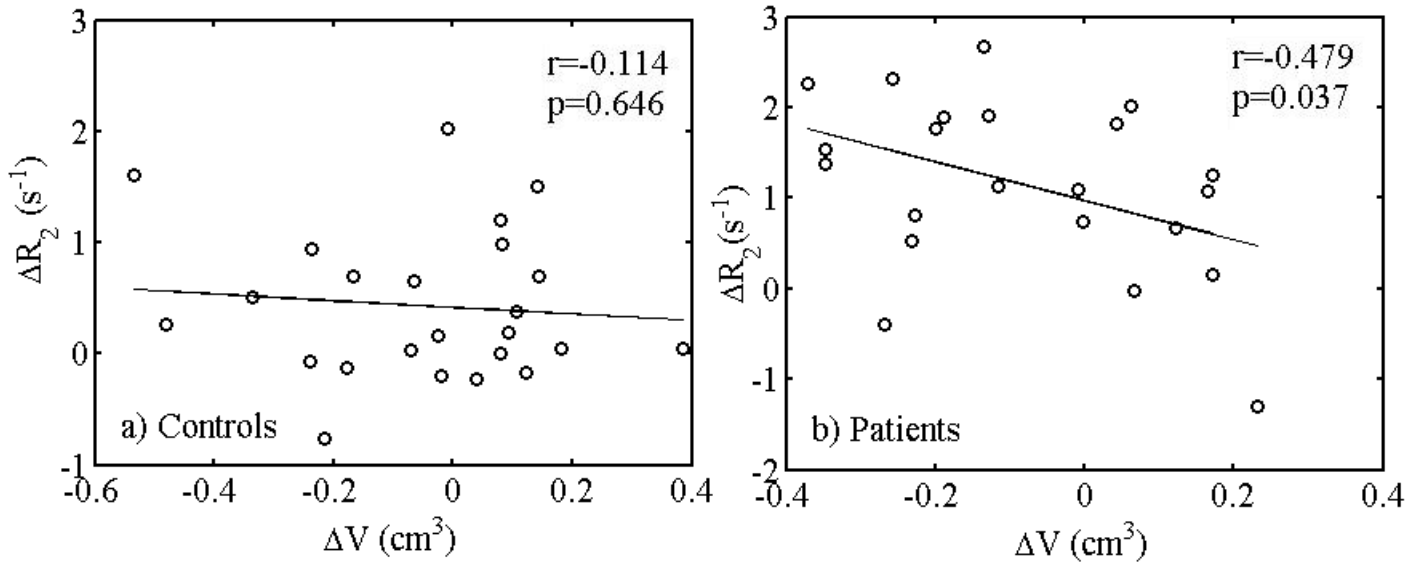


Figure 2.5: Relationship between two year changes in relaxation rate (ΔR_2) and volume (ΔV) in globus pallidus for a) controls and b) patients with MS.

2.5 Discussion

We have demonstrated 2-year R_2 changes and compared these measurements to the regional DGM atrophy in MS patients and age matched control subjects. We found that MSSS highly correlated with R_2 changes over a 2-year period, but the correlation was not statistically significant for volume changes in this short period of time. However, the atrophy of globus pallidus showed significant correlation with R_2 changes over 2 years in patient with MS.

This study was performed at 4.7 T which benefits from higher iron sensitivity compared to standard clinical systems. Compared to a recent R_2^* study using 3.0 T (13), we found larger percent change in R_2 in DGM in MS, which might be due to the use of higher field strength (4.7 T), higher EDSS score (mean 2.4 versus 2.0). In iron-rich DGM at high field, the effects of iron on R_2 play a dominant role, as indicated by the strong correlation between iron and R_2 in post-mortem studies (28,29). There are several possible reasons for iron accumulation in DGM in MS including decreased iron clearance due to neuronal loss and dysregulation of iron transport proteins because of inflammation (30). Khalil *et al.* (8) suggested that the iron deposition in DGM might be an epiphenomenon of the MS disease process.

Our longitudinal R_2 measurements in globus pallidus, pulvinar and substantia nigra showed significant correlations with MSSS compared to baseline measurements because the 2-year change eliminates baseline iron accumulation, which is known to be variable even in healthy subjects (4). Compared to the single regression model, the multiple linear regression model using 2-year difference R_2 values of globus pallidus, pulvinar, substantia nigra and thalamus as predictor variables revealed stronger association with disease severity, suggesting multiple DGM structures play role in the abnormal iron accumulation dynamics in MS.

DGM nuclei play a vital role to relay information on motor control, visual and other sensory functions, and cognitive processes through the extensive connections with cortical and subcortical structures. These DGM nuclei can be vulnerable from inflammation arising in other areas or within structures which can lead to pathologic changes. Our baseline R_2 measurements on some DGM structures correlated negatively with cortical GM, whole GM and whole WM volumes for RRMS patients. The results are consistent with previous cross-sectional studies using R_2^* mapping and QSM on MS patients (8,11,27). These correlations might be due to the consequence of neurodegenerative atrophy (8,27). In contrast, we did not find any significant correlations between baseline R_2 and cortical GM volume for controls, nor for two year difference measurements in patients or control subjects. One of the possible explanations is that the volume change in cortical GM, whole GM and whole WM might be a slow process and over 2 years this change was too small (less than 2%). We found regional DGM volumes for patients with MS were reduced by 1-4% over 2 years while for controls it was 0-2%. Our 2-year results indicate that only globus pallidus showed significant correlation between R_2 increase and its volume loss. This might be due to higher iron content in globus pallidus, whereby a few percent

change in iron content would be easier to detect, given its higher baseline value. Other DGM structures had similar within-structure trends but were not significant. Khalil *et al.* (13) reported changes in R_2^* and volume correlated negatively only for caudate nucleus in clinically isolated syndrome (CIS). A recent study showed significant volume changes (5-8%) only in putamen and globus pallidus over 5 years in MS patients (14). Similar to our results, they also found less than 1% reduction of whole brain volume per year in MS patients. Their 10 years follow-up study found increased cortical and DGM atrophy might take place during MS and is linked with disease progression at 5 years (14). In our study, MS ventricular volume was increased by ~5% after 2 years while for controls it was 1%. Increase in MS ventricular volume is associated with WM atrophy and DGM atrophy (31).

Compared to other DGM structures, thalamus and pulvinar have more extensive connection with other parts of the brain. A previous animal study has demonstrated that traumatic injury in the cortex can elevate iron levels in thalamus, suggesting that the demyelinating lesions or axonal damage in the fiber tract in MS can similarly affect the thalamus as well as DGM structures (32). In patients with MS, previous studies using T_2 hypointensity, susceptibility weighted imaging, and relaxometry mapping have also suggested iron accumulation in the thalamus (6,7,9). Our 2-year R_2 difference measurement in thalamus showed negative correlation with MSSS in linear regression. Results are consistent with recent work (13). This may be due to demyelination in the thalamus (excluding pulvinar) leading to an inverse relationship of R_2 to MSSS. Note the thalamus has the highest myelin content of the regions studied. Our thalamic volume changes over 2 years showed significant group difference. The normalized thalamic volume for MS patients was reduced by 12% compared to the controls. Previous work found that thalamic volume reduced by ~2% over 2 years in clinically defined MS and stable CIS (33). Another study reported a significant relationship between thalamic volume loss and disability progression over 5 years in RRMS patients whose disease remain stable (15). We found no significant thalamic volume loss in RRMS patients; however change in volume over 2 years correlate negatively with MSSS. Disease duration may also affect thalamic atrophy in RRMS (34).

Our study had a number of limitations. Spin-echo R_2 mapping is less sensitive to iron compared to R_2^* and QSM. R_2 mapping uses multiple RF refocusing pulses which increases tissue heating when long echo trains are used as used here (20 echoes). Recent work has

demonstrated that short echo trains may be used which would overcome the RF heating limitation (35). A further limitation is that R_2 mapping is not a part of standard clinical MRI protocols for MS. However, since proton-density and T_2 weighted fast spin-echo images are often acquired, it may be possible to obtain accurate R_2 maps from these existing sequences in clinical protocols (36). Age is an important factor for iron accumulation in DGM nuclei. Though age was included as a covariate in the linear regression models and 2-year age changes were relatively small, we cannot completely rule out aging as a potential confounding factor. Age was not significantly different between controls and MS patients in our study. In this study, volume measurements were performed using the FSL-FIRST segmentation while R_2 measurements were performed only from the central portion of the structure due to limited slice coverage. For mean R_2 measurement manual tracing of the boundaries on a 4 mm thick slice were used for maximal accuracy. We did not include other DGM structures such as accumbens, amygdala, and hippocampus because our R_2 maps did not cover these structures fully for all subjects and these structures exhibit reduced R_2 contrast.

In conclusion, over a short duration of 2 years, measurable differences in DGM structures using R_2 mapping showed strong association with disease severity in patients with RRMS particularly in globus pallidus and the pulvinar. Atrophy of globus pallidus over 2 years was related to R_2 increase. Therefore, the combination of spin-echo R_2 mapping and atrophy measurements can be used as biological markers to monitor disease course in RRMS.

2.6 Acknowledgements

This work was supported by grants from the Multiple Sclerosis Society of Canada, and Canadian Institutes of Health Research (CIHR).

2.7 References

1. Williams R, Buchheit CL, Berman NEJ, LeVine SM. Pathogenic implications of iron accumulation in multiple sclerosis. *Journal of Neurochemistry* 2012;120(1):7-25.
2. Drayer B, Burger P, Hurwitz B, Dawson D, Cain J. Reduced signal intensity on MR images of thalamus and putamen in multiple sclerosis: increased iron content? *American Journal of Roentgenology* 1987;149(2):357-363.

3. Hametner S, Wimmer I, Haider L, Pfeifenbring S, Brueck W, Lassmann H. Iron and Neurodegeneration in the Multiple Sclerosis Brain. *Annals of Neurology* 2013;74(6):848-861.
4. Hallgren B, Sourander P. The effect of age on the non-haemin iron in the human brain. *Journal of Neurochemistry* 1958;3(1):41-51.
5. Haacke EM, Chengb NYC, House MJ, Liu Q, Neelavalli J, Ogg RJ, Khan A, Ayaz M, Kirsch W, Obenaus A. Imaging iron stores in the brain using magnetic resonance imaging. *Magnetic Resonance Imaging* 2005;23(1):1-25.
6. Neema M, Arora A, Healy BC, Guss ZD, Brass SD, Duan Y, Buckle GJ, Glanz BI, Stazzone L, Khoury SJ, Weiner HL, Guttmann CRG, Bakshi R. Deep Gray Matter Involvement on Brain MRI Scans Is Associated with Clinical Progression in Multiple Sclerosis. *Journal of Neuroimaging* 2009;19(1):3-8.
7. Lebel RM, Eissa A, Seres P, Blevins G, Wilman AH. Quantitative high-field imaging of sub-cortical gray matter in multiple sclerosis. *Multiple Sclerosis Journal* 2012;18(4):433-441.
8. Khalil M, Langkammer C, Ropele S, Petrovic K, Wallner-Blazek M, Loitfelder M, Jehna M, Bachmaier G, Schmidt R, Enzinger C, Fuchs S, Fazekas F. Determinants of brain iron in multiple sclerosis A quantitative 3T MRI study. *Neurology* 2011;77(18):1691-1697.
9. Hagemeyer J, Weinstock-Guttman B, Heininen-Brown M, Poloni GU, Bergsland N, Schirda C, Magnano CR, Kennedy C, Carl E, Dwyer MG, Minagar A, Zivadinov R. Gray matter SWI-filtered phase and atrophy are linked to disability in MS. *Frontiers in bioscience (Elite edition)* 2013;5:525-532.
10. Zhang Y, Metz LM, Yong VW, Mitchell JR. 3 T deep gray matter T2 hypointensity correlates with disability over time in stable relapsing-remitting multiple sclerosis: A 3-year pilot study. *Journal of the Neurological Sciences* 2010;297(1-2):76-81.
11. Langkammer C, Liu T, Khalil M, Enzinger C, Jehna M, Fuchs S, Fazekas F, Wang Y, Ropele S. Quantitative Susceptibility Mapping in Multiple Sclerosis. *Radiology* 2013;267(2):551-559.

12. Walsh AJ, Blevins G, Lebel RM, Seres P, Emery DJ, Wilman AH. Longitudinal MR Imaging of Iron in Multiple Sclerosis: An Imaging Marker of Disease. *Radiology* 2014;270(1):186-196.
13. Khalil M, Langkammer C, Pichler A, Pinter D, Gatttringer T, Bachmaier G, Ropele S, Fuchs S, Enzinger C, Fazekas F. Dynamics of brain iron levels in multiple sclerosis A longitudinal 3T MRI study. *Neurology* 2015(84):2396-2402.
14. Jacobsen C, Hagemeyer J, Myhr K-M, Nyland H, Lode K, Bergsland N, Ramasamy DP, Dalaker TO, Larsen JP, Farbu E, Zivadinov R. Brain atrophy and disability progression in multiple sclerosis patients: a 10-year follow-up study. *Journal of neurology, neurosurgery, and psychiatry* 2014;85(10):1109-1115.
15. Zivadinov R, Bergsland N, Dolezal O, Hussein S, Seidl Z, Dwyer MG, Vaneckova M, Krasensky J, Potts JA, Kalincik T, Havrdova E, Horakova D. Evolution of Cortical and Thalamus Atrophy and Disability Progression in Early Relapsing-Remitting MS during 5 Years. *American Journal of Neuroradiology* 2013;34(10):1931-1939.
16. Roosendaal SD, Bendfeldt K, Vrenken H, Polman CH, Borgwardt S, Radue EW, Kappos L, Pelletier D, Hauser SL, Matthews PM, Barkhof F, Geurts JJG. Grey matter volume in a large cohort of MS patients: relation to MRI parameters and disability. *Multiple Sclerosis Journal* 2011;17(9):1098-1106.
17. Fisher E, Lee JC, Nakamura K, Rudick RA. Gray matter atrophy in multiple sclerosis: A longitudinal study. *Annals of Neurology* 2008;64(3):255-265.
18. Bergsland N, Horakova D, Dwyer MG, Dolezal O, Seidl ZK, Vaneckova M, Krasensky J, Havrdova E, Zivadinov R. Subcortical and Cortical Gray Matter Atrophy in a Large Sample of Patients with Clinically Isolated Syndrome and Early Relapsing-Remitting Multiple Sclerosis. *American Journal of Neuroradiology* 2012;33(8):1573-1578.
19. Polman CH, Reingold SC, Edan G, Filippi M, Hartung HP, Kappos L, Lublin FD, Metz LM, McFarland HF, O'Connor PW, Sandberg-Wollheim M, Thompson AJ, Weinshenker BG, Wolinsky JS. Diagnostic criteria for multiple sclerosis: 2005 Revisions to the "McDonald Criteria". *Annals of Neurology* 2005;58(6):840-846.

20. Lebel RM, Wilman AH. Transverse relaxometry with stimulated echo compensation. *Magnetic Resonance in Medicine* 2010;64(4):1005-1014.
21. Hennig J. Multiecho Imaging Sequences With Low Refocusing Flip Angles. *Journal of Magnetic Resonance* 1988;78(3):397-407.
22. Rasband W. ImageJ. US National Institutes of Health, Bethesda, Maryland, USA; 1997-2011.
23. Smith SM. Fast robust automated brain extraction. *Hum Brain Mapp* 2002;17(3):143-155.
24. Smith SM, Jenkinson M, Woolrich MW, Beckmann CF, Behrens TEJ, Johansen-Berg H, Bannister PR, De Luca M, Drobnjak I, Flitney DE, Niazy RK, Saunders J, Vickers J, Zhang YY, De Stefano N, Brady JM, Matthews PM. Advances in functional and structural MR image analysis and implementation as FSL. *Neuroimage* 2004;23:S208-S219.
25. Patenaude B, Smith SM, Kennedy DN, Jenkinson M. A Bayesian model of shape and appearance for subcortical brain segmentation. *Neuroimage* 2011;56(3):907-922.
26. Roxburgh R, Seaman SR, Masterman T, Hensiek AE, Sawcer SJ, Vukusic S, Achiti I, Confavreux C, Coustans M, le Page E, Edan G, McDonnell GV, Hawkins S, Trojano M, Liguori M, Cocco E, Marrosu MG, Tesser F, Leone MA, Weber A, Zipp F, Milterski B, Epplen JT, Oturai A, Sorensen PS, Celius EG, Lara NT, Montalban X, Villoslada P, Silva AM, Marta M, Leite I, Dubois B, Rubio J, Butzkueven H, Kilpatrick T, Mycko MP, Selmaj KW, Rio ME, Sa M, Salemi G, Savettieri G, Hillert J, Compston DAS. Multiple sclerosis severity score - Using disability and disease duration to rate disease severity. *Neurology* 2005;64(7):1144-1151.
27. Ropele S, Kilsdonk ID, Wattjes MP, Langkammer C, de Graaf WL, Frederiksen JL, Larsson HB, Yiannakas M, Wheeler-Kingshott CAM, Enzinger C, Khalil M, Rocca MA, Sprenger T, Amann M, Kappos L, Filippi M, Rovira A, Ciccarelli O, Barkhof F, Fazekas F. Determinants of iron accumulation in deep grey matter of multiple sclerosis patients. *Multiple Sclerosis Journal* 2014;20(13):1692-1698.

28. Walsh AJ, Lebel RM, Eissa A, Blevins G, Catz I, Lu J-Q, Resch L, Johnson ES, Emery DJ, Warren KG, Wilman AH. Multiple Sclerosis: Validation of MR Imaging for Quantification and Detection of Iron. *Radiology* 2013;267(2):531-542.
29. Langkammer C, Krebs N, Goessler W, Scheurer E, Ebner F, Yen K, Fazekas F, Ropele S. Quantitative MR imaging of brain iron: a postmortem validation study. *Radiology* 2010;257(2):455-462.
30. Stankiewicz J, Panter SS, Neema M, Arora A, Batt CE, Bakshi R. Iron in chronic brain disorders: imaging and neurotherapeutic implications. *Neurotherapeutics : the journal of the American Society for Experimental NeuroTherapeutics* 2007;4(3):371-386.
31. Magnano C, Schirda C, Weinstock-Guttman B, Wack DS, Lindzen E, Hojnacki D, Bergsland N, Kennedy C, Belov P, Dwyer MG, Poloni GU, Beggs CB, Zivadinov R. Cine cerebrospinal fluid imaging in multiple sclerosis. *Journal of Magnetic Resonance Imaging* 2012;36(4):825-834.
32. Onyszchuk G, LeVine SM, Brooks WM, Berman NE. Post-acute pathological changes in the thalamus and internal capsule in aged mice following controlled cortical impact injury: a magnetic resonance imaging, iron histochemical, and glial immunohistochemical study. *Neuroscience letters* 2009;452(2):204-208.
33. Zivadinov R, Havrdova E, Bergsland N, Tyblova M, Hagemeyer J, Seidl Z, Dwyer MG, Vaneckova M, Krasensky J, Carl E, Kalincik T, Horakova D. Thalamic Atrophy Is Associated with Development of Clinically Definite Multiple Sclerosis. *Radiology* 2013;268(3):831-841.
34. Wylezinska M, Cifelli A, Jezzard P, Palace J, Alecci M, Matthews PM. Thalamic neurodegeneration in relapsing-remitting multiple sclerosis. *Neurology* 2003;60(12):1949-1954.
35. Uddin MN, Lebel RM, Wilman AH. Transverse Relaxometry with Reduced Echo Train Lengths via Stimulated Echo Compensation. *Magnetic Resonance in Medicine* 2013;70(5):1340-1346.
36. McPhee KC, Wilman AH. T2 quantification from only proton density and T2-weighted MRI by modelling actual refocusing angles. *Neuroimage* 2015(118):642-650.

Chapter 3. Transverse Relaxometry with Reduced Echo Train Lengths via Stimulated Echo Compensation ²

3.1 Abstract

Transverse relaxation (T_2) mapping has many applications, including imaging of iron accumulation in grey matter. Using the typical multiple-echo spin echo sequence with long echo trains, stimulated echo compensation (SEC) can enable T_2 fitting under conditions of variable radio frequency (RF) homogeneity arising from slice profile and in-plane RF variation. Substantial reduction in the number of refocusing pulses could enable use at high magnetic fields where specific absorption rate is a major limitation, and enable multi-slice use with reduced incidental magnetization transfer at all field strengths. We examine the effect of reduced echo train lengths and multi-slice imaging on T_2 fitting using SEC applied to iron-rich subcortical gray matter in human brain at 4.7 T. Our findings indicate that reducing from 20 echoes to as few as 4 echoes can maintain consistent T_2 values when using SEC in grey and white matter, but not for cerebrospinal fluid. All territories produce marginal results when using standard exponential fitting. Savings from reduced echoes can be used to substantially increase slice coverage. In multi-slice mode, the resulting incidental magnetization transfer decreased brain signal but had minimal effect on measured T_2 values.

² A version of this section has been published. Uddin MN, Lebel RM, and Wilman AH, Transverse Relaxometry with Reduced Echo Train Lengths via Stimulated Echo Compensation. *Magnetic Resonance in Medicine* (2013) 70:1340–1346.

3.2 Introduction

Transverse relaxation (T_2) weighting provides a qualitative interpretation of disease and is used in almost all clinical MRI exams. Although T_2 -weighting is typically sufficient for standard clinical depiction, T_2 quantification provides an absolute measure that could provide additional information on disease progression and state. In the brain, shortened T_2 times in subcortical grey matter (GM) may be indicative of iron accumulation or mineralization and appear to correlate with normal aging and with disease severity in multiple sclerosis and Parkinson's disease (1-9). In white matter (WM), T_2 fitting has proven to be valuable in demyelinating diseases to assess myelin content using the short myelin water T_2 component identified through multi-component fitting (5,10-12); in GM the myelin component is much smaller (10). In addition to brain, quantification of single or multi-component T_2 can characterize tissue throughout the human body (13-21), with applications such as iron accumulation in liver or collagen-bound water in cartilage (12,22-24).

Although other approaches exist, such as DESPOT2 (25), the most common approach to T_2 measurement requires spin echo refocusing using a multi-echo spin echo sequence, whereby T_2 values are calculated from the resulting, presumed exponential, decay curve (26). However, accurate exponential fitting of T_2 times with this approach requires perfect spin echo behaviour, which is near-impossible to achieve when using slice selection due to imperfect slice profiles or when using high magnetic fields due to in-plane RF interference (27). The presence of non- 180° flip angles can lead to the generation of stimulated echoes, confounding the pure spin echo exponential decay (28). While numerous methods have been designed to minimize stimulated echo effects on the exponential decay, such as using twice-refocused adiabatic pulses (29), complex spoiler patterns (30) or extremely wide refocusing pulses (31), recent solutions have simply fit the complete spin response comprised of both spin echo and stimulated echo pathways. This idea of T_2 measurement by fitting the spin response, rather than introducing added complexities in the pulse sequence, was first proposed by Jones et al. (32), then elaborated on by Lebel and Wilman (33), with recent multi-component application by Prasloski et al. (34). This method, known as stimulated echo compensation (SEC), can account for the non-ideal nature of the refocusing pulses and enable use of more standard pulse sequences for T_2 quantification.

To date, SEC has been used with long echo trains of either 20 or 32 echoes (33,34). Performance of this method in the human brain with a small number of echoes and multi-slice imaging is unknown. Previous work with exponential fitting has demonstrated the limitations of reducing echo trains, where echo trains as low as 20 echoes were considered (35). Here, we explore vastly reduced echo numbers beginning at a maximum of 20 and reducing to as low as three, while maintaining consistent echo spacing. Particularly for high field implementation, long echo trains are constrained by increased RF heating, with RF power deposition increasing with roughly the square of the magnetic field. Shorter echo trains would reduce RF heating substantially and enable multi-slice imaging with reduced losses from incidental magnetization transfer (MT). In human brain at 4.7 T, we examine the viability of extremely short echo trains and multi-slice imaging for single component T_2 fitting using SEC.

3.3 Methods

3.3.1 MRI Acquisition

Two-dimensional multi-echo spin echo images of the human brain were obtained in single and multi-slice mode on a Varian Inova 4.7 T whole-body system. Axial, transverse relaxation maps of the human brain were obtained through the deep grey matter (DGM) including the putamen, globus pallidus and caudate nucleus. Fourteen healthy subjects (eight male, six female; mean age: 28 ± 2 years) were studied, all of whom gave written informed consent in accordance with institutional protocols. The typical scan parameters were: 4000 ms TR, 10 ms echo spacing, 20 echo train length, 4 mm slice thickness, 8 mm slice gap, 1 or 2 slices, 50 kHz receiver bandwidth, and 256×145 imaging matrix, in-plane resolution 1.00×1.25 mm². Acquisition time was 5.2 min per image set. Different multi-slice coverage was tested ranging from 2 to 8 slices, while maintaining the same total number of refocusing pulses by corresponding reduction of echo train length. Inter-echo spacing of 10 ms was maintained for all experiments. Excitation and refocusing angles were prescribed at 90° and 180° respectively with the refocusing pulse slice profile 1.75, 3.5 or 5 times wider than excitation. To minimize RF deposition, Gaussian pulses were used with durations for excitation and refocusing pulses of 4.00 ms (bandwidth of 672.5 Hz) and 2.29 ms (bandwidth of 1176.7 Hz) respectively. Images were collected with a 4-element receive array (36) paired with a birdcage coil for transmit. Maximum gradient strength was 60 mT/m with a slew rate of 120 T/m/s.

3.3.2 T_2 Fitting and Analysis

Single component T_2 fitting was carried out by fitting the full spin echo and stimulated echo response using SEC as previously described (33). This approach determines the T_2 and the relative flip angles for each voxel from examination of the spin response, beginning with knowledge of the RF pulse shapes and sequence timing. The spin response is calculated from the extended phase graph algorithm (28) and T_1 decay during the echo train is assumed negligible relative to T_2 . The signal decay curves were fit on a pixel-by-pixel basis with SEC and with a standard exponential model for different numbers of consecutive echoes obtained both retrospectively and prospectively. Using the resulting T_2 maps, bilateral regions-of-interest (ROI) were drawn on representative sections of iron-rich subcortical GM territories (including putamen, globus pallidus, and caudate nucleus), cortical GM, cerebrospinal fluid (CSF), partial volume as well as WM. For multi-slice experiments, measurements were also performed to determine the influence of incidental MT on the resulting T_2 values.

3.4 Results

Presence of stimulated echoes in the signal decay is easily recognized from an enhanced 2nd echo as shown in Figure 3.1(a). Due to high field RF non-uniformity within the slice, the more central globus pallidus has less stimulated echo component than frontal WM because the refocusing flip angles are closer to the prescribed 180° near the image center. Figure 3.1(b-f) show the population averaged T_2 from iron-rich DGM (caudate, globus pallidus), WM territories (frontal, posterior internal capsule and optic radiation), CSF, and partial volume (caudate with 20% CSF) for echo train reduction employed retrospectively using both SEC and exponential fits. The SEC is robust at most echo train lengths for GM and WM, where short echo trains are effective; however, for the long T_2 of CSF (Fig 3.1h), overestimation is observed with echo trains below six. For WM regions of high myelin content, a slight underestimation of T_2 is observed with some short echo trains (Fig 3.1f, g) due to a stronger weighting of the short myelin water T_2 over the longer components. The same effect is observed in the partial volume caudate with longer component CSF territory (Fig 3.1e), where the average T_2 decreases slightly before increasing. For GM and frontal WM, consistent T_2 relaxation times are observed as the echo train is shortened, with only 2.4% maximum variation between 4 and 20 echoes. For posterior internal capsule (IC), this variation rises to 7.7% due to increased myelin content. Similar results

were obtained with refocusing slice thickness 3.5 and 5 times larger than excitation thickness (data not shown).

For the standard exponential fit, a large variation in T_2 with echo train for all structures was observed especially with short echo trains. Signals due to stimulated echoes, which are particularly prominent in the second echo and present thereafter, lead to non-exponential decay producing increasing errors when echo trains are reduced when using an exponential fit. Even with long echo trains, exponential fit still overestimates the T_2 since stimulated echo pathways are not included; hence T_2 convergence at higher numbers of echoes is not expected.

Using SEC, the fit produces both a T_2 and a normalized flip angle map. Figure 3.2 shows the normalized flip angle maps derived from the SEC algorithm for 2, 3, 4, 20 echoes respectively. The maps maintain consistency down to 3 echoes. Figure 3.3 presents typical R_2 maps ($1/T_2$) obtained using 20 echoes (left column) then reduced retrospectively to 4 echoes (middle column); the difference images (right column) suggest the SEC (a-c) remains accurate despite drastic reduction in echo train length, while the standard exponential fit (d-f) is highly dependent on the number of echoes in the fit.

Results from multi-slice imaging, where reduced echoes are translated into increased slice coverage, are shown in Table 3.1. The average T_2 values are presented using SEC for a single slice (20 echoes), 2 slices (20 echoes), 4 slices (10 echoes) and 8 slices (5 echoes) from four subjects. Slice coverage and echo train length were varied under constant RF power deposition for the multi-slice acquisitions. Results from echo shortening in Table 3.1 follow the same trend as the retrospective case considered above, indicating minimal effect of incidental MT on the T_2 values. Example R_2 maps for various slices and echo numbers are shown in Figure 3.4, along with corresponding normalized flip angle maps obtained from the SEC fit.

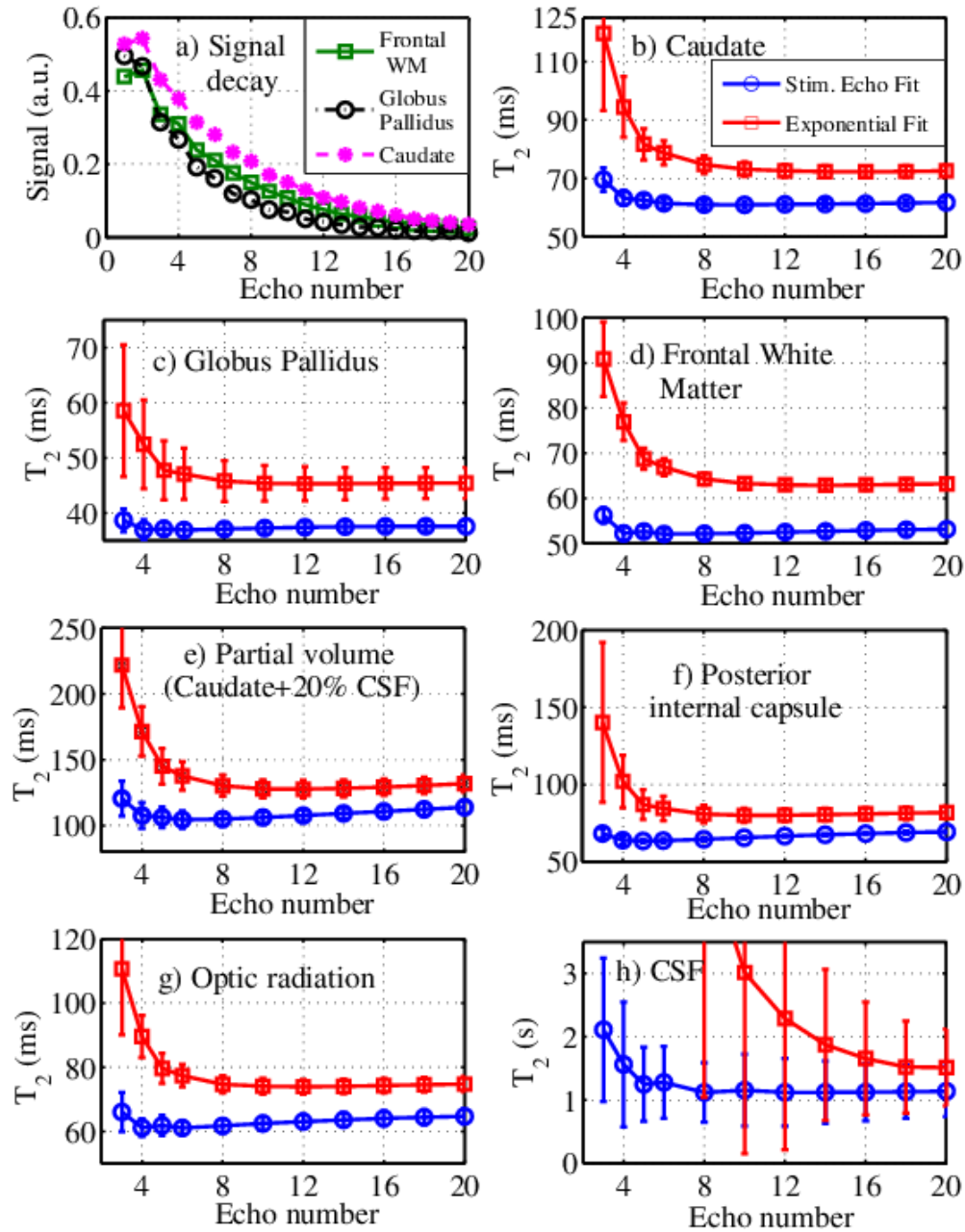


Figure 3.1: a) Signal decay from one subject for three territories, b-h) effect of number of echoes on the measured T_2 relaxation time using exponential fit or stimulated echo compensation averaged over 10 subjects in different brain regions. Error bars indicate inter-subject standard deviations. Due to heterogeneous B_1 and slice-selective refocusing, the exponential fit provides erroneous results in all cases. In contrast, stimulated echo compensation provides good results for four or more echoes, except in the case of CSF, where additional echoes are needed.

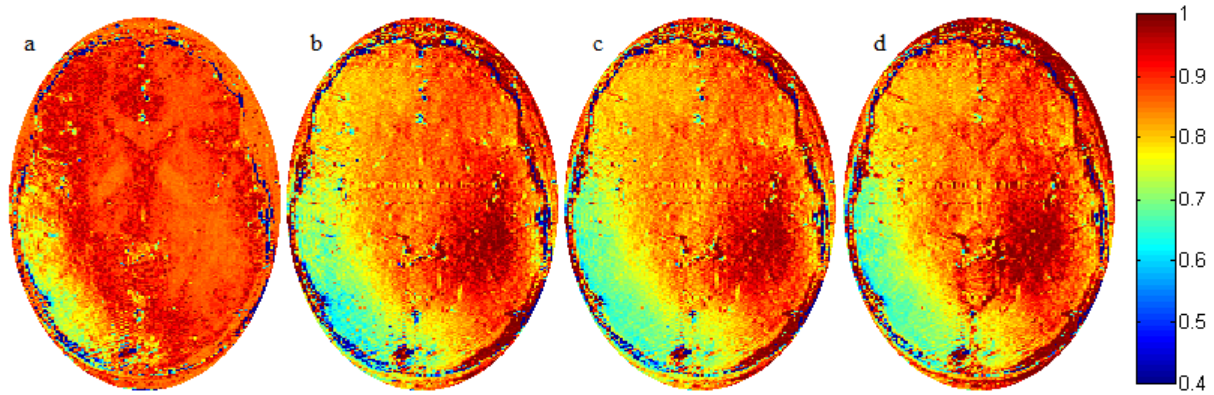


Figure 3.2: Effect of number of echoes on normalized flip angle maps (retrospective): a) 2 echoes, b) 3 echoes, c) 4 echoes and d) 20 echoes. Flip angle maps achieve stability with 3 or more echoes.

Figure 3.5 examines incidental MT resulting from multi-slice T_2 imaging using the ratio of multi-slice to single-slice image SNR from an early echo image. Reductions in SNR between 5% and 17% were observed as the number of slices increases with corresponding echo train length reduction. The observed SNR reduction is negligible for CSF as expected. Note the expected dependence on tissue type (WM versus GM) and on the flip angle (higher flip angle in center). The MT effects also have a T_1 dependence since the off-resonant slices are interleaved within the 4 s TR. For example, with two slices, off-resonant excitation occurs 2 s before acquisition.

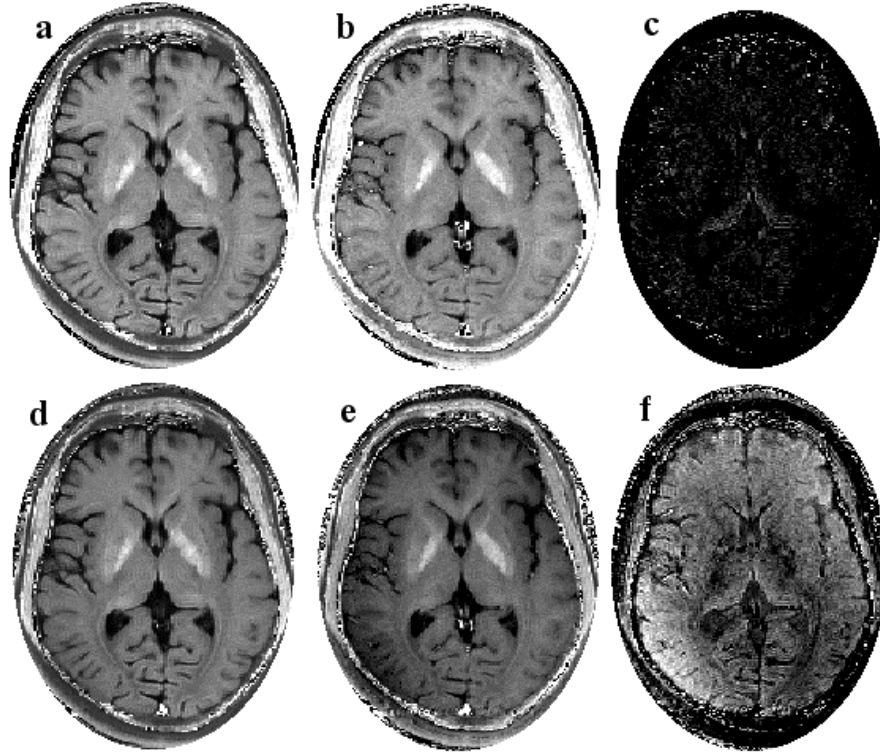


Figure 3.3: In-vivo R_2 maps: top row, stimulated echo fit; bottom row, exponential fit. In (a,d), 20 echoes are used, while (b,e) only 4 echoes. Difference maps are shown in (c,f) with stimulated echo (c) showing minimal change, but drastic differences for the exponential fit (f). Intensity scale is from 2.5 to 30 s^{-1} in images (a,b,d,e) and 0.68 to 7.5 s^{-1} for difference images (c,f).

3.5 Discussion

With SEC, we have demonstrated that short echo trains as short as 4 can be used to constrain RF power and provide similar results to long echo trains for investigation of T_2 quantification of deep grey matter structures. Results in multi-component WM had slightly increased variability. Reduced echo train lengths can enable reduced RF power deposition or an increase in slice coverage and scan efficiency. However, given sufficient time and no RF heating constraints, long echo trains can produce better results, but are not always practical at high field, especially when more than one slice is required. Indeed, reduced echo trains can lead to less accuracy, especially in a low SNR environment (35). Optimal echo train length also depends on T_2 (37), with longer train length needed for longer T_2 values. Our results clearly indicate overestimation of the CSF T_2 when the number of echoes is reduced, but demonstrate excellent results for shorter T_2 values.

Table 3.1: Average T_2 values from 4 subjects for different number of slices and echoes using the stimulated echo fit

# of Slices	# of echoes	Frontal WM	Caudate	Putamen	Globus Pallidus	Posterior IC	Optic Radiation	CSF
1	20	53.1±1.5	61.0±1.5	55.3±1.5	37.0±1.1	68.9±2.5	65.4±0.3	1132±265
2	20	53.9±0.6	60.6±2.5	52.9±3.1	37.0±1.2	68.7±2.9	65.3±0.9	1202±294
4	10	52.8±0.9	61.2±2.1	55.0±1.6	36.6±0.8	64.9±2.3	63.1±1.6	1518±590
8	5	52.5±1.1	62.9±2.2	55.3±2.2	35.0±1.0	63.1±2.7	60.3±0.5	1619±452

Note: Values reported as inter-subject mean \pm standard deviation. WM: white matter; IC: internal capsule; CSF: Cerebrospinal Fluid.

The multiple-echo spin echo technique is sensitive to RF heterogeneity that can arise from through-plane RF variation from imperfect refocusing slice profiles or in-plane variation from RF interference effects. At 4.7 T used here, and at higher fields, in-plane heterogeneity is substantial for brain imaging (see Figure 3.4e). Radiofrequency heterogeneity can be improved somewhat by using RF shimming (38,39), or using multiple lobe, shaped or double adiabatic refocusing pulses (40) which substantially increase RF power demands. Simply widening the thickness of the refocusing pulses relative to the excitation pulse can also improve the refocused slice profile (31), but limits potential for increased slice coverage. The SEC used here enables use of T_2 mapping at high magnetic field by accounting for RF field non-uniformity and enabling substantial echo reduction to minimize RF heating effects.

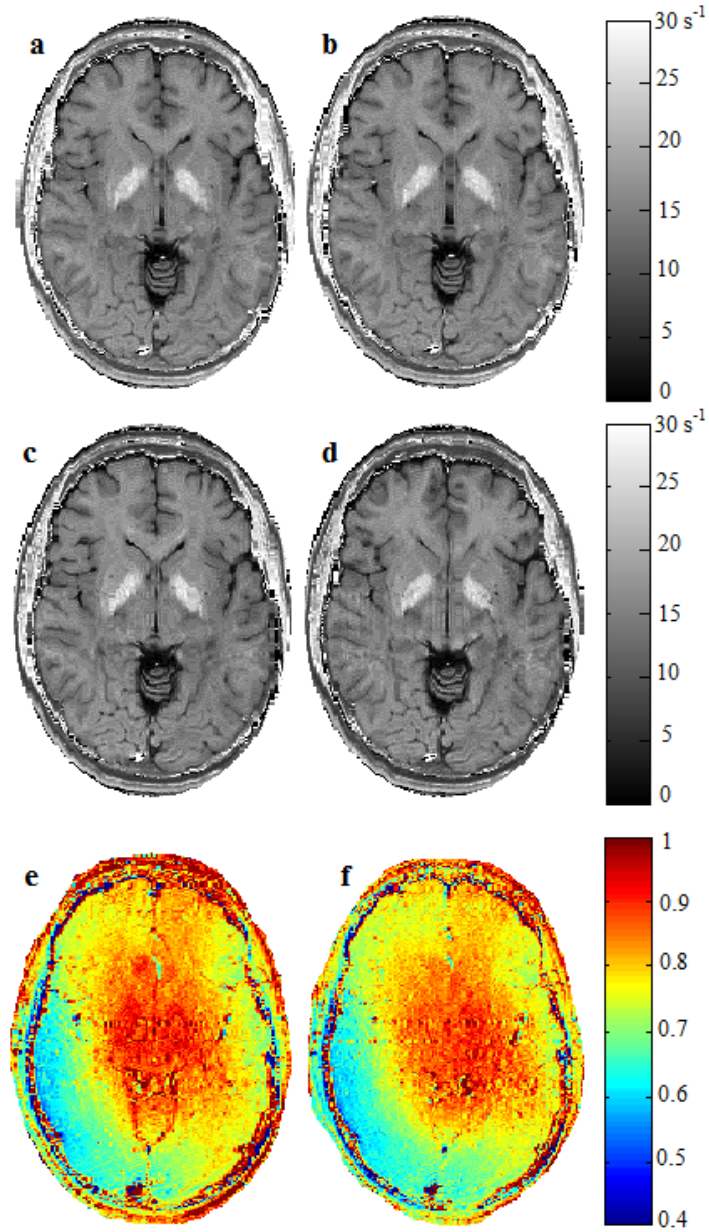


Figure 3.4: In-vivo R_2 maps using stimulated echo compensation: a) 1 slice and 20 echoes, b) 2 slices and 20 echoes, c) 4 slices and 10 echoes and d) 8 slices and 5 echoes. Corresponding normalized flip angle maps for a) and d) are shown in (e, f) respectively, demonstrating consistent flip angle estimation with short echo trains.

Increased slice coverage is necessary for future clinical application. We have demonstrated that savings in RF power through echo shortening can be applied to increase the

slice coverage, with similar T_2 results to single slice, even though there is signal reduction due to incidental MT effects (Fig. 3.5). We observed less than 15% SNR reductions from single slice to 8 slices. Although SNR was lost in multi-slice mode due to incidental MT, it did not significantly affect the mean T_2 values for GM or WM and similar results were found for either retrospective echo shortening without MT effects (Fig. 3.1), or prospective echo shortening with increased slice number and incidental MT (Table 3.1). The effect of incidental MT on the T_2 fit was minimal partly due to the small number of off-resonant RF pulses used. Specifically in WM, the delay between off-resonant excitation and on-resonant acquisition minimized differential MT effects between myelin water and other pools due to exchange (41). The MT effects due to multislice interference were previously reported for human brain using fast spin echo sequences (42-45). Our incidental MT results are consistent with others (44,45). As expected, when the flip angle is similar, WM has greater MT than GM due to higher macromolecular content (42-48). Increased MT was observed from the posterior internal capsule because of higher myelin water content and greater flip angle in this more central region.

Increased slice coverage is also possible through single slab 3D imaging without incidental MT effects (49). This has been demonstrated at 3T using multiple spin echo 3D imaging with an 8 slice matrix (49); however, lengthy T_1 times at high field may limit imaging efficiency due to the need for long repetition times.

Our current implementation of SEC is based on the assumption that magnetization involved in alternate coherence pathways experiences negligible T_1 relaxation during the echo train, which provides accurate T_2 values for T_1/T_2 ratio above ten (33), but for tissues with smaller T_1/T_2 ratios like CSF this assumption may provide underestimated T_2 values. Nevertheless, stimulated echo compensation still outperformed exponential fitting with CSF T_2 values using 5 echoes versus 20 echoes being 19% different with SEC and 2500% different for exponential fitting.

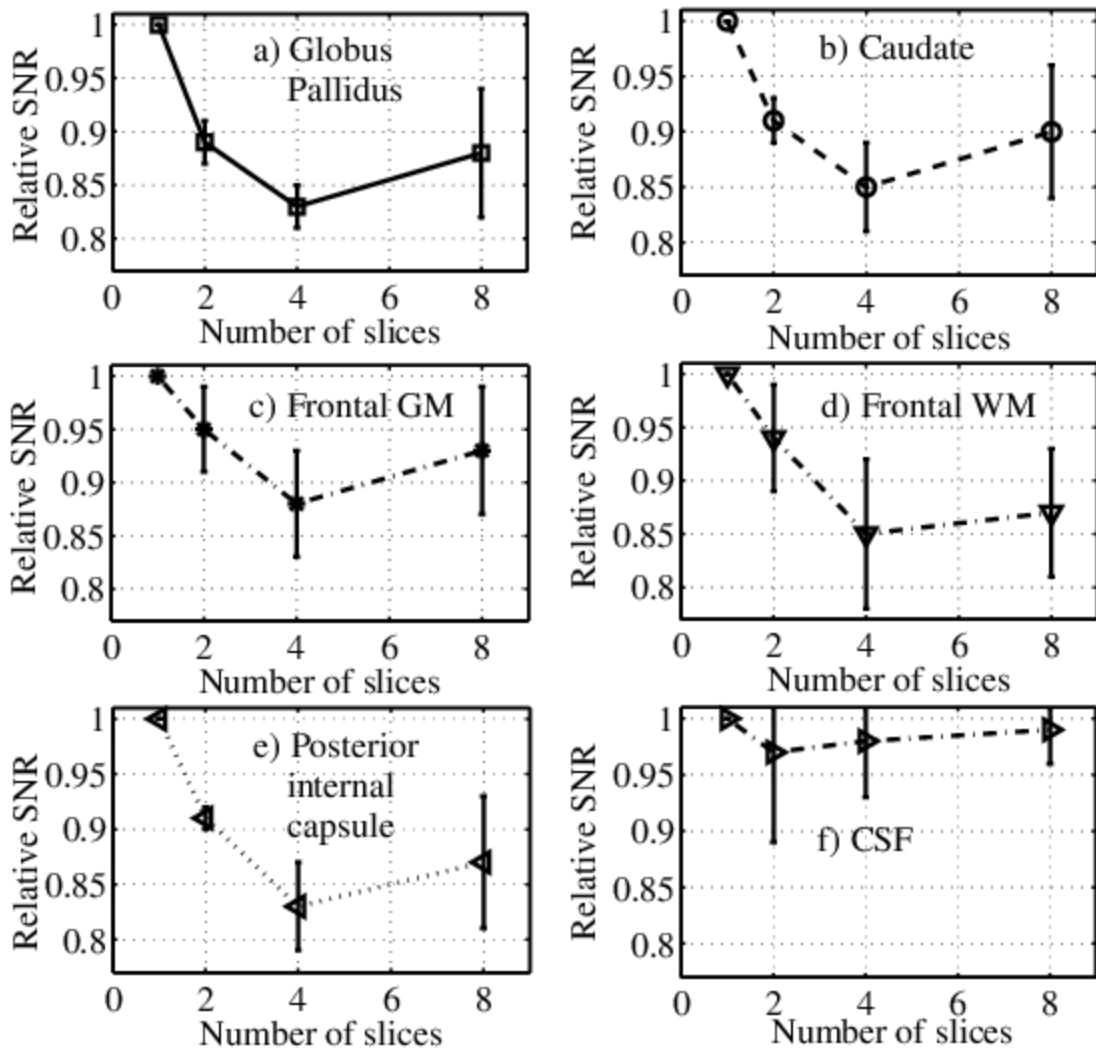


Figure 3.5: Incidental magnetization transfer (iMT) effects illustrated through the relationship between relative SNR and the number of slices acquired in four brain territories averaged over 4 subjects. As slice number was increased past 2, the number of echoes was correspondingly decreased to maintain the same total number of refocusing pulses (slices-echoes: 1-20, 2-20, 4-10, 8-5). Error bars represent inter-subject standard deviations.

Throughout this work, we maintained a constant echo spacing of 10 ms similar to previous work (33,34) to control for diffusion effects between refocusing pulses (50,51) and to maintain signal from relatively short T_2 values that arise in regions of iron-laden ferritin in GM or very short T_2 from myelin water in WM. Simulations have shown that optimal interecho

spacing and train length varies with T_2 values (37,52), however there is a wide range of T_2 values across the human brain. Combining long inter-echo spacing with few echoes, has been shown to produce poor results in human brain (53), thus a short echo spacing is preferable.

In conclusion, it was shown that in contrast to standard exponential fitting, substantial shortening of the echo train can be achieved using SEC while maintaining accurate T_2 values at 4.7 T, where there is substantial RF inhomogeneity. Radiofrequency power savings through echo reduction enabled accurate deep grey matter T_2 values using 8 slices of 5 echoes each. Incidental MT was significant in multislice mode, but had minimal effect on the T_2 values. Thus SEC with reduction of RF refocusing pulses can enable efficient use of T_2 mapping for high field or other applications where refocusing pulses are not ideal and RF power reductions are required.

3.6 Acknowledgements

This work was supported by grants from the Canadian Institutes of Health Research (CIHR) and the Natural Sciences and Engineering Research Council of Canada (NSERC).

3.7 References

1. Khalil M, Langkammer C, Ropele S, Petrovic K, Wallner-Blazek M, Loitfelder M, Jehna M, Bachmaier G, Schmidt R, Enzinger C, Fuchs S, Fazekas F. Determinants of brain iron in multiple sclerosis: A quantitative 3T MRI study. *Neurology* 2011;77(18):1691-1697.
2. Lebel RM, Eissa A, Seres P, Blevins G, Wilman AH. Quantitative high-field imaging of sub-cortical gray matter in multiple sclerosis. *Multiple Sclerosis Journal* 2012;18(4):433-441.
3. Schenck JF, Zimmerman EA. High-field magnetic resonance imaging of brain iron: birth of a biomarker? *NMR in Biomedicine* 2004;17(7):433-445.
4. Langkammer C, Krebs N, Goessler W, Scheurer E, Ebner F, Yen K, Fazekas F, Ropele S. Quantitative MR imaging of brain iron: a postmortem validation study. *Radiology* 2010;257(2):455-462.
5. MacKay AL, Vavasour IM, Rauscher A, Kolind SH, Maedler B, Moore GRW, Traboulsee AL, Li DKB, Laule C. MR Relaxation in Multiple Sclerosis. *Neuroimaging Clinics of North America* 2009;19(1):1-26.

6. Ge Y, Jensen JH, Lu H, Helpem JA, Miles L, Inglese M, Babb JS, Herbert J, Grossman RI. Quantitative assessment of iron accumulation in the deep gray matter of multiple sclerosis by magnetic field correlation imaging. *American Journal of Neuroradiology* 2007;28(9):1639-1644.
7. Bakshi R, Benedict RHB, Bermel RA, Caruthers SD, Puli SR, Tjoa CW, Fabiano AJ, Jacobs L. T₂ hypointensity in the deep gray matter of patients with multiple sclerosis - A quantitative magnetic resonance imaging study. *Archives of Neurology* 2002;59(1):62-68.
8. Drayer B, Burger P, Hurwitz B, Dawson D, Cain J. Reduced signal intensity on MR images of thalamus and putamen in multiple sclerosis: increased iron content? *American Journal of Roentgenology* 1987;149(2):357-363.
9. Ceccarelli A, Rocca MA, Neema M, Martinelli V, Arora A, Tauhid S, Ghezzi A, Comi G, Bakshi R, Filippi M. Deep gray matter T₂ hypointensity is present in patients with clinically isolated syndromes suggestive of multiple sclerosis. *Multiple sclerosis* 2010;16(1):39-44.
10. Whittall KP, MacKay AL, Graeb DA, Nugent RA, Li DKB, Paty DW. In vivo measurement of T₂ distributions and water contents in normal human brain. *Magnetic Resonance in Medicine* 1997;37(1):34-43.
11. MacKay A, Laule C, Vavasour I, Bjarnason T, Kolind S, Madler B. Insights into brain microstructure from the T₂ distribution. *Magnetic Resonance Imaging* 2006;24(4):515-525.
12. Laule C, Vavasour IM, Kolind SH, Traboulsee AL, Moore GRW, Li DKB, MacKay AL. Long T₂ water in multiple sclerosis: What else can we learn from multi-echo T₂ relaxation? *Journal of neurology* 2007;254(11):1579-1587.
13. Dardzinski BJ, Mosher TJ, Li SZ, VanSlyke MA, Smith MB. Spatial variation of T₂ in human articular cartilage. *Radiology* 1997;205(2):546-550.
14. Perry J, Haughton V, Anderson PA, Wu Y, Fine J, Mistretta C. The value of T₂ relaxation times to characterize lumbar intervertebral disks: Preliminary results. *American Journal of Neuroradiology* 2006;27(2):337-342.

15. Hosch W, Bock M, Libicher M, Ley S, Hegenbart U, Dengler TJ, Katus HA, Kauczor H-U, Kauffmann GW, Kristen AV. MR-Relaxometry of myocardial tissue - Significant elevation of T₁ and T₂ relaxation times in cardiac amyloidosis. *Investigative Radiology* 2007;42(9):636-642.
16. White LM, Sussman MS, Hurtig M, Probyn L, Tomlinson G, Kandel R. Cartilage T₂ assessment: Differentiation of normal hyaline cartilage and reparative tissue after arthroscopic cartilage repair in equine subjects. *Radiology* 2006;241(2):407-414.
17. Martin AJ, Poon CS, Thomas GM, Kapusta LR, Shaw PA, Henkelman RM. MR evaluation of cervical cancer in hysterectomy specimens: correlation of quantitative T₂ measurement and histology. *Journal of Magnetic Resonance Imaging* 1994;4(6):779-786.
18. Liney GP, Knowles AJ, Manton DJ, Turnbull LW, Blackband SJ, Horsman A. Comparison of conventional single echo and multi-echo sequences with a fast spin echo sequence for quantitative T₂ mapping: Application to the prostate. *Journal of Magnetic Resonance Imaging* 1996;6(4):603-607.
19. St Pierre TG, Clark PR, Chua-Anusorn W, Fleming AJ, Jeffrey GP, Olynyk JK, Pootrakul P, Robins E, Lindeman R. Noninvasive measurement and imaging of liver iron concentrations using proton magnetic resonance. *Blood* 2005;105(2):855-861.
20. Pai A, Li X, Majumdar S. A comparative study at 3 T of sequence dependence of T₂ quantitation in the knee. *Journal of Magnetic Resonance Imaging* 2008;26(9):1215-1220.
21. Maier CF, Tan SG, Hariharan H, Potter HG. T₂ quantitation of articular cartilage at 1.5 T. *Journal of Magnetic Resonance Imaging* 2003;17(3):358-364.
22. Papakonstantinou O, Kostaridou S, Maris T, Gouliamos A, Premetis E, Kouloulis V, Nakopoulou L, Kattamis C. Quantification of liver iron overload by T₂ quantitative magnetic resonance imaging in thalassemia: impact of chronic hepatitis C on measurements. *J Pediatr Hematol Oncol* 1999;21(2):142-148.
23. Horch RA, Nyman JS, Gochberg DF, Dortch RD, Does MD. Characterization of ¹H NMR signal in human cortical bone for magnetic resonance imaging. *Journal of Magnetic Resonance in Medicine* 2010;64(3):680-687.

24. Reiter DA, Lin P-C, Fishbein KW, Spencer RG. Multicomponent T_2 Relaxation Analysis in Cartilage. *Magnetic Resonance in Medicine* 2009;61(4):803-809.
25. Deoni SCL, Rutt BK, Peters TM. Rapid combined T_1 and T_2 mapping using gradient recalled acquisition in the steady state. *Magnetic Resonance in Medicine* 2003;49(3):515-526.
26. Poon CS, Henkelman RM. Practical T_2 quantitation for clinical applications. *Journal of Magnetic Resonance Imaging* 1992;2(5):541-553.
27. Vaughan JT, Garwood M, Collins C, Liu W, DelaBarre L, Adriany G, Andersen P, Merkle H, Goebel R, Smith M. 7T vs. 4T: RF power, homogeneity, and signal-to-noise comparison in head images. *Magnetic Resonance in Medicine* 2001;46(1):24-30.
28. Hennig J. Multiecho Imaging Sequences With Low Refocusing Flip Angles. *Journal of Magnetic Resonance* 1988;78(3):397-407.
29. Watanabe H, Takaya N, Mitsumori F. Non-uniformity correction of human brain imaging at high field by RF field mapping of B_1^+ and B_1^- . *Journal of Magnetic Resonance* 2011;212(2):426-430.
30. Does MD, Snyder RE. Multiecho imaging with suboptimal spoiler gradients. *Journal of Magnetic Resonance* 1998;131(1):25-31.
31. Pell GS, Briellmann RS, Waites AB, Abbott DF, Lewis DP, Jackson GD. Optimized clinical T_2 relaxometry with a standard CPMG sequence. *Journal of Magnetic Resonance Imaging* 2006;23(2):248-252.
32. Jones C, Xiang Q, Whittall K, MacKay A. Calculating T_2 and B_1 from decay curves collected with non-180 refocusing pulses. Proceedings 11th Scientific Meeting, International Society for Magnetic Resonance in Medicine 2003; 1018.
33. Lebel RM, Wilman AH. Transverse relaxometry with stimulated echo compensation. *Magnetic Resonance in Medicine* 2010;64(4):1005-1014.
34. Prasloski T, Mädler B, Xiang QS, MacKay A, Jones C. Applications of stimulated echo correction to multicomponent T_2 analysis. *Magnetic Resonance in Medicine* 2012;67(6):1803-1814.

35. Anastasiou A, Hall LD. Optimisation of T_2 and M_0 measurements of bi-exponential systems. *Journal of Magnetic Resonance Imaging* 2004;22(1):67-80.
36. Carmichael DW, Thomas DL, De Vita E, Fernandez-Seara MA, Chhina N, Cooper M, Sunderland C, Randell C, Turner R, Ordidge RJ. Improving whole brain structural MRI at 4.7 Tesla using 4 irregularly shaped receiver coils. *Neuroimage* 2006;32(3):1176-1184.
37. Jones JA, Hodgkinson P, Barker AL, Hore PJ. Optimal sampling strategies for the measurement of spin-spin relaxation times. *Journal of Magnetic Resonance Series B* 1996;113(1):25-34.
38. Tang L, Hue Y-K, Ibrahim TS. Studies of RF shimming techniques with minimization of RF power deposition and their associated temperature changes. *Concepts in Magnetic Resonance Part B-Magnetic Resonance Engineering* 2011;39B(1):11-25.
39. Mao W, Smith MB, Collins CM. Exploring the limits of RF shimming for high-field MRI of the human head. *Magnetic Resonance in Medicine* 2006;56(4):918-922.
40. Mitsumori F, Watanabe H, Takaya N. Estimation of brain iron concentration in-vivo using a linear relationship between regional iron and apparent transverse relaxation rate of the tissue water at 4.7T. *Magnetic Resonance in Medicine* 2009;62(5):1326-1330.
41. Vavasour IM, Whittall KP, Li DKB, MacKay AL. Different magnetization transfer effects exhibited by the short and long T_2 components in human brain. *Magnetic Resonance in Medicine* 2000;44(6):860-866.
42. Melki PS, Mulkern RV. Magnetization transfer effects in multislice RARE sequences. *Magnetic Resonance in Medicine* 1992;24(1):189-195.
43. Chang Y, Bae SJ, Lee YJ, Hwang MJ, Lee SH, Lee J, Lee SK, Woo S. Incidental magnetization transfer effects in multislice brain MRI at 3.0 T. *Journal of Magnetic Resonance Imaging* 2007;25(4):862-865.
44. Weigel M, Helms G, Hennig J. Investigation and modeling of magnetization transfer effects in two-dimensional multislice turbo spin echo sequences with low constant or variable flip angles at 3 T. *Magnetic Resonance in Medicine* 2010;63(1):230-234.

45. Lebel RM, Wilman AH. Time efficient fast spin echo imaging at 4.7 T with low refocusing angles. *Magnetic Resonance in Medicine* 2009;62(1):96-105.
46. Stanisz GJ, Odobina EE, Pun J, Escaravage M, Graham SJ, Bronskill MJ, Henkelman RM. T_1 , T_2 relaxation and magnetization transfer in tissue at 3T. *Magnetic Resonance in Medicine* 2005;54(3):507-512.
47. Santyr GE. Magnetization transfer effects in multislice MR imaging. *Journal of Magnetic Resonance Imaging* 1993;11(4):521-532.
48. Dixon WT, Engels H, Castillo M, Sardashti M. Incidental magnetization transfer contrast in standard multislice imaging. *Journal of Magnetic Resonance Imaging* 1990;8(4):417-422.
49. MacMillan EL, Maedler B, Fichtner N, Dvorak MF, Li DKB, Curt A, MacKay AL. Myelin water and T_2 relaxation measurements in the healthy cervical spinal cord at 3.0T: Repeatability and changes with age. *Neuroimage* 2011;54(2):1083-1090.
50. Bartha R, Michaeli S, Merkle H, Adriany G, Andersen P, Chen W, Ugurbil K, Garwood M. In vivo $^1\text{H}_2\text{O}$ T_2 (dagger) measurement in the human occipital lobe at 4T and 7T by Carr-Purcell MRI: Detection of microscopic susceptibility contrast. *Magnetic Resonance in Medicine* 2002;47(4):742-750.
51. Ye FQ, Martin W, Allen PS. Estimation of brain iron in vivo by means of the interecho time dependence of image contrast. *Magnetic Resonance in Medicine* 1996;36(1):153-158.
52. Dula AN, Gochberg DF, Does MD. Optimal echo spacing for multi-echo imaging measurements of Bi-exponential T_2 relaxation. *Journal of Magnetic Resonance* 2009;196(2):149-156.
53. Whittall KP, MacKay AL, Li DKB. Are mono-exponential fits to a few echoes sufficient to determine T_2 relaxation for in vivo human brain? *Magnetic Resonance in Medicine* 1999;41(6):1255-1257.

Chapter 4. Value of transverse relaxometry difference methods for iron in human brain ³

4.1 Abstract

Purpose: To investigate the brain iron dependence of transverse relaxation rate difference methods derived from spin echo and gradient echo measurements from two field strengths.

Methods: Transverse relaxation rates R_2 and R_2^* were measured in human brain in 17 healthy subjects at 1.5 T and 4.7 T using multi-slice, multiecho spin echo and gradient echo sequences. R_2 quantification used stimulated echo compensation and R_2^* quantification used linear background gradient correction at 4.7 T only. Subtraction of R_2 from R_2^* within each field strength yielded R_2' , and R_2 subtraction across fields yielded Field Dependent R_2 Increase (FDRI). All transverse relaxation measures were then correlated with published post-mortem iron concentrations using linear regression analysis. Regional differences were tested using paired t-tests. Phantom measurements of FDRI were also performed.

Results: In deep grey matter, all transverse relaxation rates (R_2 , R_2^* , R_2') at both 1.5 T and 4.7 T, and FDRI had moderate to strong correlations ($r > 0.71$, $p < 0.0001$) with estimated non-heme iron. The 4.7 T methods and FDRI had higher correlations ($r > 0.9$) than 1.5 T measures. R_2 , R_2^* , R_2' at 4.7 T and FDRI had slopes 0.49, 1.96, 1.48 and 0.33 [$s^{-1}/\text{mg Fe}/100 \text{ g wt. tissue}$] and intercepts 14.40, 16.87, 2.47 and 3.21 [s^{-1}] respectively. Even though FDRI yielded a zero intercept in phantom, in vivo FDRI was found to be ineffective at fully removing non-iron contributions and yielded a large intercept. The slope for R_2' was 3.4 times greater at 4.7 T than 1.5 T. For white matter fiber tracts oriented predominantly perpendicular versus parallel to B_0 , R_2' increased by $\sim 50\%$ at 4.7 T and $\sim 30\%$ at 1.5 T, while R_2 and FDRI in white matter was insensitive to its orientation with respect to B_0 .

Conclusion: The transverse relaxation difference methods FDRI and R_2' at 4.7 T had high correlations to predicted iron content similar to R_2 and R_2^* at 4.7 T. Although R_2' had

³ A version of this section has been published. Uddin MN, Lebel RM, Wilman AH. Value of transverse relaxometry difference methods for iron in human brain, Magnetic Resonance Imaging Journal (2015). doi: 10.1016/j.mri.2015.09.002

smaller y -intercept with estimated iron concentration than FDRI, in white matter R_2' demonstrated strongest dependence on fiber orientation with respect to B_0 . These results suggest that for brain iron correlation, there is minimal value of transverse difference methods over a single R_2^* measurement at highest available field, which was 4.7 T.

4.2 Introduction

Iron is an important factor for many biological processes including oxygen transport, mitochondrial energy generation, DNA synthesis and cellular metabolism, and is present in various complex chemical forms. Non-heme iron in brain is mostly stored within glial cells as ferritin that comprises a spherical protein shell and a superparamagnetic ferrihydrite core (1-4). However, excess iron can cause the formation of free radicals from reactive oxygen species via Fenton reaction which can exert oxidative stress, and can damage proteins, DNA and membranes (1). Brain iron levels increase progressively with normal aging until the end of the third decade (5). Abnormal iron accumulation in specific regions of the brain has been reported in neurodegenerative disorders such as Alzheimer's disease, multiple sclerosis and Parkinson's disease (3,6,7). Structures in the basal ganglia are particularly iron rich including globus pallidus, putamen, caudate, substantia nigra and red nucleus (5). White matter (WM) also contains iron, but the concentration is roughly 3-4 times lower than iron-rich basal ganglia (5,8,9). Iron creates microscopic magnetic field gradients that can change the relaxation behavior of nearby tissue water (10,11). Moreover, iron creates inhomogeneities in the local magnetic field due to the superparamagnetic properties of the ferrihydrite core contained in ferritin, which shortens the MRI transverse relaxation time (4,12-14).

The spin echo and gradient echo transverse relaxation rates R_2 and R_2^* presented in the form of relaxation-weighted images (14-18) or absolute quantitative relaxation maps (6,8,19,20) may provide information about subtle iron-related changes in the brain. In brain, R_2 and R_2^* are affected by numerous properties including water and macromolecular content, calcium, tissue microstructure, and paramagnetic blood deoxyhemoglobin which limit the specificity of R_2 and R_2^* to estimate the tissue iron content measurement (21-24). In certain regions of the brain, such as iron-rich deep grey matter (DGM), signal changes may be dominated by one factor (iron-laden ferritin), but nevertheless specificity of these measurements cannot be guaranteed. For example, tissue neurodegeneration may have contributions from both iron-independent and iron-

related processes (25,26). A correlation between R_2 and post-mortem iron concentration in deep grey matter at 1.5 T was first reported by Drayer *et al* (10) and has since been investigated extensively by other groups (12,14,20,27-31) at different field strengths ranging from 0.5 T to 7.0 T. Previous work (8,28,32) suggest that R_2^* is more sensitive to iron than R_2 and provides very strong correlations with estimated iron concentrations in GM. *In-vitro* R_2 measurements in aqueous solution of ferritin showed very high correlation between R_2 and ferritin concentration (33) however, complex tissue structures, including variable water and macromolecular content, reduce *in-vivo* correlations to iron (14,31).

Alternative approaches to increasing iron specificity in brain include relaxation rate difference methods, whereby iron-independent components that remain constant between measurements can be eliminated through subtraction of two relaxation rates. Two such methods are Field Dependent R_2 Increase (FDRI) which measures differences between relaxation rates acquired at two different field strengths, and R_2' which measures differences between R_2 and R_2^* at single field strength. R_2' reflects only the reversible contribution to R_2^* associated with static local magnetic field inhomogeneities (2,34,35). This heightened sensitivity to field inhomogeneity may require removal of background fields to enable local field inhomogeneity measurements (20,36), which can be accomplished by linear background gradient correction (37). Ordidge *et al.* (16) demonstrated the use of R_2' to study brain iron at 3.0 T when magnetic field inhomogeneity is corrected. Previous works (17,28) also showed R_2' is more effective to estimate brain iron compared to R_2 using 1.5 T and 3.0 T. Although the spin echo R_2 measurement, necessary to determine R_2' , is insensitive to static magnetic field inhomogeneity, it is highly sensitive to radiofrequency (RF) field inhomogeneity that may arise from in-plane or through-plane variations. To overcome high field RF inhomogeneity, methods such as twice refocused adiabatic pulses (31) or stimulated echo compensation (38) are required.

Subtraction of R_2 measurements between two field strengths can provide a means to increase iron specificity by using FDRI (39), since the R_2 effects due to iron are proportional to B_0 (25,29,39,40). The FDRI method is also attractive since both measures in the subtraction refocus the static background field inhomogeneities, unlike R_2' . FDRI has been applied using dual spin echo sequences at 0.5 T and 1.5 T (39) and with fast spin echo at 1.5 T and 3.0 T (41). It has been shown that, using 0.5 T and 1.5 T, or 1.5 T and 3.0 T, FDRI values correlate well with estimated iron concentrations mostly from DGM and frontal WM structures (29,39,40,42).

Greater FDRI is achieved with a larger field strength difference, such as the 1.5 T and 4.7 T used here. However, the value of this larger field difference for iron specificity of FDRI and the relationship between FDRI and R_2' is unclear. Thus, the main purpose of this work is to compare these two difference methods, FDRI and R_2' , to examine their specificity to brain iron *in-vivo* using 1.5 T and 4.7 T field strengths and healthy subjects. Both difference methods have been previously applied to estimate the sensitivity to brain iron (16,32,39-41,43-45), but they have not been directly compared in the same population, nor has FDRI been applied above 3.0 T.

In WM, transverse relaxation rates are dominated by water and macromolecular content (8,46), rather than iron concentration. For example, optic radiation and internal capsule have high relaxation rates, though they contain low iron (2,47), largely due to densely myelinated fiber pathways (2,48). The R_2^* and R_2' variation in WM, due to the myelin content and tissue microstructure, is extensive at high field (22,49,50). Recent studies documented the WM fiber orientation effects with respect to B_0 which can modulate R_2^* due to anisotropic susceptibility sources along the fiber direction in the myelin sheath (22,24,51,52). These field orientation effects do not strongly affect R_2 due to refocusing of the static field effects (26,53). As well as examining the iron dependency in GM, we also examine WM effects on the transverse relaxation difference methods.

4.3 Materials and Methods

4.3.1 MRI Acquisitions

Human and phantom MRI experiments were performed using a Varian Inova 4.7 T (Varian, Palo Alto, CA) and a Siemens Sonata 1.5 T (Erlangen, Germany). The 4.7 T system had a maximum gradient amplitude of 60 mT/m with a slew rate of 120 T/m/s; the 1.5 T had maximum gradient strength of 40 mT/m and slew rate of 200 T/m/s. Images were collected with a 4-element receive array (54) paired with a head birdcage coil for transmit at 4.7 T, while 1.5 T used the body coil for transmission and a single element head coil for reception.

Two-dimensional multiple-echo spin echo sequences were employed at both field strengths to measure R_2 . Common parameters included: 4000 ms repetition time (TR), 10 ms echo spacing (ESP), 5 echo train length (ETL), 8 slices, 4 mm slice thickness, 8 mm slice gap, in-plane resolution $1.00 \times 1.25 \text{ mm}^2$, and 256×145 matrix, 50 kHz receiver bandwidth (BW)

and scan time 6.33 min. Excitation and refocusing pulses were 90° and 180° respectively. At 4.7 T, Gaussian pulses were used to minimize RF deposition with excitation and refocusing pulses of 4.00 ms and 2.29 ms respectively. At 1.5 T, 3-lobe Gaussian-filtered sinc pulses were used with time duration of 2.56 ms for both excitation and refocusing.

Multi-echo gradient echo imaging was performed at both field strengths to obtain R_2^* maps. Both field strengths used monopolar frequency encoding gradients without flow compensation. At 4.7 T, ten echoes were recorded with first TE of 2.93 ms, 4.1 ms ESP, 44 ms TR, 10° flip angle, 2 mm slice thickness, no slice gap, in-plane resolution $1 \times 1 \text{ mm}^2$, 3D acquisition matrix $256 \times 192 \times 80$, receiver BW 90 kHz, scan time 9.39 min. At 1.5 T five echoes were recorded by performing five different single gradient echo experiments (TE 6, 13, 20, 27, 34 ms) with 44 ms TR, 10° flip angle, acquisition matrix $384 \times 384 \times 40$, 4 mm slice thickness, 2D acquisition with no slice gap, 40 slices, in-plane resolution $1 \times 1 \text{ mm}^2$ and scan time 4.55 min for each single echo experiment and total scan time was 22.75 min.

4.3.2 In-vivo Experiments

Seventeen healthy subjects (34 ± 10 years, age range 25-59 years, 12 male, 5 female) were studied after obtaining informed consent according to the institutional protocols. Each subject was imaged at both field strengths performing R_2 and R_2^* mapping from which the difference images R_2 and FDRI were formed. Two dimensional multi-echo spin echo images, capturing multiple subcortical GM and WM regions, were obtained in multi-slice mode and 3D multi-echo gradient echo images were obtained for whole head. The same slice locations were chosen at both field strengths through careful head placement and manual slice alignment based on multidirectional localizer images. Additional diffusion tensor images were obtained from two subjects at 4.7 T to illustrate predominant WM orientations.

4.3.3 Phantom Preparation

Further investigation of FDRI was performed by measuring R_2 at 1.5 T and 4.7 T in a phantom. The phantom consisted of 1% agar gel embedded with eight cylinders of 1.6 cm diameter also containing 1% agar gel and different concentrations (0.005, 0.010, 0.015, 0.020, 0.030, 0.040, 0.060 and 0.080 mM) of super paramagnetic magnetite (iron core of 10 nm) in the form of Ferex

(10 mg Fe/ml, BioPAL). These concentrations were chosen to mimic R_2 values in human brain tissue, especially iron-rich DGM ($R_2 \approx 5\text{-}50 \text{ sec}^{-1}$ at 4.7 T).

4.3.4 Data Analysis

Single component R_2 maps at 1.5 T and 4.7 T were computed on a pixel-by-pixel basis using stimulated echo compensation (38). This method extracts R_2 from the spin response calculated from the extended phase graph algorithm (55) beginning with the knowledge of sequence timing and RF pulse shapes.

R_2^* maps were fit with an exponential decay using nonlinear least squares fitting. To account for much greater air-tissue susceptibility effects at 4.7 T, R_2^* maps at 4.7 T were first corrected with 3D linear susceptibility gradient removal (56), which use the phase images to estimate the linear field gradient contamination. Effects of this correction on R_2^* values were evaluated. The raw phase data was not available at 1.5 T, so no correction was performed, although the air-tissue susceptibility effects are reduced at this lower field strength.

R_2 and R_2^* maps were skull-stripped using BET (FMRIB's brain extraction tool) (57) and then manually translated, rotated and resized to align R_2 maps with R_2^* maps using ImageJ (58). R_2' maps were obtained by subtracting R_2 maps from matched R_2^* maps, while FDRI maps were obtained by subtracting R_2 maps at 1.5 T from R_2 maps 4.7 T. Region-of-interest (ROI) analysis was performed by first manually drawing ROIs on R_2 maps at 4.7 T for each subject then using the same ROIs for all other relaxometry maps. Bilateral ROIs were chosen in iron-laden DGM (including caudate nucleus, putamen, globus pallidus, red nucleus, substantia nigra and thalamus), as well as prefrontal GM and WM territories (including frontal WM, optic radiation, parietal WM, posterior internal capsule, corpus callosum splenium, corpus callosum genu and centrum semiovale). In the phantom, 1.6 cm diameter ROIs from each cylinder were obtained across the complete range of iron (magnetite) concentrations.

4.3.5 Iron concentration using post-mortem data

For human brain, non-heme iron concentration ([Fe] mg/100 g fresh wt.) was used with estimates via age dependent equations given in Hallgren and Sourander (5). However, estimated iron concentrations for thalamus, substantia nigra and red nucleus were obtained directly from the plots and tables since no equations are provided (5). Mean iron concentrations were obtained for

each structure averaged over all 17 subjects. Error in iron measurements was also determined from the plots and tables in (5), by estimating the standard error for our age range. Note several previous studies (2,14,20,24,25,28-31,39-43,59-61) have used the age versus regional iron content best fits of post-mortem data reported by Hallgren and Sourander (5) to estimate iron content using relaxometry such as R_1 (14,60), R_2 (28,32), R_2^* (32,59) and R_2' (28,32) .

4.3.6 Statistical Analysis

Statistical analyses were performed using SPSS (IBM, Armonk, NY), and p-values less than 0.05 were considered to be statistically significant. Intra-subject reliability test was also performed for a volunteer who underwent two MRI exams 2 hours apart. Each exam was analyzed independently by the same observer with ROIs manually redrawn for each structure. Intraclass correlation was used to obtain intra-rater reliability. Linear regressions were employed to investigate the relationship between iron concentrations, and all relaxation measures using Pearson correlation coefficients. Regional comparisons in relaxation rates were performed using paired sample t-test.

4.4 Results

Average relaxation rates (R_2 , R_2^* , R_2') and FDRI from DGM and WM are presented in Tables 4.1 and 4.2 respectively. To compare to previous work, FDRI is divided by the field strength difference and demonstrates good agreement for the same age group with previous work (40) at 1.5 T and 3.0 T. The presumptive amount of iron deposits in DGM territories are also shown in Table 4.1, obtained from the previous post-mortem study of Hallgren and Sourander (5). For test-retest reliability, we found the intraclass correlation coefficients in the range of 0.928-0.995 for relaxation rates (R_2 , R_2^* and R_2') and FDRI measurements.

Table 4.1: Transverse relaxation rates (s^{-1}) and FDRI/ ΔB_0 (s^{-1}/T) in grey matter at 1.5 T and 4.7 T, with estimated iron deposits (mg/100g fresh wt.) from seventeen healthy subjects*

	Cortical GM	Thalamus	Caudate Nucleus	Putamen	Substantia Nigra	Red Nucleus	Globus Pallidus
R_2 (4.7 T)	13.8±3.4	18.2±1.1	16.6±0.8	19.3±1.4	24.4±1.1	22.4±1.1	26.0±2.9
R_2 (1.5 T)	10.6±1.2	12.7±0.6	11.7±0.47	12.7±0.7	14.7±0.8	13.6±0.7	14.7±1.4
R_2^* (4.7 T)	20.3±9.9	27.2±2.4	28.6±3.50	35.9±5.1	57.6±4.0	53.0±7.0	57.9±7.6
R_2^* (1.5 T)	12.7±2.9	17.1±0.8	15.8±0.81	18.0±2.2	25.9±3.4	23.1±2.8	24.9±3.3
R_2' (4.7 T)	6.5±1.0	8.9±2.4	12.1±3.66	16.6±2.4	33.2±4.1	30.6±3.4	31.9±3.9
R_2' (1.5 T)	2.1±1.1	4.5±0.9	4.1±0.84	5.3±1.3	11.1±3.2	9.4±2.6	10.3±2.9
FDRI/B_0	1.1±0.2	1.8±0.3	1.7±0.18	2.2±0.3	3.0±0.2	2.7±0.3	3.3±0.5
Tissue Iron⁺	2.7±0.3	5.4±0.7	8.0±0.5	10.9±2.0	18.5±3.9	19.5±4.1	20.4±2.7

* Values reported as inter-subject mean \pm standard deviation.

⁺Extrapolated iron content obtained using equations, plots or tables provided in Ref. (5) with estimates of variance therein for this age range.

Figure 4.1 illustrates R_2' and FDRI maps from a 32 year old healthy subject obtained at 1.5 T and 4.7 T, including the R_2 and R_2^* images (a-d) needed for these subtractive methods. Iron rich DGM at 4.7 T is better visualized than at 1.5 T.

Figure 4.2 provides an example of the effect of the linear background field correction used for R_2^* at 4.7 T. The strong effect of the frontal sinuses is clearly evident and the correction had the strongest effects near this region in frontal WM and caudate nucleus, which both had on average, ~22% reduction in R_2^* with correction. However, other DGM territories more distant from the frontal sinuses (thalamus, putamen, globus pallidus, substantia nigra and red nucleus) had only 4-7% reductions in average R_2^* at 4.7 T with the correction.

Table 4.2: Transverse relaxation rates (s^{-1}) and $FDRI/\Delta B_0$ (s^{-1}/T) in white matter at 1.5 T and 4.7 T, from seventeen healthy subjects*

	Frontal WM	Optic Radiation	Posterior IC	Centrum Semiovale	Splenium CC	Genu CC	Parietal WM
R_2 (4.7 T)	18.2±1.2	16.6±0.6	15.2±0.8	15.9±1.3	16.4±0.7	16.2±0.7	16.4±0.6
R_2 (1.5 T)	13.9±1.2	12.2±0.3	10.8±0.7	11.9±0.4	11.5±0.6	11.6±0.4	11.3±0.5
R_2^* (4.7 T)	30.5±3.1	31.4±2.4	24.2±0.9	25.3±1.0	29.6±1.9	28.1±1.9	25.5±1.4
R_2^* (1.5 T)	18.2±1.3	18.8±0.8	16.9±0.6	16.7±0.7	20.0±1.0	18.2±0.3	16.5±0.8
R_2' (4.7 T)	12.3±2.6	14.8±1.6	9.3±1.7	9.4±1.5	12.2±1.9	11.9±1.6	9.1±1.4
R_2' (1.5 T)	4.3±0.9	6.6±0.8	6.9±0.8	4.8±0.6	7.5±1.4	6.6±0.6	5.2±0.6
$FDRI/\Delta B_0$	1.5±0.1	1.4±0.2	1.3±0.2	1.3±0.1	1.3±0.3	1.4±0.2	1.5±0.2

*Values reported as inter-subject mean \pm standard deviation. WM, white matter; IC, internal capsule; CC, corpus callosum.

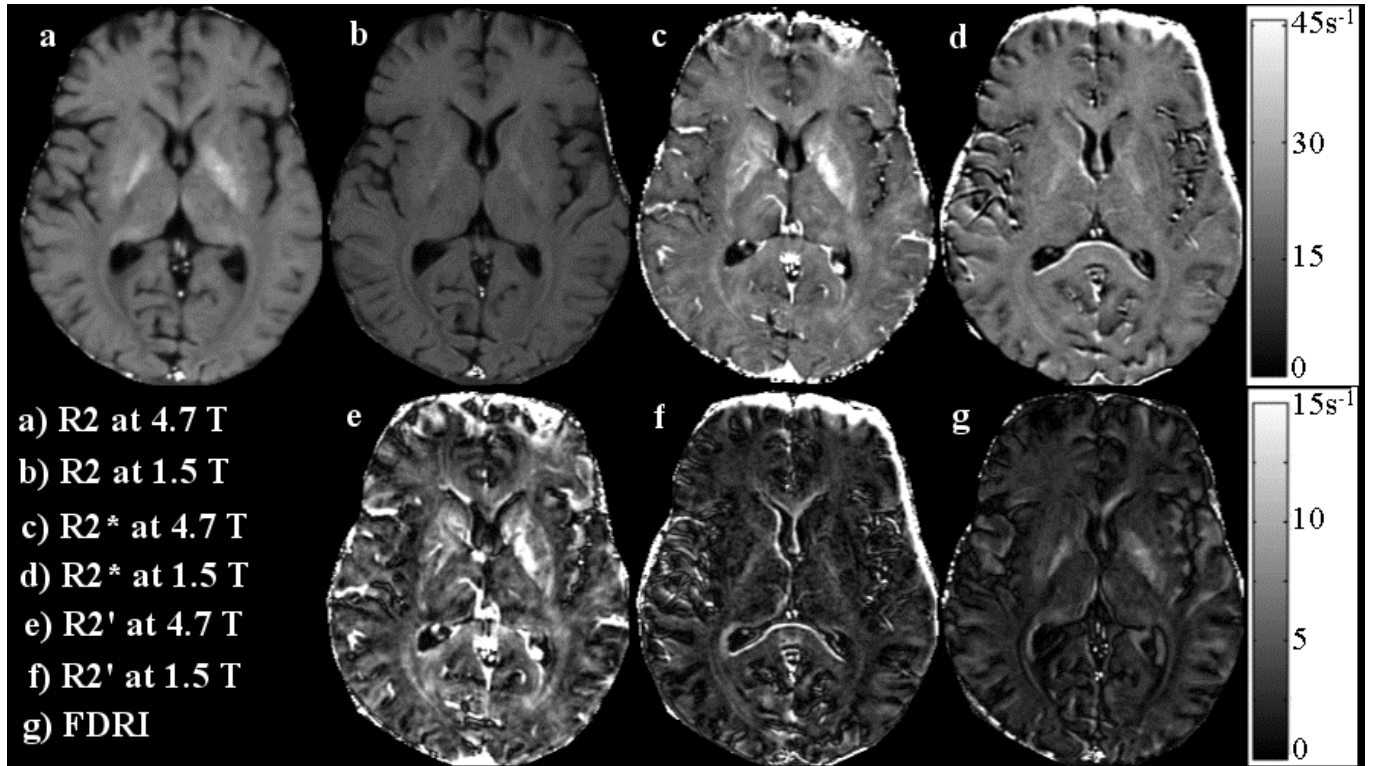


Figure 4.1: In-vivo transverse relaxation maps from 4.7 T and 1.5 T: (a, b) R_2 , (c, d) R_2^* , (e, f) R_2' , where (a, c, e) were acquired at 4.7 T and (b, d, f) at 1.5 T. FDRI, which is the R_2 difference between fields, is shown in (g). Intensity scales are shown at right for the top and bottom rows.

Transverse relaxation rates (R_2 , R_2^* , R_2') from eight brain regions (DGM and frontal WM) at 4.7 T and 1.5 T and FDRI are plotted against estimated regional non-heme iron [Fe] in Fig. 4.3. Solid lines are used to show the linear fitting considering all eight brain regions with slopes, intercepts and correlations reported for this solid line fit. R_2^* at 4.7 T is shown with background correction, which increased the slope and correlation by 3% and 8% respectively over uncorrected data. Dashed lines are for fits considering only the caudate, putamen and globus pallidus, with additional regression coefficients provided in Table 4.3. These three iron-rich territories are considered independently to enable comparison to past work (32), where only territories rich in iron and with exact age equations for iron content were used.

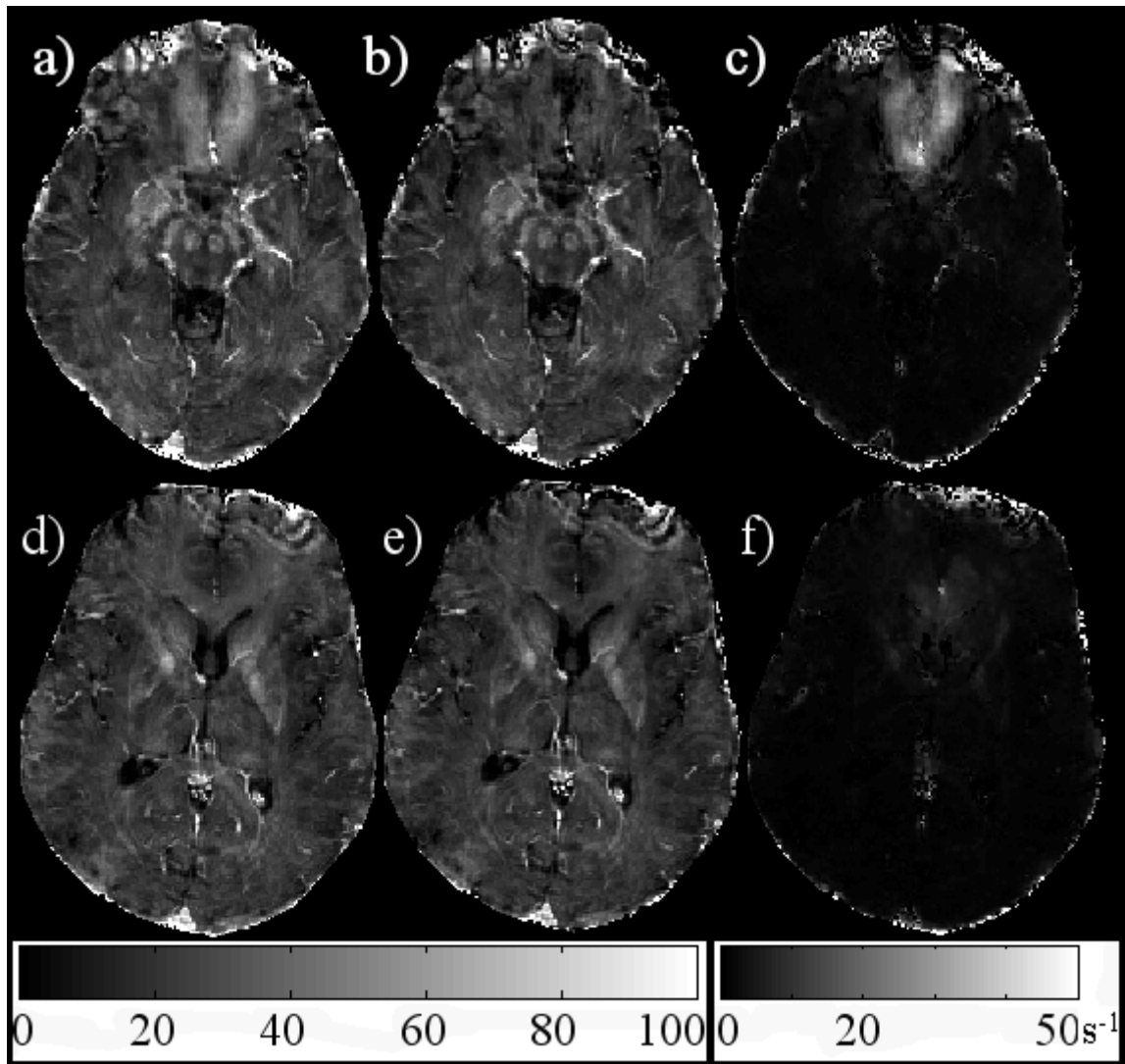


Figure 4.2: In-vivo R_2^* maps at 4.7 T showing the effect of linear background field correction. (a, d) R_2^* map without background field correction, (b, e) R_2^* after background field correction and (c, f) difference maps of (a, b) and (d, e). Intensity scale from 0 to 100 s^{-1} for (a, b, d, e), while 0 to 50 s^{-1} for (c, f). Note the strong air-tissue susceptibility gradient arising from tissue near the frontal sinuses.

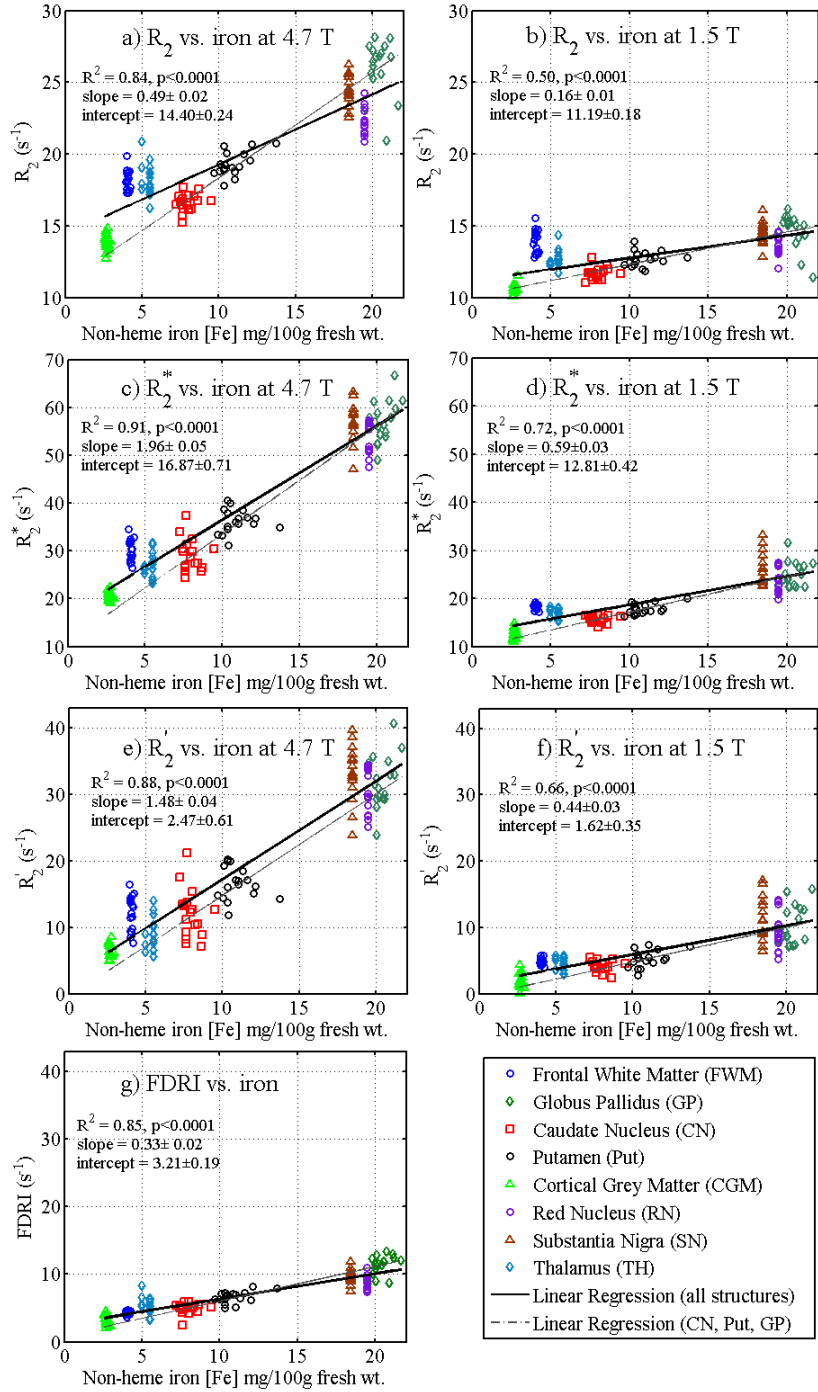


Figure 4.3: Scatter plots: Relaxation rates (R_2 , R_2^* and R_2') versus estimated post-mortem iron concentration [Fe]: (a,c,e) at 4.7 T; (b,d,f) at 1.5 T; and (g) FDRI versus [Fe]. Best fit solid lines and linear regression parameters obtained using all data are shown, while dashed lines fit only caudate, putamen and globus pallidus (with regression parameters in Table 4.3). Note three different y-axis scales are used for R_2 (a,b), R_2^* (c,d) and difference methods (e-g).

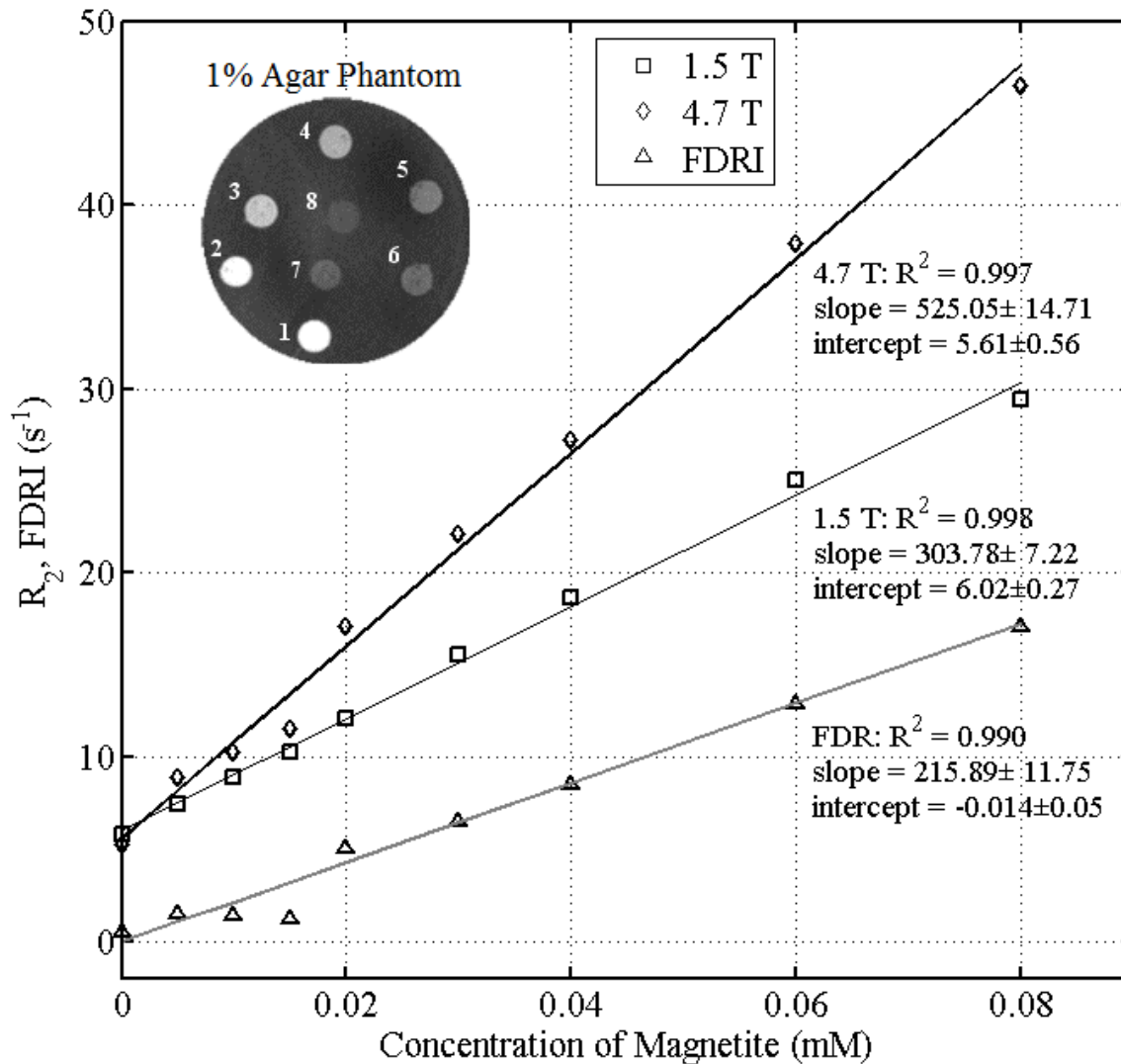


Figure 4.4: Relationship between magnetite concentrations, relaxation rate R_2 and FDR I for eight different concentrations of iron in 1% agar gel. Linear regression parameters and best fit lines are shown. An example R_2 map from 1.5 T is shown in the inset.

R_2 and R_2^* results in Fig. 4.3 indicate excellent performance at 4.7 T as evident from high correlations to iron, essentially matching those found in the best difference methods. R_2^* at 4.7 T provides highest correlation and slope with iron, but has a substantial intercept for zero iron concentration. Considering the transverse difference methods, both R_2' at 4.7 T and FDR I provide high correlation with iron, whereas R_2' at 1.5 T has similar slope to FDR I, but a reduced correlation. For all the measurements, p values were found less than 0.0001. Slope of the fitted line for R_2' was ~ 3 times greater at 4.7 T than 1.5 T indicating the linear field dependence from

ferritin-based relaxation (31). Compared to FDRI, R_2' at 4.7 T has a reduced y-intercept and slope ~ 4.5 times greater than FDRI, making R_2' at 4.7 T the preferred difference method.

Table 4.3: Slopes, y-intercepts and correlation at 1.5 T and 4.7 T obtained from caudate, putamen and globus pallidus*

Comparison	B_0 (T)	Slope ($s^{-1}/mg\ Fe/100\ g\ wt.$)	Y-Intercept (s^{-1})	Pearson correlation R^2
R_2 vs. [Fe]	4.7	0.73±0.03	11.01±0.48	0.88
	1.5	0.22±0.02	10.07±0.31	0.66
R_2^* vs. [Fe]	4.7	2.23±0.08	11.24±1.25	0.93
	1.5	0.74±0.04	9.76±0.59	0.86
R_2' vs. [Fe]	4.7	1.51±0.08	-0.23±1.25	0.89
	1.5	0.52±0.05	0.31±0.67	0.71
FDRI vs. [Fe]		0.51±0.03	0.93±0.37	0.88

*Linear regression analysis performed with post-mortem [Fe] as variable. Regression coefficients are given with standard errors and correlation significance $p < 0.001$.

Figure 4.4 illustrates the relationship between magnetite concentration, R_2 and FDRI from the agar phantom. At both field strengths R_2 varies linearly with iron concentration with subtraction yielding a negligible intercept for FDRI and maintaining the linear relationship with iron concentration. Very strong correlations ($R^2 = 0.99$, $p < 0.0001$) are found between iron concentrations and FDRI or R_2 at both field strengths.

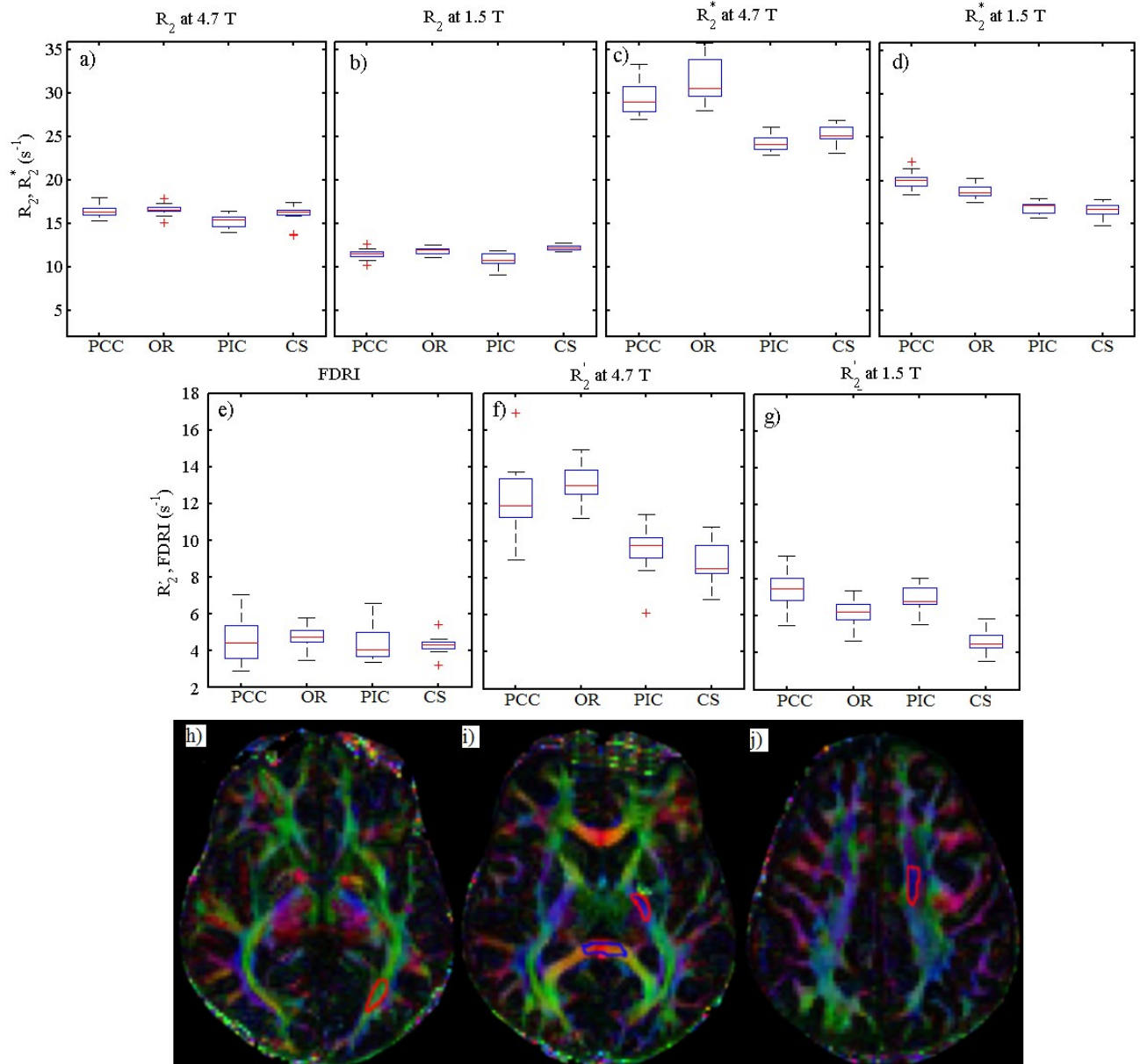


Figure 4.5: (a-g) Box plots of transverse relaxation rates (R_2 , R_2^* , R_2') and FDRI (s^{-1}) in WM from seventeen healthy subjects with fiber orientations predominantly perpendicular (posterior corpus callosum, PCC and Optic radiation, OR) or parallel (posterior internal capsule, PIC and centrum semiovale, CS) to the main magnetic field. Red plus signs in the plots are outliers. Fractional anisotropy color maps obtained at 4.7 T (h-j) from one subject showing WM ROIs and fiber directions: (h) OR (green, anterior-posterior), (i) PIC (blue, inferior-superior), PCC (red, left-right), and (j) CS (blue, inferior-superior). Note two different y-axis scales are used for R_2 , R_2^* (a-d) and difference methods (e-g).

Figure 4.5 compares relaxation rates and FDRI from ROIs drawn in WM structures where fiber tracts are predominantly parallel or perpendicular to B_0 . Fiber orientations of the posterior part of corpus callosum (PCC) and optic radiation (OR) are predominantly perpendicular to B_0 while posterior internal capsule (PIC) and centrum semiovale (CS) have fiber orientations parallel to B_0 . Diffusion tensor tractography images illustrate these locations (Fig. 4.5h-j). The FDRI values between parallel and perpendicular orientations are somewhat similar, with myelin differences likely accounting for differences. Specifically, FDRI increased by 9% ($p = 0.15$) in OR over CS, 3% ($p = 0.60$) increase in PCC relative to PIC, and 12% ($p = 0.95$) increase in OR over PIC. On the other hand, R_2' , particularly at 4.7 T, shows greater orientation dependence. R_2' is increased by an average 51% ($p < 0.0001$) in OR compared to CS at 4.7 T, with 32% ($p < 0.0001$) increase at 1.5 T. Moreover, PCC has R_2' with about 31% ($p < 0.0001$) increase relative to PIC at 4.7 T; and 8% ($p = 0.073$) at 1.5 T. Note PIC has highly compact fiber structures and higher myelin water fraction (~18%) compared to PCC (~13%) (2,21,62) and CS (~10%) (63). For R_2^* there was up to 24% ($p < 0.0001$) difference between the WM structures oriented parallel or perpendicular to B_0 while maximum variation was only 8% ($p < 0.05$) for R_2 measurements.

4.5 Discussion

Transverse relaxation rates and their differences within and across two field strengths were considered for iron measurements in human brain. In relation to estimated iron concentrations, R_2 , R_2^* and R_2' all exhibited higher coefficients of correlation and steeper slopes (2-5 times) at 4.7 T than at 1.5 T, confirming that higher field strengths provide superior sensitivity to iron. In iron-rich DGM, R_2' at 4.7 T, and FDRI yielded high correlations to estimates of non-heme iron concentration (Fig. 4.3, Table 4.3). The 4.7 T measurements of R_2 and R_2^* also provided similar high correlations with estimated iron, without the need for multiple relaxation measurements and subtraction. However, when considering the zero iron intercepts, which reveal iron independent components, the intercepts of R_2 and R_2^* were several times larger than that of R_2' and FDRI. Although iron induced relaxation rates increase with magnetic field, single field R_2 measurements cannot provide iron specificity in all tissues due to the water content/macromolecular fraction confound (31).

R_2' and FDRI should provide more specific iron measures in the brain. Compared to FDRI in DGM, 4.7 T R_2' provides similar correlations, with reduced y-intercepts and three-fold slope increase. Furthermore, R_2' offers this improved discrimination of iron content without the need for two field strengths. In general, the results from Table 4.3, which use the dashed lines from Fig. 4.3, are improved because only three structures with dominant iron contrast (globus pallidus, caudate, putamen) are considered. Negligible intercept of R_2' versus iron in Table 4.3 indicates a specific sensitivity to iron in DGM, while the FDRI intercept is much greater.

In our case, the field difference used for FDRI was 3.2 T - more than double that of past FDRI work (39,40). Increasing the field difference provides greater FDRI. Smaller field differences are clearly not as sensitive to iron. However, the macromolecular contribution to R_2 also has a field strength dependence which may serve as a confounder if higher field strength differences are used. Specifically, R_2 effects from macromolecular fraction have both field dependent and independent terms, with the field dependent term likely having quadratic dependence on field strength, with increasing prominence at magnetic fields greater than 7.0 T (31). Consequently, FDRI using higher field strengths and large field differences may not be suitable for iron quantification in the brain. FDRI measurements using field strengths differences of 1.0 or 1.5 T (0.5 T and 1.5 T, or 1.5 T and 3.0 T) have more stable macromolecular effects with field strength. Thus, FDRI using 1.5 and 4.7 T does not eliminate all the effects other than iron and has a substantial non-zero intercept versus the iron concentration fitting model. However, the *in-vitro* FDRI experiments (Fig. 4.4) had negligible intercept, because the effect of macromolecular fraction was minimal for the 1% agar phantom.

In WM, iron sensitivity measurement using MRI relaxometry is challenging due to the presence of increased macromolecular fraction and moderate to low iron concentration (31,32,51). WM contains increased myelin content compared to GM (21). Although variable, typically WM contains ~11% myelin water fraction compared to only ~3% of GM (21). Water trapped in myelin sheath has a short T_2 relaxation time of ~ 20 ms, making myelin water content a key factor in WM transverse relaxation (21). In particular, FDRI is able to remove most of the myelin effects to more closely reflect the true iron content. For example, in Fig. 4.3, for frontal WM, only FDRI values lie on the regression line, while all other methods have a higher relaxation rate for frontal WM than that of the regression line prediction. A previous study also showed that R_2 is not a reliable parameter for measuring iron in WM using a single field strength

(26). Unfortunately other WM territories were not included in the age based iron concentrations provided by Hallgren (5). As well, in cases of pathology, selective increases in water content — through for example neurodegeneration — could make FDRI more valuable by removing the variable water/macromolecular fraction confound. FDRI is also advantageous over R_2' due to complete use of spin echo refocusing, eliminating concern over static field effects arising from air-tissue interfaces.

An additional confound of transverse relaxation measures in WM is fiber orientation with respect to B_0 . R_2^* and R_2' show angular dependency as a function of the angle between the WM fiber orientation and B_0 (51,64). Higher R_2' and R_2^* values were observed in WM with fiber orientation predominantly perpendicular to the main magnetic field compared to that of parallel fiber orientation. This effect increased at 4.7 T over 1.5 T where WM structures with both perpendicular orientation relative to main magnetic field and higher myelin water fraction have greatest increases. This WM orientation dependence on B_0 has been shown previously and is an area of active investigation: Sati *et al.* in marmosets at 7.0 T found up to 50% R_2^* changes (64); Denk *et al.* in human brain at 3.0 T demonstrated 20% R_2^* changes (51); Sedlacik *et al.* in human brain at 3.0 T found ~15% R_2' increase (32). Refocusing the static field minimizes the dependency on B_0 orientation, thus FDRI and R_2 exhibit reduced effect. For iron measurements in WM, increased myelin water fraction over GM, and the presence of fiber anisotropy lead to additional confounds. R_2' at high magnetic field is more highly sensitive to these factors compared to FDRI.

Both R_2' and FDRI require spin echo R_2 maps which were performed in multi-slice acquisitions to enable more complete brain coverage. We also performed single-slice spin echo mapping and obtained very similar correlations (not shown). At 4.7 T, the multi-slice multiple spin echo train was constrained to 5 echoes to achieve more slices within RF heating limitations. Previous work using stimulated echo compensation (65) indicates that echo trains as short as four can provide accurate R_2 values for DGM when using 10 ms echo spacing as used here. Multi-slice imaging led to global signal reduction from incidental magnetization transfer; however this did not affect R_2 (65). Previous FDRI measurements (30,39,41) used exponential fitting which can overestimate T_2 ($1/R_2$) values when the refocusing angles are not precisely 180° (38), which is expected in the case of slice selective pulses unless refocusing profile widths are extremely wide in comparison to excitation profile or adiabatic refocusing is used (31,66).

There were several limitations of this study. Our sample size was relatively small. For each relaxation method, different in plane resolution was used since spin echo experiments are much slower. Different RF pulse shapes were used for R_2 , but this was corrected by stimulated echo compensation. Background gradient field correction was not available for the R_2^* sequence at 1.5 T, however since background inhomogeneity effects increase linearly with field strength, the effect at 1.5 T should be very small compared to that of at 4.7 T. For the FDRI measurements, two field strength measures are needed, which may have led to subtle positioning errors. However, In spite of these limitations, precise image subtraction was still possible by matching image resolution and slice thickness at the post-processing stage and using manual image registration. Using the age based equations provided in Hallgren's paper, regression analysis was performed for iron-rich GM, but only for frontal WM. Deoxygenated heme iron is another confounding factor that modulates R_2^* and R_2' . However, the contributions from deoxygenated hemoglobin in non-heme-iron-laden DGM territories are assumed to be negligible (23). Iron concentrations were estimated using different subjects based on the landmark post-mortem study published in 1958 (5). Though iron distributions in human brain may have changed since that time over due to changes in life style and diet, recent studies have found similar results using post-mortem study (8,26). In addition, as mentioned earlier, several other studies (2,14,20,24,25,28-31,39-43,59-61) have used the age-based equations reported by Hallgren and Sourander for brain iron estimation.

In conclusion, high correlations to brain iron content were achieved with all 4.7 T methods and with FDRI. The transverse relaxation difference methods R_2' at 4.7 T and FDRI had high correlations similar to R_2 and R_2^* at 4.7 T. FDRI was found ineffective at eliminating all non-iron contributions, due to the field strength dependence of macromolecular fraction for this large field strength difference of 3.2 T. R_2' at 4.7 T had the smallest y-intercept with estimated iron concentration, suggesting greater iron specificity over all methods including FDRI. However, in WM R_2' demonstrated the strongest dependence on fiber orientation with respect to B_0 , presenting an additional confound. These results suggest that for brain iron correlation, there is minimal value of transverse difference methods over a single R_2^* measurement at highest available field, which was 4.7 T in this study.

4.6 Acknowledgements

This work was supported by grants from the Canadian Institutes of Health Research (CIHR) and the Natural Sciences and Engineering Research Council of Canada (NSERC).

4.7 References

1. Williams R, Buchheit CL, Berman NEJ, LeVine SM. Pathogenic implications of iron accumulation in multiple sclerosis. *Journal of Neurochemistry* 2012;120(1):7-25.
2. Haacke EM, Chengb NYC, House MJ, Liu Q, Neelavalli J, Ogg RJ, Khan A, Ayaz M, Kirsch W, Obenaus A. Imaging iron stores in the brain using magnetic resonance imaging. *Magnetic Resonance Imaging* 2005;23(1):1-25.
3. Zecca L, Youdim MB, Riederer P, Connor JR, Crichton RR. Iron, brain ageing and neurodegenerative disorders. *Nature reviews Neuroscience* 2004;5(11):863-873.
4. Gossuin Y, Muller RN, Gillis P. Relaxation induced by ferritin: a better understanding for an improved MRI iron quantification. *NMR in Biomedicine* 2004;17(7):427-432.
5. Hallgren B, Sourander P. The effect of age on the non-haemin iron in the human brain. *Journal of Neurochemistry* 1958;3(1):41-51.
6. Lebel RM, Eissa A, Seres P, Blevins G, Wilman AH. Quantitative high-field imaging of sub-cortical gray matter in multiple sclerosis. *Multiple Sclerosis Journal* 2012;18(4):433-441.
7. Schenck JF, Zimmerman EA. High-field magnetic resonance imaging of brain iron: birth of a biomarker? *NMR in Biomedicine* 2004;17(7):433-445.
8. Langkammer C, Krebs N, Goessler W, Scheurer E, Ebner F, Yen K, Fazekas F, Ropele S. Quantitative MR imaging of brain iron: a postmortem validation study. *Radiology* 2010;257(2):455-462.
9. Birkl C, Langkammer C, Krenn H, Goessler W, Ernst C, Haybaeck J, Stollberger R, Fazekas F, Ropele S. Iron mapping using the temperature dependency of the magnetic susceptibility. *Magnetic Resonance in Medicine* 2015;73(3):1282-1288.

10. Drayer B, Burger P, Darwin R, Riederer S, Herfkens R, Johnson G. MRI of brain iron. *American Journal of Roentgenology* 1986;147(1):103-110.
11. Berg D, Youdim MBH. Role of iron in neurodegenerative disorders. *Topics in Magnetic Resonance Imaging* 2006;17(1):5-17.
12. Bizzi A, Brooks RA, Brunetti A, Hill JM, Alger JR, Miletich RS, Francavilla TL, Dichiro G. Role of iron and ferritin in MR Imaging of the brain - a study in primates at different field strengths. *Radiology* 1990;177(1):59-65.
13. Vymazal J, Zak O, Bulte JWM, Aisen P, Brooks RA. T1 and T2 of ferritin solutions: Effect of loading factor. *Magnetic Resonance in Medicine* 1996;36(1):61-65.
14. Vymazal J, Righini A, Brooks RA, Canesi M, Mariani C, Leonardi M, Pezzoli G. T1 and T2 in the brain of healthy subjects, patients with Parkinson disease, and patients with multiple system atrophy: Relation to iron content. *Radiology* 1999;211(2):489-495.
15. Drayer B, Burger P, Hurwitz B, Dawson D, Cain J. Reduced signal intensity on MR images of thalamus and putamen in multiple sclerosis: increased iron content? *American Journal of Roentgenology* 1987;149(2):357-363.
16. Ordidge RJ, Gorell JM, Deniau JC, Knight RA, Helpert JA. Assessment of relative brain iron concentrations using T2-weighted and T2*-weighted MRI at 3 Tesla. *Magnetic Resonance in Medicine* 1994;32(3):335-341.
17. Graham JM, Paley MNJ, Grunewald RA, Hoggard N, Griffiths PD. Brain iron deposition in Parkinson's disease imaged using the PRIME magnetic resonance sequence. *Brain* 2000;123:2423-2431.
18. Wallis LI, Paley MNJ, Graham JM, Grunewald RA, Wignall EL, Joy HM, Griffiths PD. MRI Assessment of Basal Ganglia Iron Deposition in Parkinson's Disease. *Journal of Magnetic Resonance Imaging* 2008;28(5):1061-1067.
19. Duyn JH, Van Gelderen P, Li TQ, De Zwart JA, Koretsky AP, Fukunaga M. High-field MRI of brain cortical substructure based on signal phase. *Proceedings of the National Academy of Sciences* 2007;104(28):11796-11801.

20. Hikita T, Abe K, Sakoda S, Tanaka H, Murase K, Fujita N. Determination of transverse relaxation rate for estimating iron deposits in central nervous system. *Neuroscience Research* 2005;51(1):67-71.
21. Whittall KP, MacKay AL, Graeb DA, Nugent RA, Li DKB, Paty DW. In vivo measurement of T2 distributions and water contents in normal human brain. *Magnetic Resonance in Medicine* 1997;37(1):34-43.
22. Sati P, van Gelderen P, Silva AC, Reich DS, Merkle H, de Zwart JA, Duyn JH. Micro-compartment specific T2* relaxation in the brain. *Neuroimage* 2013;77:268-278.
23. Sedlacik J, Kutschbach C, Rauscher A, Deistung A, Reichenbach JR. Investigation of the influence of carbon dioxide concentrations on cerebral physiology by susceptibility-weighted magnetic resonance imaging (SWI). *Neuroimage* 2008;43(1):36-43.
24. Li TQ, Yao B, van Gelderen P, Merkle H, Dodd S, Talagala L, Koretsky AP, Duyn J. Characterization of T2* Heterogeneity in Human Brain White Matter. *Magnetic Resonance in Medicine* 2009;62(6):1652-1657.
25. Bartzokis G, Sultzer D, Cummings J, Holt LE, Hance DB, Henderson VW, Mintz J. In vivo evaluation of brain iron in Alzheimer disease using magnetic resonance imaging. *Archives of General Psychiatry* 2000;57(1):47-53.
26. Langkammer C, Krebs N, Goessler W, Scheurer E, Yen K, Fazekas F, Ropele S. Susceptibility induced gray-white matter MRI contrast in the human brain. *Neuroimage* 2012;59(2):1413-1419.
27. Schenker C, Meier D, Wichmann W, Boesiger P, Valavanis A. Age Distribution And Iron Dependency Of The T2 Relaxation Time In The Globus-Pallidus And Putamen. *Neuroradiology* 1993;35(2):119-124.
28. Gelman N, Gorell JM, Barker PB, Savage RM, Spickler EM, Windham JP, Knight RA. MR imaging of human brain at 3.0 T: preliminary report on transverse relaxation rates and relation to estimated iron content. *Radiology* 1999;210(3):759-767.
29. Bartzokis G, Tishler TA, Lu PH, Villablanca P, Altshuler LL, Carter M, Huang D, Edwards N, Mintz J. Brain ferritin iron may influence age- and gender-related risks of neurodegeneration. *Neurobiology of Aging* 2007;28(3):414-423.

30. Hasan KM, Walimuni IS, Kramer LA, Narayana PA. Human brain iron mapping using atlas-based T2 relaxometry. *Magnetic Resonance in Medicine* 2012;67(3):731-739.
31. Mitsumori F, Watanabe H, Takaya N, Garwood M, Auerbach EJ, Michaeli S, Mangia S. Toward understanding transverse relaxation in human brain through its field dependence. *Magnetic Resonance in Medicine* 2012;68(3):947-953.
32. Sedlacik J, Boelmans K, Lobel U, Holst B, Siemonsen S, Fiehler J. Reversible, irreversible and effective transverse relaxation rates in normal aging brain at 3T. *Neuroimage* 2014;84:1032-1041.
33. Vymazal J, Brooks RA, Zak O, McRill C, Shen C, Dichiro G. T1 and T2 of ferritin at different field strengths -effect on MRI. *Magnetic Resonance in Medicine* 1992;27(2):368-374.
34. Yablonskiy DA, Haacke EM. Theory Of Nmr Signal Behavior In Magnetically Inhomogeneous Tissues - The Static Dephasing Regime. *Magnetic Resonance in Medicine* 1994;32(6):749-763.
35. Jensen JH, Chandra R. Strong field behavior of the NMR signal from magnetically heterogeneous tissues. *Magnetic Resonance in Medicine* 2000;43(2):226-236.
36. Reichenbach JR, Venkatesan R, Yablonskiy DA, Thompson MR, Lai S, Haacke EM. Theory and application of static field inhomogeneity effects in gradient-echo imaging. *Journal of Magnetic Resonance Imaging* 1997;7(2):266-279.
37. Fernandez-Seara MA, Wehrli FW. Postprocessing technique to correct for background gradients in image-based R2* measurements. *Magnetic Resonance in Medicine* 2000;44(3):358-366.
38. Lebel RM, Wilman AH. Transverse relaxometry with stimulated echo compensation. *Magnetic Resonance in Medicine* 2010;64(4):1005-1014.
39. Bartzokis G, Aravagiri M, Oldendorf WH, Mintz J, Marder SR. Field dependent transverse relaxation rate increase may be a specific measure of tissue iron stores. *Magnetic Resonance in Medicine* 1993;29(4):459-464.

40. Pfefferbaum A, Adalsteinsson E, Rohlfing T, Sullivan EV. MRI estimates of brain iron concentration in normal aging: comparison of field-dependent (FDRI) and phase (SWI) methods. *Neuroimage* 2009;47(2):493-500.
41. Sullivan EV, Adalsteinsson E, Rohlfing T, Pfefferbaum A. Relevance of Iron Deposition in Deep Gray Matter Brain Structures to Cognitive and Motor Performance in Healthy Elderly Men and Women: Exploratory Findings. *Brain Imaging and Behavior* 2009;3(2):167-175.
42. Bartzokis G, Tishler TA. MRI evaluation of basal ganglia ferritin iron and neurotoxicity in Alzheimer's and Huntington's disease. *Cellular and Molecular Biology* 2000;46(4):821-833.
43. Bartzokis G, Beckson M, Hance DB, Marx P, Foster JA, Marder SR. MR evaluation of age-related increase of brain iron in young adult and older normal males. *Magnetic Resonance Imaging* 1997;15(1):29-35.
44. Graham SJ, Stanchev PL, Bronskill MJ. Criteria for analysis of multicomponent tissue T2 relaxation data. *Magnetic Resonance in Medicine* 1996;35(3):370-378.
45. Paling D, Tozer D, Wheeler-Kingshott C, Kapoor R, Miller DH, Golay X. Reduced R2' in multiple sclerosis normal appearing white matter and lesions may reflect decreased myelin and iron content. *Journal of Neurology Neurosurgery and Psychiatry* 2012;83(8):785-792.
46. MacKay AL, Vavasour IM, Rauscher A, Kolind SH, Maedler B, Moore GRW, Traboulsee AL, Li DKB, Laule C. MR Relaxation in Multiple Sclerosis. *Neuroimaging Clinics of North America* 2009;19(1):1-26.
47. Connor JR, Snyder BS, Beard JL, Fine RE, Mufson EJ. Regional distribution of iron and iron-regulatory proteins in the brain in aging and Alzheimer's disease. *Journal of Neuroscience Research* 1992;31(2):327-335.
48. Curnes JT, Burger PC, Djang WT, Boyko OB. MR Imaging of compact white matter pathways. *American Journal of Neuroradiology* 1988;9(6):1061-1068.
49. Duyn J. MR susceptibility imaging. *Journal of Magnetic Resonance* 2013;229:198-207.

50. Li TQ, van Gelderen P, Merkle H, Talagala L, Koretsky AP, Duyn J. Extensive heterogeneity in white matter intensity in high-resolution T2*-weighted MRI of the human brain at 7.0 T. *Neuroimage* 2006;32(3):1032-1040.
51. Denk C, Hernandez Torres E, MacKay A, Rauscher A. The influence of white matter fibre orientation on MR signal phase and decay. *NMR in Biomedicine* 2011;24(3):246-252.
52. Rudko DA, Klassen LM, de Chickera SN, Gati JS, Dekaban GA, Menon RS. Origins of R2* orientation dependence in gray and white matter. *Proceedings of the National Academy of Sciences of the United States of America* 2014;111(1):E159-E167.
53. Grohn HI, Michaeli S, Garwood M, Kauppinen RA, Grohn OHJ. Quantitative T1p and adiabatic Carr-Purcell T2 magnetic resonance imaging of human occipital lobe at 4 T. *Magnetic Resonance in Medicine* 2005;54(1):14-19.
54. Carmichael DW, Thomas DL, De Vita E, Fernandez-Seara MA, Chhina N, Cooper M, Sunderland C, Randell C, Turner R, Ordidge RJ. Improving whole brain structural MRI at 4.7 Tesla using 4 irregularly shaped receiver coils. *Neuroimage* 2006;32(3):1176-1184.
55. Hennig J. Multiecho Imaging Sequences With Low Refocusing Flip Angles. *Journal of Magnetic Resonance* 1988;78(3):397-407.
56. Lebel RM, Wilman AH. Field-corrected 3D multiecho gradient echo: Simultaneous extraction of quantitative R2*, T2* weighting, SWI, and venography. *Joint Annual Meeting of ISMRM-ESMRMB*. Stockholm, Sweden; 2010. p 5002.
57. Smith SM. Fast robust automated brain extraction. *Hum Brain Mapp* 2002;17(3):143-155.
58. Rasband W. *ImageJ*. US National Institutes of Health, Bethesda, Maryland, USA; 1997-2011.
59. Peran P, Cherubini A, Luccichenti G, Hagberg G, Demonet JF, Rascol O, Celsis P, Caltagirone C, Spalletta G, Sabatini U. Volume and Iron Content in Basal Ganglia and Thalamus. *Hum Brain Mapp* 2009;30(8):2667-2675.

60. Gelman N, Ewing JR, Gorell JM, Spickler EM, Solomon EG. Interregional variation of longitudinal relaxation rates in human brain at 3.0 T: Relation to estimated iron and water contents. *Magnetic Resonance in Medicine* 2001;45(1):71-79.
61. Poynton C, Jenkinson M, Adalsteinsson E, Sullivan EV, Pfefferbaum A, Wells W. Quantitative Susceptibility Mapping by Inversion of a Perturbation Field Model: Correlation with Brain Iron in Normal Aging. *IEEE Transactions On Medical Imaging* 2015;34(1):339-353.
62. Vavasour IM, Whittall KP, MacKay AL, Li DKB, Vorobeychik G, Paty DW. A comparison between magnetization transfer ratios and myelin water percentages in normals and multiple sclerosis patients. *Magnetic Resonance in Medicine* 1998;40(5):763-768.
63. Levesque IR, Chia CLL, Pike GB. Reproducibility of In Vivo Magnetic Resonance Imaging-Based Measurement of Myelin Water. *Journal of Magnetic Resonance Imaging* 2010;32(1):60-68.
64. Sati P, Silva AC, van Gelderen P, Gaitan MI, Wohler JE, Jacobson S, Duyn JH, Reich DS. In vivo quantification of T2* anisotropy in white matter fibers in marmoset monkeys. *Neuroimage* 2012;59(2):979-985.
65. Uddin MN, Lebel RM, Wilman AH. Transverse Relaxometry with Reduced Echo Train Lengths via Stimulated Echo Compensation. *Magnetic Resonance in Medicine* 2013;70(5):1340-1346.
66. Jones C, Xiang Q, Whittall K, MacKay A. Calculating T2 and B1 from decay curves collected with non-180 refocusing pulses. *Proceedings of 11th Annual Meeting, International Society for Magnetic Resonance in Medicine*; 2003. p 1018.

Chapter 5. Quantitative T₂ and atrophy in multiple sclerosis: A retrospective 7-year feasibility study using standard clinical brain images⁴

5.1 Abstract

Objective: To examine 7-year changes in multiple sclerosis (MS) brain using only standard clinical images to determine quantitative transverse relaxation times (T₂) and atrophy.

Methods: 1.5 tesla clinical MRI exams of 14 relapsing-remitting MS subjects with scans extending back 7 years were examined retrospectively. T₂ maps were obtained using a two-point modelling approach using proton density (PD) and T₂-weighted spin echo images and accounting for the actual refocusing angles used which varied between 180 and 150°. T₂ methods were validated prospectively in 7 healthy subjects. Patient T₂ values were correlated with brain atrophy, T₂ lesion load, expanded disability status scale (EDSS) and MS severity score (MSSS).

Results: Over 7 years, significant T₂ changes of 2-4% were observed when using T₂ modelling but no significant results were found when using the commonly misused standard exponential fit, which cannot account for refocusing angle variation. Multiple regression of change in T₂ of two deep grey matter structures (head of caudate and globus pallidus) showed high correlation with final time point MSSS (r=0.76, p <0.05), and EDSS (r=0.70, p<0.05). Changes in T₂ in globus pallidus and posterior internal capsule showed correlations with change in EDSS score over time. 7-year changes in thalamic T₂ correlated with ventricular atrophy (r=-0.57, p<0.05).

⁴ A version of this section has been submitted to Journal of Magnetic Resonance Imaging, Uddin MN, McPhee KC, Wilman AH. Quantitative T₂ and atrophy in multiple sclerosis: A retrospective 7-year feasibility study using standard clinical brain images.

Conclusions: Standard clinical MS MRI exams that include PD and T₂-weighted imaging can provide quantitative T₂ to track MS disease progression. This provides an additional quantitative parameter that can be extracted from standard exams, provided the effects of actual flip angles are considered.

5.2 Introduction

Multiple sclerosis (MS) is a chronic neurological condition characterised by inflammation, demyelination, remyelination, oligodendrocyte destruction, neuronal degeneration as well as increased tissue iron accumulation (1,2). The etiology of the disease is still elusive and the variability of the disease course is noticeable among individuals. Though MS is thought to be primarily a white matter (WM) disease, there is significant involvement of deep grey matter (DGM) in the disease processes, especially through atrophy (3-5) and abnormal iron accumulation (6-8). MRI methods have a crucial role in predicting and monitoring the disease state and progression over time. Several studies have shown significant correlations between MRI measures and cognitive impairment, and disability scores (6-10).

MRI relaxometry techniques can provide more insight into the MS disease processes due to the sensitivity of relaxation times (T₁ or T₂) to changes in tissue water, myelin and iron content. These methods have been used to quantify myelin water fraction and water content in WM in MS (11-13). Qualitative T₂ weighting has been used to interpret DGM in MS disease processes by measuring the T₂ hypointensity or visual grading of the images in clinical MRI exams (10,14). However, quantitative T₂ measurements may provide more sensitive and accurate assessment by reducing the variability produced from receiver gain or flip angle variation in T₂ weighted images obtained in different time points for different subjects. Although other methods exist, such as DESPOT2 (15), quantitative T₂ measurements are usually performed by using a multi-echo spin echo (MESE) sequence, however, MESE sequences are not typically used in standard clinical exams. Proton density (PD) and T₂-weighted fast spin echo (FSE) images have been a common part of MS clinical trials and MS clinical protocols for many years, although PD images are now seeing less use in standard brain protocols. These images enable a two-point T₂ fitting method. T₂ fitting typically uses either exponential or actual signal modelling such as stimulated echo compensation (16,17). Exponential fitting is appropriate only in the case of ideal 180° refocusing pulses without slice profile effects or in-plane pulse variation. This situation is

relatively rare, causing exponential fitting to typically provide overestimated T_2 values as it does not take into account actual refocusing angles which can produce stimulated and indirect echoes that also influence the decay (16,18). Accurate two-point T_2 fitting from PD and T_2 -weighted images has recently been introduced (18) by accounting for the actual refocusing angles used in the PD and T_2 -weighted sequences. As well as quantitative T_2 , clinical images can also provide lesion load and brain volume measures.

The purpose of this study is to investigate the feasibility of tracking disease progression and state in relapsing-remitting MS (RRMS) over 7 years using retrospective standard clinical MRI obtained at 1.5 T, from which quantitative T_2 , brain volume and lesion load changes are derived.

5.3 Methods

5.3.1 Subjects

We identified 14 patients (12 female and 2 male; mean age at baseline 36 years, range 30 to 51 years) having clinically confirmed RRMS using the revised McDonald criteria (19). Ethical approval and informed consent was obtained according to institutional regulations. As part of standard clinical care, the patients identified had undergone MRI at baseline and 5 to 8 years follow-up scans between September 2004 and June 2013. The Expanded Disability Status Scale (EDSS) score was measured by an MS neurologist at baseline and at follow-up scans. The MS Severity Score (MSSS) was calculated from EDSS and disease duration using MSSStest software (20), thus MSSS represents an adjusted EDSS score for disease duration.

5.3.2 MRI data acquisition

All subjects were scanned using 1.5 T whole-body MRI systems (Sonata or Avanto; Siemens Healthcare, Erlangen, Germany). The clinical protocol consisted of PD and T_2 w Fast Spin Echo (FSE) sequences, which were used to retrospectively calculate T_2 . The protocol also included T_1 -weighted images used for brain volume calculations and T_2 w Fluid Attenuated Inversion Recovery (FLAIR) used for lesion load. All sequences used 19 slices with 5 mm thickness and in-plane resolution of $0.45 \times 0.45 \text{ mm}^2$ covering the whole brain. Typical sequence parameters included: PD-weighted FSE (repetition time [TR] 2000 ms, echo spacing [ESP] 6.5 ms, echo train length [ETL] 5, echo time [TE] 13 ms, refocusing flip angles 180° , bandwidth [BW] 195

Hz/Pixel, imaging matrix 384×512, N_{av} 2, scan time 1.8 min) and T₂w FSE (TR 4000 ms, ESP 6.5 ms, ETL 15, TE 91 ms, refocusing flip angles 180°, BW 195 Hz/Pixel, imaging matrix 384×512, N_{av} 2, scan time 1.9 min). 3-lobe Gaussian-filtered sinc pulses were used with time duration of 2.56 ms for both excitation and refocusing. Some patient datasets used PD and T₂w sequences with refocusing flip angles 150° rather than 180°. We defined the FSE pulse sequences into two types depending on flip angles: FSE180° (90x-180y-180y-180y....) and FSE150° (90x-165y-150y-150y....). The FLAIR sequence consisted of (2D sagittal, inversion time [TI] 2500 ms, TR 8500 ms, ETL 19, TE 111 ms, BW 130 Hz/Pixel, imaging matrix 512×512, scan time 3.68 min); and the T₁-weighted sequence (2D sagittal, TR 444 ms, TE 14 ms, BW 120 Hz/Pixel, imaging matrix 512×512, scan time 3.31 min).

Table 5.1: Patients demographic and clinical data

Variable	Patients
Number of participants	14
Gender, F/M	12/2
Overall Age (years)	35.95 ±6.69
Time to MRI follow-up (years)	7.03±0.99
Baseline disease duration (years) ^{†*}	2.08±2.15
Follow-up disease duration (years) ^{†*}	9.00±2.56
Baseline EDSS score ^{‡*}	2.38±0.57
Follow-up EDSS score ^{‡*}	2.96±0.86
Baseline MSSS [*]	4.37±2.38
Follow-up MSSS [*]	4.31±2.26

Note: data are means ± standard deviation for patients with MS; EDSS: Expanded Disability Status Scale; MSSS: Multiple Sclerosis Severity Score; [†]Disease duration range: 0-14 years; [‡]EDSS range: 1.5 – 4; ^{*}12 patients were included as EDSS score from two of them were unavailable.

Table 5.2: Patients morphologic data

Volume (cm ³)	Baseline	Follow-up	PC	ES
Whole brain volume	1535.0±184.2	1478.8±203.3	-3.66	<i>0.14</i>
WM volume	822.1±58.9	793.7±72.0	-3.43	0.21
GM volume	716.6±77.5	683.8±89.6	-4.71	<i>0.19</i>
Cortical GM volume	580.0±79.0	550.7±66.9	-4.76	<i>0.20</i>
Ventricular volume	31.2±5.6	34.2±5.7	10.27	<i>-0.17</i>
T ₂ lesion load	30.3±13.4	33.9±14.8	16.04	-0.79

Note: data are means \pm standard deviation; PC: Percent change; ES: effect size; GM: grey matter; WM: white matter; Volumes are normalized relative to whole head volume; Italic bold-faced values are significant with $p < 0.05$; p-values are obtained using paired sample t-test.

5.3.3 T₂ mapping

T₂ maps were computed on a pixel-by-pixel basis by modelling the spin response using the PD and T₂-weighted image, and knowledge of the refocusing flip angles (18). This method extracts T₂ from the spin response from all echo pathways providing Indirect and Stimulated Echo Compensation (ISEC). The flip angles and pulse shapes required for modelling were known, and the variation across the brain was determined through a prospective volunteer validation study. For comparison, T₂ maps were also obtained directly from the PD and T₂-weighted images using standard exponential fitting.

5.3.4 Method Validation

To validate the T₂ fitting method used, 7 healthy controls (5 male and 2 female; mean age 28 years, range 21 to 39 years) were recruited with the inclusion criteria that they had to be free of any neurological disorders or cognitive impairment. For these subjects, the same PD and T₂-weighted sequences used in the retrospective patient study were performed as well as additional PD sequences, flip angle maps and multiecho spin echo sequences to validate the T₂ fitting method.

Flip angle maps were acquired to determine the flip angle profiles across the brain and the variability of the profile between subjects. The double angle method (20) was used with correction for slice profile effects (18). We obtained two spin-echo echo planar images with

excitation angles 60° and 120° , both having same scan parameters: TR 7050 ms, TE 40 ms, BW 1630 Hz/Pixel, imaging matrix 128×128 ; FOV 240×240 mm², slice thickness 2 mm, and scan time 7 sec. Normalized flip angle maps were median filtered with 5×5 pixel filter after performing co-registration of the images using MATLAB prior to using for T_2 fitting. In addition, two dimensional multiecho spin echo (MESE) sequences were used to calculate reference T_2 values. The MESE sequence had the following scan parameters: TR 4000 ms, ESP 12.4 ms, ETL 15, TE 12.4 ms, excitation 90° and refocusing 180° , BW 195 Hz/Pixel, N_{av} 2, scan time 6.15 min.

Table 5.3: Transverse relaxation times (T_2) in ms obtained from seven healthy controls using MESE via ISEC, two- point ISEC and two-point exponential fitting

	Head of Caudate	Putamen	Globus pallidus	Thalamus	Substantia nigra	Red nucleus	Frontal WM
Flip angles (α_R) [†]	187.8±1.6	190.2±2.1	192.2±2.5	191.9±2.9	194.9±1.9	194.9±2.4	188.4±3.4
MESE	81.6±0.7	73.5±1.2	61.6±1.3	75.1±0.8	66.7±2.7	70.2±1.0	71.3±1.6
FSE180°	80.9±3.1	72.7±2.1	58.7±3.6	71.0±1.4	63.5±2.3	65.5±1.0	64.8±0.9
FSE150°	82.7±2.4	72.8±1.6	59.8±4.0	71.6±2.6	62.6±2.2	64.8±1.2	64.8±1.9
Exponential	98.3±8.4	87.6±5.2	70.8±5.2	90.1±4.7	76.9±4.5	77.7±3.1	82.2±3.4

Note: data are means \pm standard deviation over healthy subjects. [†] Flip angles in degrees obtained using 180° refocusing pulses. ISEC: Indirect and stimulated echo compensation; MESE: multiecho spin echo; T_2 obtained from two-point ISEC method with FSE180⁰ or FSE150⁰ refocusing pulses with the input of normalized flip angle map averaged over seven healthy volunteers.

Although matched TR and ETL is preferred, the retrospective patient data for PD and T_2 -weighted spin echo images had different TR and ETL (FSE180°: TR 2000 ms and ETL 5 for PD while TR 4000 ms and ETL 15 for T_2 -weighted images; FSE150°: TR 2000 ms and ETL 5 for PD while TR 3500 ms and ETL 13 for T_2 -weighted images). Thus the volunteer study also included additional sets of images with matched TR and ETL in order to determine an experimental signal correction factor for the PD images to correct for the reduced TR and ETL

used. This correction was applied prior to T_2 fitting. The experimental correction factor accounted for both reduced T_1 recovery with reduced TR and differences in incidental magnetization transfer (iMT) from multislice acquisition (21) due to both ETL and TR. Overall for reduced TR and ETL, the PD signal change was $5\pm 1\%$ signal loss in basal ganglia (globus pallidus, head of caudate, putamen, red nucleus and substantia nigra), $3\pm 1\%$ signal enhancement were identified and in WM structures (frontal WM, insular WM and occipital WM) and no change in thalamus and posterior internal capsule. Results for FSE180° and FSE150° were similar. Compared to DGM, in general WM has shorter T_1 but greater iMT effect due to higher macromolecular content (21-23), which led to higher signal when using the reduced ETL even though TR was also reduced.

5.3.5 Image analysis

Manual region-of-interest (ROI) analysis was performed for each subject using MATLAB (R2015a), and ImageJ (24). Mean T_2 values were obtained from bilateral ROIs in iron-rich DGM (globus pallidus, putamen, caudate nucleus, substantia nigra, red nucleus, and thalamus) as well as in WM (frontal WM, posterior internal capsule, insular WM and occipital WM). T_2 maps were co-registered using MATLAB ‘imregister’ function to align baseline T_2 maps with follow-up T_2 maps. Prior to computing the T_2 maps, signal corrections to the PD images were performed based on the volunteer validation study for each ROI. This correction accounted for varying T_1 recovery and iMT.

For baseline normalized volumes of whole brain, cortical grey matter (CGM), total grey matter (GM), WM and ventricular volume were obtained on 2D T_1 -weighted images using SIENAX, and percentage of brain volume change over time were measured using SIENA (25). All the volumes were then normalized relative to whole head volume for each subject. The lesion loads were calculated for each patient at baseline and follow-up by multiplying T_2 lesion masks on FLAIR images with the slice thickness of the scans. T_2 lesion masks were manually outlined on the FLAIR images using ImageJ (24).

5.3.6 Statistical analysis

Statistical analyses were performed using SPSS (IBM, Armonk, NY). A p-value of less than 0.05 was considered as statistically significant. A paired sample t-test was performed to test pairwise differences for patients over 7 years. Each exam was analysed separately by the same observer with ROIs manually drawn for each brain region. Percent change between inter-control and inter-patient mean and standard deviation was calculated for each structure in the brain for changes in T_2 and volume over time. Spearman and Pearson correlations were used to calculate the correlation coefficients between MRI measures and clinical data. Multiple linear regression models were used to determine the correlation between changes in T_2 and MSSS over 7 years. Age was used as covariate in the regression models. Due to unavailability of an initial EDSS score of two patients, we included 12 patients for EDSS and MSSS analysis.

5.4 Results

Subject demographic and clinical information of patients with MS are presented in Table 5.1. EDSS score was increased by 0.8 ± 0.6 from baseline to 7-years follow-up study. Table 5.2 reports volumetric data of patients. Volumes of whole brain, CGM, total GM, and ventricular volume showed significant changes over time with relatively small effect size. Figure 5.1 shows an example of a normalized flip angle map containing DGM structures obtained from a healthy brain (Fig. 5.1a) and the flip angle profiles (Fig. 5.1b) obtained from seven subjects. The flip angle profiles follow a similar pattern, suggesting they can be predicted without measurement at 1.5 T. The mean flip angle values within each ROI were used for the retrospective patient T_2 calculations.

Example R_2 ($1/T_2$) maps from a healthy volunteer using different sequences are shown in Fig. 5.2. Here we consider T_2 values from ISEC fitting of MESE data as reference. T_2 values obtained with two-point fitting with ISEC are underestimated by 3 to 7% compared to MESE via ISEC method. Table 5.3 lists the mean T_2 values from the volunteer validation study obtained using the MESE via ISEC method including all echoes, two-point ISEC method for FSE180° and FSE150° pulses with the inputs of a normalized flip angle maps averaged over seven healthy subjects (nB_{1av}). T_2 values were also reported for two-point ISEC fit, as well as for two-point exponential fit. The refocusing angles (α_R) from the DGM and frontal WM structures are also shown in Table 5.3, as derived from flip angle maps using double angle method. The distribution

of flip angles in different brain structures is very similar between the subjects. T_2 obtained using two-point exponential fitting are overestimated by 11-20% compared to MESE via the ISEC method.

Table 5.4: Transverse relaxation times (T_2) in ms obtained from fourteen patients with MS. Percent changes over time are reported with effect size.

	T_2 (ms) using ISEC fit				T_2 (ms) using exponential fit			
	Baseline	Follow-up	PC	ES	Baseline	Follow-up	PC	ES
Caudate head	77.7±3.6	76.4±2.0	-1.76	<i>0.22</i>	105.7±5.9	102.8±5.6	-2.78	0.24
Putamen	68.6±2.8	67.8±2.6	-1.11	0.14	91.8±6.1	87.8±3.8	-4.39	0.37
Globus pallidus	57.4±1.8	55.1±1.6	-3.89	<i>0.56</i>	73.7±2.8	72.4±3.6	-1.81	0.20
Thalamus	74.5±2.6	73.7±2.3	-0.96	0.16	91.2±4.2	91.6±4.5	0.46	-0.04
Substantia nigra	60.8±2.5	58.9±2.8	-3.00	<i>0.34</i>	78.0±4.0	76.9±4.4	-1.39	0.12
Red nucleus	63.0±3.0	61.9±3.3	-1.67	0.16	81.9±4.8	81.4±3.8	-0.64	0.06
Frontal WM	69.5±3.7	70.9±3.6	1.97	-0.19	80.9±5.6	83.9±4.1	3.69	-0.29
Posterior IC	86.5±4.7	88.5±4.5	2.42	<i>-0.21</i>	107.7±7.3	109.9±6.2	1.81	-0.16
Insular WM	75.0±4.4	76.6±6.4	2.19	-0.14	92.2±5.7	93.9±4.7	2.06	-0.17
Occipital WM	77.4±5.1	79.4±5.6	2.72	-0.18	99.0±5.9	101.5±5.7	2.65	-0.21

Note: data are means \pm standard deviation. ES: effect size; PC: percent change; WM: white matter; IC: internal capsule; ISEC: indirect and stimulated echo compensation. Italic bold-faced values are statistically significant with $p < 0.05$. p-values were obtained using paired sample t-test.

Baseline and final time point PD and T_2 -weighted images and the corresponding R_2 maps from an MS patient are shown in Fig. 5.3. Figure 5.4 presents 7-year follow-up T_2 values in DGM and WM structures for patients. Table 5.4 represents T_2 values obtained from PD and T_2 -weighted images using two-point ISEC fit and two-point exponential fit in patients with MS.

Note normalized flip angle maps averaged over the healthy volunteers were used for the patient cohort. Using T_2 fitting with two-point ISEC method, we found significant changes over time in globus pallidus (T_2 decreased by 3.9%), head of caudate (T_2 decreased by 1.8%), substantia nigra (T_2 decreased by 3.0%) and posterior internal capsule (T_2 increase by 2.4%) with moderate effect size. Other WM structures also showed increasing trend in T_2 over time, but were not statistically significant. T_2 decrease over time in WM might be due to the process of demyelination, axonal loss or increased water content. On the other hand, no significant changes in T_2 values were found for exponential fitting as inter-subject variability was higher, though larger percent changes were found in some structures.

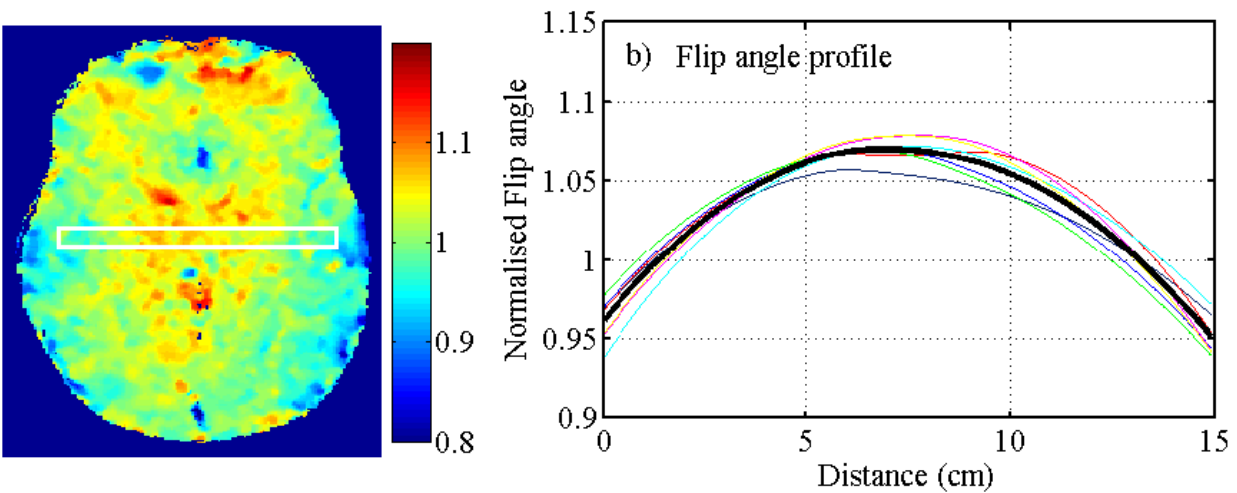


Figure 5.1: (a) Normalized flip angle map from a healthy brain obtained using double angle method at 1.5 T; (b) The normalized flip angle profiles from seven healthy subjects and the mean flip angle profile (thick line) obtained along the horizontal box in (a).

By using multiple regression analysis with two DGM structure as variables, 7-year-difference measurements with two-point T_2 mapping with ISEC has a high correlation to MSSS ($r = 0.76$, $p < 0.05$) as well as to EDSS ($r = 0.70$, $p < 0.05$) at final time point. The equation used to predict MS disease severity was as follows: $MSSS$ (at final time point) = $-0.71 \cdot \Delta T_{2GP} - 0.48 \cdot \Delta T_{2CD} + 1.83$; where ΔT_{2GP} and ΔT_{2CD} are the differences in T_2 over 7 years for globus pallidus and head of caudate respectively. Moreover, the following equation can be used to predict disability in MS: $EDSS$ (at final time point) = $-0.29 \cdot \Delta T_{2GP} - 0.13 \cdot \Delta T_{2CD} + 2.04$. At baseline, only globus pallidus showed significant correlation with MSSS ($r = -0.61$, $p = 0.032$). At

final time point, globus pallidus and head of caudate had significant correlation ($r = -0.4$ to -0.6 , $p < 0.05$) with EDSS as well as with MSSS. We also found a significant correlation between the change in T_2 and change in EDSS score over time for globus pallidus ($r = -0.69$, $p = 0.013$) and for posterior internal capsule ($r = 0.65$, $p = 0.022$).

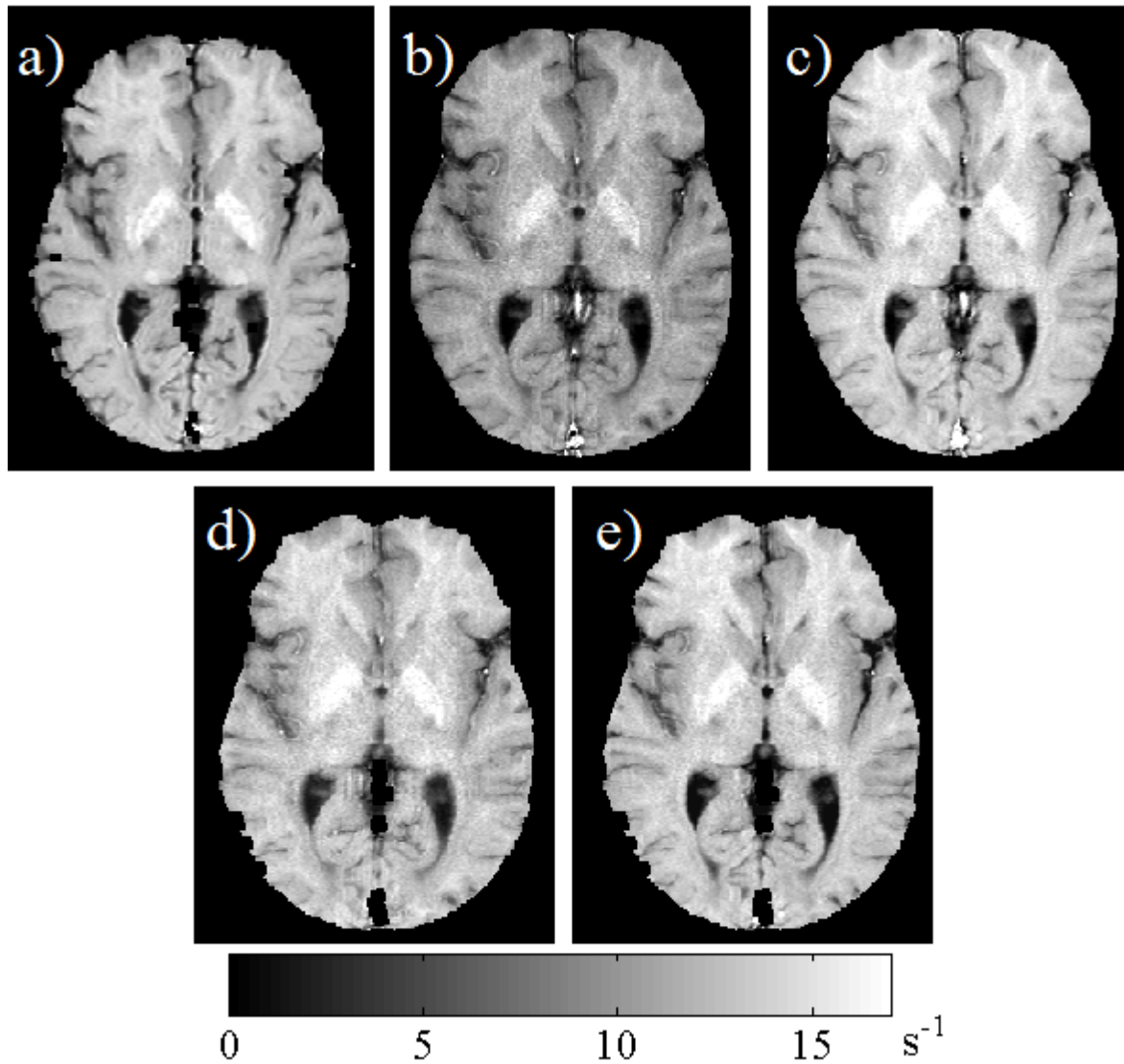


Figure 5.2: R_2 ($1/T_2$) maps obtained from a 29 year old healthy volunteer using: (a) full MESE via ISEC with actual flip angle map; (b, c) two-point exponential fit with PD and T_2 -weighted images (d, e) two-point ISEC fits using mean flip angle map averaged over seven healthy subjects; (b, d) FSE180° and (c, e) FSE150°. Note the exponential results differ greatly with flip angle (b vs. c), while the two point ISEC fits do not (d vs. e).

Single time point T_2 of putamen and posterior internal capsule correlated with CGM volumes ($r = 0.6$, $p < 0.05$). Changes in T_2 in thalamus and ventricular atrophy were correlated significantly ($r = -0.57$, $p = 0.048$). Baseline T_2 lesion load correlated with T_2 only for head of caudate ($r = -0.51$, $p = 0.044$) while change in T_2 over time correlated with T_2 lesion load at final time point only for globus pallidus (-0.58 , $p = 0.048$). Moreover, T_2 lesion load showed significant correlation with MSSS at final time point ($r = 0.59$, $p = 0.045$).

On the other hand, two-point exponential T_2 fitting showed no significant correlations over time, but only at single time point measurements for putamen ($r = -0.48$, $p = 0.047$ EDSS at baseline) and thalamus ($r = -0.50$, $p = 0.011$). While normalized T_2 hypointensity relative to cerebrospinal fluid did not show any correlation with any clinical or volumetric measurements, though normalized signal intensity was reduced by $\sim 12\%$ in DGM structures (not shown).

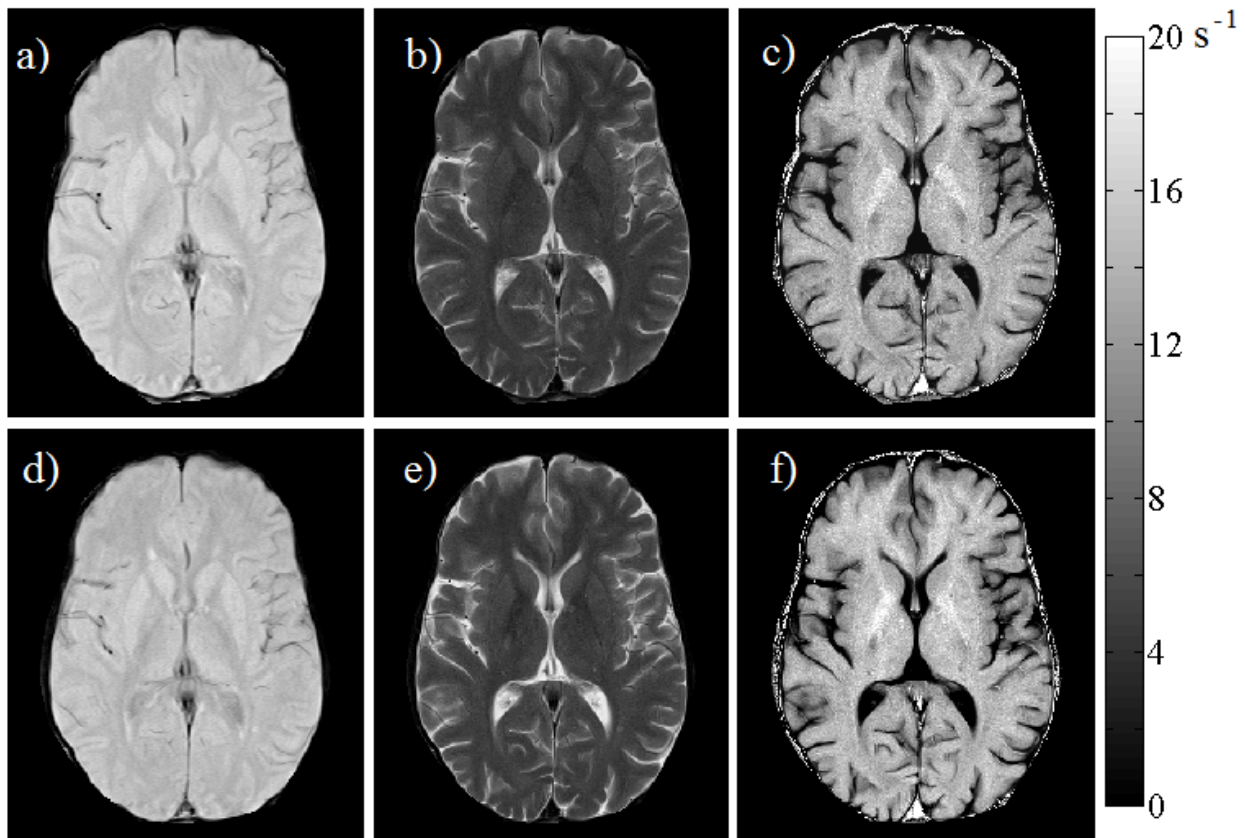


Figure 5.3: Baseline (a-c) and 7 year images (d-f) from a 31 year old MS patient. (a, d) Proton density (PD), (b, e) T_2 -weighted spin echo images and (c, f) R_2 ($1/T_2$) maps with intensity scale.. R_2 values are increased in deep grey matter (head of caudate and globus pallidus) and ventricular enlargement occurs over 7 years.

5.5 Discussion

Retrospective analysis of standard clinical exams of RRMS subjects over 7 years was performed to obtain changes in quantitative T_2 as well as lesion load and brain volume. We found EDSS, MSSS, T_2 lesion load, and ventricular atrophy correlated with the change in T_2 in some brain structures over time, and these MRI measures can be used to monitor disease progression and state in MS.

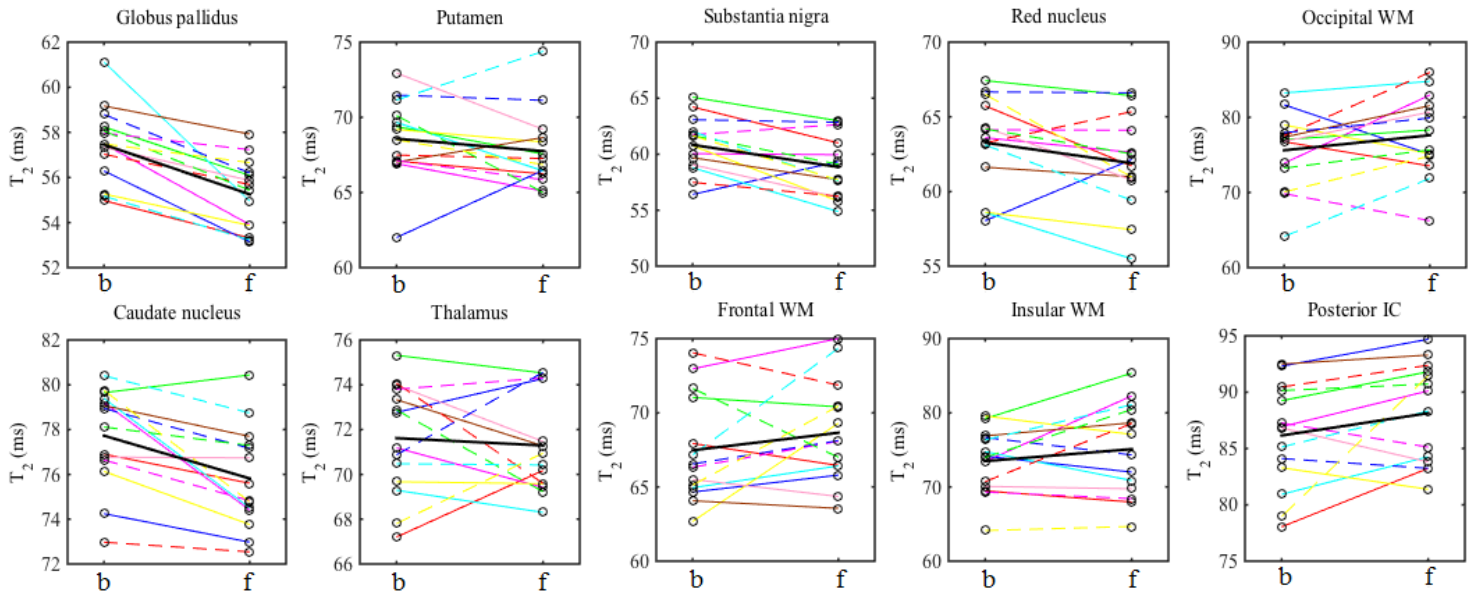


Figure 5.4: Baseline and 7-year T_2 measurements using two-point ISEC method for some DGM and WM structures from patients with MS. Thick black line is the averaged value over the MS cohort. Note different y-axis limits are used in most cases. b: baseline and f: final time point.

Compared to the exponential fitting method, T_2 values obtained with the two-point ISEC method were more effective at tracking changes over time, and this method is known to produce more accurate values (18). The two-point ISEC fitting method (18) requires knowledge of the actual flip angle and RF pulse shape. The pulse shape is available from the manufacturer or through oscilloscope measurement; however the actual flip angle must typically be measured experimentally. We found the within-subject variation in flip angles within a particular ROI was very small ($1-3^\circ$) at 1.5 T, as obtained from the normalized flip angle maps from the volunteer validation study. Consequently, the mean normalized flip angle map from seven healthy subjects could be applied to the retrospective patient data, which did not include a flip angle map. Future

prospective studies, particularly at higher fields which have greater flip angle variability, should include a flip angle mapping sequence, which can be accomplished within 10 sec as performed here.

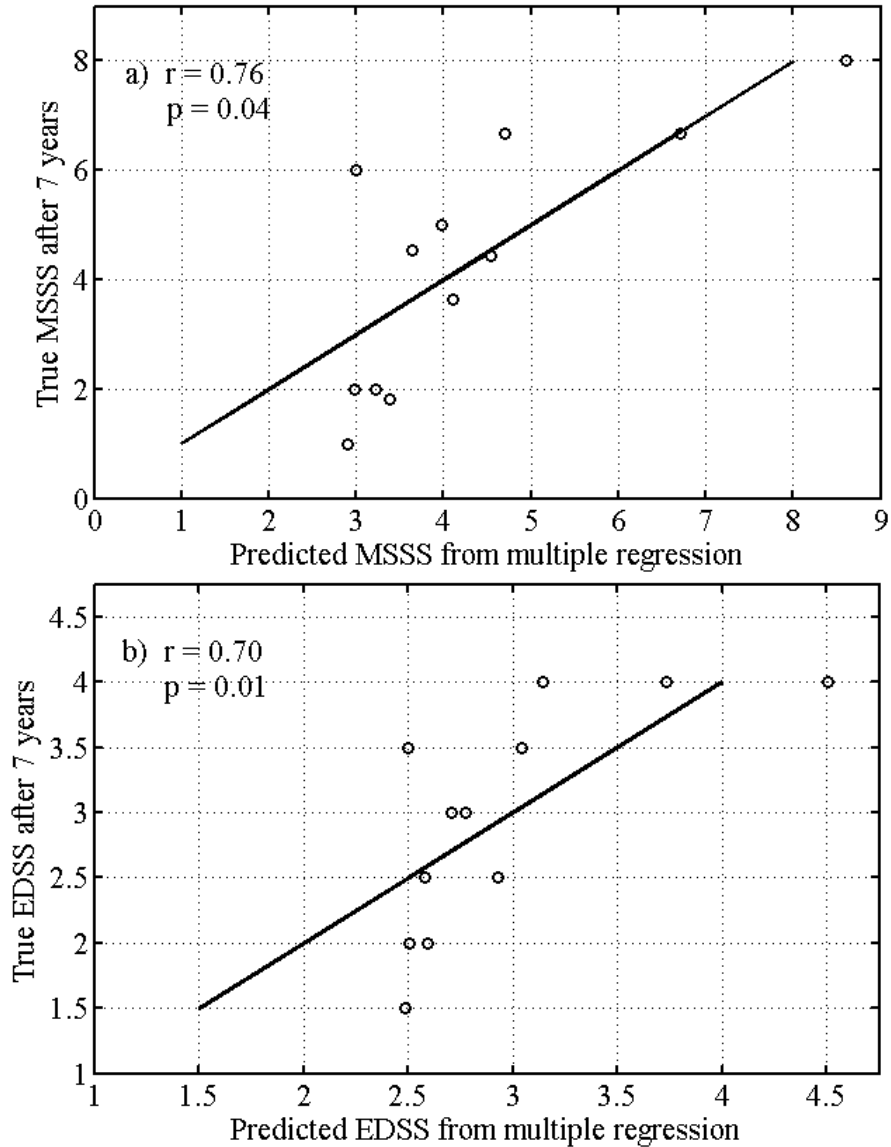


Figure 5.5: Predictors of disease severity and disability in MS using multiple regressions of the 7 year R_2 difference measurements with MS severity scores (MSSS) and with EDSS scores. Globus pallidus and caudate nucleus are included in the regression models. The regression line equations: MSSS (after 7 years) = $-0.71 \cdot \Delta T_{2GP} - 0.48 \cdot \Delta T_{2CD} + 1.83$; EDSS (after 7 years) = $-0.29 \cdot \Delta T_{2GP} - 0.13 \cdot \Delta T_{2CD} + 2.05$; where ΔT_{2GP} and ΔT_{2CD} are the differences in T_2 over 7 years for globus pallidus and head of caudate nucleus respectively.

Iron accumulation in MS DGM is a consistent finding in recent studies at 3.0 T or greater (6,7,26). Previous studies reported that normalized T_2 hypointensity measurements at 1.5 T can provide some clues regarding the iron accumulation; however T_2 -weighted intensity is affected by confounding factors that preclude evaluating iron accumulation precisely (27-29). Quantitative methods such as T_2 mapping, T_2^* mapping in combination with high magnetic field and susceptibility mapping have been used for the detection of abnormal iron accumulation in MS DGM (6-8,26,30,31). Quantitative MRI methods using clinically available sequences might be useful to track iron related changes in DGM. In this study, T_2 quantification via two-point ISEC in some DGM showed significant negative correlations with EDSS and MSSS over 7 years, implying increased iron accumulation, or some other form of mineralization, is related to disability in MS. As well, change in T_2 in globus pallidus correlated significantly with the change in EDSS score over time. Since the globus pallidus contains the highest iron concentration amongst the DGM structures, it may be most sensitive to small percentage changes (32).

Using multiple regression analyses of changes in T_2 in two DGM structures (globus pallidus and head of caudate) over 7 years showed high correlation with final time point MSSS as well as the final time point EDSS score. These regression models can be used as predictors for disability and disease severity in patients with MS. Iron may accumulate in different DGM structures at different rates (32), and the dynamics may vary within structures and with disease course in MS. A more localized DGM analysis may bring out more findings than the whole structure analysis used here (33). For example, in the thalamus, iron accumulation in the pulvinar might be offset by demyelination in other regions, since T_2 is strongly affected by both processes.

Using the two-point ISEC method, T_2 in WM structures increased over 7 years, however only posterior internal capsule was significant of the WM regions measured. This T_2 increase in posterior internal capsule might be due to the demyelination and axonal loss in this dense myelinated fiber pathway (34,35). We found the change in T_2 in internal capsule correlated with final time point disability score as well as disease severity scores in MS. Multi-component T_2 analysis can provide greater insight into myelin water changes (12), but requires a specialized MESE sequence.

Ventricular atrophy might play an important role in disease progression in MS. Jacobsen et al. (3) reported that ventricles were enlarged by ~22% over 10 years. However, we found ~10% increase in ventricular volumes over 7 years. Previous studies have demonstrated the association between ventricular enlargement and disease progression in MS (36-38). In our work, no significant correlation was found between ventricular atrophy and disability or disease severity score. However, we found that change in T_2 in thalamus significantly negatively correlated with the change in ventricular volumes in MS over 7 years. A recent longitudinal study showed that thalamic atrophy is related to ventricular enlargement in MS (39). Compared to DGM structures, thalamus has extensive connections with other parts of the brain. Thalamic axons are known to transmit information among the other subcortical GM structures in the brain, and the damage in thalamus and other related structures impairs the disability and disease severity in MS (40). T_2 lesion loads at 7 years correlated significantly with MSSS indicating that lesion loads during disease progression might contribute to disease severity. Lesion loads can be used as predictors for long term disability in MS (38).

There were many limitations in this study, which relied on retrospective clinical MRI exams. This study used a small sample size since it was a feasibility study to investigate retrospective T_2 mapping. Healthy subjects were included in the study to validate the two-point T_2 method, but not to compare with the patient group due to age differences and the lack of time course data. The 1.5 T field strength used was a limitation for DGM T_2 mapping due to its poor iron sensitivity, which led to relatively small changes in T_2 over time. Iron sensitivity increases linearly with field strength (41), hence future studies using 3.0 T or higher will likely show improved significance. For example, a recent 4.7 T study on 2-year evolution in MS showed larger T_2 differences in DGM than those seen here over 7 years (42). The T_2 maps were computed using actual flip angle modeling to account for both the slice profile and variable refocusing angle, which requires a flip angle map. Due to the retrospective and clinical nature of the study, a flip angle map was not available; however, the flip angle distribution was obtained from an average flip angle map from healthy subjects. Also different PD and T_2 -weighted TR's required correction. Future studies could use a dual echo PD and T_2 -weighted sequence for increased efficiency and to avoid TR and iMT variations, or simply match TR's and ETL if the sequences are performed independently. Age might be considered as a confounding factor in the analysis; however age was used as a covariate in the linear regression models. The atrophy of

DGM was not included in this study because T_1 images had large 5 mm slice thickness that precludes proper DGM segmentation. Similarly, the 5 mm slice thickness used for all images may have introduced partial volume effects in all results for T_2 maps, lesion load and brain volumes.

In conclusion, changes in T_2 in brain structures particularly in globus pallidus, caudate and posterior internal capsule showed significant correlations with EDSS and MSSS scores over 7 years. These changes were not significant when using a standard exponential T_2 fit. The change in thalamic T_2 was correlated with ventricular atrophy. Therefore, combining the long term retrospective two-point T_2 and atrophy measurements can be used to track the disease course in RRMS. Given the wide use of PD and T_2 -weighted FSE in MS clinical trials, this retrospective T_2 method may provide an additional measure of disease evolution. Furthermore, the use of a dual echo PD and T_2 -weighted FSE would enable tracking of quantitative T_2 in clinical exams.

5.6 Acknowledgements

This work was supported by grants from the Multiple Sclerosis Society of Canada, and Canadian Institutes of Health Research (CIHR).

5.7 References

1. Hametner S, Wimmer I, Haider L, Pfeifenbring S, Brueck W, Lassmann H. Iron and Neurodegeneration in the Multiple Sclerosis Brain. *Annals of Neurology* 2013;74(6):848-861.
2. Stephenson E, Nathoo N, Mahjoub Y, Dunn JF, Yong VW. Iron in multiple sclerosis: roles in neurodegeneration and repair. *Nature Reviews Neurology* 2014;10(8):459-468.
3. Jacobsen C, Hagemeyer J, Myhr K-M, Nyland H, Lode K, Bergsland N, Ramasamy DP, Dalaker TO, Larsen JP, Farbu E, Zivadinov R. Brain atrophy and disability progression in multiple sclerosis patients: a 10-year follow-up study. *Journal of neurology, neurosurgery, and psychiatry* 2014;85(10):1109-1115.
4. Bergsland N, Horakova D, Dwyer MG, Dolezal O, Seidl ZK, Vaneckova M, Krasensky J, Havrdova E, Zivadinov R. Subcortical and Cortical Gray Matter Atrophy in a Large

- Sample of Patients with Clinically Isolated Syndrome and Early Relapsing-Remitting Multiple Sclerosis. *American Journal of Neuroradiology* 2012;33(8):1573-1578.
5. Benedict RH, Ramasamy D, Munschauer F, Weinstock-Guttman B, Zivadinov R. Memory impairment in multiple sclerosis: correlation with deep grey matter and mesial temporal atrophy. *Journal of Neurology, Neurosurgery & Psychiatry* 2009;80(2):201-206.
 6. Lebel RM, Eissa A, Seres P, Blevins G, Wilman AH. Quantitative high-field imaging of sub-cortical gray matter in multiple sclerosis. *Multiple Sclerosis Journal* 2012;18(4):433-441.
 7. Ropele S, Kilsdonk ID, Wattjes MP, Langkammer C, de Graaf WL, Frederiksen JL, Larsson HB, Yiannakas M, Wheeler-Kingshott CAM, Enzinger C, Khalil M, Rocca MA, Sprenger T, Amann M, Kappos L, Filippi M, Rovira A, Ciccarelli O, Barkhof F, Fazekas F. Determinants of iron accumulation in deep grey matter of multiple sclerosis patients. *Multiple Sclerosis Journal* 2014;20(13):1692-1698.
 8. Khalil M, Langkammer C, Pichler A, Pinter D, Gatttringer T, Bachmaier G, Ropele S, Fuchs S, Enzinger C, Fazekas F. Dynamics of brain iron levels in multiple sclerosis A longitudinal 3T MRI study. *Neurology* 2015(84):2396-2402.
 9. Neema M, Arora A, Healy BC, Guss ZD, Brass SD, Duan Y, Buckle GJ, Glanz BI, Stazzone L, Khoury SJ, Weiner HL, Guttmann CRG, Bakshi R. Deep Gray Matter Involvement on Brain MRI Scans Is Associated with Clinical Progression in Multiple Sclerosis. *Journal of Neuroimaging* 2009;19(1):3-8.
 10. Khalil M, Langkammer C, Ropele S, Petrovic K, Wallner-Blazek M, Loitfelder M, Jehna M, Bachmaier G, Schmidt R, Enzinger C, Fuchs S, Fazekas F. Determinants of brain iron in multiple sclerosis A quantitative 3T MRI study. *Neurology* 2011;77(18):1691-1697.
 11. Laule C, Vavasour IM, Moore GRW, Oger J, Li DKB, Paty DW, MacKay AL. Water content and myelin water fraction in multiple sclerosis - A T2 relaxation study. *Journal of neurology* 2004;251(3):284-293.
 12. Laule C, Vavasour IM, Kolind SH, Traboulsee AL, Moore GRW, Li DKB, MacKay AL. Long T2 water in multiple sclerosis: What else can we learn from multi-echo T2 relaxation? *Journal of neurology* 2007;254(11):1579-1587.

13. Liang AL, Vavasour IM, Mädler B, Traboulsee AL, Lang DJ, Li DK, MacKay AL, Laule C. Short-term stability of T 1 and T 2 relaxation measures in multiple sclerosis normal appearing white matter. *Journal of neurology* 2012;259(6):1151-1158.
14. Zhang Y, Metz LM, Yong VW, Mitchell JR. 3 T deep gray matter T2 hypointensity correlates with disability over time in stable relapsing-remitting multiple sclerosis: A 3-year pilot study. *Journal of the Neurological Sciences* 2010;297(1-2):76-81.
15. Deoni SCL, Rutt BK, Peters TM. Rapid combined T1 and T2 mapping using gradient recalled acquisition in the steady state. *Magnetic Resonance in Medicine* 2003;49(3):515-526.
16. Lebel RM, Wilman AH. Transverse relaxometry with stimulated echo compensation. *Magnetic Resonance in Medicine* 2010;64(4):1005-1014.
17. MacKay A, Laule C, Vavasour I, Bjarnason T, Kolind S, Madler B. Insights into brain microstructure from the T2 distribution. *Magnetic Resonance Imaging* 2006;24(4):515-525.
18. McPhee KC, Wilman AH. T2 quantification from only proton density and T2-weighted MRI by modelling actual refocusing angles. *Neuroimage* 2015(118):642-650.
19. Polman CH, Reingold SC, Edan G, Filippi M, Hartung HP, Kappos L, Lublin FD, Metz LM, McFarland HF, O'Connor PW, Sandberg-Wollheim M, Thompson AJ, Weinshenker BG, Wolinsky JS. Diagnostic criteria for multiple sclerosis: 2005 Revisions to the "McDonald Criteria". *Annals of Neurology* 2005;58(6):840-846.
20. Stollberger R, Wach P. Imaging of the active B-1 field in vivo. *Magnetic Resonance in Medicine* 1996;35(2):246-251.
21. Weigel M, Helms G, Hennig J. Investigation and modeling of magnetization transfer effects in two-dimensional multislice turbo spin echo sequences with low constant or variable flip angles at 3 T. *Magnetic Resonance in Medicine* 2010;63(1):230-234.
22. Melki PS, Mulkern RV. Magnetization transfer effects in multislice RARE sequences. *Magnetic Resonance in Medicine* 1992;24(1):189-195.

23. Chang Y, Bae SJ, Lee YJ, Hwang MJ, Lee SH, Lee J, Lee SK, Woo S. Incidental magnetization transfer effects in multislice brain MRI at 3.0 T. *Journal of Magnetic Resonance Imaging* 2007;25(4):862-865.
24. Rasband W. *ImageJ*. US National Institutes of Health, Bethesda, Maryland, USA; 1997-2011.
25. Smith SM, Jenkinson M, Woolrich MW, Beckmann CF, Behrens TEJ, Johansen-Berg H, Bannister PR, De Luca M, Drobnjak I, Flitney DE, Niazy RK, Saunders J, Vickers J, Zhang YY, De Stefano N, Brady JM, Matthews PM. Advances in functional and structural MR image analysis and implementation as FSL. *Neuroimage* 2004;23:S208-S219.
26. Walsh AJ, Blevins G, Lebel RM, Seres P, Emery DJ, Wilman AH. Longitudinal MR Imaging of Iron in Multiple Sclerosis: An Imaging Marker of Disease. *Radiology* 2014;270(1):186-196.
27. Bakshi R, Benedict RHB, Bermel RA, Caruthers SD, Puli SR, Tjoa CW, Fabiano AJ, Jacobs L. T2 hypointensity in the deep gray matter of patients with multiple sclerosis - A quantitative magnetic resonance imaging study. *Archives of Neurology* 2002;59(1):62-68.
28. Bakshi R, Dmochowski J, Shaikh ZA, Jacobs L. Gray matter T2 hypointensity is related to plaques and atrophy in the brains of multiple sclerosis patients. *Journal of the Neurological Sciences* 2001;185(1):19-26.
29. Neema M, Stankiewicz J, Arora A, Dandamudi VSR, Batt CE, Guss ZD, Al-Sabbagh A, Bakshi R. T1 and T2 based MRI measures of diffuse gray matter and white matter damage in patients with multiple sclerosis. *Journal of Neuroimaging* 2007;17:16S-21S.
30. Langkammer C, Liu T, Khalil M, Enzinger C, Jehna M, Fuchs S, Fazekas F, Wang Y, Ropele S. Quantitative Susceptibility Mapping in Multiple Sclerosis. *Radiology* 2013;267(2):551-559.
31. Walsh AJ, Lebel RM, Eissa A, Blevins G, Catz I, Lu J-Q, Resch L, Johnson ES, Emery DJ, Warren KG, Wilman AH. Multiple Sclerosis: Validation of MR Imaging for Quantification and Detection of Iron. *Radiology* 2013;267(2):531-542.

32. Hallgren B, Sourander P. The effect of age on the non-haemin iron in the human brain. *Journal of Neurochemistry* 1958;3(1):41-51.
33. Cobzas D, Sun H, Walsh AJ, Lebel RM, Blevins G, Wilman AH. Subcortical gray matter segmentation and voxel-based analysis using transverse relaxation and quantitative susceptibility mapping with application to multiple sclerosis. *Journal of Magnetic Resonance Imaging* 2015.
34. Curnes JT, Burger PC, Djang WT, Boyko OB. MR Imaging of compact white matter pathways. *American Journal of Neuroradiology* 1988;9(6):1061-1068.
35. Haacke EM, Chengb NYC, House MJ, Liu Q, Neelavalli J, Ogg RJ, Khan A, Ayaz M, Kirsch W, Obenaus A. Imaging iron stores in the brain using magnetic resonance imaging. *Magnetic Resonance Imaging* 2005;23(1):1-25.
36. Benedict RH, Bruce JM, Dwyer MG, Abdelrahman N, Hussein S, Weinstock-Guttman B, Garg N, Munschauer F, Zivadinov R. Neocortical atrophy, third ventricular width, and cognitive dysfunction in multiple sclerosis. *Archives of Neurology* 2006;63(9):1301-1306.
37. Lukas C, Minneboo A, De Groot V, Moraal B, Knol DL, Polman CH, Barkhof F, Vrenken H. Early central atrophy rate predicts 5 year clinical outcome in multiple sclerosis. *Journal of Neurology, Neurosurgery & Psychiatry* 2010;jnnp. 2009.199968.
38. Popescu V, Agosta F, Hulst HE, Sluimer IC, Knol DL, Sormani MP, Enzinger C, Ropele S, Alonso J, Sastre-Garriga J. Brain atrophy and lesion load predict long term disability in multiple sclerosis. *Journal of Neurology, Neurosurgery & Psychiatry* 2013;84(10):1082-1091.
39. Zivadinov R, Havrdova E, Bergsland N, Tyblova M, Hagemeyer J, Seidl Z, Dwyer MG, Vaneckova M, Krasensky J, Carl E, Kalincik T, Horakova D. Thalamic Atrophy Is Associated with Development of Clinically Definite Multiple Sclerosis. *Radiology* 2013;268(3):831-841.
40. Rocca MA, Mesaros S, Pagani E, Sormani MP, Comi G, Filippi M. Thalamic Damage and Long-term Progression of Disability in Multiple Sclerosis 1. *Radiology* 2010;257(2):463-469.

41. Mitsumori F, Watanabe H, Takaya N, Garwood M, Auerbach EJ, Michaeli S, Mangia S. Toward understanding transverse relaxation in human brain through its field dependence. *Magnetic Resonance in Medicine* 2012;68(3):947-953.
42. Uddin MN, Lebel RM, Seres P, Blevins G, Wilman AH. Spin echo transverse relaxation and atrophy in multiple sclerosis deep gray matter: A two-year longitudinal study. *Multiple Sclerosis Journal* 2015(In press):1-11.

Chapter 6. Conclusion

6.1 Research Outcomes

Quantitative Transverse relaxometry methods can be informative of tissue specific changes and may provide more insight into the disease course of MS. Work presented in this thesis investigated methods for transverse relaxations in human brain, and application of these methods to iron accumulation and MS. Brain atrophy in multiple sclerosis was also studied.

6.1.1 Iron dynamics in MS DGM using 2-year longitudinal study

An association between MS and iron accumulation in DGM has been recognized for decades. It is still unclear whether iron acts as a mediator of damage or an epiphenomenon. In this context, it is important to evaluate the iron dynamics in MS using quantitative MRI methods and/or using high field MRI systems and compare the results with healthy controls. Very few studies have been conducted so far. In this work, a two year longitudinal study was conducted to evaluate the changes in iron accumulation in MS DGM using R_2 mapping method and atrophy measurements. This is the first longitudinal study using the R_2 mapping method. The results indicated that change in R_2 in some DGM structures correlated with baseline disease severity score and can be used as a predictor. Globus pallidus, substantia nigra and pulvinar nucleus showed positive correlation with MS severity score which might be due to iron accumulation while thalamus excluding pulvinar showed negative correlation which might be due to demyelination. Compared to controls, the MS patients had smaller DGM volumes and increased iron content in the DGM structures over two years, but significant changes were found only in globus pallidus. Therefore, combination of atrophy and R_2 measurements in DGM can be used as biomarkers to monitor disease progression and dynamics of iron accumulation in MS.

6.1.2 R_2 mapping using reduced echoes

At the high magnetic field of 4.7 T, RF heterogeneity and SAR are major limitations to obtain R_2 mapping using a multi-echo spin echo sequence. The RF heterogeneity arises from through-plane imperfect refocusing slice profiles and in-plane RF interference effects. Quantitative R_2 mapping

via stimulated echo compensation is a promising method that provides tissue specific absolute measures and is insensitive to heterogeneous RF fields because it accounts for them in the fitting process. This study addressed means to overcome the SAR limitations to enable more rapid multi-slice R_2 mapping. The SAR limitations were overcome by shortening the echo train lengths. Consistent R_2 values were found with as few as 4 echoes compared to 20 echoes. RF power savings through the use of reduced number of echoes enabled increased slice coverage. While available signal was decreased from incidental magnetization transfer, the R_2 values were not affected. This R_2 mapping approach is useful for obtaining accurate R_2 values in GM and WM in the brain.

6.1.3 Value of transverse relaxometry difference methods

Quantitative relaxometry methods (R_2 , R_2^* , R_2' and FDRI) can all be used to evaluate iron accumulation in human brain. The two difference methods using subtraction within field or between field (R_2' and FDRI) provide more specific iron sensitivity measurements by removing less specific components via subtraction. We compared the benefits and limitations of these methods for iron accumulation in human brain and iron-doped agar phantom. Using 4.7 T, R_2^* was preferable in iron-rich deep grey matter while R_2' provides more specific iron measures due to its small intercept with estimated post-mortem iron concentration, and both methods require only one field. In WM, R_2' is highly sensitive to fiber orientation relative to B_0 which increases with field strength, while FDRI is much less sensitive to this orientation. However, FDRI using a large field difference (3.2 T in our case) is limited by the fact that macromolecular effects are also field dependent. FDRI can be more effective using lower field strengths with smaller difference, where macromolecular effects are more stable. These findings can be used as reference for further study in patients with neurological disorders including MS.

6.1.4 Long-term change in MS using only retrospective clinical MRI

PD and T_2 -weighted images are frequently used in clinical MS exams. From these images, quantitative R_2 may be determined to serve as an absolute parameter to examine brain changes, rather than using weighted images. However, a simple exponential fit is not appropriate and more advanced modelling is required. R_2 mapping using two-point fitting approach is a promising new method which requires a priori knowledge of refocusing flip angles. That is, a

prospective flip angle map is required for accurate R_2 quantification. However, we demonstrate that at 1.5 T on a clinical system, the flip angles can be accurately predicted, enabling retrospective R_2 mapping from clinical datasets. This R_2 mapping method was validated in healthy subjects and then applied to a long-term study of patients with MS. R_2 values were correlated with disability score as well as with atrophy measurements on retrospective data over 7 years. This R_2 mapping method can be used to identify the disease progression and state of MS using clinically available data. This method may help advance quantitative approaches in MS, since no additional scans are required.

6.2 Significant findings

In this thesis, a series of advances have been introduced in the means to perform transverse relaxation mappings and their applications to multiple sclerosis. We found that MRI transverse relaxometry mappings were useful for evaluating brain iron and tracking disease progression and state in MS using either standard clinical images or high field multi-echo spin echo images. We also clarified the iron sensitivity of all transverse relaxation mapping methods (R_2 , R_2^* , R_2' and FDRI) and demonstrated that reduced echoes may be used to quantify R_2 more precisely in human brain.

6.3 Summary of the findings

- We used multi-echo spin echo R_2 mapping (20 echoes and 2 slices) to evaluate iron dynamics and predict disease severity as well as volume changes in MS DGM.
- We demonstrated R_2 mapping with more brain coverage by reducing the echo trains (5 echoes and 8 slices).
- We examined iron sensitivity in human brain using relaxation mapping methods with emphasis on difference methods demonstrating the specificity of these methods in comparison to standard approaches.
- We demonstrated the feasibility of tracking disease course in MS over 7 years using retrospective clinical MRI from where quantitative R_2 and volume changes were derived. R_2 maps were obtained using PD and T_2 weighed images (2 echoes and 19 slices).

6.4 Limitations

Although standard multiple-echo spin echo R_2 mapping using stimulated echo compensation is a robust technique at high magnetic field, it has some shortcomings at 4.7 T. Due to the RF heating limitation; we obtained R_2 maps only from a limited number of slices that precludes analysing whole brain. This limitation can be overcome with reduced echo methods, either 4 consecutive echoes [1], or the use of proton density and T_2 -weighted images with a prior flip angle map [2]. Flip angle maps can be obtained in as little as 10 s, so this is quite feasible. For R_2 and FDMI measurements, subtraction between two relaxometry maps requires proper image registration. Automated registration protocols such as FSL cannot be used due to the limited number of slices. These automated alignment and segmentation software sometimes give misleading outcome, if images with appropriate resolution are not provided. Manual image registration (registration of images involved rotating, translating the images using imageJ) was performed in this thesis. Use of multiple processing steps might reduce the accuracy of the subtraction measurements. An additional limitation of all spin echo methods is that they are slower than gradient echo approaches, nevertheless, the refocusing of static field inhomogeneity removes a significant potential cause of artifact near air-tissue interfaces, particularly at high field.

Evaluating potential biomarkers of MS can be assessed in different ways. A multiple regression model was used to predict disease severity, where R_2 of iron-rich DGM structures was selected in the regression model; however combination of R_2 , volume, lesion load etc. can be used in the model to predict the disease state. The strong effect of age on iron accumulation requires accurate age matching between groups. Two year changes in R_2 and DGM atrophy were correlated in our study, however T_1 -weighted MPRAGE images were used in automatic DGM atrophy measurements, which provides poor contrast between the DGM regions [3] due to longer T_1 relaxation times of the brain tissue at high magnetic field as we employed 4.7 T [4]. Moreover, longitudinal data analysis might suffer from error due to manual registrations. Consequently, partial volume effects between different brain tissues might produce error. For retrospective data, different scan parameters were used in different time points. Proper signal correction is required to obtain accurate R_2 maps. Moreover, MRI measures might be biased due to lack of proper registration of images from two different time points.

6.5 Future Work

Quantitative relaxometry methods at 4.7 T are sensitive to evaluate iron in DGM. R_2 and R_2^* mapping methods used in this study used mono-exponential fittings. However, multi-exponential signal decay occurs in brain tissue especially in WM [5, 6]. Consideration of multiple component fitting for both R_2^* and R_2 could extend the specificity of imaging methods. Myelin water imaging methods using GRASE [7] or mcDESPOT [8, 9] can be applied relatively quickly to get more insight into the disease state of MS.

Our work focused on whole structure iron measurements and could benefit from more local analysis in future studies using either voxel-based or cluster-based methods [3]. Increased iron specificity using quantitative susceptibility mapping (QSM) [10, 11] is also a direction of future work, since this method is less sensitive to water content, although demyelination and iron accumulation affect QSM in the same way.

Abnormal iron accumulation has been known to exist in DGM as well as in some WM lesions [12-16]. Five-year longitudinal study of MS using high field MRI (4.7 T) may provide more information about iron dynamics in DGM structures. The change in relaxation rates and atrophy over 5 years might be a better predictor to disease severity. Moreover, relaxometry methods as well as other iron sensitive methods including QSM can be used to evaluate iron accumulation in WM lesions since a single method is not enough to evaluate precisely iron in lesions [17]. The roles of iron in lesion formation and for inflammation, as well as the exact mechanism of lesion development in MS are unknown. However, if iron accumulation is a driving force for the inflammation, it should be detected at the early stage of the lesion's development [18]. Longitudinal MRI study for iron accumulation in lesion might show the pattern of iron accumulation in lesions as well as to monitor the lesion dynamics.

6.6 In Closing

The central objective of this thesis was to track disease progression and state in patients with relapsing-remitting MS using quantitative transverse relaxometry methods. We attempted to understand the iron dynamics in MS DGM using R_2 mapping, and the relationship between iron accumulation and atrophy to predict the disease severity. Our study focused on the iron-rich DGM structures. We then optimized the R_2 mapping method and extended it for multislice

imaging. Furthermore, we evaluated iron sensitivity not only in DGM but also in WM structures by employing a series of transverse relaxometry methods and the relaxation deference methods. Later we extended the work on clinically available retrospective data at 1.5 T and correlated the findings with atrophy and clinical scores to understand the disease course for relatively longer time difference. Overall the thesis has shown the viability of R_2 mapping for tracking MS disease progression, particularly at 4.7T, which takes advantage of the increasing iron sensitivity and specificity of R_2 with increasing field strength.

6.7 References

1. Uddin MN, Lebel RM and Wilman AH. Transverse Relaxometry with Reduced Echo Train Lengths via Stimulated Echo Compensation. *Magnetic Resonance in Medicine*. 2013; 70: 1340-6.
2. McPhee KC and Wilman AH. T2 quantification from only proton density and T2-weighted MRI by modelling actual refocusing angles. *Neuroimage*. 2015: 642-50.
3. Cobzas D, Sun H, Walsh AJ, Lebel RM, Blevins G and Wilman AH. Subcortical gray matter segmentation and voxel-based analysis using transverse relaxation and quantitative susceptibility mapping with application to multiple sclerosis. *Journal of Magnetic Resonance Imaging*. 2015.
4. Rooney WD, Johnson G, Li X, et al. Magnetic field and tissue dependencies of human brain longitudinal $^1\text{H}_2\text{O}$ relaxation in vivo. *Magnetic Resonance in Medicine*. 2007; 57: 308-18.
5. Whittall KP, MacKay AL, Graeb DA, Nugent RA, Li DKB and Paty DW. In vivo measurement of T2 distributions and water contents in normal human brain. *Magnetic Resonance in Medicine*. 1997; 37: 34-43.
6. Mackay A, Whittall K, Adler J, Li D, Paty D and Graeb D. In-Vivo Visualization Of Myelin Water In Brain By Magnetic-Resonance. *Magnetic Resonance in Medicine*. 1994; 31: 673-7.
7. Prasloski T, Rauscher A, MacKay AL, et al. Rapid whole cerebrum myelin water imaging using a 3D GRASE sequence. *Neuroimage*. 2012; 63: 533-9.

8. Zhang J, Kolind SH, Laule C and MacKay AL. Comparison of myelin water fraction from multiecho T2 decay curve and steady-state methods. *Magnetic Resonance in Medicine*. 2015; 73: 223-32.
9. Deoni SC, Rutt BK, Arun T, Pierpaoli C and Jones DK. Gleaning multicomponent T1 and T2 information from steady-state imaging data. *Magnetic Resonance in Medicine*. 2008; 60: 1372-87.
10. Sun H, Walsh AJ, Lebel RM, et al. Validation of quantitative susceptibility mapping with Perls' iron staining for subcortical gray matter. *Neuroimage*. 2015; 105: 486-92.
11. Langkammer C, Liu T, Khalil M, et al. Quantitative Susceptibility Mapping in Multiple Sclerosis. *Radiology*. 2013; 267: 551-9.
12. Drayer B, Burger P, Hurwitz B, Dawson D and Cain J. Reduced signal intensity on MR images of thalamus and putamen in multiple sclerosis: increased iron content? *American Journal of Roentgenology*. 1987; 149: 357-63.
13. Lebel RM, Eissa A, Seres P, Blevins G and Wilman AH. Quantitative high-field imaging of sub-cortical gray matter in multiple sclerosis. *Multiple Sclerosis Journal*. 2012; 18: 433-41.
14. Craelius W, Migdal MW, Luessenhop CP, Sugar A and Mihalakis I. Iron deposits surrounding multiple-sclerosis plaques. *Archives of pathology & laboratory medicine*. 1982; 106: 397-9.
15. Hagemeyer J, Heininen-Brown M, Poloni GU, et al. Iron deposition in multiple sclerosis lesions measured by susceptibility-weighted imaging filtered phase: A case control study. *Journal of Magnetic Resonance Imaging*. 2012; 36: 73-83.
16. Yao B, Ikonomidou VN, Cantor FK, Ohayon JM, Duyn J and Bagnato F. Heterogeneity of Multiple Sclerosis White Matter Lesions Detected With T2*-Weighted Imaging at 7.0 Tesla. *Journal of Neuroimaging*. 2015.
17. Walsh AJ, Lebel RM, Eissa A, et al. Multiple Sclerosis: Validation of MR Imaging for Quantification and Detection of Iron. *Radiology*. 2013; 267: 531-42.
18. Zamboni P. The big idea: iron-dependent inflammation in venous disease and proposed parallels in multiple sclerosis. *Journal of the Royal Society of Medicine*. 2006; 99: 589-93.

Bibliography

1. Ray Hashman Hashemi WGB, Christopher J. Lisanti. *MRI: The Basics*. Third ed.: Lippincott Williams & Wilkins, 2010, p.400.
2. Tofts P. *Quantitative MRI of the Brain: Measuring Changes Caused by Disease*. Oxford: Blackwell Science Publ, 2003, p.1-657.
3. Matt A. Bernstein KFK, Xiaohong Joe Zhou *Handbook of MRI Pulse Sequences*. 1 edition ed.: Academic Press, 2004.
4. Zhi-Pei Liang PCL. *Principles of Magnetic Resonance Imaging: A Signal Processing Perspective*. 1 edition ed.: Wiley-IEEE Press, 1999, p.416.
5. E. Mark Haacke RWBMRT, Ramesh Venkatesan. *MRI Physical Principles and Sequence Design*. 1 edition ed.: Wiley-Liss, 1999.
6. de Graaf RA. *In vivo NMR spectroscopy: principles and techniques*. 2nd edition ed.: John Wiley @ Sons, Ltd., 2007.
7. Bloembergen N, Purcell EM and Pound RV. Relaxation effects in nuclear magnetic resonance absorption. *Physical Review*. 1948; 73: 679-712.
8. Abragam A. *The principles of nuclear magnetism* Oxford : Clarendon Press, 1961, p.599.
9. Stark DD. *Magnetic resonance imaging*. St. Louis : C.V. Mosby Co., 1992.
10. Allen D. Elster MD JHBM. *Questions and Answers in Magnetic Resonance Imaging*. 2nd ed.: Mosby, 2000.
11. McRobbie DW. *MRI from Picture to Proton*. 2nd ed.: Cambridge University Press, 2007.
12. Eng J, Ceckler TL and Balaban RS. Quantitative ¹H magnetization transfer imaging in vivo. *Magnetic Resonance in Medicine*. 1991; 17: 304-14.
13. De Boer R. Magnetization transfer contrast.
14. Hoult DI. The principle of reciprocity in signal strength calculations - A mathematical guide. *Concepts in magnetic Resonance*. 2000; 12: 173-87.

15. Collins CM, Liu W, Schreiber W, Yang QX and Smith MB. Central brightening due to constructive interference with, without, and despite dielectric resonance. *Journal of Magnetic Resonance Imaging*. 2005; 21: 192-6.
16. Lauterbur PC. Image Formation by Induced Local Interactions: Examples Employing Nuclear Magnetic Resonance. *Nature*. 1973: 190-1.
17. D Hoult CNC. *Biomedical Magnetic Resonance Technology* Taylor & Francis, 1989, p.250.
18. Michaeli S, Garwood M, Zhu XH, et al. Proton T2 relaxation study of water, N-acetylaspartate, and creatine in human brain using Hahn and Carr-Purcell spin echoes at 4T and 7T. *Magnetic Resonance in Medicine*. 2002; 47: 629-33.
19. Norris DG. High field human imaging. *Journal of Magnetic Resonance Imaging*. 2003; 18: 519-29.
20. Schenck JF and Zimmerman EA. High-field magnetic resonance imaging of brain iron: birth of a biomarker? *NMR in Biomedicine*. 2004; 17: 433-45.
21. de Graaf RA, Brown PB, McIntyre S, Nixon TW, Behar KL and Rothman DL. High magnetic field water and metabolite proton T1 and T2 relaxation in rat brain in vivo. *Magnetic Resonance in Medicine*. 2006; 56: 386-94.
22. Rooney WD, Johnson G, Li X, et al. Magnetic field and tissue dependencies of human brain longitudinal $^1\text{H}_2\text{O}$ relaxation in vivo. *Magnetic Resonance in Medicine*. 2007; 57: 308-18.
23. Johnson GA, Herfkens RJ and Brown MA. Tissue relaxation time - invivo field-dependence. *Radiology*. 1985; 156: 805-10.
24. Mitsumori F, Watanabe H and Takaya N. Estimation of Brain Iron Concentration In Vivo Using a Linear Relationship Between Regional Iron and Apparent Transverse Relaxation Rate of the Tissue Water at 4.7T. *Magnetic Resonance in Medicine*. 2009; 62: 1326-30.
25. Mitsumori F, Watanabe H, Takaya N, et al. Toward understanding transverse relaxation in human brain through its field dependence. *Magnetic Resonance in Medicine*. 2012; 68: 947-53.

26. Gelman N, Gorell JM, Barker PB, et al. MR imaging of human brain at 3.0 T: preliminary report on transverse relaxation rates and relation to estimated iron content. *Radiology*. 1999; 210: 759-67.
27. Gelman N, Ewing JR, Gorell JM, Spickler EM and Solomon EG. Interregional variation of longitudinal relaxation rates in human brain at 3.0 T: Relation to estimated iron and water contents. *Magnetic Resonance in Medicine*. 2001; 45: 71-9.
28. Hoult DI, Chen CN and Sank VJ. The field-dependence of NMR imaging .2. Arguments concerning an optimal field-strength. *Magnetic Resonance in Medicine*. 1986; 3: 730-46.
29. Lebel RM, Eissa A, Seres P, Blevins G and Wilman AH. Quantitative high-field imaging of sub-cortical gray matter in multiple sclerosis. *Multiple Sclerosis Journal*. 2012; 18: 433-41.
30. MacKay AL, Vavasour IM, Rauscher A, et al. MR Relaxation in Multiple Sclerosis. *Neuroimaging Clinics of North America*. 2009; 19: 1-26.
31. Dardzinski BJ, Mosher TJ, Li SZ, VanSlyke MA and Smith MB. Spatial variation of T2 in human articular cartilage. *Radiology*. 1997; 205: 546-50.
32. St Pierre TG, Clark PR, Chua-Anusorn W, et al. Non-invasive measurement and imaging of liver iron concentrations using proton magnetic resonance. *Blood*. 2005; 105: 855-61.
33. Perry J, Haughton V, Anderson PA, Wu Y, Fine J and Mistretta C. The value of T2 relaxation times to characterize lumbar intervertebral disks: Preliminary results. *American Journal of Neuroradiology*. 2006; 27: 337-42.
34. Hosch W, Bock M, Libicher M, et al. MR-Relaxometry of myocardial tissue - Significant elevation of T1 and T2 relaxation times in cardiac amyloidosis. *Investigative Radiology*. 2007; 42: 636-42.
35. White LM, Sussman MS, Hurtig M, Probyn L, Tomlinson G and Kandel R. Cartilage T2 assessment: Differentiation of normal hyaline cartilage and reparative tissue after arthroscopic cartilage repair in equine subjects. *Radiology*. 2006; 241: 407-14.
36. Martin AJ, Poon CS, Thomas GM, Kapusta LR, Shaw PA and Henkelman RM. MR evaluation of cervical cancer in hysterectomy specimens: correlation of quantitative T2 measurement and histology. *J Magn Reson Imaging*. 1994; 4: 779-86.

37. Liney GP, Knowles AJ, Manton DJ, Turnbull LW, Blackband SJ and Horsman A. Comparison of conventional single echo and multi-echo sequences with a fast spin echo sequence for quantitative T2 mapping: Application to the prostate. *Journal of Magnetic Resonance Imaging*. 1996; 6: 603-7.
38. Whittall KP, MacKay AL, Graeb DA, Nugent RA, Li DKB and Paty DW. In vivo measurement of T2 distributions and water contents in normal human brain. *Magnetic Resonance in Medicine*. 1997; 37: 34-43.
39. MacKay A, Laule C, Vavasour I, Bjarnason T, Kolind S and Madler B. Insights into brain microstructure from the T2 distribution. *Magnetic Resonance Imaging*. 2006; 24: 515-25.
40. Poon CS and Henkelman RM. Practical T2 quantitation for clinical applications. *Journal of Magnetic Resonance Imaging*. 1992; 2: 541-53.
41. Deichmann R, Adolf H, Noth U, Morrissey S, Schwarzbauer C and Haase A. Fast T2 mapping with snapshot flash imaging. *Magnetic Resonance Imaging*. 1995; 13: 633-9.
42. Schmitt P, Griswold MA, Jakob PM, et al. Inversion recovery TrueFISP: Quantification of T1, T2, and spin density. *Magnetic Resonance in Medicine*. 2004; 51: 661-7.
43. Bieri O, Scheffler K, Welsch GH, Tractnig S, Mamisch TC and Ganter C. Quantitative Mapping of T2 Using Partial Spoiling. *Magnetic Resonance in Medicine*. 2011; 66: 410-8.
44. Deoni SCL, Rutt BK and Peters TM. Rapid combined T1 and T2 mapping using gradient recalled acquisition in the steady state. *Magnetic Resonance in Medicine*. 2003; 49: 515-26.
45. Hahn EL. Spin echoes. *Physical Review*. 1950; 80: 580-94.
46. Carr HY and Purcell EM. Effects of diffusion on free precession in nuclear magnetic resonance experiments. *Physical Review*. 1954; 94: 630-8.
47. Meiboom S and Gill D. Modified spin-echo method for measuring nuclear relaxation times. *Rev Sci Instrum*. 1958; 29: 688-91.
48. Whitaker CDS SP, Beversdorf DQ, Santi MS, Dashner RA, Chakeres DW, Schmalbrock P. T2 and T2* Relaxation in Normal and Alzheimer's Formalin Fixed Hippocampus at 8 T. *International Society of Magnetic Resonance in Medicine*. Honolulu, Hawaii.2002, p. 1274.

49. Ye FQ, Martin W and Allen PS. Estimation of brain iron in vivo by means of the interecho time dependence of image contrast. *Magnetic Resonance in Medicine*. 1996; 36: 153-8.
50. Bartha R, Michaeli S, Merkle H, et al. In vivo (H₂O) H₁ T₂(dagger) measurement in the human occipital lobe at 4T and 7T by Carr-Purcell MRI: Detection of microscopic susceptibility contrast. *Magnetic Resonance in Medicine*. 2002; 47: 742-50.
51. Hardy P and Henkelman RM. On the transverse relaxation rate enhancement induced by diffusion of spins through inhomogeneous fields. *Magnetic Resonance in Medicine*. 1991; 17: 348-56.
52. Weisskoff RM, Zuo CS, Boxerman JL and Rosen BR. Microscopic susceptibility variation and transverse relaxation - theory and experiment. *Magnetic Resonance in Medicine*. 1994; 31: 601-10.
53. Yablonskiy DA and Haacke EM. Theory of NMR signal behavior in magnetically inhomogeneous tissues - the static dephasing regime. *Magnetic Resonance in Medicine*. 1994; 32: 749-63.
54. Lebel RM and Wilman AH. Transverse relaxometry with stimulated echo compensation. *Magnetic Resonance in Medicine*. 2010; 64: 1005-14.
55. Haacke EM, Brown R, Thompson M and Venkatesan R. Magnetic resonance imaging: physical principles and sequence design. 1999. *New York: A John Wiley and Sons*.
56. FDA. Criteria for Significant Risk Investigations of Magnetic Resonance Diagnostic Devices. In: Staff GfIaFaDA, (ed.). USA2014.
57. Weigel M, Helms G and Hennig J. Investigation and modeling of magnetization transfer effects in two-dimensional multislice turbo spin echo sequences with low constant or variable flip angles at 3 T. *Magnetic Resonance in Medicine*. 2010; 63: 230-4.
58. Chang Y, Bae SJ, Lee YJ, et al. Incidental magnetization transfer effects in multislice brain MRI at 3.0 T. *Journal of Magnetic Resonance Imaging*. 2007; 25: 862-5.
59. Miller DH, Johnson G, Tofts PS, Macmanus D and McDonald WI. Precise relaxation-time measurements of normal-appearing white matter in inflammatory central nervous-system disease. *Magnetic Resonance in Medicine*. 1989; 11: 331-6.

60. Prasloski T, Mädler B, Xiang QS, MacKay A and Jones C. Applications of stimulated echo correction to multicomponent T2 analysis. *Magnetic Resonance in Medicine*. 2012; 67: 1803-14.
61. Jensen JH, Chandra R and Yu H. Quantitative model for the interecho time dependence of the CPMG relaxation rate in iron-rich gray matter. *Magnetic Resonance in Medicine*. 2001; 46: 159-65.
62. Ye FQ, Martin WRW and Allen PS. Estimation of brain iron in vivo by means of the interecho time dependence of image contrast. *Magnetic Resonance in Medicine*. 1996; 36: 153-8.
63. Jones JA, Hodgkinson P, Barker AL and Hore PJ. Optimal sampling strategies for the measurement of spin-spin relaxation times. *Journal of Magnetic Resonance Series B*. 1996; 113: 25-34.
64. Dula AN, Gochberg DF and Does MD. Optimal echo spacing for multi-echo imaging measurements of Bi-exponential T2 relaxation. *Journal of Magnetic Resonance*. 2009; 196: 149-56.
65. Hennig J, Nauerth A and Friedburg H. RARE imaging - a fast imaging method for clinical MR. *Magnetic Resonance in Medicine*. 1986; 3: 823-33.
66. Jones C, Xiang Q, Whittall K and MacKay A. Calculating T2 and B1 from decay curves collected with non-180 refocusing pulses. Proceedings of 11th Annual Meeting, International Society for Magnetic Resonance in Medicine, 2003, p. 1018.
67. Hennig J. Multiecho Imaging Sequences With Low Refocusing Flip Angles. *Journal of Magnetic Resonance*. 1988; 78: 397-407.
68. Wild JM, Martin WRW and Allen PS. Multiple gradient echo sequence optimized for rapid, single-scan mapping of R-2(*) at high B-0. *Magnetic Resonance in Medicine*. 2002; 48: 867-76.
69. Yang QX, Williams GD, Demeure RJ, Mosher TJ and Smith MB. Removal of local field gradient artifacts in T-2*-weighted images at high fields by gradient-echo slice excitation profile imaging. *Magnetic Resonance in Medicine*. 1998; 39: 402-9.

70. Cho ZH and Ro YM. Reduction of susceptibility artifact in gradient-echo imaging. *Magnetic Resonance in Medicine*. 1992; 23: 193-200.
71. Chen NK and Wyrwicz AM. Removal of intravoxel dephasing artifact in gradient-echo images using a field-map based RF refocusing technique. *Magnetic Resonance in Medicine*. 1999; 42: 807-12.
72. Fernandez-Seara MA and Wehrli FW. Postprocessing technique to correct for background gradients in image-based R2* measurements. *Magnetic Resonance in Medicine*. 2000; 44: 358-66.
73. Bartzokis G, Beckson M, Hance DB, Marx P, Foster JA and Marder SR. MR evaluation of age-related increase of brain iron in young adult and older normal males. *Magnetic Resonance Imaging*. 1997; 15: 29-35.
74. Sedlacik J, Boelmans K, Lobel U, Holst B, Siemonsen S and Fiehler J. Reversible, irreversible and effective transverse relaxation rates in normal aging brain at 3T. *Neuroimage*. 2014; 84: 1032-41.
75. Ropele S, Kilsdonk ID, Wattjes MP, et al. Determinants of iron accumulation in deep grey matter of multiple sclerosis patients. *Multiple Sclerosis Journal*. 2014; 20: 1692-8.
76. Bartzokis G, Sultzer D, Mintz J, et al. In-vivo evaluation of brain iron in Alzheimers-disease and normal subjects using MRI. *Biological Psychiatry*. 1994; 35: 480-7.
77. Ordidge RJ, Gorell JM, Deniau JC, Knight RA and Helpert JA. Assessment of relative brain iron concentrations using T2-weighted and T2*-weighted MRI at 3 Tesla. *Magnetic Resonance in Medicine*. 1994; 32: 335-41.
78. Vymazal J, Righini A, Brooks RA, et al. T1 and T2 in the brain of healthy subjects, patients with Parkinson disease, and patients with multiple system atrophy: Relation to iron content. *Radiology*. 1999; 211: 489-95.
79. Frederic H. Martini JLN, Edwin F. Bartholomew. *Fundamentals of Anatomy & Physiology*. 9th edition ed.: Benjamin Cummings, 2011.
80. Youdim MBH, Benschachar D and Riederer P. Iron in brain-function and dysfunction with emphasis on Parkinsons-disease. *European Neurology*. 1991; 31: 34-40.

81. Benarroch EE. Brain iron homeostasis and neurodegenerative disease. *Neurology*. 2009; 72: 1436-40.
82. Hallgren B and Sourander P. The effect of age on the non-haemin iron in the human brain. *Journal of Neurochemistry*. 1958; 3: 41-51.
83. Brooks RA, Vymazal J, Goldfarb RB, Bulte JWM and Aisen P. Relaxometry and magnetometry of ferritin. *Magnetic Resonance in Medicine*. 1998; 40: 227-35.
84. Andrews SC, Arosio P, Bottke W, et al. Structure, function, and evolution of ferritins. *Journal of Inorganic Biochemistry*. 1992; 47: 161-74.
85. Makhlof SA, Parker FT and Berkowitz AE. Magnetic hysteresis anomalies in ferritin. *Physical Review B*. 1997; 55: 14717-20.
86. Cowley JM, Janney DE, Gerkin RC and Buseck PR. The structure of ferritin cores determined by electron nanodiffraction. *Journal of Structural Biology*. 2000; 131: 210-6.
87. S C Andrews AT, and P M Harrison. Siderosomal ferritin. The missing link between ferritin and haemosiderin? *Biochem J*. 1987: 439-46
88. Drayer B, Burger P, Darwin R, Riederer S, Herfkens R and Johnson G. MRI of brain iron. *American Journal of Roentgenology*. 1986; 147: 103-10.
89. Connor JR, Menzies SL, Stmartin SM and Mufson EJ. Cellular-distribution of transferrin, ferritin, and iron in normal and aged human brains. *Journal of Neuroscience Research*. 1990; 27: 595-611.
90. Koppenol WH. The Haber-Weiss cycle - 70 years later. *Redox Rep*. 2001; 6: 229-34.
91. Galaris D and Pantopoulos K. Oxidative stress and iron homeostasis: Mechanistic and health aspects. *Critical Reviews in Clinical Laboratory Sciences*. 2008; 45: 1-23.
92. Kell DB. Iron behaving badly: inappropriate iron chelation as a major contributor to the aetiology of vascular and other progressive inflammatory and degenerative diseases. *Bmc Medical Genomics*. 2009; 2.

93. Dexter DT, Carayon A, Javoyagid F, et al. Alterations in the levels of iron, ferritin and other trace-metals in parkinsons-disease and other neurodegenerative diseases affecting the basal ganglia. *Brain*. 1991; 114: 1953-75.
94. Bartzokis G, Aravagiri M, Oldendorf WH, Mintz J and Marder SR. Field dependent transverse relaxation rate increase may be a specific measure of tissue iron stores. *Magnetic Resonance in Medicine*. 1993; 29: 459-64.
95. Sullivan EV, Adalsteinsson E, Rohlfing T and Pfefferbaum A. Relevance of Iron Deposition in Deep Gray Matter Brain Structures to Cognitive and Motor Performance in Healthy Elderly Men and Women: Exploratory Findings. *Brain Imaging and Behavior*. 2009; 3: 167-75.
96. Parsey RV and Krishnan KRR. A new MRI ratio method for in-vivo estimation of signal hypointensity in aging and Alzheimer's disease. *Progress in Neuro-Psychopharmacology & Biological Psychiatry*. 1997; 21: 1257-67.
97. Schenck JF. Imaging of brain iron by magnetic resonance: T2 relaxation at different field strengths. *Journal of the Neurological Sciences*. 1995; 134: 10-8.
98. Compston A and Coles A. Multiple sclerosis. *Lancet*. 2008; 372: 1502-17.
99. Rosati G. The prevalence of multiple sclerosis in the world: an update. *Neurological Sciences*. 2001; 22: 117-39.
100. Kurtzke JF. Multiple sclerosis in time and space: Geographic clues to cause. *Journal of Neurovirology*. 2000; 6: S134-S40.
101. Beck CA, Metz LM, Svenson LW and Patten SB. Regional variation of multiple sclerosis prevalence in Canada. *Multiple sclerosis*. 2005; 11: 516-9.
102. Compston A and Coles A. Multiple sclerosis *Lancet*. 2002; 360: 648-.
103. Kurtzke JF. Rating Neurologic Impairment In Multiple-Sclerosis - An Expanded Disability Status Scale (EDSS). *Neurology*. 1983; 33: 1444-52.
104. Lassmann H, Brueck W and Lucchinetti CF. The immunopathology of multiple sclerosis: An overview. *Brain Pathology*. 2007; 17: 210-8.

105. Fransson ME, Liljenfeldt LSE, Fagius J, Totterman TH and Loskog ASI. The T-cell pool is anergized in patients with multiple sclerosis in remission. *Immunology*. 2009; 126: 92-101.
106. Benveniste EN. Role of macrophages/microglia in multiple sclerosis and experimental allergic encephalomyelitis. *Journal of Molecular Medicine-Jmm*. 1997; 75: 165-73.
107. Kirov II, Patil V, Babb JS, Rusinek H, Herbert J and Gonen O. MR spectroscopy indicates diffuse multiple sclerosis activity during remission. *Journal of Neurology Neurosurgery and Psychiatry*. 2009; 80: 1330-6.
108. Vercellino M, Masera S, Lorenzatti M, et al. Demyelination, Inflammation, and Neurodegeneration in Multiple Sclerosis Deep Gray Matter. *Journal of Neuropathology and Experimental Neurology*. 2009; 68: 489-502.
109. Ormerod IEC, Bronstein A, Rudge P, et al. Magnetic-Resonance-Imaging In Clinically Isolated Lesions Of The Brain-Stem. *Journal of Neurology Neurosurgery and Psychiatry*. 1986; 49: 737-43.
110. Vanwalderveen MAA, Barkhof F, Hommes OR, et al. Correlating MRI and clinical-disease activity in Multiple-Sclerosis - relevance of hypointense lesions on short-TR short-TE (T1-weighted) spin-echo images. *Neurology*. 1995; 45: 1684-90.
111. Miki Y, Grossman RI, Udupa JK, et al. Relapsing-remitting multiple sclerosis: Longitudinal analysis of MR images - Lack of correlation between changes in T2 lesion volume and clinical findings. *Radiology*. 1999; 213: 395-9.
112. Henkelman RM, Stanisz GJ and Graham SJ. Magnetization transfer in MRI: a review. *NMR in Biomedicine*. 2001; 14: 57-64.
113. Schmierer K, Wheeler-Kingshott CAM, Tozer DJ, et al. Quantitative magnetic resonance of postmortem multiple sclerosis brain before and after fixation. *Magnetic Resonance in Medicine*. 2008; 59: 268-77.
114. Mackay A, Whittall K, Adler J, Li D, Paty D and Graeb D. In-Vivo Visualization Of Myelin Water In Brain By Magnetic-Resonance. *Magnetic Resonance in Medicine*. 1994; 31: 673-7.

115. Laule C, Vavasour IM, Moore GRW, et al. Water content and myelin water fraction in multiple sclerosis - A T2 relaxation study. *Journal of neurology*. 2004; 251: 284-93.
116. Hammond KE, Metcalf M, Carvajal L, et al. Quantitative In Vivo Magnetic Resonance Imaging of Multiple Sclerosis at 7 Tesla with Sensitivity to Iron. *Annals of Neurology*. 2008; 64: 707-13.
117. Haacke EM, Makki M, Ge Y, et al. Characterizing Iron Deposition in Multiple Sclerosis Lesions Using Susceptibility Weighted Imaging. *Journal of Magnetic Resonance Imaging*. 2009; 29: 537-44.
118. Eissa A, Lebel RM, Korzan JR, et al. Detecting Lesions in Multiple Sclerosis at 4.7 Tesla Using Phase Susceptibility-Weighting and T2-Weighting. *Journal of Magnetic Resonance Imaging*. 2009; 30: 737-42.
119. Craelius W, Migdal M, Luessenhop C, Sugar A and Mihalakis I. Iron deposits surrounding multiple sclerosis plaques. *Archives of pathology & laboratory medicine*. 1982; 106: 397.
120. Anderson VM, Fox NC and Miller DH. Magnetic resonance imaging measures of brain atrophy in multiple sclerosis. *Journal of Magnetic Resonance Imaging*. 2006; 23: 605-18.
121. Bermel RA and Bakshi R. The measurement and clinical relevance of brain atrophy in multiple sclerosis. *Lancet neurology*. 2006; 5: 158-70.
122. Coffey CE, Wilkinson WE, Parashos IA, et al. Quantitative cerebral anatomy of the aging human brain - a cross-sectional study using magnetic resonance imaging. *Neurology*. 1992; 42: 527-36.
123. Kalkers NF, Ameziane N, Bot JCJ, Minneboo A, Polman CH and Barkhof F. Longitudinal brain volume measurement in multiple sclerosis - Rate of brain atrophy is independent of the disease subtype. *Archives of Neurology*. 2002; 59: 1572-6.
124. Dalton CM, Miskiel KA, O'Connor PW, Plant GT, Rice GPA and Miller DH. Ventricular enlargement in MS - One-year change at various stages of disease. *Neurology*. 2006; 66: 693-8.

125. De Stefano N, Cocco E, Lai M, et al. Imaging brain damage in first-degree relatives of sporadic and familial multiple sclerosis. *Annals of Neurology*. 2006; 59: 634-9.
126. Fisniku LK, Chard DT, Jackson JS, et al. Gray matter atrophy is related to long-term disability in multiple sclerosis. *Annals of Neurology*. 2008; 64: 247-54.
127. Fisher E, Lee JC, Nakamura K and Rudick RA. Gray matter atrophy in multiple sclerosis: A longitudinal study. *Annals of Neurology*. 2008; 64: 255-65.
128. Roosendaal SD, Bendfeldt K, Vrenken H, et al. Grey matter volume in a large cohort of MS patients: relation to MRI parameters and disability. *Multiple Sclerosis Journal*. 2011; 17: 1098-106.
129. Henry RG, Shieh M, Okuda DT, Evangelista A, Gorno-Tempini ML and Pelletier D. Regional grey matter atrophy in clinically isolated syndromes at presentation. *Journal of Neurology Neurosurgery and Psychiatry*. 2008; 79: 1236-44.
130. Zivadinov R, Havrdova E, Bergsland N, et al. Thalamic Atrophy Is Associated with Development of Clinically Definite Multiple Sclerosis. *Radiology*. 2013; 268: 831-41.
131. Audoin B, Zaaraoui W, Reuter F, et al. Atrophy mainly affects the limbic system and the deep grey matter at the first stage of multiple sclerosis. *Journal of Neurology Neurosurgery and Psychiatry*. 2010; 81: 690-5.
132. Bergsland N, Horakova D, Dwyer MG, et al. Subcortical and Cortical Gray Matter Atrophy in a Large Sample of Patients with Clinically Isolated Syndrome and Early Relapsing-Remitting Multiple Sclerosis. *American Journal of Neuroradiology*. 2012; 33: 1573-8.
133. Calabrese M, Rinaldi F, Mattisi I, et al. The predictive value of gray matter atrophy in clinically isolated syndromes. *Neurology*. 2011; 77: 257-63.
134. Filippi M and Agosta F. Imaging Biomarkers in Multiple Sclerosis. *Journal of Magnetic Resonance Imaging*. 2010; 31: 770-88.
135. Khalil M, Langkammer C, Pichler A, et al. Dynamics of brain iron levels in multiple sclerosis A longitudinal 3T MRI study. *Neurology*. 2015: 2396-402.
136. Pelletier D, Garrison K and Henry R. Measurement of whole-brain atrophy in multiple sclerosis. *Journal of Neuroimaging*. 2004; 14: 11S-9S.

137. Bermel RA, Puli SR, Fabiano AJ, et al. Gray matter MRI T2 hypointensity predicts longitudinal brain atrophy in multiple sclerosis: Effect of intramuscular interferon beta-1a treatment. *Neurology*. 2003; 60: A422-A.
138. Horsfield MA, Rovaris M, Rocca MA, et al. Whole-brain atrophy in multiple sclerosis measured by two segmentation processes from various MRI sequences. *Journal of the Neurological Sciences*. 2003; 216: 169-77.
139. Smith SM, Zhang YY, Jenkinson M, et al. Accurate, robust, and automated longitudinal and cross-sectional brain change analysis. *Neuroimage*. 2002; 17: 479-89.
140. Smith SM. Fast robust automated brain extraction. *Hum Brain Mapp*. 2002; 17: 143-55.
141. Smith SM, De Stefano N, Jenkinson M and Matthews PM. Normalized accurate measurement of longitudinal brain change. *Journal of Computer Assisted Tomography*. 2001; 25: 466-75.
142. Patenaude B, Smith SM, Kennedy DN and Jenkinson M. A Bayesian model of shape and appearance for subcortical brain segmentation. *Neuroimage*. 2011; 56: 907-22.
143. Williams R, Buchheit CL, Berman NEJ and LeVine SM. Pathogenic implications of iron accumulation in multiple sclerosis. *Journal of Neurochemistry*. 2012; 120: 7-25.
144. Drayer B, Burger P, Hurwitz B, Dawson D and Cain J. Reduced signal intensity on MR images of thalamus and putamen in multiple sclerosis: increased iron content? *American Journal of Roentgenology*. 1987; 149: 357-63.
145. Hametner S, Wimmer I, Haider L, Pfeifenbring S, Brueck W and Lassmann H. Iron and Neurodegeneration in the Multiple Sclerosis Brain. *Annals of Neurology*. 2013; 74: 848-61.
146. Haacke EM, Chengb NYC, House MJ, et al. Imaging iron stores in the brain using magnetic resonance imaging. *Magnetic Resonance Imaging*. 2005; 23: 1-25.
147. Neema M, Arora A, Healy BC, et al. Deep Gray Matter Involvement on Brain MRI Scans Is Associated with Clinical Progression in Multiple Sclerosis. *Journal of Neuroimaging*. 2009; 19: 3-8.
148. Khalil M, Langkammer C, Ropele S, et al. Determinants of brain iron in multiple sclerosis A quantitative 3T MRI study. *Neurology*. 2011; 77: 1691-7.

149. Hagemeyer J, Weinstock-Guttman B, Heininen-Brown M, et al. Gray matter SWI-filtered phase and atrophy are linked to disability in MS. *Frontiers in bioscience (Elite edition)*. 2013; 5: 525-32.
150. Zhang Y, Metz LM, Yong VW and Mitchell JR. 3 T deep gray matter T2 hypointensity correlates with disability over time in stable relapsing-remitting multiple sclerosis: A 3-year pilot study. *Journal of the Neurological Sciences*. 2010; 297: 76-81.
151. Langkammer C, Liu T, Khalil M, et al. Quantitative Susceptibility Mapping in Multiple Sclerosis. *Radiology*. 2013; 267: 551-9.
152. Walsh AJ, Blevins G, Lebel RM, Seres P, Emery DJ and Wilman AH. Longitudinal MR Imaging of Iron in Multiple Sclerosis: An Imaging Marker of Disease. *Radiology*. 2014; 270: 186-96.
153. Jacobsen C, Hagemeyer J, Myhr K-M, et al. Brain atrophy and disability progression in multiple sclerosis patients: a 10-year follow-up study. *Journal of neurology, neurosurgery, and psychiatry*. 2014; 85: 1109-15.
154. Zivadinov R, Bergsland N, Dolezal O, et al. Evolution of Cortical and Thalamus Atrophy and Disability Progression in Early Relapsing-Remitting MS during 5 Years. *American Journal of Neuroradiology*. 2013; 34: 1931-9.
155. Polman CH, Reingold SC, Edan G, et al. Diagnostic criteria for multiple sclerosis: 2005 Revisions to the "McDonald Criteria". *Annals of Neurology*. 2005; 58: 840-6.
156. Rasband W. ImageJ. US National Institutes of Health, Bethesda, Maryland, USA1997-2011.
157. Smith SM, Jenkinson M, Woolrich MW, et al. Advances in functional and structural MR image analysis and implementation as FSL. *Neuroimage*. 2004; 23: S208-S19.
158. Roxburgh R, Seaman SR, Masterman T, et al. Multiple sclerosis severity score - Using disability and disease duration to rate disease severity. *Neurology*. 2005; 64: 1144-51.
159. Walsh AJ, Lebel RM, Eissa A, et al. Multiple Sclerosis: Validation of MR Imaging for Quantification and Detection of Iron. *Radiology*. 2013; 267: 531-42.

160. Langkammer C, Krebs N, Goessler W, et al. Quantitative MR imaging of brain iron: a postmortem validation study. *Radiology*. 2010; 257: 455-62.
161. Stankiewicz J, Panter SS, Neema M, Arora A, Batt CE and Bakshi R. Iron in chronic brain disorders: imaging and neurotherapeutic implications. *Neurotherapeutics : the journal of the American Society for Experimental NeuroTherapeutics*. 2007; 4: 371-86.
162. Magnano C, Schirda C, Weinstock-Guttman B, et al. Cine cerebrospinal fluid imaging in multiple sclerosis. *Journal of Magnetic Resonance Imaging*. 2012; 36: 825-34.
163. Onyszchuk G, LeVine SM, Brooks WM and Berman NE. Post-acute pathological changes in the thalamus and internal capsule in aged mice following controlled cortical impact injury: a magnetic resonance imaging, iron histochemical, and glial immunohistochemical study. *Neuroscience letters*. 2009; 452: 204-8.
164. Wylezinska M, Cifelli A, Jezard P, Palace J, Alecci M and Matthews PM. Thalamic neurodegeneration in relapsing-remitting multiple sclerosis. *Neurology*. 2003; 60: 1949-54.
165. Uddin MN, Lebel RM and Wilman AH. Transverse Relaxometry with Reduced Echo Train Lengths via Stimulated Echo Compensation. *Magnetic Resonance in Medicine*. 2013; 70: 1340-6.
166. McPhee KC and Wilman AH. T2 quantification from only proton density and T2-weighted MRI by modelling actual refocusing angles. *Neuroimage*. 2015: 642-50.
167. Ge Y, Jensen JH, Lu H, et al. Quantitative assessment of iron accumulation in the deep gray matter of multiple sclerosis by magnetic field correlation imaging. *American Journal of Neuroradiology*. 2007; 28: 1639-44.
168. Bakshi R, Benedict RHB, Bermel RA, et al. T2 hypointensity in the deep gray matter of patients with multiple sclerosis - A quantitative magnetic resonance imaging study. *Archives of Neurology*. 2002; 59: 62-8.
169. Ceccarelli A, Rocca MA, Neema M, et al. Deep gray matter T2 hypointensity is present in patients with clinically isolated syndromes suggestive of multiple sclerosis. *Multiple sclerosis*. 2010; 16: 39-44.

170. Laule C, Vavasour IM, Kolind SH, et al. Long T2 water in multiple sclerosis: What else can we learn from multi-echo T2 relaxation? *Journal of neurology*. 2007; 254: 1579-87.
171. St Pierre TG, Clark PR, Chua-Anusorn W, et al. Noninvasive measurement and imaging of liver iron concentrations using proton magnetic resonance. *Blood*. 2005; 105: 855-61.
172. Pai A, Li X and Majumdar S. A comparative study at 3 T of sequence dependence of T2 quantitation in the knee. *Magnetic Resonance Imaging*. 2008; 26: 1215-20.
173. Maier CF, Tan SG, Hariharan H and Potter HG. T2 quantitation of articular cartilage at 1.5 T. *Journal of Magnetic Resonance Imaging*. 2003; 17: 358-64.
174. Papakonstantinou O, Kostaridou S, Maris T, et al. Quantification of liver iron overload by T2 quantitative magnetic resonance imaging in thalassemia: impact of chronic hepatitis C on measurements. *J Pediatr Hematol Oncol* 1999; 21: 142-8.
175. Horch RA, Nyman JS, Gochberg DF, Dortch RD and Does MD. Characterization of 1H NMR signal in human cortical bone for magnetic resonance imaging. *Magnetic Resonance in Medicine*. 2010; 64: 680-7.
176. Reiter DA, Lin P-C, Fishbein KW and Spencer RG. Multicomponent T2 Relaxation Analysis in Cartilage. *Magnetic Resonance in Medicine*. 2009; 61: 803-9.
177. Vaughan JT, Garwood M, Collins C, et al. 7T vs. 4T: RF power, homogeneity, and signal-to-noise comparison in head images. *Magnetic Resonance in Medicine*. 2001; 46: 24-30.
178. Watanabe H, Takaya N and Mitsumori F. Non-uniformity correction of human brain imaging at high field by RF field mapping of B(1)(+) and B(1)(-). *Journal of Magnetic Resonance*. 2011; 212: 426-30.
179. Does MD and Snyder RE. Multiecho imaging with suboptimal spoiler gradients. *Journal of Magnetic Resonance*. 1998; 131: 25-31.
180. Pell GS, Briellmann RS, Waites AB, Abbott DF, Lewis DP and Jackson GD. Optimized clinical T2 relaxometry with a standard CPMG sequence. *Journal of Magnetic Resonance Imaging*. 2006; 23: 248-52.
181. Anastasiou A and Hall LD. Optimisation of T2 and M0 measurements of bi-exponential systems. *Magnetic Resonance Imaging*. 2004; 22: 67-80.

182. Carmichael DW, Thomas DL, De Vita E, et al. Improving whole brain structural MRI at 4.7 Tesla using 4 irregularly shaped receiver coils. *Neuroimage*. 2006; 32: 1176-84.
183. Tang L, Hue Y-K and Ibrahim TS. Studies of RF Shimming Techniques with Minimization of RF Power Deposition and Their Associated Temperature Changes. *Concepts in Magnetic Resonance Part B-Magnetic Resonance Engineering*. 2011; 39B: 11-25.
184. Mao W, Smith MB and Collins CM. Exploring the limits of RF shimming for high-field MRI of the human head. *Magnetic Resonance in Medicine*. 2006; 56: 918-22.
185. Vavasour IM, Whittall KP, Li DKB and MacKay AL. Different magnetization transfer effects exhibited by the short and long T2 components in human brain. *Magnetic Resonance in Medicine*. 2000; 44: 860-6.
186. Melki PS and Mulkern RV. Magnetization transfer effects in multislice RARE sequences. *Magnetic Resonance in Medicine*. 1992; 24: 189-95.
187. Lebel RM and Wilman AH. Time efficient fast spin echo imaging at 4.7 T with low refocusing angles. *Magnetic Resonance in Medicine*. 2009; 62: 96-105.
188. Stanisz GJ, Odrobina EE, Pun J, et al. T1, T2 relaxation and magnetization transfer in tissue at 3T. *Magnetic Resonance in Medicine*. 2005; 54: 507-12.
189. Santyr GE. Magnetization transfer effects in multislice MR imaging. *Magnetic Resonance Imaging*. 1993; 11: 521-32.
190. Dixon WT, Engels H, Castillo M and Sardashti M. Incidental magnetization transfer contrast in standard multislice imaging. *Magnetic Resonance Imaging*. 1990; 8: 417-22.
191. MacMillan EL, Maedler B, Fichtner N, et al. Myelin water and T2 relaxation measurements in the healthy cervical spinal cord at 3.0T: Repeatability and changes with age. *Neuroimage*. 2011; 54: 1083-90.
192. Whittall KP, MacKay AL and Li DKB. Are mono-exponential fits to a few echoes sufficient to determine T-2 relaxation for in vivo human brain? *Magnetic Resonance in Medicine*. 1999; 41: 1255-7.
193. Zecca L, Youdim MB, Riederer P, Connor JR and Crichton RR. Iron, brain ageing and neurodegenerative disorders. *Nature reviews Neuroscience*. 2004; 5: 863-73.

194. Gossuin Y, Muller RN and Gillis P. Relaxation induced by ferritin: a better understanding for an improved MRI iron quantification. *NMR in Biomedicine*. 2004; 17: 427-32.
195. Birkl C, Langkammer C, Krenn H, et al. Iron mapping using the temperature dependency of the magnetic susceptibility. *Magnetic Resonance in Medicine*. 2015; 73: 1282-8.
196. Berg D and Youdim MBH. Role of iron in neurodegenerative disorders. *Topics in Magnetic Resonance Imaging*. 2006; 17: 5-17.
197. Bizzi A, Brooks RA, Brunetti A, et al. Role of iron and ferritin in MR Imaging of the brain - a study in primates at different field strengths. *Radiology*. 1990; 177: 59-65.
198. Vymazal J, Zak O, Bulte JWM, Aisen P and Brooks RA. T1 and T2 of ferritin solutions: Effect of loading factor. *Magnetic Resonance in Medicine*. 1996; 36: 61-5.
199. Graham JM, Paley MNJ, Grunewald RA, Hoggard N and Griffiths PD. Brain iron deposition in Parkinson's disease imaged using the PRIME magnetic resonance sequence. *Brain*. 2000; 123: 2423-31.
200. Wallis LI, Paley MNJ, Graham JM, et al. MRI Assessment of Basal Ganglia Iron Deposition in Parkinson's Disease. *Journal of Magnetic Resonance Imaging*. 2008; 28: 1061-7.
201. Duyn JH, Van Gelderen P, Li TQ, De Zwart JA, Koretsky AP and Fukunaga M. High-field MRI of brain cortical substructure based on signal phase. *Proceedings of the National Academy of Sciences*. 2007; 104: 11796-801.
202. Hikita T, Abe K, Sakoda S, Tanaka H, Murase K and Fujita N. Determination of transverse relaxation rate for estimating iron deposits in central nervous system. *Neuroscience Research*. 2005; 51: 67-71.
203. Sati P, van Gelderen P, Silva AC, et al. Micro-compartment specific T2* relaxation in the brain. *Neuroimage*. 2013; 77: 268-78.
204. Sedlacik J, Kutschbach C, Rauscher A, Deistung A and Reichenbach JR. Investigation of the influence of carbon dioxide concentrations on cerebral physiology by susceptibility-weighted magnetic resonance imaging (SWI). *Neuroimage*. 2008; 43: 36-43.
205. Li TQ, Yao B, van Gelderen P, et al. Characterization of T2* Heterogeneity in Human Brain White Matter. *Magnetic Resonance in Medicine*. 2009; 62: 1652-7.

206. Bartzokis G, Sultzer D, Cummings J, et al. In vivo evaluation of brain iron in Alzheimer disease using magnetic resonance imaging. *Archives of General Psychiatry*. 2000; 57: 47-53.
207. Langkammer C, Krebs N, Goessler W, et al. Susceptibility induced gray-white matter MRI contrast in the human brain. *Neuroimage*. 2012; 59: 1413-9.
208. Schenker C, Meier D, Wichmann W, Boesiger P and Valavanis A. Age Distribution And Iron Dependency Of The T2 Relaxation Time In The Globus-Pallidus And Putamen. *Neuroradiology*. 1993; 35: 119-24.
209. Bartzokis G, Tishler TA, Lu PH, et al. Brain ferritin iron may influence age- and gender-related risks of neurodegeneration. *Neurobiology of Aging*. 2007; 28: 414-23.
210. Hasan KM, Walimuni IS, Kramer LA and Narayana PA. Human brain iron mapping using atlas-based T2 relaxometry. *Magnetic Resonance in Medicine*. 2012; 67: 731-9.
211. Vymazal J, Brooks RA, Zak O, McRill C, Shen C and Dichiro G. T1 and T2 of ferritin at different field strengths -effect on MRI. *Magnetic Resonance in Medicine*. 1992; 27: 368-74.
212. Jensen JH and Chandra R. Strong field behavior of the NMR signal from magnetically heterogeneous tissues. *Magnetic Resonance in Medicine*. 2000; 43: 226-36.
213. Reichenbach JR, Venkatesan R, Yablonskiy DA, Thompson MR, Lai S and Haacke EM. Theory and application of static field inhomogeneity effects in gradient-echo imaging. *Journal of Magnetic Resonance Imaging*. 1997; 7: 266-79.
214. Pfefferbaum A, Adalsteinsson E, Rohlfing T and Sullivan EV. MRI estimates of brain iron concentration in normal aging: comparison of field-dependent (FDRI) and phase (SWI) methods. *Neuroimage*. 2009; 47: 493-500.
215. Bartzokis G and Tishler TA. MRI evaluation of basal ganglia ferritin iron and neurotoxicity in Alzheimer's and Huntington's disease. *Cellular and Molecular Biology*. 2000; 46: 821-33.
216. Graham SJ, Stanchev PL and Bronskill MJ. Criteria for analysis of multicomponent tissue T2 relaxation data. *Magnetic Resonance in Medicine*. 1996; 35: 370-8.

217. Paling D, Tozer D, Wheeler-Kingshott C, Kapoor R, Miller DH and Golay X. Reduced R2' in multiple sclerosis normal appearing white matter and lesions may reflect decreased myelin and iron content. *Journal of Neurology Neurosurgery and Psychiatry*. 2012; 83: 785-92.
218. Connor JR, Snyder BS, Beard JL, Fine RE and Mufson EJ. Regional distribution of iron and iron-regulatory proteins in the brain in aging and Alzheimer's disease. *Journal of Neuroscience Research*. 1992; 31: 327-35.
219. Curnes JT, Burger PC, Djang WT and Boyko OB. MR Imaging of compact white matter pathways. *American Journal of Neuroradiology*. 1988; 9: 1061-8.
220. Duyn J. MR susceptibility imaging. *Journal of Magnetic Resonance*. 2013; 229: 198-207.
221. Li TQ, van Gelderen P, Merkle H, Talagala L, Koretsky AP and Duyn J. Extensive heterogeneity in white matter intensity in high-resolution T2*-weighted MRI of the human brain at 7.0 T. *Neuroimage*. 2006; 32: 1032-40.
222. Denk C, Hernandez Torres E, MacKay A and Rauscher A. The influence of white matter fibre orientation on MR signal phase and decay. *NMR in Biomedicine*. 2011; 24: 246-52.
223. Rudko DA, Klassen LM, de Chickera SN, Gati JS, Dekaban GA and Menon RS. Origins of R2* orientation dependence in gray and white matter. *Proceedings of the National Academy of Sciences of the United States of America*. 2014; 111: E159-E67.
224. Grohn HI, Michaeli S, Garwood M, Kauppinen RA and Grohn OHJ. Quantitative T1p and adiabatic Carr-Purcell T2 magnetic resonance imaging of human occipital lobe at 4 T. *Magnetic Resonance in Medicine*. 2005; 54: 14-9.
225. Lebel RM and Wilman AH. Field-corrected 3D multiecho gradient echo: Simultaneous extraction of quantitative R2*, T2* weighting, SWI, and venography. *Joint Annual Meeting of ISMRM-ESMRMB*. Stockholm, Sweden 2010, p. 5002.
226. Peran P, Cherubini A, Luccichenti G, et al. Volume and Iron Content in Basal Ganglia and Thalamus. *Hum Brain Mapp*. 2009; 30: 2667-75.
227. Poynton C, Jenkinson M, Adalsteinsson E, Sullivan EV, Pfefferbaum A and Wells W. Quantitative Susceptibility Mapping by Inversion of a Perturbation Field Model: Correlation with Brain Iron in Normal Aging. *IEEE Transactions On Medical Imaging* 2015; 34: 339-53.

228. Vavasour IM, Whittall KP, MacKay AL, Li DKB, Vorobeychik G and Paty DW. A comparison between magnetization transfer ratios and myelin water percentages in normals and multiple sclerosis patients. *Magnetic Resonance in Medicine*. 1998; 40: 763-8.
229. Levesque IR, Chia CLL and Pike GB. Reproducibility of In Vivo Magnetic Resonance Imaging-Based Measurement of Myelin Water. *Journal of Magnetic Resonance Imaging*. 2010; 32: 60-8.
230. Sati P, Silva AC, van Gelderen P, et al. In vivo quantification of T2* anisotropy in white matter fibers in marmoset monkeys. *Neuroimage*. 2012; 59: 979-85.
231. Stephenson E, Nathoo N, Mahjoub Y, Dunn JF and Yong VW. Iron in multiple sclerosis: roles in neurodegeneration and repair. *Nature Reviews Neurology*. 2014; 10: 459-68.
232. Benedict RH, Ramasamy D, Munschauer F, Weinstock-Guttman B and Zivadinov R. Memory impairment in multiple sclerosis: correlation with deep grey matter and mesial temporal atrophy. *Journal of Neurology, Neurosurgery & Psychiatry*. 2009; 80: 201-6.
233. Liang AL, Vavasour IM, Mädler B, et al. Short-term stability of T 1 and T 2 relaxation measures in multiple sclerosis normal appearing white matter. *Journal of neurology*. 2012; 259: 1151-8.
234. Stollberger R and Wach P. Imaging of the active B-1 field in vivo. *Magnetic Resonance in Medicine*. 1996; 35: 246-51.
235. Bakshi R, Dmochowski J, Shaikh ZA and Jacobs L. Gray matter T2 hypointensity is related to plaques and atrophy in the brains of multiple sclerosis patients. *Journal of the Neurological Sciences*. 2001; 185: 19-26.
236. Neema M, Stankiewicz J, Arora A, et al. T1 and T2 based MRI measures of diffuse gray matter and white matter damage in patients with multiple sclerosis. *Journal of Neuroimaging*. 2007; 17: 16S-21S.
237. Cobzas D, Sun H, Walsh AJ, Lebel RM, Blevins G and Wilman AH. Subcortical gray matter segmentation and voxel-based analysis using transverse relaxation and quantitative susceptibility mapping with application to multiple sclerosis. *Journal of Magnetic Resonance Imaging*. 2015.

238. Benedict RH, Bruce JM, Dwyer MG, et al. Neocortical atrophy, third ventricular width, and cognitive dysfunction in multiple sclerosis. *Archives of Neurology*. 2006; 63: 1301-6.
239. Lukas C, Minneboo A, De Groot V, et al. Early central atrophy rate predicts 5 year clinical outcome in multiple sclerosis. *Journal of Neurology, Neurosurgery & Psychiatry*. 2010; jnnp. 2009.199968.
240. Popescu V, Agosta F, Hulst HE, et al. Brain atrophy and lesion load predict long term disability in multiple sclerosis. *Journal of Neurology, Neurosurgery & Psychiatry*. 2013; 84: 1082-91.
241. Rocca MA, Mesaros S, Pagani E, Sormani MP, Comi G and Filippi M. Thalamic Damage and Long-term Progression of Disability in Multiple Sclerosis 1. *Radiology*. 2010; 257: 463-9.
242. Uddin MN, Lebel RM, Seres P, Blevins G and Wilman AH. Spin echo transverse relaxation and atrophy in multiple sclerosis deep gray matter: A two-year longitudinal study. *Multiple Sclerosis Journal*. 2015: 1-11.
243. Prasloski T, Rauscher A, MacKay AL, et al. Rapid whole cerebrum myelin water imaging using a 3D GRASE sequence. *Neuroimage*. 2012; 63: 533-9.
244. Zhang J, Kolind SH, Laule C and MacKay AL. Comparison of myelin water fraction from multiecho T2 decay curve and steady-state methods. *Magnetic Resonance in Medicine*. 2015; 73: 223-32.
245. Deoni SC, Rutt BK, Arun T, Pierpaoli C and Jones DK. Gleaning multicomponent T1 and T2 information from steady-state imaging data. *Magnetic Resonance in Medicine*. 2008; 60: 1372-87.
246. Sun H, Walsh AJ, Lebel RM, et al. Validation of quantitative susceptibility mapping with Perls' iron staining for subcortical gray matter. *Neuroimage*. 2015; 105: 486-92.
247. Craelius W, Migdal MW, Luessenhop CP, Sugar A and Mihalakis I. Iron deposits surrounding multiple-sclerosis plaques. *Archives of pathology & laboratory medicine*. 1982; 106: 397-9.

248. Hagemeyer J, Heininen-Brown M, Poloni GU, et al. Iron deposition in multiple sclerosis lesions measured by susceptibility-weighted imaging filtered phase: A case control study. *Journal of Magnetic Resonance Imaging*. 2012; 36: 73-83.
249. Yao B, Ikonomidou VN, Cantor FK, Ohayon JM, Duyn J and Bagnato F. Heterogeneity of Multiple Sclerosis White Matter Lesions Detected With T2*-Weighted Imaging at 7.0 Tesla. *Journal of Neuroimaging*. 2015.
250. Zamboni P. The big idea: iron-dependent inflammation in venous disease and proposed parallels in multiple sclerosis. *Journal of the Royal Society of Medicine*. 2006; 99: 589-93.